ROBUST GPS ATTITUDE DETERMINATION FOR SPACECRAFT

A DISSERTATION

SUBMITTED TO THE DEPARTMENT OF AERONAUTICS & ASTRONAUTICS

AND THE COMMITTEE ON GRADUATE STUDIES

OF STANFORD UNIVERSITY

IN PARTIAL FULFILLMENT OF THE REQUIREMENTS

FOR THE DEGREE OF

DOCTOR OF PHILOSOPHY

John Carl Adams

December 1999

Copyright © 2000 by John Carl Adams

All Rights Reserved.

I certify that I have read this dissertation and that in my opinion it is fully adequate, in scope and quality, as a dissertation for the degree of Doctor of Philosophy.

Jonathan How

Jonathan P. How
Department of Aeronautics and Astronautics
(Principal Adviser)

I certify that I have read this dissertation and that in my opinion it is fully adequate, in scope and quality, as a dissertation for the degree of Doctor of Philosophy.

J. David Powell
Department of Aeronautics and Astronautics

I certify that I have read this dissertation and that in my opinion it is fully adequate, in scope and quality, as a dissertation for the degree of Doctor of Philosophy.

Per Enge
Department of Aeronautics and Astronautics

Approved for the University Committee on Graduate Studies:

Thomas Wasow

To Family and Friends

Abstract

The space environment presents challenging operating conditions for a GPS attitude receiver. While spacecraft vehicle attitude dynamics may be at a lower rate than terrestrial vehicles or aircraft, spacecraft may undergo a much more general attitude motion. For example, for inertially fixed or spinning spacecraft there is no preferred orientation of an array of antennas with aligned boresights that will give good GPS constellation visibility and ensure continuous attitude solution availability over an entire orbit. For these cases of general vehicle attitude motion, continuous attitude solution availability can be achieved using an array of antennas pointing in different directions. However, such a non-aligned antenna array requires modifications to the receiver signal processing algorithms to make attitude determination possible and to achieve accuracies comparable to an aligned array. Non-aligned antenna arrays introduce LOS dependent phase errors into the differential carrier phase measurements, the most significant of which are; the right hand circular polarization (RHCP) contribution to the carrier phase, antenna phase center variations, and multipath error.

In this dissertation, the results of two experimental laboratory demonstrations of attitude determination using measurements from a non-aligned antenna array are presented, along with a simulation study for the on-orbit case. In the first laboratory demonstration, attitude estimation was done (in post processing) using a passive,

spinning platform with only single degree of freedom rotation, in a laboratory environment that had very significant reflected multipath signals, and near transmitters. The experiment used a 2-D air cushion vehicle on a granite table top with a single antenna baseline measurement. The results of this experiment showed that robust attitude solutions could be attained from differential carrier phase measurements taken from an array of non-aligned antennas, but also highlighted the importance of compensating for the RHCP in the measurement.

A spinning 3-D test platform was also constructed to allow for full motion attitude sensing and closed loop control in a laboratory environment with much larger transmitter distances. The test platform has a non-aligned array of four antennas connected to a center node that is suspended from an overhead cable. The platform has three axis attitude control, and rate gyros to provide attitude truth measurements. This new 3-D experiment platform was used to demonstrate real-time attitude estimation, including real-time measurement bias estimation for periodically occluded measurements. A comparison of two techniques for compensating for the RHCP of the incoming GPS wavefront is presented, one which explicitly includes the RHCP in the measurement model, at the cost of higher computational load, and another method that subtracts the predicted RHCP phase component from the carrier phase measurements. A method for calibrating modeled antenna phase center variation out of the differential carrier phase measurement is demonstrated in simulation for the non-aligned antenna array. The results of this 3D experiment demonstrated that robust, real-time attitude solutions can be derived from differential carrier phase measurements from a set of antennas with non-aligned boresights. The experimental results also demonstrated the improved attitude estimate accuracy that can be achieved by

incorporating dynamic model information for the vehicle into the estimation. Continuous attitude estimates with RMS errors on the order of 0.25°-0.50° were achieved using antenna baselines on the order of 1.0 m, after compensating for the limitations of an indoor GPS laboratory multipath environment.

Acknowledgments

I would first like to thank my primary research advisor, Professor Jonathan How, for the many years of creative input he has given to my research work. Without his enthusiastic guidance and support this project could not have been accomplished.

There are multiple research sponsors who have contributed to this research project. First and foremost I'd like to thank my employer, the Lockheed Martin Missiles and Space, Co., Advanced Technology Center, and in particular Dr. Larry Capots the Director of Advanced Concepts, Larry Burriesci, manager for the Electronics and Controls Organization, and Dr. Ken Lorell, former manager for the Dynamics and Controls Laboratory. Next, I'd like to thank my sponsors at NASA Goddard Spaceflight Center; Dr. Frank Bauer and Dr. E. Glenn Lightsey for their support under the 'GPS-on-a-Chip' program (NAG5-6233).

Also, advice and support was provided by the GPS receiver design group at NASA Jet Propulsion Laboratory under the direction of Tom Meehan, the Charles Stark Draper Laboratories under contract DL-H-505325 with Dr. Timothy Brand as technical monitor, and a research grant from Honeywell.

Many thanks go to my other dissertation reading committee members; Professors Per Enge, and J. David Powell, for their technical insight and encouragement, and to my oral exam committee members Professors Claire Tomlin and Paul Segall.

I would also like to acknowledge my research colleagues in the GPS group for their support, in particular Dr. E. Glenn Lightsey, Dr. Hiro Uematsu, Dr. Kurt Zimmerman, Eric Olsen, Chan Woo Park, Franz Busse, Andrew Roberson, Tobe' Corazzini, Bob Kindel, Jonathan Stone, Roger Hayward, and Rich Fuller. I also want to acknowledge the input I received from Gad Shelef of the Aerospace Robotics Laboratory on mechanical design of my experiment, Aldo Rossi for help in machining the parts, and the assistance I received from Carolyn Edwards and Sally Gressens.

This dissertation is dedicated to all my family and friends who helped me through my graduate school years.

~

Contents

Abstract v

Acknowledgments viii

List of Tables xvii

List of Figures xix

List of Symbols xxvii

List of Acronyms xxxi

1 Introduction 1

1.1 Benefits of Spacecraft GPS Sensing 5

1.1.1 Cost Savings 6

1.1.2 Reliability Improvements 7

1.1.3 Enhanced Autonomy 8

1.2 Research Problem Statement 9

1.2.1 GPS Sensing in Space Environment 9

1.2.2 Goals and Approaches 12

1.3 Previous Work 13

1.3.1 GPS Attitude Determination 14
1.3.2 Spacecraft Flight Experiments 15
1.3.3 Ground Experiments and Analysis 19
1.3.4 Required Extensions to Previous Work 22
1.4 Research Areas 22
1.4.1 Measurement Model 22
1.4.2 Attitude Estimation 23
1.4.3 Satellite/Channel Allocation 24
1.4.4 Signal Acquisition Speed 24
1.5 Enabling Technology 24
1.5.1 Space Station Inspection 25
1.5.2 Distributed Spacecraft Interferometry 26
1.6 Summary of Contributions 27
1.6.1 Improved Measurement Model 27
1.6.2 Real-time Dynamic Attitude Estimation 29
1.6.3 Validation for On-Orbit Case 29

2 GPS Measurement Model **33**
2.1 GPS Sensing Fundamentals 34
2.1.1 GPS Measurement Observables 34
2.1.2 Space Environment 37
2.2 Non-aligned Antenna Array DCP Components 39
2.2.1 DCP Geometry Definition 40
2.2.2 LOS Dependent Phase Components 42
2.2.3 LOS Dependent DCP Compensation 45
2.3 RHCP Model 46

2.3.1 Spherical Trigonometric Model 47
2.3.2 E-field Vector Projection Models 48
2.3.3 Improved Near Transmitter Model 53
2.4 Single Rotation Examples 55
2.4.1 Example 1 - RHCP with Transmitter at Zenith 56
2.4.2 Example 2 - Static Validation Experiment Data 57
2.4.3 Example 3 - Simulation of RHCP DCP vs. LOS 59
2.4.4 Example 4 - RHCP DCP for Near/Far Transmitter 59
2.4.5 Example 5 - RHCP Formulation Comparison 61
2.5 Antenna Phase Center Variation(PCV) Model 62
2.6 Unmodeled DCP Effects 64

3 Attitude Determination Algorithms **67**
3.1 GPS Attitude Determination Basics 68
3.1.1 Far Transmitter Formulations 71
3.1.2 Near Transmitter Formulations 73
3.1.3 ADOP Definition 78
3.2 Extensions to Algorithms 79
3.2.1 Measurement Vector Redundancy 80
3.2.2 Fixed Estimator Size - Selection Matrix 82
3.2.3 Extended Kalman Filter 84
3.2.4 Continuous Bias Re-acquisition 90
3.3 LOS Dependent Phase Compensation 92
3.3.1 Stability of Estimation Algorithm 93
3.3.2 Single Baseline Example 95
3.4 Attitude Simulation Results 98

3.4.1 2D Simulations 99
3.4.2 3D Simulations 102

4 On-Orbit Simulations **105**
4.1 General LEO Mission Study 106
4.2 Satellite/Channel Allocation Simulations 111
4.3 ORION Mission Simulations 116
4.3.1 Signal Acquisition Requirements 118
4.3.2 Antenna Array Requirements 120

5 Laboratory Test Setup **123**
5.1 Near Transmitter Laboratory 126
5.2 2D Laboratory Platform 129
5.2.1 Air-bearing Table Vehicle 129
5.2.2 Modular GPS Receiver - GPSOAC 130
5.3 Far Transmitter Laboratory 135
5.4 3D Laboratory Platform 139
5.4.1 Cable Supported Vehicle 139
5.4.2 Onboard GPS Receiver - ORION 145

6 Laboratory Experiment Results **149**
6.1 2D Laboratory Experiments 150
6.2 3D Laboratory Experiments 154
6.2.1 Open-loop Attitude Estimation - IWLS 154
6.2.2 Open-loop Attitude Estimation - IEKF 159
6.2.3 Closed-loop Attitude Control 161

7 Conclusions and Future Work **163**

7.1 Conclusions 163

7.2 Summary of Contributions 165

7.3 Recommendations for Future Work 166

7.4 Upcoming Spacecraft GPS Missions 167

7.4.1 Gravity Probe-B Mission 168

7.4.2 ORION Formation Flying Mission 169

A GPS Receiver Test Data **171**

A.1 GPSOAC Receiver Tracking Loop Software 171

A.1.1 Tracking Loop Modifications 172

A.1.2 Tracking Loop Tests 173

A.2 ORION Receiver Timing Tests 177

A.2.1 Receiver Synchronization 177

A.2.2 Timing Test Results 178

B Linearized Measurement Matrix with RHCP **181**

Bibliography **195**

~

List of Tables

1.1 Cost savings for applying GPS sensing to spacecraft (NASA GSFC Guidance Navigation and Control Technology Office [FB98]) 6

3.1 CPU Load vs. RHCP Compensation Technique, in units of FLOPS (Floating Point Operations) per iteration. 78

3.2 Simulation results for attitude estimation - Planar 1-DOF Rotation 100

3.3 Simulation results for attitude estimation, 3D General Rotation - *RHCP compensation.* 103

3.4 Simulation results for attitude estimation, 3D General Rotation - *Phase center variation compensation.* 104

4.1 LEO simulation study results summary - equatorial orbit. Large improvement in attitude estimation continuity and accuracy when antennas increased from 4 to 6. Smaller improvement when the number of antennas is increased from 6 to 8. Assumes 0.5 m antenna baselines. 110

4.2 Satellite/channel allocation simulation results. A comparison of the total tracking channels required and mean pitch estimate error STD for three different methods of channel allocation. 115

4.3 ORION formation flying mission spacecraft simulation results. . . . 121

6.1 Experimental results for 2D attitude estimation. Results when compensating for RHCP in measurement versus results when not compensating for RHCP. 152

6.2 Experimental results for 3D attitude estimation. Results when compensating for RHCP in estimation versus results when RHCP is not accounted for in measurement. 155

6.3 Experimental results for 3D attitude estimation. Kinematic weighted least squares estimator results versus dynamic extended Kalman estimator results. In both cases, the RHCP measurement components are accounted for in the estimation. 159

List of Figures

1.1 The GPS Attitude and Navigation Experiment 'GANE' experiment platform before installation in the Space Shuttle Orbiter payload bay. 2

1.2 GlobalStar telecommunication satellite in highbay and after deployment from launch vehicle. 3

1.3 Spacecraft GPS antenna array with aligned and non-aligned boresights. 10

1.4 An example of precision orbit determination achieved through applying GPS sensing - the TOPEX/Poseidon Mission. 14

1.5 Air Force RADCAL mission, first demonstration of spacecraft GPS attitude from post-processed differential carrier phase measurements. 16

1.6 Crista-SPAS mission and GADACS/REXII mission. 17

1.7 Gravity Probe-B vehicle with proposed non-aligned antenna array. . 20

1.8 Autonomous inspection vehicle - AERCAM/Sprint. 25

1.9 A concept for a 5 spacecraft formation for a separated spacecraft interferometer. 26

1.10 2D test vehicle with non-aligned antenna array and diagram of the test vehicle. 30

1.11 3D test vehicle with non-aligned antenna array and diagram of the vehicle. 31
2.1 Basic time of flight pseudorange measurement. 35
2.2 Integrated carrier phase measurement observable. 35
2.3 GPS constellation geometry relative to orbit altitude. 36
2.4 Average GPS satellite visibility versus circular orbit altitude. 38
2.5 Maximum GPS carrier Doppler shift versus altitude. (The region shown with a dotted line represents altitudes too low for orbit and too high for aircraft.) 39
2.6 Carrier phase measurement model geometry definition. 40
2.7 Experimental DCP data for non-aligned antennas. One antenna is periodically occluded. 44
2.8 Angle definition for spherical trigonometric RHCP formulation. . . 47
2.9 Vector projection of circularly polarized wave E-field vector on plane of GPS receive patch antenna. 49
2.10 Spherically Radiated E-field Vector. For helical transmit antenna, the far-field radiated E-field vector has no radial component. 49
2.11 Definition of Transmitter Coordinate Frame. 50
2.12 Modeled RHCP component with no compensation for atan discontinuity. 56
2.13 Antenna geometry for RHCP Example 1. Transmit antenna directly above receive antenna. 57
2.14 Single antenna baseline DCP measurement geometry used for static validation test of RHCP model. 58
2.15 Change in DCP with Antenna Tilt Angle - Experiment vs. Simulation. 58

2.16 Single antenna baseline DCP measurement from a single transmitter with varying elevation angle and antenna boresights. 60
2.17 Simulated RHCP component of differential carrier phase measurement for varying transmitter LOS - Tilt Angle-1 = 0°, Tilt Angle-2 = 90°. 60
2.18 Simulated RHCP component, near vs far transmitters. 61
2.19 Modeled RHCP component, spherical trigonometric formulation vs. vector projection. 62
2.20 Phase center variation data and polynomial model fit for the Trimble GPS antenna used on the TANS Vector attitude receiver. 63
2.21 Phase center variation component of differential carrier phase measurement for varying transmitter LOS. 64
3.1 Far and near transmitter DCP geometry. 69
3.2 Independent vs. redundant DCP measurement vector definition. . . 80
3.3 Antenna array and ±90° pitch oscillation for Figure 3.4. Four antennas, non-aligned array with baseline tilt angles of 45°. 82
3.4 Total number of independent measurements available for the redundant and non-redundant measurement vector definitions. 83
3.5 3D vehicle dynamic model - center of mass offset from cable attach point causes gravity restoring torque and cable attach point damps oscillations. 86
3.6 Diagram of planar vehicle for simulation. Tilt angle antenna 1 = 0°, and tilt angle antenna 2 = 90°. 88
3.7 Attitude estimation - Tilt angle antenna 1 = 0°, tilt angle antenna 2 = 90°. Estimate error for the IWLS case. 89

3.8 Simulated DCP measurement with periodic dropout and RHCP bias increasing with each rotation. 90
3.9 Single antenna baseline with single transmitter - planar case for estimation stability analysis. 95
3.10 Stability bound for attitude estimation - *Single Transmitter.* 96
3.11 Stability bound for attitude estimation - *Two Transmitters.* 97
3.12 Antenna array geometries simulated in 2D simulation results table. Antenna baseline separation is 0.5 meters. 99
3.13 Attitude Estimate Error vs. Antenna Tilt Angle, 2D case - *without* and *with* RHCP Compensation. 101
3.14 Antenna array geometries simulated in 3D simulation results table. 102
4.1 GPS antenna array geometries for LEO mission study. Symmetric design for maximizing sky coverage. 108
4.2 Satellite/channel allocation simulation antenna array configuration. 6 antennas arranged on the face of a cube on 0.5 m baselines. 112
4.3 Total valid and independent DCP measurements over one orbit, and tracking channel requirements for ABIV satellite/channel allocation. 114
4.4 ORION spacecraft formation flying mission. Preliminary design configuration for spacecraft, 6 antenna array. 116
4.5 Antenna array geometries for ORION mission study, and simulated attitude pitch rotation. 117
4.6 Lock-on time requirements for re-acquisition and lock-on time capability for ORION receiver versus Doppler shift due to rotation rate. 119
5.1 Plot of near versus far transmitter definition boundary for various receiver noise STD. 124

5.2 GPS pseudolite transmitter layout in near transmitter indoor laboratory. 126
5.3 2D Testbed - Air-bearing granite table top, air-bearing vehicles (left), and ceiling mounted GPS pseudolite L1 C/A code transmitter (right). 127
5.4 Example DCP measurement for rotating 2D vehicle - unmodeled multipath component on order of 0.25 wavelength. 128
5.5 2D air-bearing test vehicle. 130
5.6 Development attitude receiver based on GEC Plessey Builder 2 receiver cards, and 2D experiment ground station computer. 131
5.7 Functional block diagram of 2D vehicle experiment lab setup. . . . 132
5.8 Four antenna array - Boresights aligned and at 90° tilt angles. This antenna array was used for static outdoor testing. 133
5.9 GPS pseudolite transmitter layout in far transmitter laboratory highbay, top view on the left and end view of the Stanford HEPL End Station III on the right. 136
5.10 Highbay laboratory - cable suspended vehicle in center with winch hoists on each side and suspension cross member at the top. 137
5.11 Typical multipath component of a single DCP measurement vs. vehicle yaw angle for the 3D vehicle. 138
5.12 3D cable suspended test vehicle. 140
5.13 Functional block diagram of 3D vehicle experiment lab setup. . . . 141
5.14 Central node electronics. Radio modem, rate gyros, GPS attitude receiver, onboard computer and power regulation anddistribution. . 142
5.15 Yaw and roll axis propeller actuators (left) and actuator speed controllers (right). 143

5.16 Onboard computer; top board, the HC11 computer, bottom board, custom built card for multiplexing, communication, and power regulation. 144
5.17 Onboard Motorola HC11 embedded computer card, and power distribution and serial card, stacked components and in enclosure. 144
5.18 Receiver clock synchronization functional block diagram for the ORION receiver. 146
5.19 Mitel Plessey 'Orion' receiver board photo (Top side - right, Bottom side - left). 147
5.20 4 antenna GPS attitude receiver based on dual Orion receiver cards(left) and in enclosure with battery power and output attenuators (right). 147
6.1 Yaw angle estimate error time history for 2D spinning test vehicle. Three antenna tilt angle cases are presented (see Figure 3.12). . . . 151
6.2 3D attitude estimation using IWLS; yaw estimate, pitch estimate, and pitch estimate after multipath calibration. Antenna tilt angles = 45°. 156
6.3 3D Attitude estimation using IWLS; vehicle Euler angles, yaw, pitch and roll. The attitude derived from rate gyro data (dashed lines) is compared with GPS determined attitude (solid lines). Antenna tilt angles = 45°. 157
6.4 3D Attitude estimation using IEKF; Comparing vehicle pitch estimate for GPS and gyro derived attitude. Antenna tilt angles = 45°. . . . 160
6.5 Closed-loop attitude control, step pitch command of 5°. 161
7.1 Gravity Probe-B spacecraft. NAA mission scheduled to fly Sept. 2001. 168
7.2 ORION spacecraft for LEO formation flying experiment. NAA mission scheduled to fly ≈ Jan. 2001. Interior and exterior views. . . . 169

A.1 Carrier phase correlation process block diagram. 173

A.2 Zero baseline, single receiver card, FLL tracking loop in-phase (I) and quadrature phase (Q) correlation components, and differential phase. 174

A.3 Zero baseline, single receiver card, combined FLL/PLL tracking loop in-phase (I) and quadrature phase (Q) correlation components, and differential phase. 175

A.4 Time history and histogram of I and Q correlation values for new coherent PLL tracking loop. 176

A.5 Moving zero baseline DCP error test results for the ORION receiver. 3–4 mm DCP noise for after synchronization. 178

~

List of Symbols

ψ	Vehicle Euler yaw angle
θ	Vehicle Euler pitch angle
ϕ	Vehicle Euler roll angle
$\underline{P}$	Vehicle position, $[p_x, p_y, p_z]$
$\underline{Q}$	Transmitter position, $[q_x, q_y, q_z]$
$\underline{D}$	Receive antenna position w.r.t. transmit, $[D_x, D_y, D_z]$
$\underline{V}$	Vehicle position w.r.t. transmit antenna, $[V_x, V_y, V_z]$
$\underline{b}$	Receive antenna position w.r.t. vehicle, $[b_x, b_y, b_z]$
R	Rotation matrix - vehicle fixed frame to inertial frame
R_A	Rotation matrix - receive antenna frame to vehicle frame
R_T	Rotation matrix - transmit antenna frame to inertial frame
ω_{L1}	GPS L_1 frequency, 1.575 GHz
ν	Receiver electronics noise (white)
ϕ_{ICP}	Integrated carrier phase observable
ϕ_{ik}	Carrier phase measurement
$\Delta\phi_{ijk}$	Differential carrier phase (DCP) measurement
λ_{L1}	GPS L_1 carrier wavelength, 19.02 cm
K_{ijk}	Geometric carrier integer ambiguity
c	Speed of light
τ_{ik}	Receiver-Transmitter clock bias
β_{ijk}	Antenna line bias

$\Delta\phi_{LOS_{ijk}}$	LOS dependent DCP measurement components
$\Delta\phi_{RHCP_{ijk}}$	Right hand circular polarization component of DCP measurement
$\Delta\phi_{\mathrm{PCV_{ijk}}}$	Right hand circular polarization component of DCP measurement
$\Delta\phi_{\mathrm{MP_{ijk}}}$	Multipath component of DCP measurement
M_{ijk}	Line bias carrier integer ambiguity
P_{ijk}	Polarization carrier integer ambiguity
B_{ijk}	Combined floating point measurement bias
$\underline{X}$	Combined vehicle position and attitude state
$\alpha,\ \beta,\ \gamma$	Spherical triangle angles - RHCP formulation
$a,\ b,\ c$	Interior angles - RHCP formulation
$\underline{E}^{\mathrm{TRANS}}$	Transmitted E-field vector, $[\mathcal{E}_\theta, \mathcal{E}_\phi, \mathcal{E}_r]$
$\underline{E}^{\mathrm{REC}}$	Received E-field vector
$r(t)$	Received signal voltage
$T_{\mathrm{TR-REC}}$	Transmit antenna to receive antenna rotation matrix
Δr_{ijk}	Derived differential range measurement
$\underline{\hat{s}}$	Transmitter LOS unit vector
$\underline{h}$	Nonlinear DCP measurement function
$\underline{h}_D$	Portion of nonlinear DCP measurement due to differential range
$\underline{h}_{\mathrm{RHCP}}$	Portion of nonlinear DCP measurement due to RHCP
$\underline{z}$	Measurement vector
$\underline{\bar{X}}$	State estimate prior to measurement update
$\underline{\hat{X}}$	State estimate after measurement update
H	Jacobian of measurement function w.r.t. state
H_{D}	Portion of linearized measurement due to differential range
H_{RHCP}	Portion of linearized measurement due to RHCP
S	Measurement noise covariance matrix
$J(R)$	Attitude estimation cost function
R_0	Initial attitude matrix estimate

$\underline{\partial\theta}$	Vector of fixed axis small rotations, $[\partial\theta_x, \partial\theta_y, \partial\theta_z]$
$\theta^{\times}$	Skew symmetric rotation matrix of $\underline{\partial\theta}$
$\underline{V}$	Satellite visibility vector
W_v	Measurement selection matrix
$\bar{P}$	Estimate error covariance matrix prior to measurement update
$\hat{P}$	Estimate error covariance matrix after measurement update
Q	Process noise covariance matrix
Φ	Vehicle dynamic model state transition matrix
Γ	Vehicle dynamic model input matrix
Γ_w	Vehicle dynamic model noise input matrix

~

List of Acronyms

ADOP	Attitude dilution of precision
ASIC	Application specific integrated circuit
DCP	Differential carrier phase
DOF	Degree of freedom
EKF	Extended Kalman filter
GADACS	GPS attitude determination and control system
GANE	GPS attitude and navigation experiment
GDOP	Geometric dilution of precision
GEO	Geosynchronous earth orbit
GNC	Guidance, navigation and control
GPB	Gravity Probe-B
GPS	Global positioning system
GPSOAC	GPS-on-a-chip
GSFC	Goddard Space Flight Center
HEO	High earth orbit
IBLS	Integrity Beacon Landing System
ICP	Integrated carrier phase
IEKF	Iterated extended Kalman filter
ISA	Industry standard adapter

IWLS	Iterated weighted least squares
JPL	Jet Propulsion Laboratory
LEO	Low earth orbit
LOS	Line of sight
LQR	Linear quadratic regulator
LVLH	Local vertical, local horizontal
NAA	Non-aligned antenna array
NASA	National Aeronautics and Space Administration
PCV	Phase center variation
PLL	Phase-locked Loop
PWM	Pulse-width modulated
RADCAL	Radar calibration satellite
RC	Radio controlled
RF	Radio frequency
RHCP	Right hand circular polarization
RMS	Root mean squared
SNR	Signal to noise ratio
STD	Standard deviation
WLS	Weighted least squares

Chapter 1

Introduction

The Global Positioning System (GPS) is a satellite based navigation system consisting of 24 spacecraft in semi-synchronous 12 hour orbits, known as the NAVSTAR satellite constellation. It also includes the ground stations and support equipment for operating the satellite system, and the user receivers. These satellites broadcast a spread spectrum RF ranging signal encoded with information allowing users with a GPS receiver to determine their position in an earth fixed coordinate frame with great accuracy. Originally developed as a navigation sensing system for military applications, there has been a recent proliferation in civil, scientific, and commercial applications for GPS sensing. Applications to vehicle positioning have been demonstrated for a variety of vehicles ranging from ships [LK89], to aircraft [DL96] [FVG91], to autonomous agricultural [MOC97] and mining [JS98] equipment.

A natural extension to these terrestrial applications is the use of GPS for spacecraft sensing applications. Because of the high orbits of the NAVSTAR satellites, their signals are readily visible to spacecraft in low earth orbit (LEO) and partially visible even at altitudes as high as geosynchronous earth orbit (GEO). However,

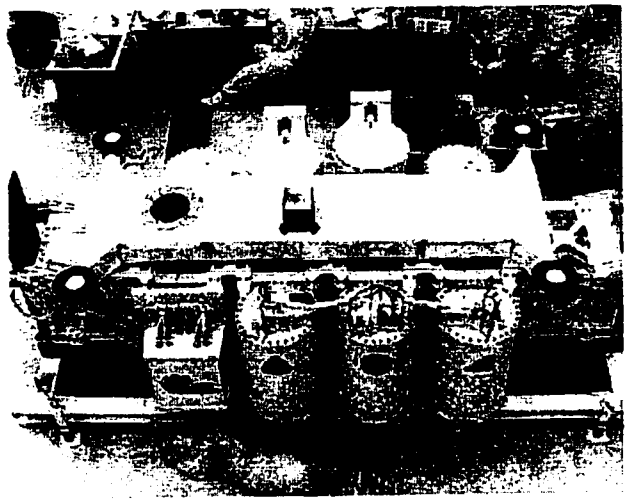

Figure 1.1: The GPS Attitude and Navigation Experiment 'GANE' experiment platform before installation in the Space Shuttle Orbiter payload bay.

due to the increased signal Doppler shift, rapidly shifting transmitter line-of-sights (LOS), and demanding radiation environment, there are several challenges that must be addressed in GPS receiver hardware and software design before the NAVSTAR navigation signals can successfully be used in orbit [GL97]. Despite these challenges, several spacecraft missions have successfully demonstrated the use of GPS sensing for precise, real-time and post processed orbit determination [TY96].

More accurate ranging measurements can be made by using the GPS signal carrier phase observable, as was first exploited by the surveying community [CG96]. But more importantly, differential carrier phase measurements from multiple antennas on a single vehicle enable another useful application of GPS sensing; attitude determination [VS76] [JE79]. The application of differential carrier phase (DCP) GPS measurements to spacecraft attitude determination has great potential for reducing costs and increasing the autonomy of spacecraft [FB98]. The potential benefits of

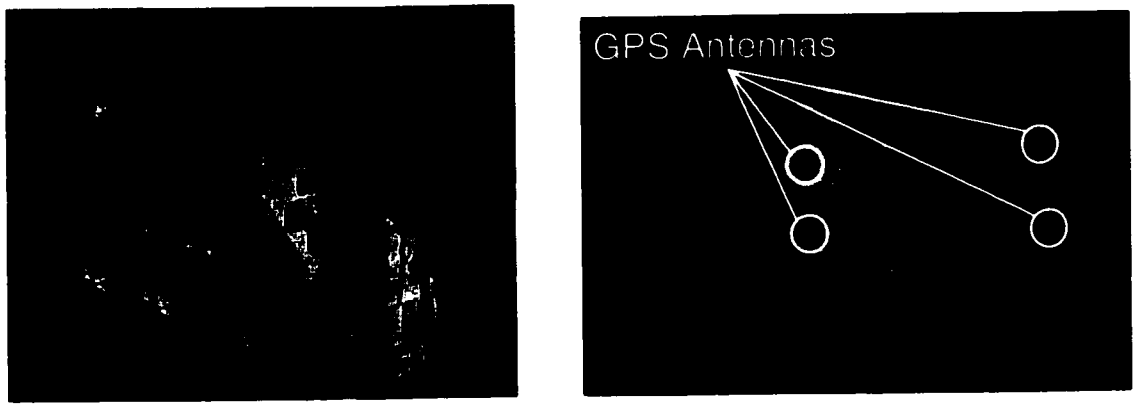

Figure 1.2: GlobalStar telecommunication satellite in highbay and after deployment from launch vehicle. Array of four GPS patch antennas just visible on side facing camera.

using GPS for spacecraft sensing are discussed further in Section 1.1. GPS attitude determination has been demonstrated on several spaceflight experiments and has been used as a backup sensor for guidance navigation and control (GNC) on commercial spacecraft [KB94], and as a primary GNC sensor on scientific [FB96] and military spacecraft (see Section 1.3).

Two examples of spacecraft using GPS attitude systems are presented in Figure 1.1 and Figure 1.2. The GANE (GPS Attitude and Navigation Experiment) flight test shown in Figure 1.1, used a modified Trimble TANS vector GPS receiver to make DCP measurements from an array of four antennas in the Space Shuttle orbiter payload bay to determine the orbiter's attitude. The GPS based attitude solution was then compared to the attitude solution from the orbiter's precise inertial measurement unit and star tracker data. This comparison showed the GPS attitude solution to be accurate to within 0.4°, in the presence of significant reflected multipath signals.

GPS attitude determination has been demonstrated on a commercially deployed system on the GlobalStar spacecraft, shown in Figure 1.2 before launch and just after separation from its launch vehicle. This satellite is part of a LEO telecommunications

constellation of 48 satellites that includes a GPS attitude receiver on each vehicle as the primary navigation sensor, but with GPS measurements used for backup attitude determination. The array of four GPS antennas used for DCP GPS measurements are visible in the on-orbit photo.

In both of these examples, the DCP GPS measurements for attitude determination are made from an array of antennas with boresights aligned in the same direction. This is done so that common mode, LOS dependent, carrier phase measurement disturbances will be removed by differencing, and has been done on virtually all spacecraft missions using GPS for attitude. In addition, the attitude dynamics of the vehicles are limited in both attitude rate and range, with the vehicles nominally stabilized in an earth pointing attitude. Aligned boresight antenna arrays and limited range attitude motion are typical of the terrestrial GPS attitude applications from which these initial spacecraft GPS attitude systems were derived. For terrestrial applications, an aligned antenna array with the boresights pointed vertically up will usually result in good satellite coverage. However, it is this design heritage that raises potential attitude determination robustness problems when terrestrial attitude receivers are used for spacecraft applications. (This will be discussed in more detail in Section 1.2.)

The focus of the research work described in this dissertation is to improve the versatility of spacecraft GPS attitude systems. To expand the range of space missions which can use GPS attitude systems it is necessary to increase the range of possible spacecraft attitude motion while maintaining continuous attitude solution coverage over the entire orbit. One approach to obtain continuous attitude solution availability is to design a GPS attitude system where the antenna array boresights

can be pointed in general directions. The research issues involved in achieving this enhanced capability are presented in Section 1.4.

This research represents the first successful real-time dynamic demonstration of GPS attitude determination using DCP measurements from an antenna array with non-aligned boresights. New receiver algorithms were developed and tested experimentally on two laboratory test vehicles. The first tests were done on a 2D, planar, air-bearing vehicle capable of single degree of freedom rotation, and the second set of tests were done on a 3D, free-spinning, cable supported vehicle capable of three degree of freedom rotation (see Chapter 6). Two separate custom-made GPS attitude receivers were constructed for these tests, and the algorithms, software, and ground support computers necessary for the laboratory experiments were also developed (see Chapter 5). In addition, the capability enhancements for spacecraft GPS attitude systems were validated in simulation for a set of representative spacecraft missions (see Chapter 4).

1.1 Benefits of Spacecraft GPS Sensing

There are many benefits of using GPS sensing on spacecraft, as a replacement for or as a complement to more conventional GNC sensors. There are benefits in terms of cost reduction, improvements in system reliability, and enhanced system capability. The cost benefits can be categorized as both direct cost reductions in the spacecraft design, and indirect cost reductions from simplifying spacecraft operations and from enhancements to the performance of the spacecraft system in terms of reliability and autonomy. A study done at the NASA Goddard Space Flight Center (GSFC)

Table 1.1: Cost savings for applying GPS sensing to spacecraft (Compiled by NASA GSFC Guidance Navigation and Control Technology Office [FB98])

Spacecraft System	Potential Savings	Achieved Through	Other Improvements
Operational Savings			
Ground Operations and Scheduling	\$100k's-\$M's/year	Autonomous vehicle operations	Hand-off operation, formation flight
Navigation Tracking	\$100k's/year	On-orbit Navigation	Better accuracy, real-time positioning
Design Savings			
Precision Timing	\$1M	Replaces on-board atomic clocks	Synchronization across multiple spacecraft
Attitude Determination	\$100k's	Replaces other attitude sensors	Improved reliability, reduced power and mass
Spacecraft Design and Testing	\$100k's	Reduces interfaces, COTS hardware	Quicker design time, less project risk

Guidance Navigation and Control Technology Office (GTO) [FB98] in 1997 attempted to quantify these potential cost savings, and the results are presented in Table 1.1.

1.1.1 Cost Savings

Applying GPS sensing to spacecraft applications can reduce costs in different ways. During the design cycle for the spacecraft, a direct cost reduction can occur through the consolidation and reduction of the number of sensors on the vehicle, by combining navigation and attitude functions. This reduction in components also entails a cost benefit in terms of reduced system interfaces, and reduced testing requirements. The attitude measurement functions that have conventionally been divided among many sensors (*e.g.* star trackers, horizon and sun sensors, magnetometers, and inertial measurement units) can be combined into a single non-mechanical sensor that provides navigation and time transfer capabilities as well as attitude determination. By combining several sensors that have traditionally been applied separately to the

problems of navigation, attitude determination, and time transfer into a single GPS based sensor, studies have predicted [GL97] that a reduction in cost of between a factor of 5-10 can be achieved over traditional sensing technologies. The NASA GSFC GTO study (Table 1.1) predicts savings of $100K's for spacecraft attitude determination applications, which is based on an anticipated attitude receiver cost in the range of $50-$100K's replacing a star tracker ($500K) or navigation-grade inertial system ($1M).

If the performance requirements permit it (attitude accuracy 0.25°, position accuracy submeter), only the additional sensors needed for redundancy or safe mode concerns need be included in the design. Large-scale telecommunications satellite constellations now being developed, such as the GlobalStar, Iridium, and Teledesic systems, require pointing accuracies that are within the capability of DCP GPS sensing (typically on the order of 0.25°-0.5°). Since these type of spacecraft systems involve large numbers of satellites, the cost savings from an integrated, single sensor system to cover both attitude and navigation functions will be magnified by the high volume of spacecraft being built.

An additional observation is that it is possible to replace onboard precision time references with common GPS timing for some applications where the requirements can be met (0.1 μsec accuracy).

1.1.2 Reliability Improvements

The reduction in the number of spacecraft GNC sensor subsystems also entails an improvement in reliability, since many optical systems and electromechanical systems such as inertial measurement units, can now be replaced with a single solid state GPS

based sensor. Reducing the number of components and interfaces improves overall system reliability and reduces testing costs.

1.1.3 Enhanced Autonomy

The results presented in Table 1.1 further refine these potential cost savings into those achievable through the spacecraft design, fabrication, integration and test process, and savings achievable during spacecraft operations. Spacecraft ground operations costs can be significantly reduced due to the enhanced autonomy enabled by onboard real-time GPS orbit determination and maneuver generation [PA91].

Applying GPS sensing to onboard spacecraft navigation will enhance the autonomy of spacecraft clusters, such as Teledesic, where the costs associated with using conventional ground operations methods are magnified by the size of the constellation. For Teledesic, the current system design calls for 288 satellites in LEO. Using conventional ground tracking and uplinking orbit maintenance commands individually to all spacecraft would require an army of ground controllers. GPS sensing on each spacecraft will give them the autonomy necessary to perform onboard autonomous orbit determination and generation of orbit correction maneuvers, resulting in an enormous reduction in operations costs.

In addition to the potential cost savings of using GPS sensing for spacecraft applications, these sensing techniques are an enabling technology for an entire new class of missions that involve precise relative position and attitude sensing of vehicles flying in formation. This will be further examined in the applications Section 1.5.

1.2 Research Problem Statement

1.2.1 GPS Sensing in Space Environment

The space environment presents many challenges for GPS receiver operation. There are the usual radiation impacts on the receiver electronics in orbit, but there are also many signal processing and satellite visibility issues that must be addressed.

There are three important differences in making DCP GPS measurements in LEO (high earth orbit and GEO spacecraft have other issues concerning visibility that are not addressed in this thesis). They are;

- Enhanced visibility
- Increased Doppler shift in GPS signal
- Rapidly changing GPS satellite LOS

The first difference is an advantage. There are generally more GPS satellites in view in LEO than for a terrestrial user. There are $\approx$ 12–16 visible satellites on average over a given orbit as compared to $\approx$ 6–8 visible for a ground based or aircraft user.

The second difference represents a problem, because a spacecraft is moving at orbit velocities of $\approx$ 7 km/sec, the relative Doppler shift range between vehicle and GPS satellite is now on the order of $\pm$40KHz, compared to $\pm$5KHz for a terrestrial user, increasing the difficulty and time required for signal acquisition.

And finally, signal acquisition becomes more difficult given the rapid line-of-sight motion of the NAVSTAR spacecraft on orbit which greatly decreases the time that a satellite is visible. While there may be more satellites in view, any given satellite will rise and set much more quickly than for an Earthbound user. The time that a satellite is visible will be $\approx$ 30 minutes in LEO compared with $\approx$ 6 hours on the

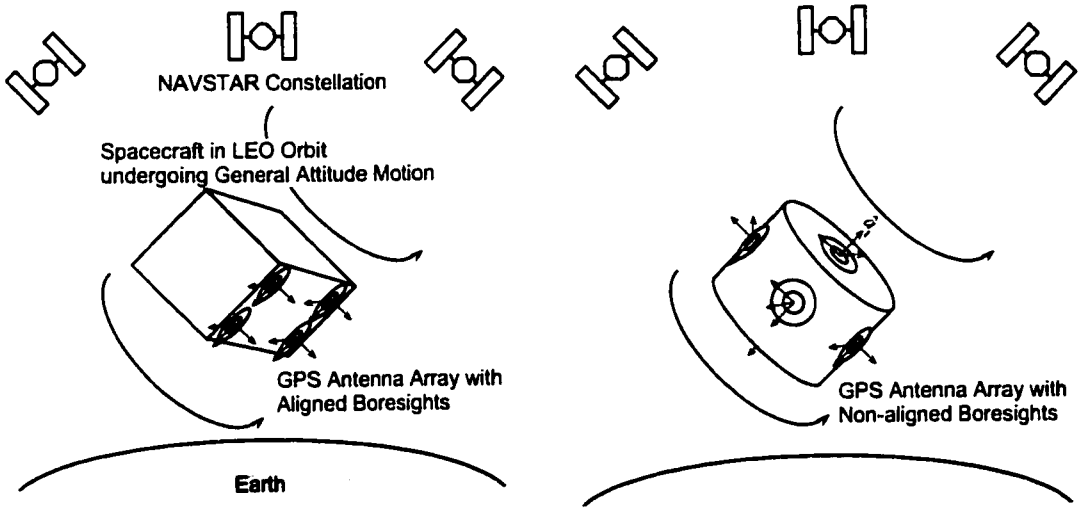

Figure 1.3: Spacecraft GPS antenna array with aligned and non-aligned boresights.

ground. This further complicates the *cold start* signal acquisition problem, where by definition there is little or no apriori knowledge of the vehicle position in orbit, since the receiver may search for GPS satellite PRN codes that are not visible.

The spacecraft GPS attitude determination problem also differs from the terrestrial vehicle attitude problem. In particular, spacecraft attitude motion can be more general, involving large angle changes and continuous rotation. Compared to the typical aircraft application that may involve high bank angles or an occasional barrel roll, the visibility of the spacecraft antenna array to the GPS constellation will be much worse. Spacecraft attitude motion can include tumbling during deployment, spinning, and inertial attitude hold (see Figure 1.3). In fact, it was shown [GL97] that for a LEO spacecraft rotating about an inertially fixed axis, and assuming that each antenna provides only hemispherical coverage, there is no preferred direction that an array of antennas with aligned boresights should be pointed to maintain constellation

visibility over the entire orbit. For this attitude motion profile, the aligned antenna array will be pointing towards the ground half the time. Attitude solutions from the GPS measurements will typically only be available for 50% of the time over the orbit.

One further point is that restricting the GPS antenna array to have aligned boresights does not allow the spacecraft designer to angle antennas away from multipath reflected signal sources on the vehicle, such as solar panels or instrument booms, and these reflected multipath signals are the dominant source of error for a spacecraft GPS attitude system [GL97].

The benefit of making DCP GPS measurements using an array with many antennas pointing in multiple directions has been shown in simulation [EGL96] in terms of increased sky coverage (and therefore attitude solution availability). A non-aligned antenna configuration also helps to decrease the effect of multipath from vehicle self-reflections. By increasing the number of antenna inputs from 4 to 6, increasing the number of tracking channels in the spacecraft GPS receiver, and implementing an all-baselines-in-view measurement strategy [EGL96], continuous attitude and navigation solutions could be obtained throughout the entire LEO orbit for a spinning spacecraft.

These previous results presented a compelling case for increasing the capabilities of present spacecraft attitude receivers. To achieve this goal, the attitude estimation algorithms must also be modified to handle the measurements from a non-aligned antenna array (NAA), and the receiver hardware must be modified to include many more antenna inputs and tracking channels. Most current receiver designs do not have the modular hardware or open software architecture necessary to meet these requirements.

1.2.2 Goals and Approaches

The general goal of this research has been to investigate techniques for improving the robustness of GPS attitude determination on spacecraft. Specifically, this involves three goals;

- General spacecraft attitude motion
- Continuous attitude solution
- Improved attitude solution accuracy

The first goal is to enhance the capability of spacecraft GPS attitude receivers to include general spacecraft attitude motion relative to the NAVSTAR constellation. As a design reference mission, the GP-B spacecraft is a good example [HU95]. The attitude profile for GP-B is a continuous rotation about an inertially fixed axis at spinrates up to 1 RPM. The second goal is to maintain continuous attitude solution availability over the entire LEO spacecraft orbit. And the third goal is to improve the accuracy of the attitude solution as well as the availability, by compensating for measurement effects introduced by using DCP measurements from a NAA.

There are different approaches that can and have been taken to achieve these goals of improved attitude system robustness, including

- Additional attitude aiding sensors
- Multiple attitude systems with aligned arrays
- General antenna pointing geometry

The first approach is to use additional aiding sensors for the attitude problem, such as rate gyros or star trackers. While these additional sensors are an added cost

and weight for the spacecraft, it is clear that some supplemental attitude sensing capability will be required for redundancy or in case of unexpected RF interference with the GPS signal. This option is not addressed in this work, as the primary focus of this research was to investigate improvements of GPS attitude determination as a stand alone sensor. Additional sensors can always be added.

Another way to achieve continuous attitude solution availability is to fly multiple aligned arrays facing in opposite directions on the spacecraft. This has been shown to improve constellation visibility [GL97], but also involves additional cost and weight for the spacecraft.

The most direct approach is to allow for general antenna pointing geometry in the receiver hardware and software design (see right side of Figure 1.3). This method is enabled by new receiver technologies, and is the approach taken in this research. The challenge is that using measurements from an array of antennas with non-aligned boresights introduces new measurement components that must be accounted for in the attitude determination algorithms.

1.3 Previous Work

The first application of GPS sensing to spacecraft was for orbit determination. An example of precision orbit determination using GPS was the TOPEX/Poseidon mission (see Figure 1.4), an ocean altimetry mission launched in 1992. Operating in a 1336 km altitude orbit, the spacecraft made precise range measurements to the sea surface, and required accurate post-processed orbit knowledge to deduce the sea surface height. Using GPS pseudorange and dual frequency carrier phase measurements,

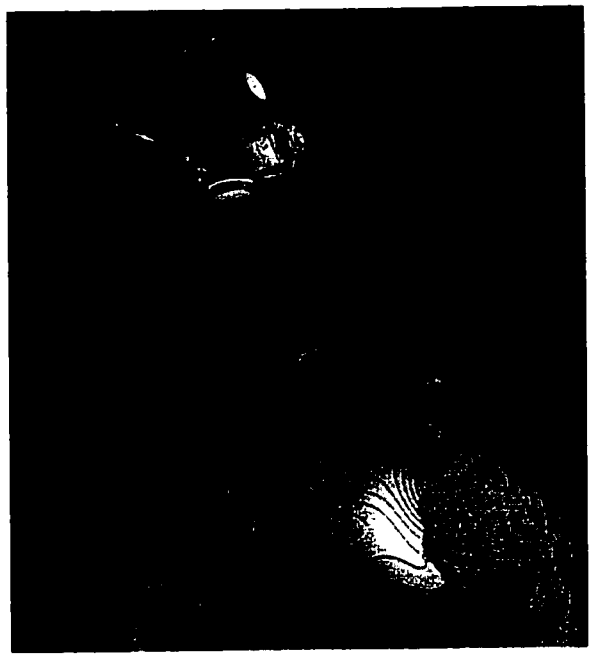

Figure 1.4: An example of precision orbit determination achieved through applying GPS sensing to spacecraft navigation - the TOPEX/Poseidon Mission.

and an accurate dynamic model for the orbit disturbances, RMS altitude errors of less than 10 cm were achieved [TY96].

After the basic spacecraft GPS receiver development was accomplished, the next spacecraft application widely pursued was attitude determination, as described in the following sections. A recently emerging application is relative spacecraft positioning for formation flying, which will be described in Section 1.5.

1.3.1 GPS Attitude Determination

GPS attitude determination was first proposed by Spinney [VS76] in 1976. In that work, he developed the basic idea of determining antenna baseline vectors in earth fixed frame based on differential range measurements from GPS carrier phase, and examined the basic performance parameterization for GPS attitude determination

in terms of DCP measurement error, GDOP, ADOP, antenna baseline length, and antenna baseline knowledge accuracy.

Ellis [JE79] was the first to suggest a spacecraft application for GPS attitude determination, and Kruczynski [LK89], et. al., performed the first real-time GPS vehicle attitude determination experiments on the USS Yorktown in 1988. This was followed in 1991 by the first aircraft attitude tests on a DC3 at Ohio University, conducted by Van Graas and Braasch [FVG91].

Research at Stanford by Cohen [CC92] produced the first practical, commercially available attitude receiver, a multiplexed version of the Trimble TANS, the TANS Vector.

1.3.2 Spacecraft Flight Experiments

GPS based attitude determination has also been successfully demonstrated on orbit. The receiver developed by Cohen was flown on the Air Force RADCAL satellite (see Figure 1.5), the first spacecraft GPS attitude experiment. Post-processed attitude estimates with an accuracy of 0.5°–1.0°, in comparison to spacecraft magnetometer data, were achieved using downlinked DCP measurements. On the RADCAL mission the four GPS antennas were canted 17.5° from a central gravity gradient boom on the spacecraft. The effect of this small mis-alignment of antenna boresights was not taken into account in the post-processing of the measurement data for attitude determination.

Another important development was the GPS Tensor receiver, a derivative of the TANS Vector receiver built by Space Systems Loral, which was the first radiation hardened attitude receiver designed specifically for the space environment [KB94]. The CRISTA-SPAS experiment on STS-66 in November 1994 used the Tensor receiver

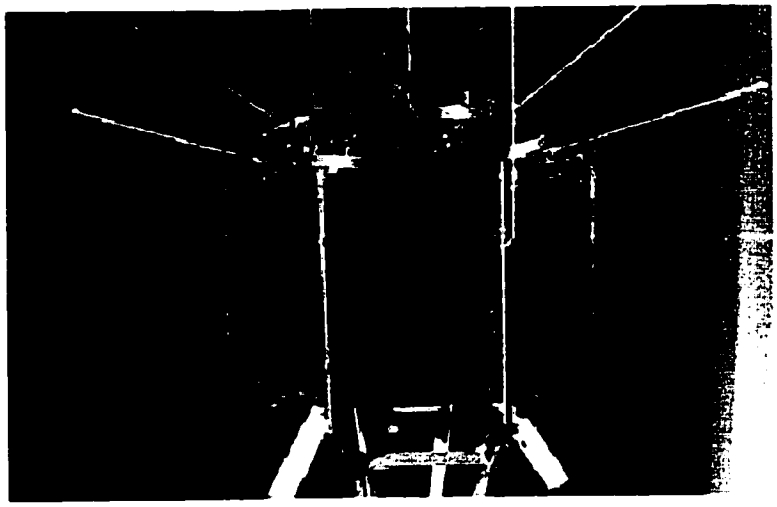

Figure 1.5: Air Force RADCAL mission, first demonstration of spacecraft GPS attitude from post-processed differential carrier phase measurements.

in the first demonstration of real-time GPS attitude determination in orbit [KB95], with an attitude accuracy of 0.2°–0.3°. The CRISTA-SPAS spacecraft flew out of the Space Shuttle payload bay and is shown on the left side of Figure 1.6.

The TANS Vector was later modified by Lightsey at Stanford and flown on the REX II and GADACS missions [FB98], on a Spartan spacecraft shown on the right side of Figure 1.6. The REX-II experiment in March, 1996 was the first successful demonstration of real-time attitude determination and closed-loop control using differential carrier phase GPS.

In each of these missions, the antenna array used for producing the differential carrier phase measurements had the antenna boresights aligned in the same direction (or nearly aligned for RADCAL). This alignment helps eliminate common mode error sources, such as the circular polarization component of the phase of the GPS signal, and the antenna phase center variation. These previous demonstrations of on-orbit

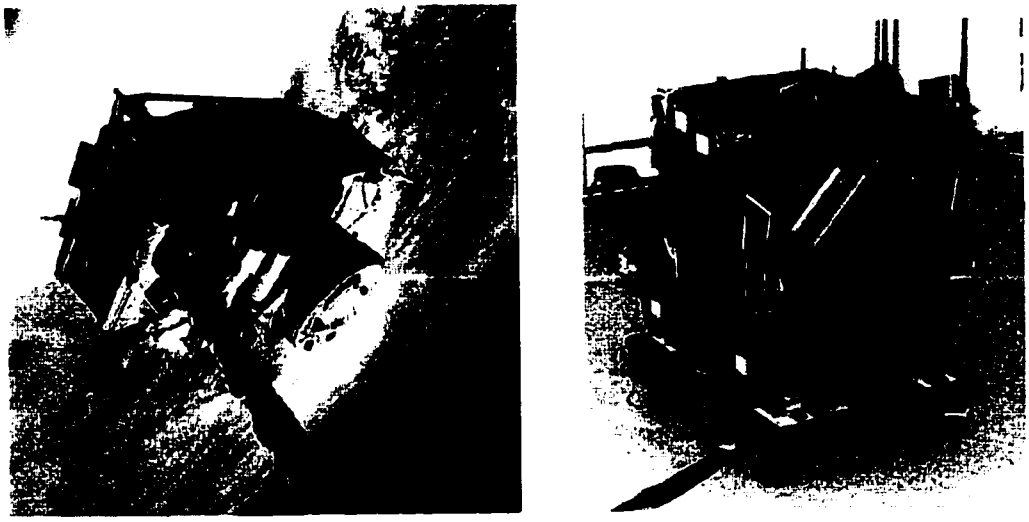

Figure 1.6: Crista-SPAS mission, first real-time on-orbit GPS attitude. GADACS/REXII, missions, first GPS attitude and closed loop control.

attitude determination were also done with the spacecraft remaining aligned with local vertical/local horizontal, and relatively benign spacecraft attitude motion relative to the orbit frame. Since the NAVSTAR constellation was originally designed for terrestrial users, in these cases an aligned array that points away from the earth ensures good satellite coverage.

Lessons Learned from GlobalStar

In light of the previously presented successful demonstrations of GPS attitude determination on flight experiments, it is also useful to note some of the problems that have been encountered in the first, large scale commercial application of GPS attitude determination on spacecraft: the TENSOR receiver on the GlobalStar constellation. There were significant cost and schedule problems encountered during the development of this receiver that should serve as caveats to the spacecraft GPS application

developer. Most of the problems encountered in this program can be traced to unfortunate design decisions that resulted from trying to develop a fully space qualified receiver by directly upgrading a terrestrial design, in this case the Trimble TANS Vector attitude receiver [RF97]. This qualification required parts substitutions, particularly in the receiver processor and GPS chip-set ASIC's, that resulted in design changes which significantly impacted the software development required for the receiver. The software development became much more complicated than simply having to port existing TANS Vector code to a new platform.

While the performance of the TENSOR receiver on the GlobalStar mission for navigation and time transfer between the vehicles has been a success, the role of GPS attitude determination has been minimal. The reported on-orbit attitude determination accuracies [RF97] are in the range that was predicted; between 0.16° and 0.44°, and these results have the potential to be improved by better real-time calibration of the thermal shifts in the antenna electrical line biases. But this performance comes at a much higher receiver cost than was anticipated, because the receiver development must be amortized over a relatively low volume of production units. Instead of an integrated navigation and attitude sensor in the $50-100K range, it has turned out to be closer to $250-500K.

There is still great potential for reducing the number of sensors on spacecraft by consolidating and combining navigation and attitude functions in a single, non-mechanical RF sensing system. Researchers at the University of Surrey have demonstrated that an incremental upgrade of terrestrial receiver designs with judicious use of radiation testing can produce a low cost GPS attitude system for spacecraft, but these are still experimental systems. The lessons learned from the TENSOR development indicate the difficulties involved in developing a space qualified system, and

that there is still research to be done before an off-the-shelf GPS attitude receiver for spacecraft will become available.

1.3.3 Ground Experiments and Analysis

In parallel with these flight experiments, there has been important work in the area of modeling GPS measurements from non-aligned antenna arrays, starting with the work by Wu [JW91] at JPL which examined the effect of antenna orientation on carrier phase measurement. He developed a formulation of the largest effect due to the right hand circular polarization (RHCP) of the GPS signal on the DCP measurement.

The Stanford GPS Laboratory has been involved in a variety of research projects in the field of spacecraft attitude determination. Some of that work has dealt with issues involving measurements from non-aligned antennas.

Uematsu [HU95] examined the problem of attitude determination using a non-aligned antenna array in the context of the GP-B mission, and looked at optimal satellite/channel allocation schemes given the limited number of channels available on his flight receiver. He examined the effect of vehicle rotation on the availability of attitude solutions and has proposed a non-aligned array of four antennas to provide the necessary satellite visibility (see Figure 1.7). Issues dealing with the changes in the measurement model necessary for making differential carrier phase measurements from non-aligned antennas were not addressed in his work.

Lightsey [EGL96] performed attitude tests on a static, outdoor, ground-based non-aligned antenna array of four antennas, where two of the antenna boresights were vertical and two were tilted at 30° to vertical. These tests were a validation of a spherical trigonometric formulation of the polarization effect (for far transmitters) on the differential carrier phase measurement. By calibrating the polarization component

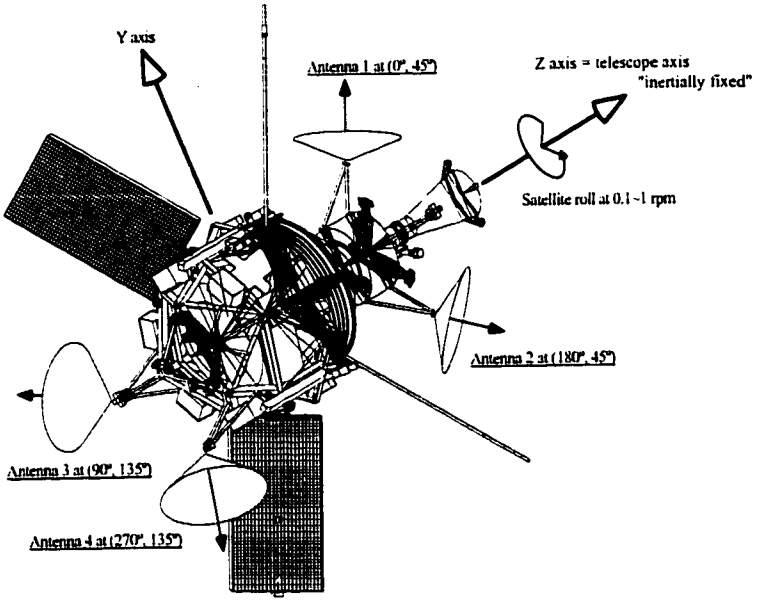

Figure 1.7: Gravity Probe-B vehicle with proposed non-aligned antenna array.

out of the phase measurements, he was able to successfully achieve attitude estimates with mean errors on the order of 0.2°. The experiment results also indicated that the increased multipath reflected signals received by having some of the antenna boresights tilted towards horizontal resulted in a 50% increase in the attitude estimate error over that achieved using an aligned array with vertical boresights.

Lawrence [DL96] looked at using a NAA to improve visibility during steep aircraft banking as a part of the *Integrity Beacon Landing System* (IBLS) aircraft landing system project. To address the antenna occlusion problem, Lawrence used a second, non-aligned antenna on the underside of the aircraft to ensure satellite coverage during steep bank angles. A measurement model of the circular polarization phase component associated with the non-aligned antenna was also developed, with the assumption of a large distance to the transmitter. This work focused primarily on using

carrier phase measurements for relative positioning, not attitude, and did not deal with the effects on the measurement associated with a continuously rotating vehicle.

Zimmerman [KZ95] developed an indoor GPS laboratory environment to demonstrate the use of differential carrier phase GPS for spacecraft rendezvous and capture. The system consists of two vehicles that float on a granite table. As part of an error analysis of this system, Zimmerman determined the difference in the DCP measurements caused by the circular polarization of the incoming GPS signal at the master antennas on two separate vehicles. His formulation of the polarization phase component extended Lawrence's to include the near transmitter case. However, this measurement error was not included in the real-time estimation of vehicle state and was not a factor in the experiments because the antenna boresights on the two vehicles were kept nearly aligned.

Stone [JS98] developed a new, near transmitter DCP measurement model that incorporated the circular polarization component of a GPS signal where the transmit antenna is a microstrip patch antenna [JSGPS99]. This measurement model was used in an application for positioning of mining vehicles using a combination of pseudolites and NAVSTAR satellite signals.

Hayward [RH98] also looked at the line-of-sight dependent DCP phase effects, as they pertain to attitude determination using measurements from ultra-short antenna baselines. His work successfully demonstrates the calibration and elimination of effects due to antenna phase center variation, vehicle self-reflected multipath, and near antenna phase pattern interactions for an aircraft attitude application.

1.3.4 Required Extensions to Previous Work

This dissertation research extends the previous work to a real-time, dynamic demonstration of attitude determination using measurements from a NAA, and develops the improved measurement model and attitude estimation algorithms necessary to achieve more robust spacecraft attitude determination. While the previous flight experiments and ground tests have explored the fundamentals of using GPS sensing for spacecraft attitude determination, and using DCP measurements from antennas with non-aligned boresights, there remained a need to further develop and test the new receiver algorithms on a 3D rotating vehicle in real-time. The modifications to the DCP measurement model to account for the additional phase effects, such as the RHCP of the GPS signal and the antenna phase center variation that become important when the antennas are non-aligned, will be further explored in Chapter 2.

1.4 Research Areas

The research activities for this dissertation fell into four categories, which are briefly discussed here and further developed in subsequent chapters.

1.4.1 Measurement Model

When using measurements from an aligned antenna array, common mode errors in the carrier phase measurement are removed through differencing, but there is a limited attitude motion range for which attitude solutions are continuously available. To use measurements from a non-aligned array, modifications need to be made to the receiver signal processing algorithms. The measurement model for GPS carrier phase

measurements must be modified to include the dominant line-of-sight dependent effects that are no longer removed through differencing. The LOS dependent effects on the DCP measurement are separated into those that are easily modeled and those that require some calibration measurement or must be treated as measurement disturbances. In the first category is the effect of GPS signal polarization, and to some extent, the antenna phase center variation, while the latter category includes vehicle self-reflected multipath and antenna/structure phase pattern interactions [RH98].

1.4.2 Attitude Estimation

The attitude estimation algorithms must be modified to account for the frequent and periodic occlusion of the GPS signals that comes with general or continuously rotating spacecraft motion. The definition of the measurement vector and order of the attitude estimator need to be re-examined when estimating attitude from measurements using a NAA.

Because transmitter signals are continually being lost and re-acquired, a method for continuous, real-time measurement bias reacquisition is required. This issue is addressed in this work, but not the bias initialization problem, which has been well researched in other work [DK94] [AH96].

There are different methods of incorporating the new DCP measurement model into the attitude estimation which need to be examined. One method is to explicitly include the LOS dependent phase components in the nonlinear and linearized measurement model in the filter. Another method, which reduces the computation load in the estimator, is to calibrate the LOS dependent phase components out of the measurements. These two approaches are examined and a proof of the validity of

using a calibration approach to mitigate the effect of the RHCP in the measurement is presented in Chapter 3.

1.4.3 Satellite/Channel Allocation

The satellite/channel allocation problem is different due to the use of carrier phase tracking schemes that have no master antenna. With limited common visibility between antennas to any given transmitter, it becomes increasingly important to make use of any available DCP measurement, leading to an all-baselines-in-view tracking strategy that increases the required number of tracking channels on the receiver.

1.4.4 Signal Acquisition Speed

The rapid changes in transmitter visibility that occur during general spacecraft rotation require addressing concerns about the signal acquisition speed. Improvements to receiver tracking loops to decrease signal lock-on times, and an envelope for maximum vehicle rotation rates for a given receiver re-acquisition speed are required.

1.5 Enabling Technology

Spaceborne GPS is an enabling technology for space vehicle autonomy, ground station autonomy, and *virtual spacecraft busses* [FB98] composed of multiple spacecraft flying in precise formation.

Separated spacecraft operations require DCP measurements from antennas with non-aligned antenna arrays. Therefore, research into the GPS sensing problem for multiple spacecraft formation flying has many similar characteristics to the work done in this research.

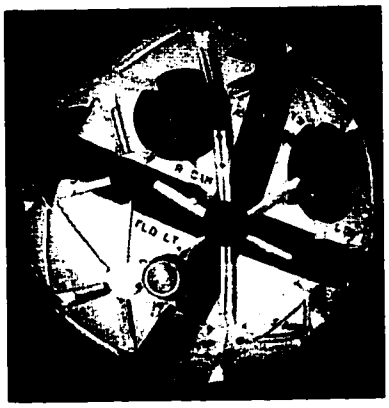

Figure 1.8: Autonomous inspection vehicle - AERCAM/Sprint. Relative positioning from local transmitters, and DCP measurements from a non-aligned antenna array on a spherical vehicle.

GPS sensing for relative spacecraft position sensing will be an enabling technology for several future distributed spacecraft science missions for applications ranging from stellar interferometry to atmospheric modeling. Orbit determination to submeter accuracy and relative ranging to subcentimeter levels are possible using DCP GPS measurements. For the separated spacecraft stellar interferometry mission, the sensing requirements are very challenging. The relative range accuracy of millimeters and bearing angle accuracy of arcminutes can be achieved using GPS derived sensing systems that are further enhanced by the use of onboard transmitters. Two potential applications that are being explored, are spacecraft inspection, and separated spacecraft interferometry.

1.5.1 Space Station Inspection

The first application, shown in Figure 1.8 is autonomous rendezvous and docking or proximity operations around the International Space Station. The AERCAM/Sprint

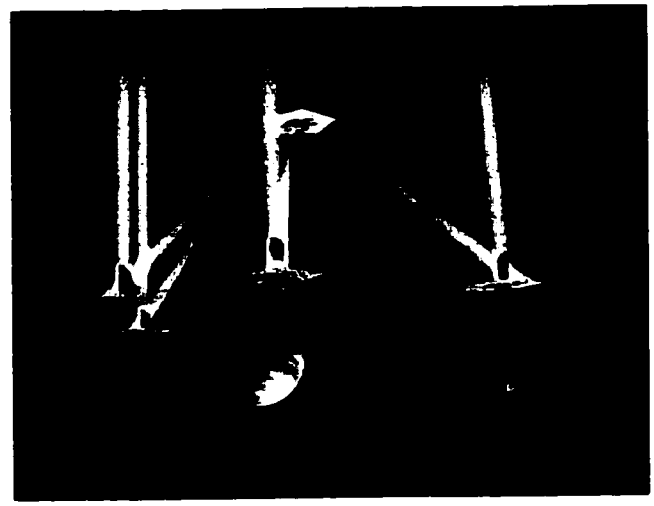

Figure 1.9: A concept for a 5 spacecraft formation for a separated spacecraft interferometer. Here, 4 'collector' spacecraft reflect light from a distant star to a central 'combiner' spacecraft that produces the optical interference pattern and phase measurement. DCP measurements from separated vehicles require modeling effects of non-aligned antennas.

vehicle is an experimental inspection vehicle flown from the Shuttle payload bay. Using a set of GPS pseudolite transmitters on the Space Station, real-time positioning and autonomous maneuvering of an inspection vehicle similar the AERCAM vehicle will be possible with centimeter level accuracy. A small, spherical vehicle such as AERCAM could potentially have several GPS patch antennas with non-aligned boresights located all over the surface vehicle.

1.5.2 Distributed Spacecraft Interferometry

A more challenging example of distributed spacecraft formation flying is a separated spacecraft stellar interferometer, as shown in Figure 1.9. In this concept, several 'collector' spacecraft would reflect light from a distant star back to a central 'combiner'

spacecraft, which would then form a white light interference pattern for reconstructing the Fourier image of the star, and any planets surrounding it. This requires regulating the optical path length of the interferometer to within a wavelength of light, which can be accomplished using a multi-layered sensing approach. A GPS derived transceiver system would be used for the outer loop sensing to form a 'self-constellation' of the vehicles, while an inner loop using an optical metrology system would precisely measure and control the optical path lengths. The relative range and line of sight bearing angles between the vehicles would be measured to within a centimeter and an arc minute, respectively, over vehicle baseline separations on the order of kilometers.

1.6 Summary of Contributions

The main contributions of this thesis research project include algorithm development for improved GPS spacecraft attitude determination, laboratory validation experiments using these new algorithms, and spacecraft simulations using realistic mission scenarios. These contributions are summarized in the following sections.

1.6.1 Improved Measurement Model

Attitude determination was demonstrated for both the near and far transmitter cases, and an improved measurement model for the GPS signal polarization was developed that corrects for measurement singularities and discontinuities that occur in previous models and become important when performing attitude estimation in real-time. Modifications were made to the measurement model, based on the RHCP formulation derived by Zimmerman [KZ96], to remove a singularity as the transmit antenna passes

through the receive antenna LOS zenith, and to account for a discontinuity inherit in the phase model formulation.

In addition, a characterization of the impact of antenna phase center variation (PCV) was done in simulation. For attitude determination using measurements from aligned, or nearly aligned, antenna arrays, Hayward [RH98] has shown that the antenna phase center variations are the dominant line-of-sight measurement disturbance, particularly for the short antenna baseline case. In this work, I have shown that the PCV is a secondary source of error, by roughly an order of magnitude compared to the RHCP phase component, in attitude estimation using highly non-aligned antenna arrays.

This measurement model was incorporated into a new attitude estimation algorithm which also compensates for the rapidly changing satellite visibility and corresponding measurement availability. The receiver attitude estimation algorithms were modified to include the effects of occluded measurements by redefining the measurement vector and applying a weighting matrix to account for unavailable measurements. The estimator was extended from the conventional kinematic weighted least squares filter to a dynamic extended Kalman filter, with a demonstrated improvement in attitude estimate accuracy.

A stability proof is provided for the method of calibrating out LOS dependent phase effects, such as the RHCP, from the measurement vector as opposed to explicitly including them in the linearized measurement in a kinematic filter. More detail will be presented on the algorithm development work in Chapters 2 and 3.

1.6.2 Real-time Dynamic Attitude Estimation

The experimental contribution of this research is that modifications were made to the receiver algorithms in the areas described in Section 1.4, and improved robustness of a GPS attitude determination system was demonstrated in a real-time, dynamic laboratory experiment. This was done for two experiments; one on a 2D test vehicle, as shown in Figure 1.10, and one on a 3D test vehicle, as shown in Figure 1.11. The 2D test was done for a single antenna baseline and a single degree of freedom rotation. Attitude estimates were done off-board the vehicle and in post-processing.

The 3D test used an array of four antennas, and the attitude estimation was done in real-time, using measurements from an onboard receiver. The demonstration was done in a laboratory environment that did not include the overhead vision system previously used to resolve the differential carrier phase measurement biases, so a new real-time bias resolution algorithm was implemented. Attitude solutions based on rate gyro measurements were used as a truth comparison for the GPS derived attitude. The 3D platform had more general attitude motion and showed that the attitude estimation algorithms can compensate for the rapidly changing satellite visibility and corresponding measurement availability.

More detail will be presented on the indoor GPS laboratories and research apparatus used for these experiments in Chapter 5, and a summary and analysis of the data for these validation experiments is presented in Chapter 6.

1.6.3 Validation for On-Orbit Case

These attitude estimation algorithms were validated through simulation of realistic LEO spacecraft missions. A set of representative design missions based on previous work [GL97], the GP-B mission, and the ORION mission [JH99] were examined.

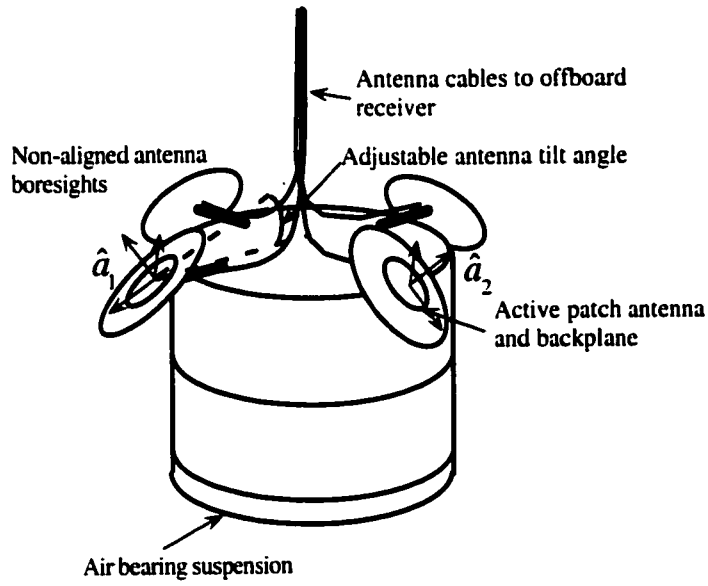

Figure 1.10: 2D test vehicle with non-aligned antenna array and diagram of the test vehicle.

These simulations validated the new robust attitude estimation algorithms under realistic orbit conditions of spacecraft attitude motion and transmitter visibility. The

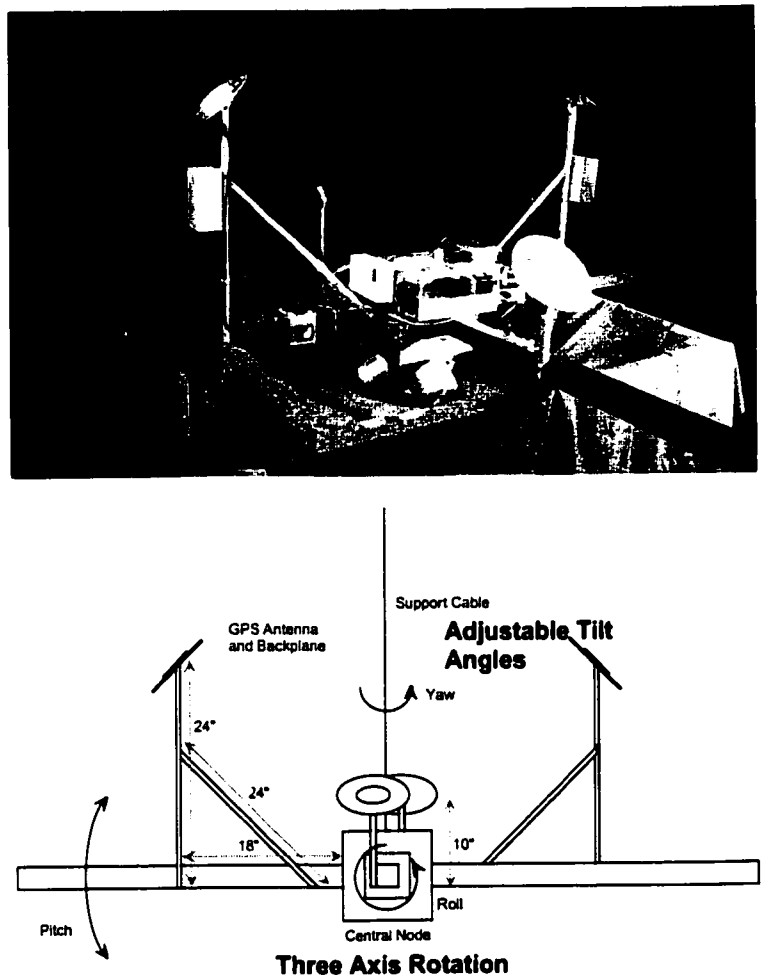

Figure 1.11: 3D test vehicle with non-aligned antenna array and diagram of the vehicle.

on-orbit simulations examined three aspects of GPS attitude determination performance. First, different non-aligned antenna array geometries were simulated to determine their effect on attitude estimation accuracy. Different algorithms for allocating the finite number of flight receiver tracking channels to the visible transmitters were simulated. And finally, the signal re-acquisition lock-on time requirements for varying vehicle rotation rates were examined for a set of non-aligned antenna geometries. More detail will be presented on the spacecraft simulation studies in Chapter 4.

~

Chapter 2

GPS Measurement Model

In this chapter, and the following two, details are presented on the algorithm work done in this research. This work falls into four categories. The first is improving the GPS differential carrier phase measurement model for line-of-sight dependent effects. The second is modifying the attitude estimation algorithms to improve their robustness under general attitude motion. The third is an examination of the satellite/channel allocation problem given a non-master/slave channel tracking architecture and an 'all-baselines-in-view' measurement approach. And the last algorithm issue in this research involves the requirements on signal acquisition speed that occur due to general vehicle rotation.

This chapter deals specifically with the differential carrier phase measurement model, and how this measurement model must be modified for a non-aligned antenna array to account for phase components that can be ignored, or are not significant, for measurements from an aligned array. The basic GPS carrier phase observable is presented, the basic measurement geometry and variables are defined, and the important LOS dependent phase measurement components are identified.

The dominant LOS dependent phase component is shown to be that due to the circular polarization of the GPS signal. A summary and comparison of the mathematical models of this polarization component are presented, along with the improved model developed in this work due to the requirements of real-time attitude determination using measurements from a NAA. The results of a static single antenna baseline validation test of this polarization model are shown.

An empirical model of the antenna phase center variation component of the DCP measurement is compared to the effect due to circular polarization, and simulation results for a single antenna baseline with one DOF rotation are presented to show the relative magnitudes of these two effects.

2.1 GPS Sensing Fundamentals

2.1.1 GPS Measurement Observables

There are three basic measurement observables that can be derived from the NAVSTAR signals; pseudorange, integrated carrier phase, and signal Doppler shift.

The pseudorange measurement is the fundamental ranging measurement as originally envisioned by the GPS system designers. By detecting a correlation peak between a replica pseudo-random noise code and the modulated code on the incoming signal, the received navigation message can be demodulated and used to determine the time of flight between the satellite transmitter and the receiver (see Figure 2.1). By multiplying this time of flight by the speed of light, a range measurement with an accuracy of 10's of meters is produced, subject to errors due to clock drifts on the satellite or in the receiver, atmospheric effects, and errors in the knowledge of the satellite's position.

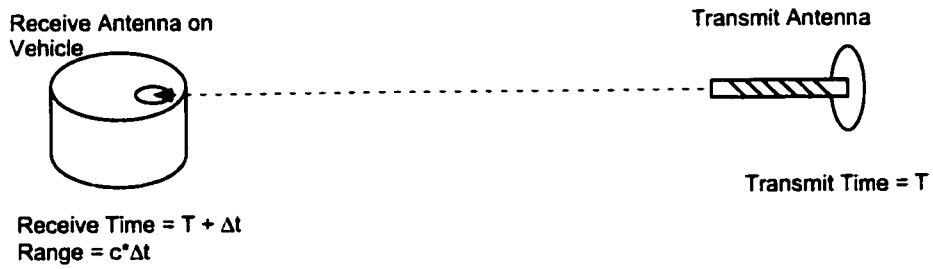

Figure 2.1: Basic time of flight pseudorange measurement.

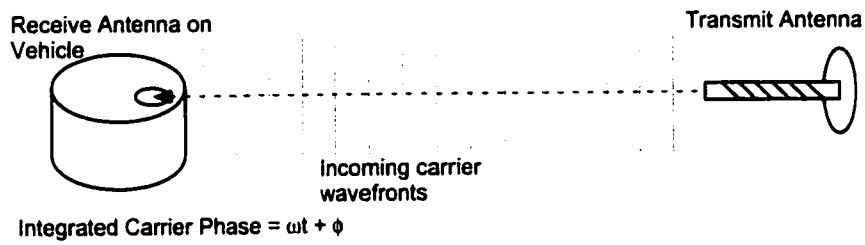

Figure 2.2: Integrated carrier phase measurement observable.

Another measurement observable is the integrated carrier phase (ICP) of the received signal. This measurement is a byproduct of the signal tracking process. On most receivers, a software phase-locked loop (PLL) is used to track the Doppler shifts in the GPS carrier signal that occur due to satellite motion. This involves a correlation process similar to the code correlation, where a replica carrier signal is shifted in frequency to produce a correlation peak with the incoming signal. Subsequent tracking of the passing carrier wavefronts can then be determined from the PLL replica carrier as the total integer and fractional carrier cycles that have passed the receive antenna during the measurement interval (see Figure 2.2), giving a highly precise relative ranging measurement that can be used for interferometric attitude determination. It is important (see Appendix A of Teague [HT97]) to note that this integrated carrier observable is an advancing function of time (see Equation 2.1), as the receiver will track the incoming wavefronts and the ICP will continually ramp-up,

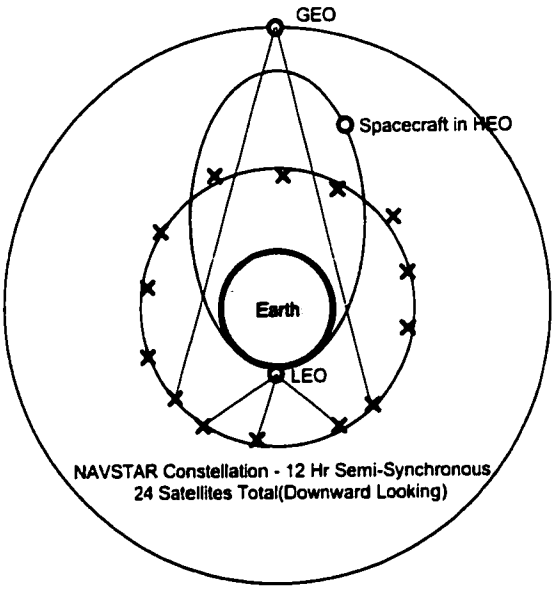

Figure 2.3: GPS constellation geometry relative to orbit altitude.

as given by

$$\phi_{ICP} = \left(\frac{\lambda}{2\pi}\right)(\omega - \omega_c)t + \phi_0 + \nu \tag{2.1}$$

In this equation, ω is the received GPS signal frequency (with any distortions), ω_c is the receiver down conversion frequency, t is the time since signal lock-on, ν is random receiver electrical noise, and ϕ_0 is the fractional phase component due to initial lock-on time, antenna phase pattern, signal polarization, and antenna line bias.

Consequently, the measurement is only useful as a ranging signal in the differential sense, and then only after synchronization issues between the receive antennas have been resolved. By differencing between two ICP measurements that have been synchronized to the same time reference, a differential range measurement (plus an arbitrary floating point bias) can be obtained.

Also as a result of the carrier tracking process, the feedback signal of the PLL tracking loop can be used as a measurement of GPS signal Doppler shift, and can be

used for coarse relative velocity measurement. However, since this observable lumps together frequency effects due to clock instabilities as well as vehicle motion, there is again an issue of resolving the clock bias between the receiver and transmitter before this measurement can be used.

Of these basic GPS measurement observables, the ICP measurement is used for attitude determination. The effect of the spacecraft environment, in terms of signal availability and Doppler shift will now be examined.

2.1.2 Space Environment

The GPS measurement for a spacecraft user is affected by the space environment. There is less ionospheric and tropospheric error in the code and carrier phase measurement. GPS constellation visibility can vary greatly, since spacecraft GPS users can range in altitude from LEO to GEO, or be on transfer orbits inbetween (See Figure 2.3). While the antennas on the GPS satellites are downward pointing, the footprint of the antenna pattern is slightly larger than the limb of the earth, making some GPS satellites visible to spacecraft even in HEO and GEO orbits.

In Figure 2.4, the average number of visible GPS satellites over one circular orbit is plotted versus the orbit altitude. It has been previously noted that a spacecraft in LEO can see more GPS spacecraft than a typical terrestrial user, between 12-16 as compared to 6-8, because of the expanded horizons in orbit. This figure shows that this trend continues until it reaches a peak of 18 satellites visible at roughly an HEO altitude of 3000 km. Higher than this altitude, GPS constellation visibility again decreases, but even for orbits higher than the NAVSTAR orbit, satellites are still visible close to the earth's limb.

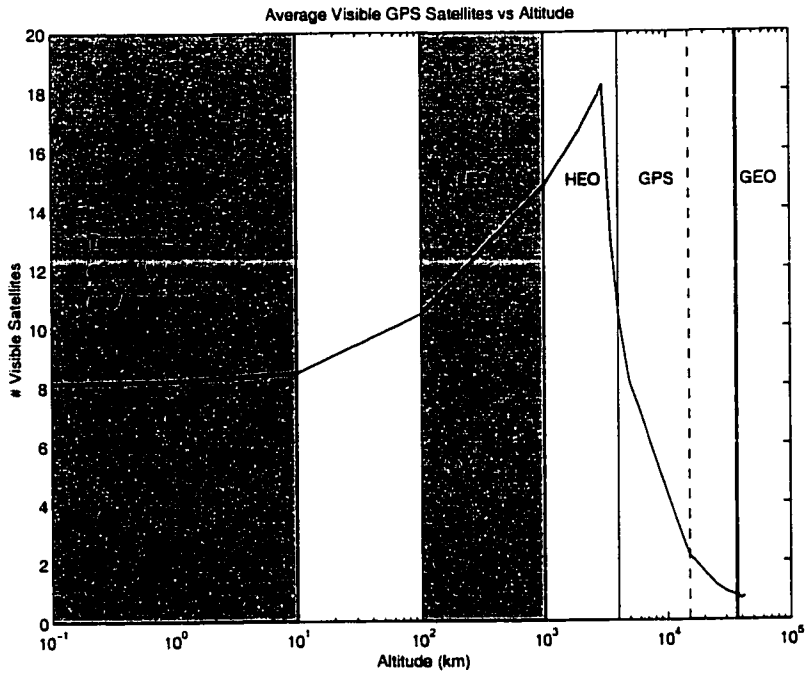

Figure 2.4: Average GPS satellite visibility versus circular orbit altitude.

While the constellation visibility decreases with higher orbit altitudes, there is a benefit in terms of the signal Doppler. As was previously noted in Section 1.2, a LEO spacecraft receiver will have to acquire and track at higher signal Doppler shifts than a terrestrial receiver due to the relative orbit velocities experienced in space. However, as shown in Figure 2.5, as the orbit altitude increases to altitudes greater than LEO, the relative orbit velocity between the user and the GPS spacecraft decreases and the corresponding expected maximum Doppler shift in the GPS signal decreases from ±40KHz to ±15KHz, making signal acquisition faster and easier.

As shown, the space environment increases the difficulty of making GPS measurements in different ways. GPS satellite visibility becomes more of a problem with altitude while relative signal Doppler shift decreases with altitude. Additionally, there are challenges due to general spacecraft attitude motion that becomes possible in orbit. Vehicles can freely rotate, rotate continuously, or maintain a constant

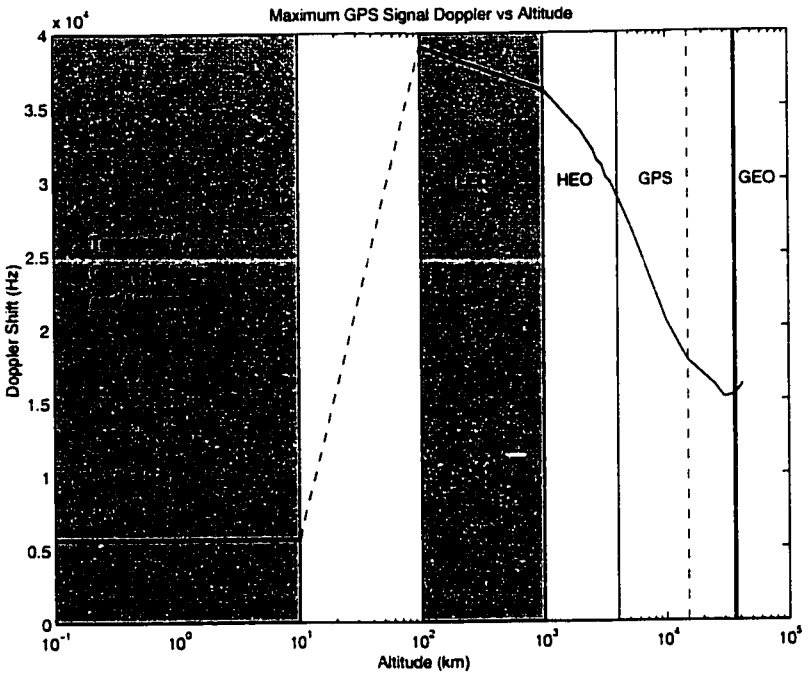

Figure 2.5: Maximum GPS carrier Doppler shift versus altitude. (The region shown with a dotted line represents altitudes too low for orbit and too high for aircraft.)

inertial attitude that is arbitrary with respect to the NAVSTAR constellation. Making measurements from a NAA with general attitude motion introduces new DCP components into the measurement. These additional measurement components are examined in the next section.

2.2 Non-aligned Antenna Array DCP Components

Assuming that adequate synchronization has been made for ICP measurements on separate antennas, the instantaneous carrier phase measurement can be modeled as a function of the range between transmit and receive antennas. When making measurements from an array of antennas with non-aligned boresights, there are additional

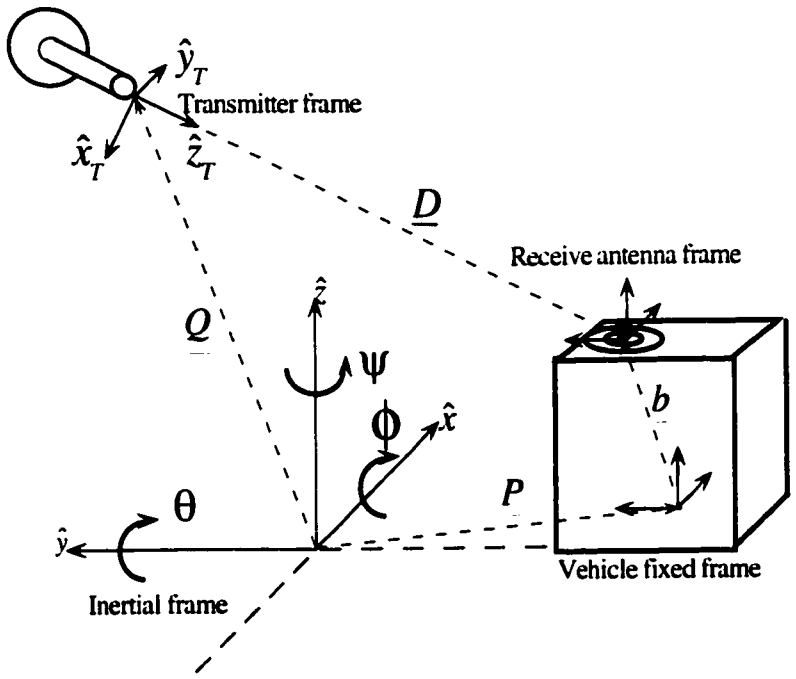

Figure 2.6: Carrier phase measurement model geometry definition.

phase components that must be modeled. In this section, an extended measurement model is developed that is valid for both the near and far transmitter case.

2.2.1 DCP Geometry Definition

The measurement model for carrier phase measurements for a near transmitter is typically expressed as a function of the distance between the transmit and receive antenna phase centers (see Figure 2.6), receiver clock bias, some internal line bias and receiver noise [KZ96] (see Equation 2.2). For antenna i and transmitter k, the measured carrier phase ϕ_{ik} is (symbols defined in Equation 2.4)

$$\phi_{ik} = |\underline{D}_{ik}| - \lambda K_{ik} + c\tau_{ik} + \beta_i + \nu_{ik} + \phi_{LOS_{ik}} \tag{2.2}$$

The additional components to the carrier phase measurement that become important

when the antenna boresights are not aligned are the phase due to the polarization of the incoming signal, the variation of the antenna phase center with transmitter LOS, and the LOS dependent multipath (see Equation 2.3).

$$\begin{aligned}\phi_{ik} &= |\underline{D}_{ik}| - \lambda K_{ik} + c\tau_{ik} + \beta_i + \nu_{ik} \\ &\quad + \underbrace{\phi_{\mathrm{RHCP_{ik}}} + \phi_{\mathrm{PCV_{ik}}} + \phi_{\mathrm{MP_{ik}}}}_{\text{Additional transmitter LOS dependent terms}}\end{aligned} \tag{2.3}$$

where

$$\begin{aligned}\underline{D}_{ik} &= \text{Position antenna } i \text{ rel. to transmitter } k \\ K_{ik} &= \text{Integer carrier wavelengths from antenna } i \\ &\quad \text{to transmitter } k \text{ (geometric integer ambiguity)} \\ \tau_{ik} &= \text{Receiver-transmitter clock bias} \\ \beta_i &= \text{Antenna line bias} = \beta_{\mathrm{frac_i}} + \lambda M_i \\ \beta_{\mathrm{frac_i}} &= \text{Fractional part of line bias antenna } i \\ M_i &= \text{Integer portion of line bias antenna } i \\ \nu_{ik} &= \text{Receiver noise (Normal)} \\ \phi_{\mathrm{RHCP_{ik}}} &= \text{Polarization phase component(fractional and integer portions)} \\ &= \phi_{\mathrm{RHCPfrac_{ik}}} + \lambda P_{ik} \\ \phi_{\mathrm{PCV_{ik}}} &= \text{Antenna phase center variation} \\ \phi_{\mathrm{MP_{ik}}} &= \text{Multipath phase component}\end{aligned} \tag{2.4}$$

The phase component due to the clock bias between transmitter and receiver is removed through single differencing between antenna i and antenna j. The resulting single difference measurement is then the sum of integer and non-integer wavelength components. Differencing Equation 2.3 over the antennas i and j for transmitter k

yields

$$\begin{aligned}\Delta\phi_{ijk} &= |\underline{D}_{ik}| - |\underline{D}_{jk}| + \Delta\phi_{\mathrm{RHCP_{ijk}}} + \Delta\phi_{\mathrm{PCV_{ijk}}} + \nu_{ijk} \\ &\quad + \underbrace{\beta_{\mathrm{frac_{ij}}}}_{\text{Non-integer bias term}} \\ &\quad + \underbrace{\lambda\left(-K_{ijk} + M_{ij} + P_{ijk}\right)}_{\text{Integer bias terms}}\end{aligned} \tag{2.5}$$

The components of the measurement model are divided into terms that are time varying functions of the system state and those which are biases, that must be removed. The biases in turn are separated into non-integer biases and integer wavelength biases. In Equation 2.5, the integer bias K_{ijk} is the same geometric bias that is encountered with an aligned array, and M_{ij} is the constant integer portion of the antenna line bias. A new bias term, P_{ijk}, is introduced with a non-aligned array due to the polarization of the incoming wavefront. P_{ijk} is a time varying integer bias that is dependent on the past history of visibility of the two antennas to a common transmitter.

If we define the vehicle combined position and attitude state as $\underline{X}$, the antenna positions in the vehicle frame as $\underline{b}_i$ and $\underline{b}_j$, and the position of the transmitter as $\underline{Q}_k$, then the DCP measurement can be written in terms of the nonlinear measurement function h, and the combined integer and non-integer measurement bias B_{ijk} (see Equation 2.6).

$$\Delta\phi_{ijk} = h(\underline{X}, \underline{b}_i, \underline{b}_j, \underline{Q}_k) + B_{ijk} + \nu_{ijk} \tag{2.6}$$

2.2.2 LOS Dependent Phase Components

The three important line-of-sight dependent phase components identified in the measurement model are the circular polarization, the phase center variation associated with the receive antenna, and the vehicle self-reflected multipath reflected signals.

As is further shown in Section 2.3, the RHCP component of the DCP measurement is the dominant LOS dependent effect. For example, consider a case similar to that in Figure 2.6, but with two receive antennas on top; one with the boresight vertical and the other with the boresight horizontal, and the vehicle rotating about the vertical axis. As the vehicle rotates, the vertical antenna will be in constant view of the transmitter, while the horizontal antenna will be periodically occluded. The carrier phase component due to RHCP tracked by the antenna with continuous view of the transmitter will increase by one cycle per rotation, while the occluded antenna will not see this integer cycle increase in the tracked phase. The differential phase measurement between the two antennas will increase by one integer cycle per rotation of the spinning spacecraft, if measurement bias re-acquisition is not performed on each rotation. This effect can be seen in experimentally collected DCP data (see Figure 2.7), and is the largest part of the DCP measurement between two antennas in this case. The polarization bias must be accounted for either in the measurement function h in Equation 2.6, or as part of the measurement bias acquisition each time a DCP measurement becomes visible. The fractional portion of the RHCP DCP component can be modeled as a function of the transmitter LOS.

The phase center is an idealized point on a transmitting antenna that can be defined as the location about which there is no angular dependence of the carrier phase of the spherically radiating wavefront in the far-field. An analogous point can be defined for a receiving antenna, where the measured phase of incoming wavefronts has no angular dependence [CB82]. In practice, there are no ideal antennas, i.e. with no carrier phase dependence on LOS to the transmitter. However, this LOS dependence in the antenna phase pattern can be modeled as variations in the location of the ideal phase center. These phase center variations (PCV) can be modeled, but

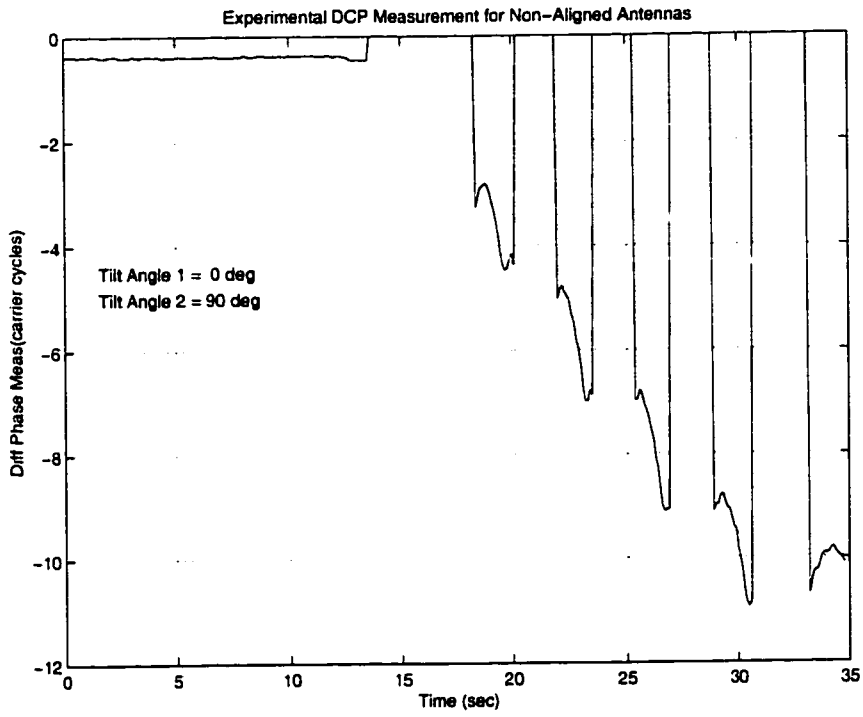

Figure 2.7: Experimental DCP data for non-aligned antennas. One antenna is periodically occluded. The phase measured by the antenna that has continuous view of transmitter increases by one cycle for each revolution of antenna baseline, causing a ramping of the DCP measurement.

are dependent on phase pattern interactions between the antenna and groundplane, antenna and surrounding vehicle structure, and inter-antenna phase pattern effects for small baselines [RH98]. When making DCP measurements from antennas with non-aligned boresights, this LOS dependent effect is not differenced out. The angular dependence of the phase pattern for an antenna and groundplane can be characterized experimentally using a transmitter in an anechoic chamber [SAC94]. The magnitude of the PCV component of the DCP is examined in Section 2.5.

In orbit, the only source of multipath reflected signals are from the vehicle itself. This self-reflected multipath is then solely a function of the LOS to the transmitter.

For attitude systems, this has been quantified to be on the order of 0.5 cm, and is the largest DCP measurement disturbance for on-orbit attitude applications [GL97]. This phase component is difficult to model due to the complicated reflection geometry present on most spacecraft. It is also difficult to calibrate using measurements on the ground since it requires the vehicle to be fully assembled and in flight configuration with all appendages, such as solar panels and antenna booms, deployed.

For the experiments done in this research, only the dominant effect on the DCP due to the RHCP is modeled. Modeling of the PCV effect on the DCP based on empirical data is examined only in simulation. The self-reflected multipath effect on the DCP measurement is treated as a measurement disturbance.

2.2.3 LOS Dependent DCP Compensation

Once the LOS dependent DCP components have been identified, there are two approaches to compensating for them in the attitude estimation process. One approach is to model the significant effects that can be modeled. Another approach, as demonstrated in Hayward [RH98], is to perform a real-time calibration of the LOS dependent phase effects based on an additional gyro measurement of vehicle attitude and subtract them from the GPS measurements.

The calibration measurement approach has the advantage of being more adaptive, handling both measurement disturbances and system parameter error effects on the DCP model. Calibration is good for effects that are not easily modeled, such as self-reflected multipath and small antenna baseline phase pattern effects, or time varying effects such as thermal shifts in the antenna line biases. The disadvantage of determining LOS dependent DCP components from a calibration 'map' is that it

requires an additional truth sensor for vehicle attitude and a calibration time period for collecting the data to construct the LOS dependent phase disturbance map.

By modeling the dominant phase effect, in this case polarization, as a function of transmitter line-of-sight, the method used in this research compensates for the dominant effect without extra sensors, and does so instantaneously without a calibration period, but treats PCV and multipath as measurement disturbances. In reality, modeling and calibration measurements are complementary and can be used concurrently.

2.3 RHCP Model

The GPS signal was designed to be broadcast with a right hand circularly polarized electromagnetic field. This was done to facilitate multipath rejection [AJVD96]. Since a right hand polarized wave tends to be reflected as either a linearly or left hand circularly polarized wave, a receive antenna that is right hand circularly polarized will tend to filter out these reflected signals. As the use of carrier phase measurements became more prevalent, the impact of the polarization on the measurement was examined as a DCP measurement error for both attitude systems and relative vehicle positioning [JW91]. Any DCP measurement between antennas that are non-aligned will see this effect.

This section summarizes the development of models for the RHCP portion of the DCP measurement. Two approaches to the model formulation are presented and compared. One is based on the vector projection of the signal E-field vector and the other on spherical trigonometry. Modifications to a near transmitter RHCP model developed by Zimmerman [KZ96] that are necessary for real-time attitude

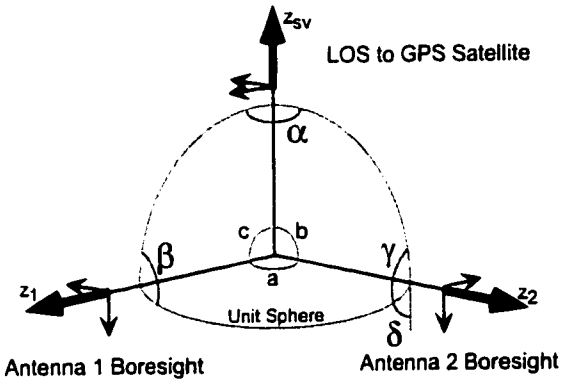

Figure 2.8: Angle definition for spherical trigonometric RHCP formulation.

determination under general attitude motion are also given. Also, the results of a static validation experiment of this modified RHCP model are shown.

2.3.1 Spherical Trigonometric Model

One method for formulating the RHCP component of the DCP measurement is based on heuristically derived rules observed when moving the boresight of a receive antenna [EGL96]. The first observed effect is that rotation of an antenna about its boresight vector will increase the measured carrier phase in direct proportion to that rotation angle. The second heuristic is that rotation of the receive antenna boresight vector about an axis perpendicular to the plane formed by the boresight vector and the LOS vector to the transmitter will cause no change to the measured carrier phase.

Lightsey derived a model for the RHCP contribution to the measured DCP, based on these heuristic rules, in terms of three unit vectors; the boresight vectors of the two receive antennas and the LOS vector to the transmitter. By rotating the two antennas in a DCP antenna baseline pair until their boresight vectors are aligned with the LOS vector to the transmitter through a series of rotations that are either about the antenna boresight or in the plane of the LOS vector, the RHCP contribution

to the DCP is then found to be the sum of the interior angles of a spherical triangle (α, β, γ) formed by the three unit vectors, plus a bias angle (δ) due to an initial rotation between the two antennas as they are placed on the vehicle (see Figure 2.8). Using this model, the additional phase can be written as $\Delta\phi_{\text{RHCP}} = \alpha+\beta+\gamma+\delta$. The angles of the spherical triangle formed by the antenna boresight and transmitter LOS unit vectors can be found from the interior angles formed by these three vectors using the cosine and sine law for spherical triangles (Equations 2.8). The interior angles can be found from the dot products of the triad of unit vectors ((Equations 2.7).

$$\begin{aligned} a &= \cos^{-1}\left(\hat{\underline{z}}_1 \bullet \hat{\underline{z}}_2\right) \\ b &= \cos^{-1}\left(\hat{\underline{z}}_2 \bullet \hat{\underline{z}}_{SV}\right) \\ c &= \cos^{-1}\left(\hat{\underline{z}}_1 \bullet \hat{\underline{z}}_{SV}\right) \end{aligned} \tag{2.7}$$

$$\begin{aligned} \alpha &= \cos^{-1}\left[\frac{\cos(a)-\cos(b)\cos(c)}{\sin(b)\sin(c)}\right] \\ \beta &= \sin^{-1}\left[\left(\frac{b}{a}\right)\sin(\alpha)\right] \\ \gamma &= \sin^{-1}\left[\left(\frac{c}{a}\right)\sin(\alpha)\right] \end{aligned} \tag{2.8}$$

This formulation is simple and intuitive, but assumes that the transmitters are very far from the receiving vehicle so that the LOS to each antenna are parallel. This assumption was valid for the case analyzed by Lightsey, but is not true for indoor laboratory conditions or the case where pseudolites are used to augment the GPS constellation for close-in operations of an autonomous servicing vehicle. A more general model for the RHCP phase contribution, based on antenna theory, is necessary to simultaneously handle both near and far transmitters.

2.3.2 *E*-field Vector Projection Models

Lawrence [DL96] and Zimmerman [KZ96] used a different approach to define the polarization component of the measurement model, similar to that proposed by

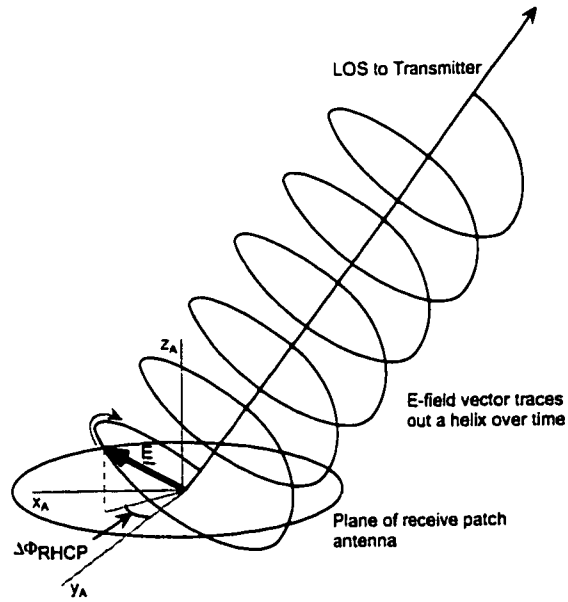

Figure 2.9: Vector projection of circularly polarized wave E-field vector on plane of GPS receive patch antenna.

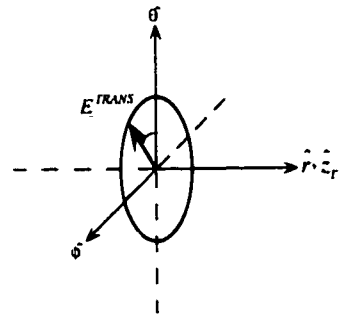

Figure 2.10: Spherically Radiated E-field Vector. For helical transmit antenna, the far-field radiated E-field vector has no radial component, and rotates in time.

Wu [JW91]. In their formulations, the E-field vector for the far-field model of a right hand polarized helical transmitter antenna is defined first. The phase component due to polarization is then found by determining the projection of this E-field vector onto the plane of the receiving patch antenna (see Figure 2.9). Lawrence's

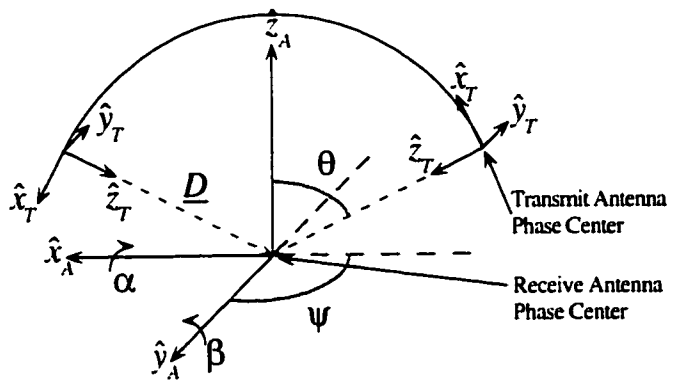

Figure 2.11: Definition of Transmitter Coordinate Frame. Zimmerman RHCP model rotation definition - angles ψ and θ. Improved RHCP model rotation definition - angles α and β.

derivation assumed both receive antennas had the same LOS to the transmitter (essentially the far transmitter case), whereas Zimmerman's model was defined for both the near and far transmitter case.

The transmitted E-field is a spherically symmetric rotating vector (see Figure 2.10) that has no radial component in the far-field approximation, and the component of this rotating vector in the plane of the receive antenna can be formulated as a function of the rotation matrix from the frame of the transmit antenna to the frame of the receive antenna frames. The difference between a near transmitter and a far transmitter is then just whether one assumes this rotation matrix is the same for separate receive antennas on the vehicle [KZ95]. A similar formulation that incorporated the effects of a near transmitting antenna was developed in the work by Stone [JS98] [JS99]. The near transmitter effect introduces an additional carrier phase shift that must be modelled as rotation of the transmitted E-field vector into a frame fixed along the line-of-sight to the transmit antenna. If both receive antenna boresights remain aligned, Stone has shown that the near transmitter differential phase correction for

polarization is simply the difference in the azimuth angles from the transmitter to each receive antenna.

For a spherically transmitting helical antenna, the far field E-field vector is defined as [CB92]

$$\underline{E}^{\text{TRANS}} = \mathcal{E}_\theta \hat{\theta} + \mathcal{E}_\phi \hat{\phi} + \mathcal{E}_r \hat{r} \tag{2.9}$$

$$\underline{E}^{\text{TRANS}} = \begin{bmatrix} \cos(\omega_{L1} t) \\ e \sin(\omega_{L1} t) \\ 0 \end{bmatrix} \tag{2.10}$$

This vector is in general not exactly circularly polarized, but has some ellipticity, e, on the order of 10%. As shown in Figure 2.11, the transmitting antenna frame $(\hat{x}_T, \hat{y}_T, \hat{z}_T)$ is defined with the z-axis aligned with the line-of-sight from the transmit antenna phase center to each receive antenna phase center. The projection of the E-field vector in the plane of the antenna is then found by rotating the E-field vector by the transformation $T_{\text{TR-REC}}$.

$$\underline{E}^{\text{REC}} = T_{\text{TR-REC}} \underline{E}^{\text{TRANS}} = (R R_A)^T R_T \underline{E}^{\text{TRANS}} \tag{2.11}$$

$$\begin{aligned} R &= \text{Rotation matrix, vehicle frame to inertial frame} \\ R_A &= \text{Rotation matrix, receive antenna frame to vehicle frame} \\ R_T &= \text{Rotation matrix, transmitter frame to inertial frame} \end{aligned} \tag{2.12}$$

The vehicle rotation matrix, R, is a function of the attitude Euler angles, and each antenna rotation matrix, R_A, is a function of the boresight vector defined in the vehicle frame. The transmitter rotation matrix, R_T, is defined by the LOS vector from the transmit antenna phase center to the receive antenna phase center.

The received signal voltage, $r(t)$, is the superposition of the x and y components of the projected E-field vector, with the y component delayed by a quarter cycle.

$$\begin{aligned} r(t) &= E_x^{\mathrm{REC}}(t) + E_y^{\mathrm{REC}}\left(t - 2\pi/(4\omega_{L1})\right) \\ &= a\cos(\omega_{L1}t) + b\sin(\omega_{L1}t) \\ &= (\sqrt{a^2+b^2})\cos\left[\omega_{L1}t - \arctan(b/a)\right] \end{aligned} \tag{2.13}$$

From Equations 2.10, 2.11, and 2.13, the coefficients a and b can be derived as a function of the transmitter to receive antenna rotation matrix $T_{\mathrm{TR-REC}}$

$$a = T_{11} - e\,T_{22}\,. \quad b = T_{21} + e\,T_{12} \tag{2.14}$$

The phase component of the received signal due to polarization, $\arctan(b/a)$, is then a function of the transmit antenna to receive antenna rotation matrix $T_{\mathrm{TR-REC}}$ elements T_{11}, T_{12}, T_{21}, and T_{22};

$$T_{\mathrm{TR-REC}} = \begin{bmatrix} T_{11} & T_{12} & T_{13} \\ T_{21} & T_{22} & T_{23} \\ T_{31} & T_{32} & T_{33} \end{bmatrix} \tag{2.15}$$

$$\phi_{\mathrm{RHCP}} = \arctan\left(\frac{T_{21} + e\,T_{12}}{T_{11} - e\,T_{22}}\right) \tag{2.16}$$

Zimmerman [KZ96] defined the rotation from the transmit antenna frame to the inertial frame in terms of the LOS azimuth angle and the complement of the LOS elevation angle, ϕ and θ (see Figure 2.11) respectively, as

$$R_T = \begin{bmatrix} \cos\phi\cos\theta & -\sin\phi & \cos\phi\sin\theta \\ \sin\phi\cos\theta & \cos\phi & \sin\phi\sin\theta \\ -\sin\theta & 0 & \cos\theta \end{bmatrix} \tag{2.17}$$

$$\theta = \arctan\left(\frac{\sqrt{D_x^2 + D_y^2}}{D_z}\right), \quad \phi = \arctan\left(\frac{D_y}{D_x}\right) \tag{2.18}$$

D_x, D_y, D_z are the components of $\underline{D}$, the vector position of the receive antenna phase center relative to the transmit antenna phase center. This definition has a singularity when the location of the transmitter LOS coincides with the antenna boresight, *i.e.* when the transmitter is located at the receive antenna zenith, *i.e.* $D_x = D_y = 0$. In this orientation, there is an ambiguity as to which direction the transmitted E-field vector is pointing. In previous work, this formulation of the RHCP correction was only applied in post-processing to cases where the antenna geometry was such that placing the transmit antenna directly above a a receive antenna could be avoided. To make the compensation for polarization in the measurement more robust for the real-time case with general attitude motion, a formulation is required that corrects for the singularity.

2.3.3 Improved Near Transmitter Model

The following shows a formulation similar to that just shown, but the approach has been modified to remove the singularity found in Zimmerman's formulation [JCA98]. A change in the definition of the transmit antenna frame was made to remove the singularity that occurs in the rotation matrix when the transmitter was at the receive antenna zenith. The singularity was moved to the plane of the receive antenna. This is a much better location for the singularity because the antenna visibility is limited in that direction, and signals acquired at low elevation angle are typically masked out by the receiver software. Since the focus of this research was to produce attitude estimation algorithms that are robust to general spacecraft attitude motion, where the line of sight to the transmitter easily fall along the receive antenna boresight, this singularity problem in the polarization model needed to be addressed.

The rotation matrix from the transmitter frame is then written in terms of the fixed rotation angles α and β about the x_A and y_A axes of the antenna frame respectively (see Figure 2.11).

$$R_T = \begin{bmatrix} \cos\beta & 0 & \sin\beta \\ \sin\beta\sin\alpha & \cos\alpha & -\cos\beta\sin\alpha \\ -\sin\beta\cos\alpha & \sin\alpha & \cos\beta\cos\alpha \end{bmatrix} \tag{2.19}$$

This rotation matrix can be rewritten in terms of the components of $\underline{D}$, which is defined as

$$\begin{aligned} \underline{D}_{ik} &= \underline{P} + R\,\underline{b}_i - \underline{Q}_k \\ \underline{P} &= \text{position of vehicle, inertial frame} \\ \underline{b}_i &= \text{position of antenna } i\text{, vehicle frame} \\ \underline{Q}_k &= \text{position of transmitter } k\text{, inertial frame} \end{aligned} \tag{2.20}$$

The rotation matrix from the transmitter to inertial frame is then

$$R_T = \begin{bmatrix} \frac{\sqrt{D_y^2+D_z^2}}{|\underline{D}|} & 0 & \frac{D_x}{|\underline{D}|} \\ \frac{-D_xD_y}{|\underline{D}|\sqrt{D_y^2+D_z^2}} & \frac{D_z}{\sqrt{D_y^2+D_z^2}} & \frac{D_y}{|\underline{D}|} \\ \frac{-D_xD_z}{|\underline{D}|\sqrt{D_y^2+D_z^2}} & \frac{-D_y}{\sqrt{D_y^2+D_z^2}} & \frac{D_z}{|\underline{D}|} \end{bmatrix} \tag{2.21}$$

Using the definitions in equation 2.21, R, and R_A, the elements of the $T_{\text{TR-REC}}$ matrix can be calculated and the RHCP DCP component can be found from 2.16. This model is equally valid for both the near transmitter and far transmitter cases. For the far transmitter case, the LOS to the transmit antenna is the same for all receive antennas, and the vector D_{ik} can be redefined as V_k where

$$\underline{V}_k = \underline{P} - \underline{Q}_k. \tag{2.22}$$

The transmitter rotation matrix can be re-written as

$$R_T = \begin{bmatrix} \frac{\sqrt{V_y^2+V_z^2}}{|\underline{V}|} & 0 & \frac{V_x}{|\underline{V}|} \\ \frac{-V_xV_y}{|\underline{V}|\sqrt{V_y^2+V_z^2}} & \frac{V_z}{\sqrt{V_y^2+V_z^2}} & \frac{V_y}{|\underline{V}|} \\ \frac{-V_xV_z}{|\underline{V}|\sqrt{V_y^2+V_z^2}} & \frac{-V_y}{\sqrt{V_y^2+V_z^2}} & \frac{V_z}{|\underline{V}|} \end{bmatrix} \tag{2.23}$$

In the far transmitter case, the transmitter to receive antenna rotation matrix is no longer a function of antenna position on the vehicle.

Another modification was made to compensate for the discontinuity of the arctan function in this formulation of RHCP phase component. The range of the atan function output is $\pm\pi$ radians, thus there will be some attitudes for which the modeled RHCP phase for a given antenna will wrap by one rotation using this model. This is solely an artifact of the modeling, as the actually measured phase from a GPS receiver will increase to ranges greater than $\pm\pi$ radians. The problem occurs when the modeled RHCP phase for one antenna is wrapped by 2π radians while the modeled phase for another antenna has not wrapped (see Figure 2.12). It is necessary to unwrap the modeled RHCP phase, taking into account common transmitter visibility, to remove the periodic discontinuities that occur in the modeled DCP measurement that includes the RHCP component.

2.4 Single Rotation Examples

A few single baseline examples are now developed to compare the RHCP formulations defined in the previous section. The near transmitter formulation is determined for a simple example case, the spherical and vector projection formulations are compared, and the near and far transmitter formulations are compared.

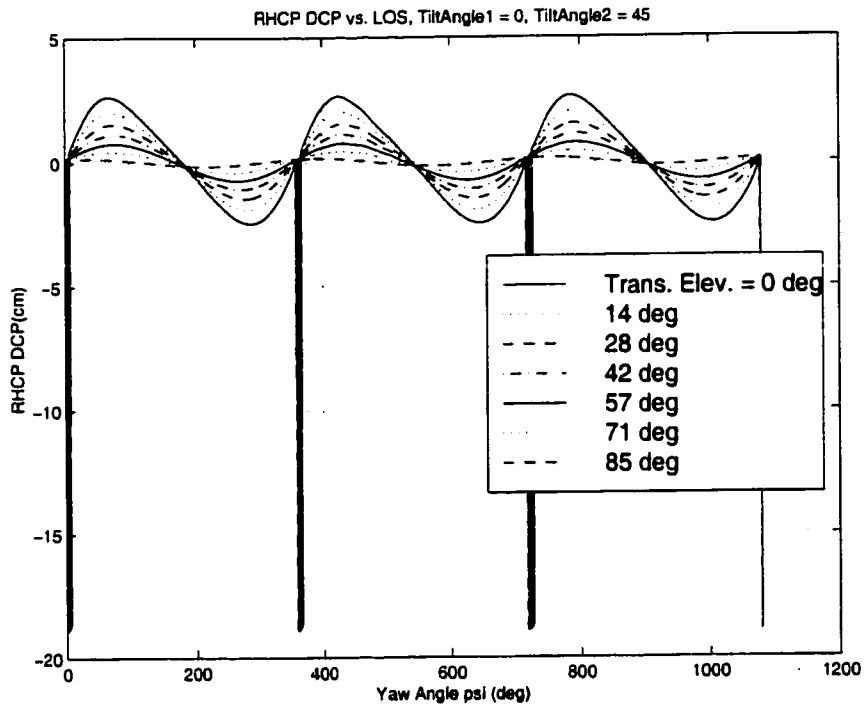

Figure 2.12: Modeled RHCP component with no compensation for atan discontinuity.

2.4.1 Example 1 - RHCP with Transmitter at Zenith

A simple example can be defined where the antenna coordinate frame is aligned with the vehicle frame, the transmitter is located directly above the receive antenna, and the vehicle is constrained to planar motion with only yaw angle ψ changes in attitude (see Figure 2.13). Then $R_A = I_{3\times3}$, and

$$R_T = \begin{bmatrix} 1 & 0 & 0 \\ 0 & -1 & 0 \\ 0 & 0 & -1 \end{bmatrix}, R = \begin{bmatrix} \cos\psi & -\sin\psi & 0 \\ \sin\psi & \cos\psi & 0 \\ 0 & 0 & 1 \end{bmatrix} \tag{2.24}$$

$$T_{\text{TR-REC}} = (RR_A)^T R_T \tag{2.25}$$

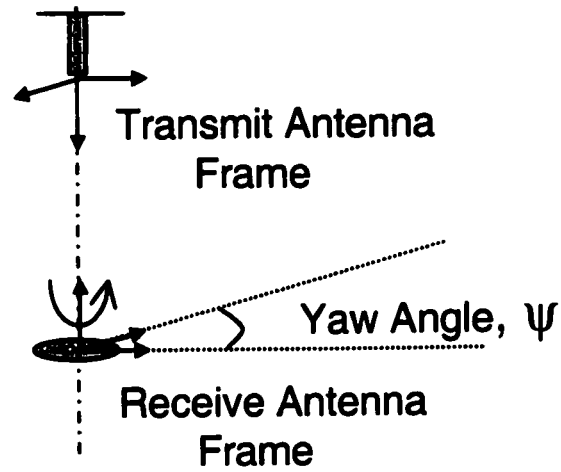

Figure 2.13: Antenna geometry for RHCP Example 1. Transmit antenna directly above receive antenna.

$$T_{\text{TR-REC}} = \begin{bmatrix} \cos\psi & -\sin\psi & 0 \\ -\sin\psi & -\cos\psi & 0 \\ 0 & 0 & -1 \end{bmatrix}. \tag{2.26}$$

The RHCP phase component measured at that the antenna is then

$$\begin{aligned} \phi_{\text{RHCP}} &= \arctan\left(\frac{-\sin\psi - e\sin\psi}{\cos\psi + e\cos\psi}\right) \\ &= -\arctan\left(\frac{\sin\psi}{\cos\psi}\right) \quad = -\psi \end{aligned} \tag{2.27}$$

This result agrees with the first rule described in Section 2.3.1, observable in simple experiments, that rotating an antenna about the boresight vector gives an increase in the measured differential carrier phase proportional to the angle of rotation.

2.4.2 Example 2 - Static Validation Experiment Data

A static test of this measurement model was conducted by making single baseline DCP measurements on a stationary antenna baseline and increasing the tilt angle of the antennas in 5° increments. A plot of the change in DCP from the aligned case

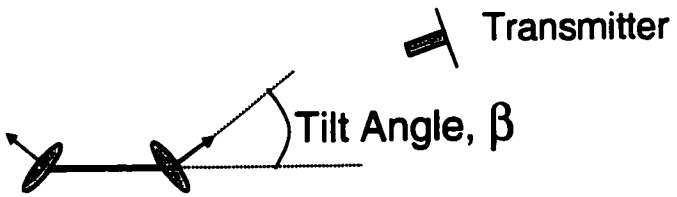

Figure 2.14: Single antenna baseline DCP measurement from a single transmitter with varying antenna boresight tilt angles, β, from 0° to 90°. Geometry used for static validation test of RHCP model.

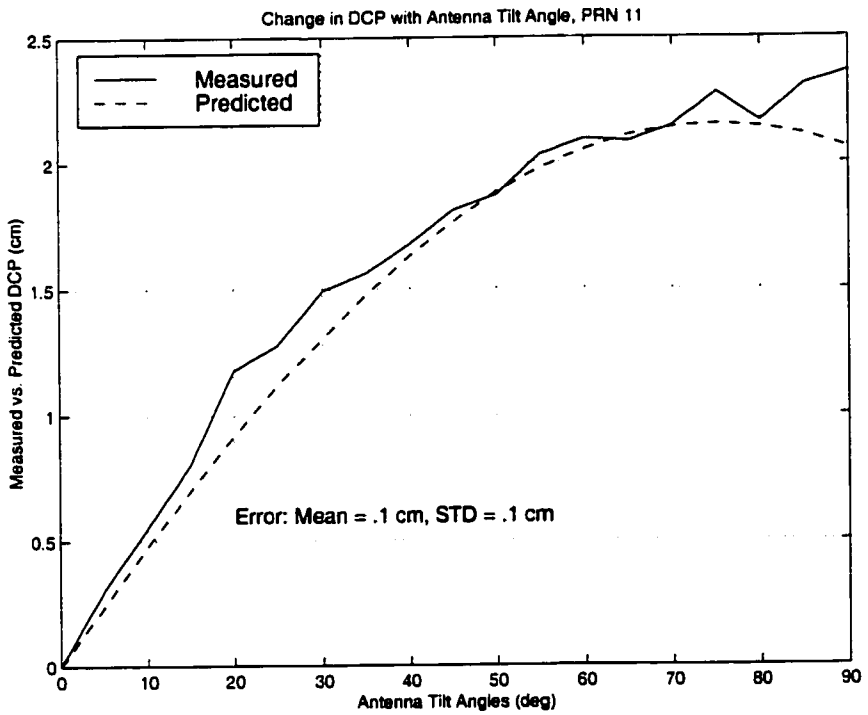

Figure 2.15: Change in DCP with Antenna Tilt Angle - Experiment vs. Simulation.

versus the tilt angle of the antenna is plotted in Figure 2.15, along with the change in DCP predicted from the measurement model. The change in DCP is shown for a single transmitter visible to both antennas during the test in the laboratory. The match between predicted and measured DCP is good, with error between the modeled

and measured DCP on the order of 2–3 mm, which is within the receiver phase noise of the measurement. There is some increase in the error for larger tilt angles, which is expected due to the unmodeled phase center variation and multipath in the data. But this comparison provides a good validation of the model for the dominant polarization component of the measurement, for the static case.

2.4.3 Example 3 - Simulation of RHCP DCP vs. LOS

A plot of the RHCP phase component as a function of transmitter LOS, parameterized by baseline rotation yaw angle and transmitter elevation angle, is presented in Figure 2.17. The plots are for a single antenna baseline with one antenna boresight vertical and the other horizontal (See Figure 2.16). This baseline is then rotated about the vertical axis and the RHCP phase is plotted for varying transmitter elevation. Figure 2.17 shows that, for certain transmitter elevations and baseline yaw angles, the RHCP measurement component can be as large as 9-10 cm, or half the L_1 carrier wavelength.

2.4.4 Example 4 - RHCP DCP for Near/Far Transmitter

In Figure 2.18, a comparison is made between the modeled RHCP phase component assuming near transmitters and far transmitters. The comparison is for a transmitter at zero elevation with a radial distance of 3 m and the single antenna baseline case shown in Figure 2.16. This transmitter distance is typical of one of the indoor laboratories used in this research. This comparison shows that, if the near transmitter effects are ignored, then the error in the modeled RHCP phase component to the DCP measurement is significant (as large as 2 cm). The near transmitter component of the RHCP DCP is not symmetric with rotation since the antenna baseline, as shown

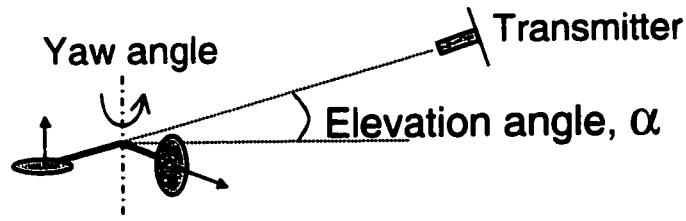

Figure 2.16: Single antenna baseline DCP measurement from a single transmitter with varying elevation angle, α, from 0° to 90°, and antenna boresights at 90° to each other. As baseline is rotated in yaw and elevation, LOS to transmitter is mapped out.

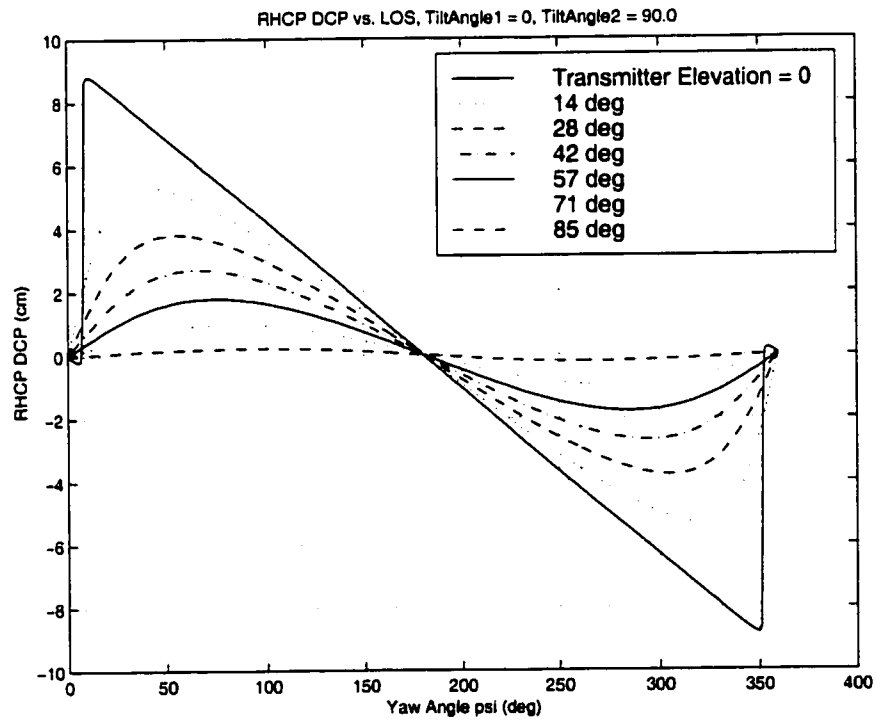

Figure 2.17: Simulated RHCP component of differential carrier phase measurement for varying transmitter LOS - Tilt Angle-1 = 0°, Tilt Angle-2 = 90°.

in Figure 2.16, is rotating about a point offset from the center of the line connecting the two antenna phase centers.

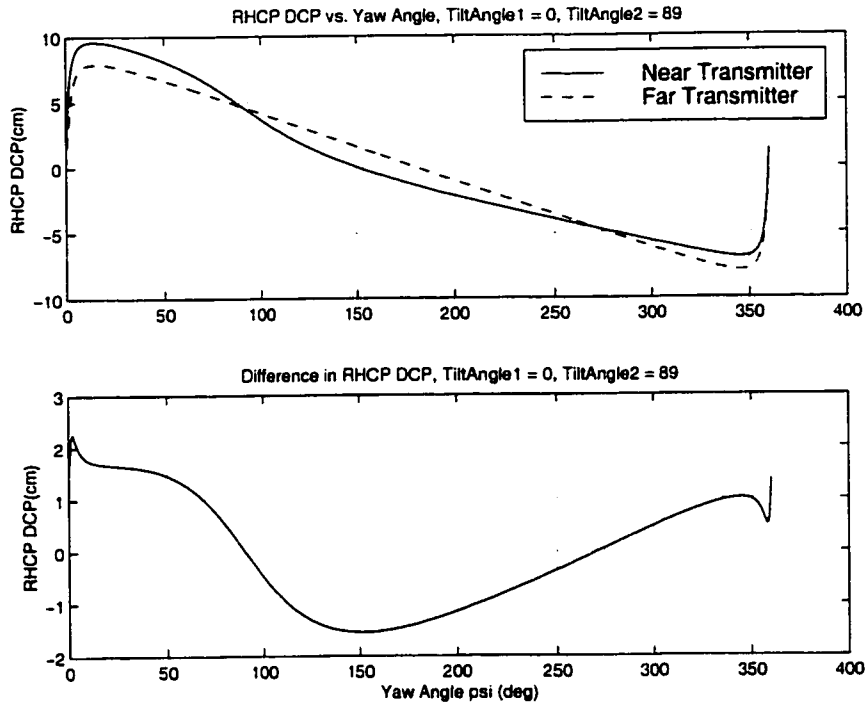

Figure 2.18: Simulated RHCP component, near vs far transmitters.

2.4.5 Example 5 - RHCP Formulation Comparison

In Figure 2.19, a comparison is made between the modeled RHCP phase component using the spherical trigonometric formulation described in Section 2.3.1, and the E-field vector projection formulation described in Section 2.3.2. Again this is for the single baseline geometry shown in Figure 2.16, and zero transmitter elevation angle. For most baseline yaw angles, there is a slight difference between the two formulations that averages less than 1 cm. This difference is due to the heuristics used to deduce the spherical trigonometric formulation which assumed linearly increasing RHCP DCP with rotation about the boresight. However, this increase is not linear because it changes with the angle at which the E-field vector is projected onto the plane of the antenna. This effect is included in the formulation based on the E-field projection.

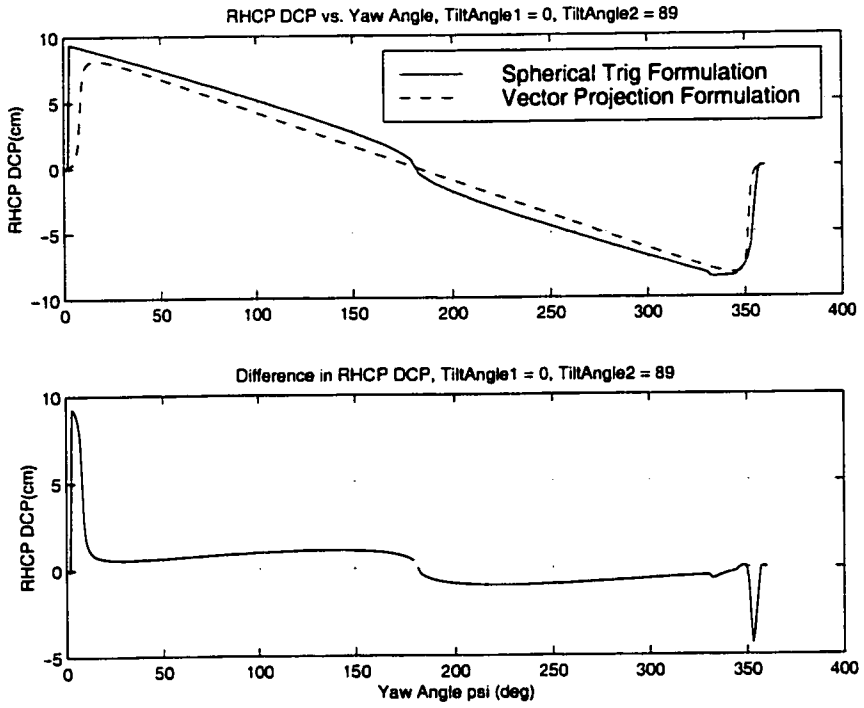

Figure 2.19: Modeled RHCP component, spherical trigonometric formulation vs. vector projection.

After presenting some examples that analytically, experimentally, and through simulation predict the RHCP component of a single baseline DCP measurement, the next section will present a model for the antenna phase center variation (PCV) component of the DCP measurement.

2.5 Antenna Phase Center Variation(PCV) Model

The next most significant LOS dependent measurement effect is the phase center variation [SAC94]. The phase pattern of a GPS antenna will vary with LOS to the transmitter, as well as with the surrounding environment. An isolated antenna and backplane can be calibrated for phase center variation with transmitter LOS, and previous studies have shown that for typical GPS antennas, this variation is on the

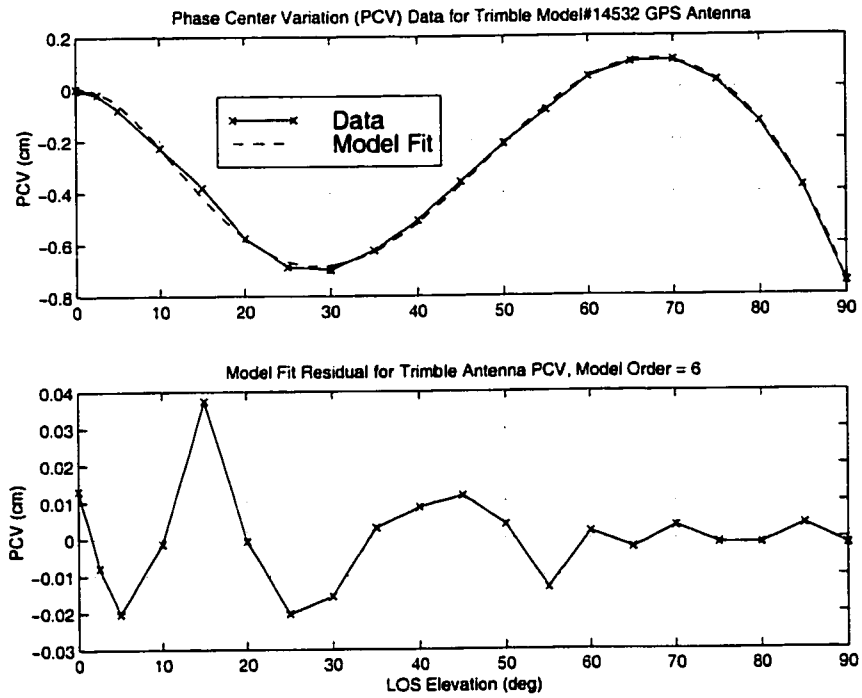

Figure 2.20: Phase center variation data and 6th order polynomial model fit for the Trimble GPS antenna used on the TANS Vector attitude receiver, versus antenna LOS elevation angle. (PCV is symmetric about the antenna azimuth).

order of 8 mm (2–3 mm for survey quality antennas). The phase center variation (PCV) is generally symmetric about the antenna boresight, and varies periodically with transmitter LOS elevation. A simple polynomial fit model for the PCV derived from the antenna pattern data in [SAC94] is shown in Figure 2.20. For this particular antenna, the Trimble Model 14532 used on the TANS Vector attitude receiver, the maximum phase center variation is 6 mm.

Figure 2.21 shows the magnitude of the modeled PCV DCP component, based on the polynomial fit model shown in Figure 2.20, as a function of transmitter LOS, parameterized by baseline rotation yaw angle and transmitter elevation angle. The PCV component can vary up to ±0.77 cm, or about an order of magnitude less than

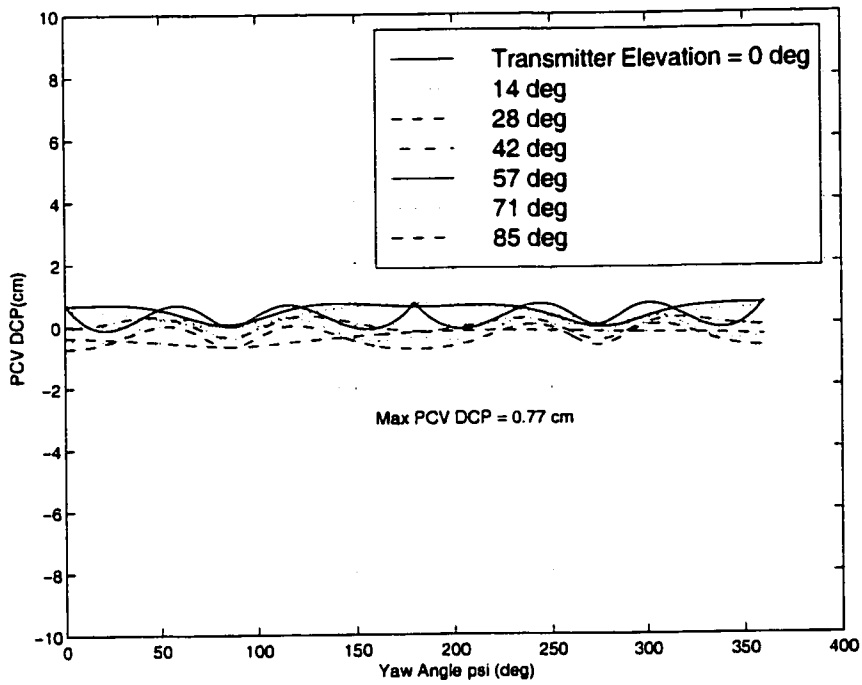

Figure 2.21: Phase center variation component of differential carrier phase measurement for varying transmitter LOS - Tilt Angle-1 = 0°, Tilt Angle-2 = 90°.

the RHCP component of the DCP. As was successfully demonstrated for aircraft by Hayward [RH98], the PCV component can be mapped as a function of transmitter line-of-sight by performing a calibration on the spacecraft, either in orbit or in a ground based anechoic chamber test.

2.6 Unmodeled DCP Effects

In addition to the two previous modeled phase effects, there are other unmodeled measurement disturbances that are significant, particularly for the indoor laboratory tests we performed. The unmodeled effects include phase pattern effects due to surrounding vehicle structure, phase variations due to receiver tracking loop errors,

and the most significant, multipath reflected signals. The multipath error in our laboratory is discussed in Chapter 5.

Multipath errors in the DCP measurement are difficult to model, and since for spacecraft all multipath signals are self-reflected, the multipath is LOS dependent (just like PCV phase). Calibration procedures have been proposed for spacecraft [CC92] and demonstrated for aircraft [RH98], where the total phase disturbance as a function of LOS to the transmitter, including both PCV and multipath components, is measured and subtracted from the DCP measurements. For the aircraft problem, these calibration measurements can be made while in flight, where the multipath component of the measurement due to reflections from fixed sources are small. For the spacecraft problem, a calibration enviroment where the multipath component of the measurement is primarily due to self-reflections off the vehicle itself could be achieved using a GPS transmitter in an anechoic environment, or on-orbit using additional attitude sensors, as shown in the work by Hayward [RH98]. This method may be necessary for certain precise DCP applications, such as vehicle formation sensing for separated spacecraft interferometry [KL97], despite the requirement of testing a fully integrated spacecraft, and the associated costs. But this type of calibration is not practical for a vehicle in a laboratory environment, where the majority of the multipath signal is not self-reflected. The calibration methods, receiver tracking loop designs, and antenna designs currently being explored to mitigate multipath effects on the DCP measurement are not addressed in this research.

In summary, the components of the DCP measurement model that become significant when making measurements from antennas with non-aligned boresights have been presented here. The methods for including these measurement components in the attitude estimation algorithms are presented in Chapter 3.

~

Chapter 3

Attitude Determination Algorithms

Robust attitude determination is defined in this research as providing continuous attitude solution availability during general attitude motion of the spacecraft. It also means improving the performance of the attitude estimation in terms of accuracy as well as the availability. The approach taken in this thesis to achieve this goal is to modify the GPS attitude receiver algorithms to produce attitude solutions using DCP measurements from a non-aligned antenna array (NAA).

The modifications necessary to the attitude estimation algorithms to achieve robust performance are examined in this chapter. These modifications include; redefinition of the DCP measurement vector to include redundant measurements, real-time handling of frequent measurement dropouts due to transmitter occlusion, and implementation of a real-time measurement bias re-acquisition algorithm. It also includes an extension of the estimation algorithm to include the vehicle dynamic model in a full extended Kalman filter (EKF). It was shown in Chapter 2 that it is necessary to make

changes in the DCP measurement model to account for LOS dependent effects that are present when using a NAA. Two methods for compensating for these effects were implemented and compared for processing requirements, and an analytic proof of the stability of the estimation algorithm is given. Finally, simulation results based on our laboratory tests are presented to show the improved performance of these modified attitude estimation algorithms for both single and three DOF attitude motions.

3.1 GPS Attitude Determination Basics

Many attitude estimation algorithms have already been demonstrated, using different attitude representations and different solution techniques for the resulting set of non-linear equations [VS76] [FVG91] [CC92]. The following is a brief overview of some ways to formulate this problem, followed by the modifications that were made in this research to perform attitude estimation using measurements from a NAA.

Once the measurement biases have been resolved, and if we ignore receiver noise, the phase measurements are effectively just differential range measurements between any two receive antennas (in a baseline pair) and a given transmitter. For the far transmitter case, this differential range measurement can be thought of as the projection of the baseline vector between two receive antennas i and j, $\underline{b}_{ij}$, onto the line-of-sight vector to a transmitter k, $\hat{\underline{s}}_k$,

$$\Delta r^F_{ijk} = \hat{\underline{s}}_k^T R \underline{b}_{ij} \tag{3.1}$$

where R is the rotation matrix from the vehicle fixed to inertial coordinate frame. In this case, the LOS vectors for each antenna to a given satellite are parallel, and perpendicular to the planar incoming signal wavefronts (see left side of Figure 3.1). The

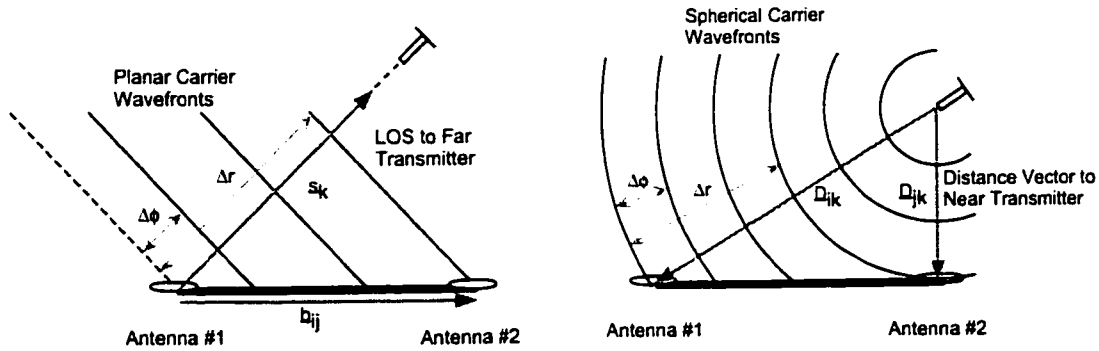

Figure 3.1: Far and near transmitter DCP geometry.

differential range measurements are solely a function the vehicle attitude. This decouples the attitude determination problem from the position determination problem for the far transmitter case.

In the case of near transmitters, the incoming wavefronts are spherical in the antenna far-field radiation pattern (see right side of Figure 3.1). The transmitter LOS vector for receive antenna i is not parallel to that for receive antenna j, and the differential range measurement is the difference in the magnitudes of the vector positions of the phase center of each receive antenna with respect to the transmit antenna,

$$\Delta r_{ijk}^{N} = |\underline{D}_{ik}| - |\underline{D}_{jk}| \tag{3.2}$$

The measurement is now a function of both vehicle attitude and position, coupling the attitude and position determination problems together [KZ96].

In both cases, vehicle attitude can be estimated given a sufficient number of differential range measurements. Attitude can be represented by a vehicle rotation matrix, a set of Euler rotation angles, or an attitude quaternion [JW78]. The optimal estimated state is then typically found by minimizing a cost function, J, based on the current set of differential range measurements. In most cases this cost function is the

weighted quadratic error in the measurement residual [CC96] [GL97] [FVG91]. Then the nonlinear measurement function, $\underline{h}$, is the vector of differential range measurements for each combination of antenna baseline and transmitter,

$$\underline{z} = \underline{h}(\underline{X}) = \underline{\Delta r} \tag{3.3}$$

Where $\underline{X}$ is the state of the vehicle to which the antennas are rigidly attached. To solve for the vehicle state, the nonlinear measurement function is linearized about an *apriori* state estimate, $\bar{\underline{X}}$. The Jacobian of the measurement function is defined as H where,

$$\underline{z} \approx \underline{h}\left(\bar{\underline{X}}\right) + \left.\frac{\partial \underline{h}}{\partial \underline{X}}\right|_{\bar{\underline{X}}} \left(\underline{X} - \bar{\underline{X}}\right) + \cdots \tag{3.4}$$

Truncating to first order, we then have,

$$\underline{\Delta z} \equiv \underline{z} - \underline{h}\left(\bar{\underline{X}}\right) = H\underline{\Delta X} \tag{3.5}$$

where $\underline{\Delta z}$, the measurement residual, and $\underline{\Delta X}$, the state estimate error, are defined as,

$$\underline{\Delta X} = \underline{X} - \bar{\underline{X}}, \quad \underline{\Delta z} = \underline{z} - \bar{\underline{z}}, \tag{3.6}$$

where $\bar{\underline{z}}$ is the estimated measurement $H\bar{\underline{X}}$. If we scale the measurement residual by the inverse of the measurement error covariance matrix, S, the optimal weighted least squares (WLS) estimate for the vehicle state at each measurement epoch can be found [AG74] as $\hat{X}$, and

$$\hat{\underline{X}} = \bar{\underline{X}} + \left(H^T S^{-1} H\right)^{-1} H^T S^{-1} \left(\underline{z} - H\bar{\underline{X}}\right) \tag{3.7}$$

Because the measurement function is nonlinear, it is necessary to iterate on Equation 3.7 at each measurement epoch, such that for each iteration, i, the updated state estimate, $\hat{\underline{X}}$, for an iterated weighted least squares (IWLS) solution is [AG74]

$$\hat{\underline{X}}_i = \bar{\underline{X}}_i + \left(H_i^T S^{-1} H_i\right)^{-1} H_i^T S^{-1} \left(\underline{z} - \underline{h}_i(\bar{\underline{X}}_i)\right) \tag{3.8}$$

where

$$\bar{\underline{X}}_i = \hat{\underline{X}}_{i-1}, \quad \text{and} \quad H_i = \left.\frac{\partial \underline{h}}{\partial \underline{X}}\right|_{\bar{\underline{X}}_i} \tag{3.9}$$

Many applications have used either WLS and IWLS algorithms for attitude estimation [EO98] [KZ95] [KB94]. The differences in the attitude estimation algorithms exist in how the linearized measurement matrix, H, is defined, depending on transmitter distance, antenna baseline separation, and receive noise characteristics [HT97] [KZ96]. In the following two sections, methods for attitude solution are presented for the far transmitter case, and for the near transmitter case. The near transmitter formulation, which was used in the experimental portion of this research using measurements from a NAA, is modified to included the linearization for the RHCP component of the measurement vector.

3.1.1 Far Transmitter Formulations

For the far transmitter case, the nonlinear cost function, J, is defined based on the attitude matrix, R, which is the rotation matrix from the vehicle fixed to inertial coordinates, and the differential range measurements as defined in Equation 3.1. In this case, the vehicle state is a function of attitude only [CC92].

$$J(R) = \sum_{i=1}^{i=N_a-1} \sum_{j=i+1}^{j=N_a} \sum_{k=1}^{j=N_t} w_{ijk} \left(\Delta r_{ijk} - \underline{s}_k^T R \underline{b}_{ij}\right)^2 \tag{3.10}$$

N_a is the number of antennas and N_t is the number of transmitters. This cost function can be linearized about the current attitude matrix estimate, R_0, to yield updates to the estimate based on the current set of measurements [GL97]. For antennas i and j, and transmitter k, the linearized measurement is

$$\delta \Delta r_{ijk} = -\underline{s}_k^T R_0 b_{ij}^{\times} \underline{\delta\theta} \tag{3.11}$$

where $\underline{\delta\theta}$ is a desired vector of small, fixed axis, rotation angles about the vehicle-fixed axes to be solved for, and $b_{ij}^{\times}$ is the skew symmetric matrix formed from the antenna baseline vector.

$$\underline{\delta\theta} = \begin{bmatrix} \delta\theta_x \\ \delta\theta_y \\ \delta\theta_z \end{bmatrix}, \quad b_{ij}^{\times} = \begin{bmatrix} 0 & -b_{ijz} & b_{ijy} \\ b_{ijz} & 0 & -b_{ijx} \\ -b_{ijy} & b_{ijx} & 0 \end{bmatrix}. \quad \underline{b}_{ij} = \begin{bmatrix} b_{ijx} \\ b_{ijy} \\ b_{ijz} \end{bmatrix} \tag{3.12}$$

These linearized measurements for each antenna baseline (i, j) can be stacked to form the linearized measurement matrix, H, where

$$H_{m\times n} = \begin{bmatrix} \vdots \\ -\underline{s}_k^T R_0 b_{ij}^{\times} \\ \vdots \end{bmatrix}, \quad \begin{array}{rcl} m & = & \text{number of DCP measurements,} \\ n & = & \text{number of attitude states} \end{array} \tag{3.13}$$

and

$$\delta\underline{\Delta r} = H\underline{\delta\theta} \tag{3.14}$$

This H matrix can be used in the WLS or IWLS equations in Equations 3.7 and 3.8 to solve for the incremental change in the fixed axis rotation angles, $\hat{\underline{X}} = \underline{\delta\theta}$, using the current set of differential range measurements, $\underline{z} = \underline{\Delta r}$. The incremental rotation, $\underline{\delta\theta}$, is used in Equation 3.15 to solve for the updated estimate of the vehicle attitude matrix R given the current estimate R_0.

$$R = R_0\left(I + \theta^{\times}\right), \quad \text{where,} \quad \theta^{\times} = \begin{bmatrix} 0 & -\delta\theta_z & \delta\theta_y \\ \delta\theta_z & 0 & -\delta\theta_x \\ -\delta\theta_y & \delta\theta_x & 0 \end{bmatrix} \tag{3.15}$$

This method of linearization and solution for the attitude matrix for the far transmitter case was applied by Lightsey [GL97] and further developed in the work of Crassidis [JC97]. From the rank of the H matrix, it can be seen that it is necessary to have measurements from at least two transmitters to two non-colinear antenna

baselines (3 antennas minimum) for the attitude determination problem to be determined.

The quadratic cost function shown in Equation 3.10 is not the only way to formulate the estimation problem. In order to minimize the processing time required in the receiver, Cohen [CC92] proposed posing the attitude determination problem as a case of 'Wahba's problem', or finding attitude from vector observations, for which many efficient solution algorithms exist. For this far transmitter formulation, the cost function is redefined as

$$J(R) = \sum_{i=1}^{i=N_a-1} \sum_{j=i+1}^{j=N_a} \sum_{k=1}^{j=N_t} w_{ijk} \left(\Delta r_{ijk} - \underline{s}_k^T R \underline{b}_{ij} \right) \Rightarrow J(R) = \sum_{v=1}^{v=n} W_v \left| \hat{\underline{s}}_{Bv} - R \hat{\underline{s}}_{Iv} \right| \quad (3.16)$$

These two cost functions appear quite similar in that both take a set of vector observations given in the body frame, $\hat{\underline{s}}_{Bv}$, and the corresponding set of known vectors given in the inertial frame, $\hat{\underline{s}}_{Iv}$, and solve for vehicle attitude by minimizing the resulting cost function. The Wahba formulation is efficient because, through judicious choice of the weights, W_v, the problem reduces to a singular value decomposition problem.

The Wahba formulation has been successfully used in many applications, most notably on the Trimble TANS Vector GPS attitude receiver [CC92]. However, while this approach is faster, it is not possible to use this formulation with coplanar baselines, therefore at least 4 antennas are necessary. Like the previous approach, it also solves for the attitude matrix directly.

3.1.2 Near Transmitter Formulations

For the near transmitter case, the differential range measurements are a function of both the attitude and position of the vehicle. Zimmerman [KZ96] showed that the near transmitter case can be handled by assuming circular wavefronts as shown in

Figure 3.1. The boundary between the near and far transmitter assumption depends on three parameters; antenna baseline separation, transmitter range, and receiver noise. If the differential range between two receive antennas and the transmitter divided by their baseline separation is comparable to the receiver carrier phase tracking noise (in radians), then the near transmitter assumption is made [HT97].

When making measurements using a NAA, as was shown in Chapter 2, LOS dependent terms are part of the model. The linearization of the measurement model for the case where the LOS dependent RHCP phase term is included is presented in this section. The linearized measurement matrix, H, used in the attitude estimation is found for the case where vehicle state includes both position and attitude. If we model the polarization, and assume that all of the measurement biases have been resolved, then from Equation 3.2

$$\Delta r_{ijk} = |\underline{D}_{ik}| - |\underline{D}_{jk}| + \Delta\phi_{RHCP_{ijk}} \quad \Rightarrow \quad \Delta r_{ijk} = \Delta\phi_{D_{ijk}} + \Delta\phi_{RHCP_{ijk}} \tag{3.17}$$

where $\Delta\phi_{RHCP_{ijk}}$, the dominant RHCP phase component has been added. The measurement vector, Δr, is formed by stacking the measurements in Equation 3.17 for all transmitters and baselines. The H matrix is defined as the Jacobian of the measurement vector with respect to the vehicle state, which in this case includes the vehicle position.

$$H = \frac{\partial \underline{\Delta r}}{\partial \underline{X}} = \left[\frac{\partial \underline{\Delta r}}{\partial P_x}, \frac{\partial \underline{\Delta r}}{\partial P_y}, \frac{\partial \underline{\Delta r}}{\partial P_z}, \frac{\partial \underline{\Delta r}}{\partial \psi}, \frac{\partial \underline{\Delta r}}{\partial \theta}, \frac{\partial \underline{\Delta r}}{\partial \phi}\right] \tag{3.18}$$

Given the vehicle state definition, $\underline{X} = [P_x, P_y, P_z, \psi, \theta, \phi]^T$ the first three columns of the H matrix only become important for the near transmitter case. The linearization of the measurement vector is separated into four terms,

$$H = H_D + H_{\text{RHCP}} = \left[\frac{\partial \underline{\Delta\phi}_D}{\partial \underline{P}} + \frac{\partial \Delta\phi_{RHCP}}{\partial \underline{P}}, \frac{\partial \underline{\Delta\phi}_D}{\partial \underline{\Theta}} + \frac{\partial \Delta\phi_{RHCP}}{\partial \underline{\Theta}}\right] \tag{3.19}$$

where the vehicle position and attitude states are defined as $\underline{P} = [P_x, P_y, P_z]^T$ and $\underline{\Theta} = [\psi, \theta, \phi]^T$, differentiating the delta range portion of the measurement and the RHCP portion of the measurement with respect to the vehicle position and attitude, respectively.

Using the Euler angle sequence (ψ – yaw, θ – pitch, ϕ – roll) to represent vehicle attitude, the delta range term, $\underline{\Delta\phi}_D$, in the DCP equation is first differentiated with respect to vehicle attitude, $\underline{\Theta}$. The derivative of the measurement with respect to the yaw Euler angle is

$$\frac{\partial \underline{\Delta\phi}_D}{\partial \psi} = \frac{\partial \underline{\phi}_{D1}}{\partial \psi} - \frac{\partial \underline{\phi}_{D2}}{\partial \psi} \tag{3.20}$$

Looking at just the range term for antenna 1 in the measurement equation, and using the antenna range geometry defined in Equation 2.20,

$$\frac{\partial \underline{\phi}_{D1}}{\partial \psi} = \frac{\partial}{\partial \psi}\left(|\underline{D}_1|\right) = \frac{\partial}{\partial \psi}\left(\left|\underline{P} + R\underline{b}_1 - \underline{Q}\right|\right) \tag{3.21}$$

Substituting in the components of $\underline{D}$, the range vector,

$$\frac{\partial \underline{\phi}_{D1}}{\partial \psi} = \frac{1}{2}\left(D_{1x}^2 + D_{1y}^2 + D_{1z}^2\right)^{-\frac{1}{2}} \frac{\partial}{\partial \psi}\left(D_{1x}^2 + D_{1y}^2 + D_{1z}^2\right) \tag{3.22}$$

$$\frac{\partial \underline{\phi}_{D1}}{\partial \psi} = \frac{1}{2\,|\underline{D}_1|}\left[2D_{1x}\frac{\partial D_{1x}}{\partial \psi} + 2D_{1y}\frac{\partial D_{1y}}{\partial \psi} + 2D_{1z}\frac{\partial D_{1z}}{\partial \psi}\right] \tag{3.23}$$

From Equation 3.21, and since the vehicle position $\underline{P}$ and transmitter position $\underline{Q}$ are not functions of the attitude angle ψ, the derivatives of the components of $\underline{D}_1$ can be expressed in terms of the rows of the vehicle rotation matrix, R,

$$\frac{\partial \underline{\phi}_{D1}}{\partial \psi} = \frac{1}{|\underline{D}_1|}\left[D_{1x}\frac{\partial R(1,:)}{\partial \psi}\underline{b}_1 + D_{1y}\frac{\partial R(2,:)}{\partial \psi}\underline{b}_1 + D_{1z}\frac{\partial R(3,:)}{\partial \psi}\underline{b}_1\right] \tag{3.24}$$

which becomes,

$$\frac{\partial \underline{\phi}_{D1}}{\partial \psi} = \frac{1}{|\underline{D}_1|}\left[\underline{D}_1^T\frac{\partial R}{\partial \psi}\underline{b}_1\right] \tag{3.25}$$

Similarly, for the θ and ϕ Euler rotation angles,

$$\frac{\partial \underline{\phi}_{D1}}{\partial \theta} = \frac{1}{|\underline{D}_1|}\left[\underline{D}_1^T \frac{\partial R}{\partial \theta}\underline{b}_1\right] \quad \text{and} \quad \frac{\partial \underline{\phi}_{D1}}{\partial \phi} = \frac{1}{|\underline{D}_1|}\left[\underline{D}_1^T \frac{\partial R}{\partial \phi}\underline{b}_1\right] \tag{3.26}$$

These derivative definitions can be differenced between antennas to provide the corresponding elements of the H_D matrix for each measurement. The $\underline{\Delta\phi}_{D1}$ term in the measurement equation is next differentiated with respect to the x-component of the vehicle position,

$$\frac{\partial \underline{\phi}_{D1}}{\partial P_x} = \frac{1}{|\underline{D}_1|}\left[D_{1x}\frac{\partial D_{1x}}{\partial P_x} + D_{1y}\frac{\partial D_{1y}}{\partial P_x} + D_{1z}\frac{\partial D_{1z}}{\partial P_x}\right] \tag{3.27}$$

And since $\frac{\partial D_{1x}}{\partial P_x} = 1$ and $\frac{\partial D_{1y}}{\partial P_x} = \frac{\partial D_{1z}}{\partial P_x} = 0$, the derivative of $\underline{\phi}_{D1}$ is simply,

$$\frac{\partial \underline{\phi}_{D1}}{\partial P_x} = \frac{D_{1x}}{|\underline{D}_1|} \tag{3.28}$$

which is the component of the transmitter LOS in the x-direction. Similarly, for P_y and P_z,

$$\frac{\partial \underline{\phi}_{D1}}{\partial P_y} = \frac{D_{1y}}{|\underline{D}_1|}, \quad \frac{\partial \underline{\phi}_{D1}}{\partial P_z} = \frac{D_{1z}}{|\underline{D}_1|} \tag{3.29}$$

This is the familiar result that the linearized portion of the DCP due to differential range forms the components of the transmitter line-of-sight vector [GPS96].

Now we linearize the polarization component of the measurement with respect to vehicle attitude, starting with the yaw angle, ψ,

$$\frac{\partial \underline{\Delta\phi}_{RHCP}}{\partial \psi} = \frac{\partial \underline{\phi}_{RHCP_1}}{\partial \psi} - \frac{\partial \underline{\phi}_{RHCP_2}}{\partial \psi} \tag{3.30}$$

Looking at the phase component for a single antenna and using the definition of the phase due to RHCP in Equation 2.16,

$$\frac{\partial \underline{\phi}_{RHCP_1}}{\partial \psi} = \frac{\partial}{\partial \psi}\left(\arctan\left(\frac{T_{21} + eT_{12}}{T_{11} - eT_{22}}\right)\right) \tag{3.31}$$

where, $T = T_{TR-REC}$, the transmit to receive antenna frame rotation matrix. From the definition of the derivative of the arctan function, $\frac{\partial \arctan(u)}{\partial x} = \frac{1}{1+u^2}\frac{\partial u}{\partial x}$, we then

get that,

$$\frac{\partial \phi_{RHCP_1}}{\partial \psi} = \frac{(T_{11} - eT_{22})^2}{(T_{11} - eT_{22})^2 + (T_{21} + eT_{12})^2} \frac{\partial}{\partial \psi} \left(\frac{T_{21} + eT_{12}}{T_{11} - eT_{22}} \right) \tag{3.32}$$

The derivative can be expressed as a function of the components of the T_{TR-REC} matrix and their derivatives.

$$\frac{\partial \phi_{RHCP_1}}{\partial \psi} = \frac{(T_{11} - eT_{22}) \left(\frac{\partial T_{21}}{\partial \psi} + \frac{\partial T_{12}}{\partial \psi} \right) - (T_{21} + T_{12}) \left(\frac{\partial T_{11}}{\partial \psi} - e \frac{\partial T_{22}}{\partial \psi} \right)}{(T_{11} - eT_{22})^2 + (T_{21} + eT_{12})^2} \tag{3.33}$$

Similar expressions can be derived for the θ and ϕ rotation angles and vehicle position. From the definition of the transmit to receive antenna rotation matrix, T_{TR-REC},

$$T_{\text{TR-REC}} = (RR_A)^T R_T \tag{3.34}$$

where

$$R = \begin{bmatrix} c\theta c\psi & c\psi s\theta s\phi - s\psi c\phi & c\psi s\theta c\phi + s\psi s\phi \\ c\theta s\psi & s\psi s\theta s\phi + c\psi c\phi & s\psi s\theta c\phi - c\psi s\phi \\ -s\theta & c\theta s\phi & c\theta c\phi \end{bmatrix} \tag{3.35}$$

$$R_A = \begin{bmatrix} c\theta_A c\psi_A & c\psi_A s\theta_A s\phi_A - s\psi_A c\phi_A & c\psi_A s\theta_A c\phi_A + s\psi_A s\phi_A \\ c\theta_A s\psi_A & s\psi_A s\theta_A s\phi_A + c\psi_A c\phi_A & s\psi_A s\theta_A c\phi_A - c\psi_A s\phi_A \\ -s\theta_A & c\theta_A s\phi_A & c\theta_A c\phi_A \end{bmatrix} \tag{3.36}$$

where $(\psi_A, \theta_A, \phi_A)$ are the fixed Euler angle rotations of the receive antenna frame with respect to the vehicle frame, and $c\psi = \cos\psi$, $c\theta = \cos\theta$, $c\phi = \cos\phi$, $s\psi = \sin\psi$, $s\theta = \sin\theta$, and $s\phi = \sin\phi$. Also, we have that,

$$R_T = \begin{bmatrix} \frac{\sqrt{D_y^2 + D_z^2}}{|\underline{D}|} & 0 & \frac{D_x}{|\underline{D}|} \\ \frac{-D_x D_y}{|\underline{D}|\sqrt{D_y^2 + D_z^2}} & \frac{D_z}{\sqrt{D_y^2 + D_z^2}} & \frac{D_y}{|\underline{D}|} \\ \frac{-D_x D_z}{|\underline{D}|\sqrt{D_y^2 + D_z^2}} & \frac{-D_y}{\sqrt{D_y^2 + D_z^2}} & \frac{D_z}{|\underline{D}|} \end{bmatrix} \tag{3.37}$$

The components of the T_{TR-REC} matrix and their derivatives with respect to the vehicle attitude and position states can be found from these definitions. It is apparent that the T_{TR-REC} is a complicated function of vehicle attitude and position

Table 3.1: CPU Load vs. RHCP Compensation Technique, in units of FLOPS (Floating Point Operations) per iteration.

	CPU Load (FLOPS) Near Transmitters	CPU Load Far Transmitters
RHCP Linearized Model	5176	4422
RHCP Nonlinear Model	248	227

for the near transmitter case, and that an analytic expression for the derivative of the polarization measurement component with respect to vehicle state, derived using Maple, will be quite large, as can be seen in Appendix B. The number of floating point operations necessary to calculate the linearized RHCP term is large compared to that required to calculate the nonlinear model (see Table 3.1), particularly in the near transmitter case. For this reason, the RHCP measurement component as given here was not explicitly included in the measurement model during attitude estimation, but was treated as a measurement disturbance and calibrated out. The results shown in Table 3.1, found using a Matlab implementation of both the linearized and nonlinear measurement functions, show this is a more tractable approach. The implications of this for estimator stability are discussed in Section 3.3. We will next describe how the linearized measurement matrix shown in this derivation is used in the definition of the attitude dilution of precision.

3.1.3 ADOP Definition

Another basic concept of GPS attitude determination is that of attitude dilution of precision (ADOP). As a way of comparing different antenna configurations and

pointing geometries, the ADOP is defined as [CC92], where H is the linearized measurement matrix,

$$\mathrm{ADOP} = \sqrt{\mathrm{TRACE}\,(\mathrm{A})}, \quad \mathrm{A} = \left(\mathrm{H}^{\mathrm{T}}\mathrm{H}\right)^{-1}_{3\times 3} \tag{3.38}$$

$$\begin{aligned} \psi\mathrm{DOP} &= \sqrt{A\,(1,1)} \\ \theta\mathrm{DOP} &= \sqrt{A\,(2,2)} \\ \phi\mathrm{DOP} &= \sqrt{A\,(3,3)} \end{aligned} \tag{3.39}$$

The ADOP scales the differential carrier phase ranging accuracy into attitude estimation accuracy. It is a function of satellite visibility, which depends both on antenna array geometry and the attitude motion profile, unlike the GDOP for position determination, which varies only with GPS satellite motion. The value of the ADOP for an aligned array with good constellation visibility is approximately one, but this value can significantly increase when using a NAA on a vehicle undergoing rotation.

Now that the basic attitude determination approaches and linearization of the RHCP phase have been presented, the modifications to the near transmitter estimation algorithms that were made for this research will be discussed.

3.2 Extensions to Algorithms

The attitude estimation algorithms outlined in Section 3.1 need to be extended to improve the robustness of spacecraft attitude determination. For a spacecraft using measurements from a NAA and undergoing general attitude motion, the antennas will be frequently and periodically occluded from view of the transmitters, requiring modifications to the definition of the estimation measurement vector, and real-time measurement bias re-acquisition. The rapidly changing measurement environment requires modifications to the attitude estimation algorithm for selecting a current set

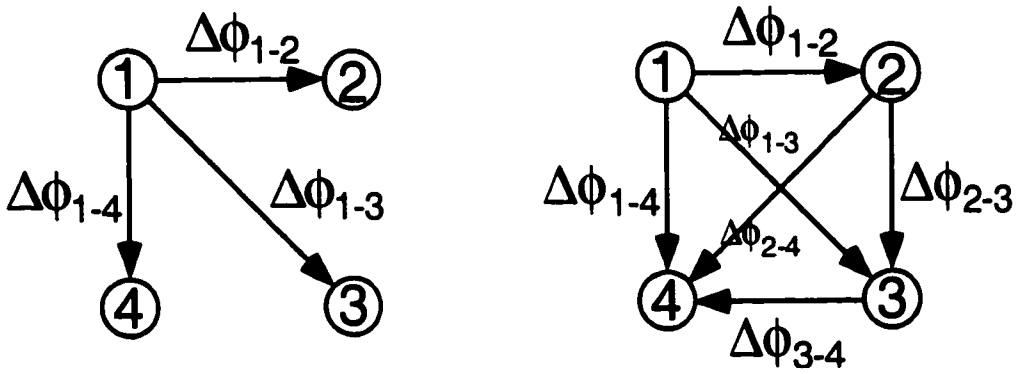

Independent Measurements

$$N_{\text{MEAS}} = (N_{\text{ANT}} - 1)N_{\text{TRANS}}$$

Redundant Measurements

$$N_{\text{MEAS}} = \frac{N_{\text{ANT}}(N_{\text{ANT}} - 1)}{2} N_{\text{TRANS}}$$

Figure 3.2: Independent vs. redundant DCP measurement vector definition.

of valid measurements. And the predictable attitude dynamics of most spacecraft suggests that extending the estimation algorithm from a kinematic filter to one that includes a model of the vehicle dynamics will improve performance. These issues are addressed in the following sections.

3.2.1 Measurement Vector Redundancy

Another issue for the attitude estimation algorithms on a rotating vehicle is the definition of the measurement vector. For receivers such as the Trimble TANS vector, used extensively in previous spacecraft GPS attitude work, carrier phase is tracked on slave antennas referenced to a single master (see left side of Figure 3.2), and therefore all the differential measurements are independent. However, if the master antenna is not visible to a given transmitter, any information that is available from the other three antennas visible to that transmitter is lost. As was shown in the work by Stone [JS97], our receiver is capable of tracking carrier phase independently on each antenna, without designating a *master* antenna. Therefore the measurement vector

can be defined to be a redundant set of differences (see right side of Figure 3.2) that contain the permutations of all possible phase differences,

$$\underline{z} = \left[\underbrace{\begin{matrix} \Delta\phi_{121} \; \Delta\phi_{131} \; \Delta\phi_{141} \; \Delta\phi_{231} \; \Delta\phi_{241} \; \Delta\phi_{341} \; \cdots \\ \Delta\phi_{12k} \; \Delta\phi_{13k} \; \Delta\phi_{14k} \; \Delta\phi_{23k} \; \Delta\phi_{24k} \; \Delta\phi_{34k} \end{matrix}}_{\substack{\text{Set of DCP measurements} \\ \text{Repeated for each transmitter, } k}} \right]_T \tag{3.40}$$

This measurement vector definition yields a much larger total number of measurements, but the differential measurements are not independent, since $\Delta\phi_{13k} = \Delta\phi_{12k} + \Delta\phi_{23k}$, for example. The advantage of this approach is that, in the event that one of the antennas loses sight of a transmitter, the information from the phase difference between the other antennas is still available. For example, the $\Delta\phi_{23}$ measurement is still available even when antenna 1 is blocked and $\Delta\phi_{12}$ and $\Delta\phi_{13}$ are not available. In addition, this allows the measurement vector to be defined as a fixed size based on the number of antennas and maximum number of transmitters, simplifying the measurement book-keeping and making the attitude estimator matrices constant size.

To illustrate the effect of defining the measurement vector based on a redundant set of measurements, in Figure 3.4 the number of measurements available from a 4 antenna array with visibility to 6 transmitters and undergoing a -90 to +90 degree pitch rotation (see Figure 3.3) is plotted. This motion causes the array to go through periods of low constellation visibility. The plot in Figure 3.4 shows the total number of available measurements for a measurement vector defined with only independent measurements versus one defined with redundant measurements. The redundant set yields more measurements, for example, $N_{\text{MEAS}} = 10$ for the redundant case versus $N_{\text{MEAS}} = 5$ for the independent case at $T = 12$ sec. The graph also clearly

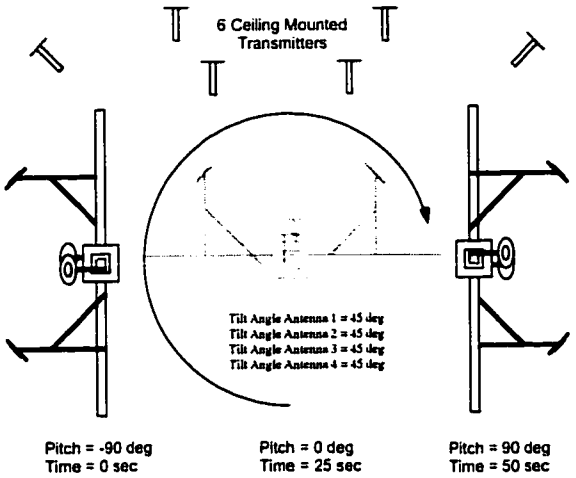

Figure 3.3: Antenna array and ±90° pitch oscillation for Figure 3.4. Four antennas, non-aligned array with baseline tilt angles of 45°.

shows that there are periods with no measurements available from the independent set (dashed line). However, some attitude information is still available from the other measurements for the redundant set (solid line). Attitude estimation simulation results will be presented in subsequent sections that analyze the impact of these measurement outages on the accuracy of the estimate.

3.2.2 Fixed Estimator Size - Selection Matrix

Signals that are not available in the measurement vector can be deselected using a selection matrix in the estimator. This is achieved by multiplying the weighting matrix in the measurement update of the IEKF by a selection matrix that zeros the rows and columns of measurements that are unavailable at any given time.

$$\underline{V} = \{v_{ijk}\} = \begin{cases} 1 \ , & \text{if } \Delta\phi_{ij} \text{ visible for transmitter } k \\ 0 \ , & \text{if } \Delta\phi_{ij} \text{ not visible for transmitter } k \end{cases} \tag{3.41}$$

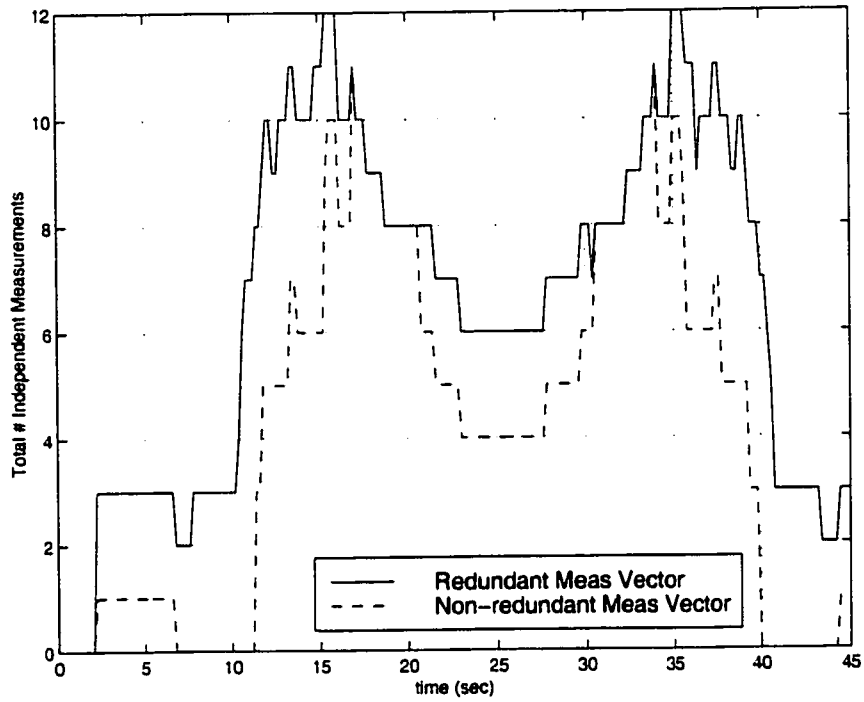

Figure 3.4: Total number of independent measurements available for the redundant and non-redundant measurement vector definitions. Vehicle motion is a ±90° pitch oscillation, and the antenna tilt angle are all 45°.

$$W_v = \mathrm{Diag}\,(\underline{V}) = \begin{bmatrix} 1 & 0 & \cdots & \cdots & \cdots & \cdots & 0 \\ 0 & 0 & & & & & \vdots \\ \vdots & & 1 & & & & \vdots \\ \vdots & & & 1 & & & \vdots \\ \vdots & & & & 0 & & \vdots \\ \vdots & & & & & \ddots & 0 \\ 0 & \cdots & \cdots & \cdots & \cdots & 0 & 1 \end{bmatrix} \tag{3.42}$$

$$S_{\text{valid}}^{-1} = W_v S^{-1} W_v \quad \text{and} \quad \Delta\underline{z}_{\text{valid}} = W_v \Delta\underline{z} \tag{3.43}$$

This selection matrix was determined from an additional measurement of satellite visibility on any given antenna, which is provided by the receiver as a DCP lock flag for a given antenna pair and transmitter. Formulating the estimation problem this way allows the filter to remain constant size, which significantly reduces the

complexity and computational burden of compiling the vector of valid differential phase measurements at each measurement epoch. This is particularly true for double differenced phase measurements.

3.2.3 Extended Kalman Filter

Applying knowledge of the vehicle dynamic model to the attitude determination problem can improve the performance of an attitude receiver, and this has been demonstrated by many researchers. Cohen [CC92] showed improved attitude estimation performance in his aircraft GPS attitude tests, where he included knowledge of the effects of wing flexure in a kinematic estimation filter. Hayward [RH97] and Gebre-Egziabher [DGE98] have demonstrated that inexpensive gyros can be used to smooth the GPS attitude solution, for aircraft applications. In their work, the dynamic model of the gyro was incorporated in a Kalman filter for combining the GPS and gyro attitude information.

There are also several applications where the dynamic model of the spacecraft on which the attitude receiver was mounted was included in the attitude estimation filter to smooth the solution. Melvin [PM93] [PM96] used a Kalman filter for attitude determination on a slowly rotating gyrostat in LEO, and incorporated a model of the on-orbit gravity gradient restoring torque to the dynamic model for the vehicle. Active control inputs were included in the Kalman filter implemented by Galdos [JG94] for spacecraft attitude determination. Ward used a Kalman filter that included the vehicle dynamic model for both post-processed attitude solutions for the RADCAL mission [LW95], and for combined estimation of attitude and antenna baseline shifts on-orbit [LW96].

For spacecraft applications, using knowledge of the vehicle dynamic model to smooth the GPS attitude solution is not typically done because it is not certain in advance what vehicle a receiver will be used on, and also it requires communicating the control torques generated on the vehicle to the receiver processor. However, a dynamic filter is well suited to the spacecraft attitude determination problem, since the dynamics are usually very predictable, simple, rigid body rotational dynamics.

In this work, the extended Kalman filter is applied to the case where the GPS measurements are made from a NAA. It is particularly useful in this case because information about the vehicle dynamics can be used to smooth the attitude estimate during times when transmitter visibility is degraded or measurements are not available. The dynamic model for the 3D vehicle was simple rigid body rotational dynamics with a restoring torque and damping torque. The model was linearized about a zero pitch and roll attitude state, and the Euler coupling torques between principal axes of the vehicle were ignored due to the small angular rates at which the vehicle was spinning. The 2D vehicle dynamic model is a rigid body.

The 3D vehicle has a small gravity restoring torque due to a small offset between the center of mass and the support cable attach point (see left side of Figure 3.5). There is also a slight damping torque exerted by the cable connection to the central node. These torques were characterized through system identification tests on the 3D vehicle and included in the vehicle model (see right side of Figure 3.5). Other than the disturbance torques from the cable support, there was no appreciable process noise in the model for the vehicle dynamics, and no yaw torque during open-loop motion.

The linearized equations of motion in terms of the yaw, pitch, and roll Euler angles are shown in Equations 3.44. The state space systems dynamics matrix, F where $\dot{\underline{X}} = F\underline{X}$, is defined in Equation 3.45, for a state vector definition that includes both

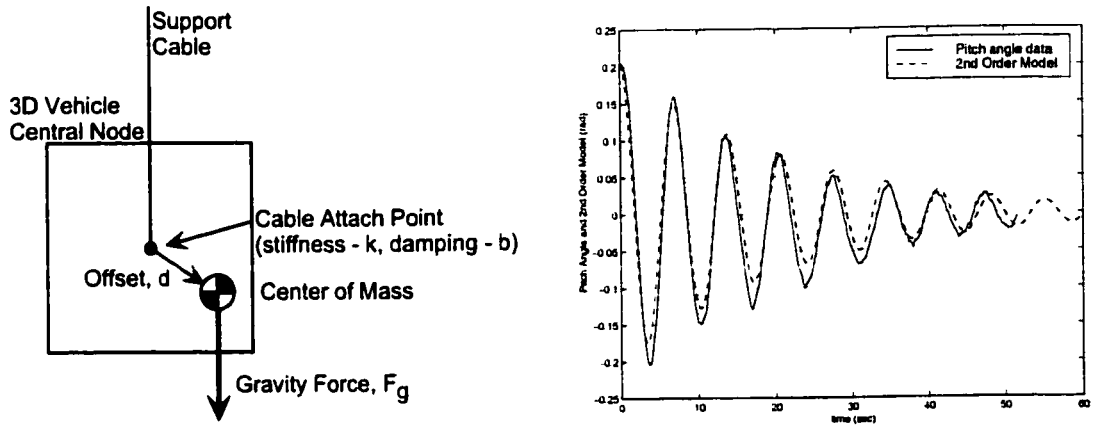

Figure 3.5: 3D vehicle dynamic model - center of mass offset from cable attach point causes gravity restoring torque and cable attach point damps oscillations. A second order model is fitted to the system ID data shown in the plot, with natural frequency $\omega_n = 0.91$ rad/sec and damping ratio $\zeta = 0.05$.

Euler angles and Euler angle rates, $\underline{X} = [\psi, \theta, \phi, \dot{\psi}, \dot{\theta}, \dot{\phi}]^T$.

$$\begin{aligned} \ddot{\psi} &= 0 \\ \ddot{\theta} &= -(k/I_{22})\theta - (b/I_{22})\dot{\theta} \\ \ddot{\phi} &= -(k/I_{11})\phi - (b/I_{11})\dot{\phi} \end{aligned} \tag{3.44}$$

$$F = \begin{bmatrix} 0 & 0 & 0 & 1 & 0 & 0 \\ 0 & 0 & 0 & 0 & 1 & 0 \\ 0 & 0 & 0 & 0 & 0 & 1 \\ 0 & 0 & 0 & 0 & 0 & 0 \\ 0 & -(k/I_{22}) & & 0 & -(b/I_{22}) & 0 \\ 0 & 0 & -(k/I_{11}) & 0 & 0 & -(b/I_{11}) \end{bmatrix} \tag{3.45}$$

and

$$k/I_{11} = k/I_{22} = \omega_n^2 = (0.91)^2 \text{ (rad/sec)}^2 \text{ and } \mathrm{b/I_{11}} = \mathrm{b/I_{22}} = 0.05 \text{ (rad/sec)} \tag{3.46}$$

For the spacecraft case, the attitude equations of motion would include the gravity gradient restoring torques, and other small disturbance torques experienced in the space environment [JW78].

The equations for an iterated extended Kalman filter time update are presented here as an extension to the IWLS equation defined in Section 3.1. The IEKF is time varying since the H matrix is time-varying.

The IEKF measurement update at each epoch, k, is similar to the IWLS measurement update but now has the apriori state estimate covariance, $\bar{P}$, included [AG74]

$$\underline{\hat{X}}_i = \underline{\bar{X}}_i + \left(\bar{P} + H_i^T S^{-1} H_i\right)^{-1} H_i^T S^{-1} \left(\underline{z} - H_i \underline{\bar{X}}_i\right) \tag{3.47}$$

The state estimate covariance matrix is updated at each measurement epoch k based on the model of the covariance of the sensor noise, S,

$$\hat{P}_k = \left(\bar{P}_k^{-1} + H^T S^{-1} H\right)^{-1} \tag{3.48}$$

The state estimate is propagated to the next time step using a model of the vehicle dynamics state transition matrix, Φ, and a model of the input control, $\underline{u}$, the process noise, $\underline{w}$, and the input matrices, Γ and Γ_w.

$$\underline{\bar{X}}_k = \Phi_k \underline{\hat{X}}_{k-1} + \Gamma \underline{u}_k + \Gamma_w \underline{w} \tag{3.49}$$

The estimate error covariance matrix is propagated using a model of the process noise covariance, Q.

$$\bar{P}_k = \Phi_k \hat{P}_{k-1} \Phi_k^T + \Gamma_w Q \Gamma_w^T \tag{3.50}$$

The 3D vehicle experiments using the IEKF filter were done open loop because of the difficulty of modeling the thruster torque input for the time update in the filter, and the separation of the control and attitude sensing on different computers. The 2D vehicle experiments using the IEKF filter were also done open loop. Since in the open loop case there is no control input and there is little process noise in the plant dynamics, Γ, Γ_w, Q, $\underline{w}$, and $\underline{u}$ can be ignored in Equations 3.49 and 3.50. The IEKF

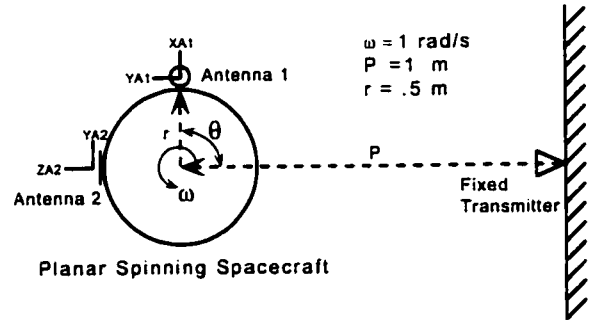

Figure 3.6: Diagram of planar vehicle for simulation. Tilt angle antenna 1 = 0°, and tilt angle antenna 2 = 90°.

time update equations then simplify and become,

$$\underline{\bar{X}}_k = \Phi_k \underline{\hat{X}}_{k-1} \tag{3.51}$$

and

$$\bar{P}_k = \Phi_k \hat{P}_{k-1} \Phi_k^T \tag{3.52}$$

The Φ matrix is the discrete version [FPW80] of the linearized system dynamics matrix, F.

A simple 1-DOF simulation was performed to validate the performance of the extended IEKF attitude estimation algorithm, using a model of our 2D test vehicle in the indoor laboratory, a single antenna baseline measurement, and a single transmitter (see Figure 3.6). From the diagram shown in Figure 3.6, it can be seen that antenna 2 will not be visible to the transmitter when $0 < \theta < \pi$, resulting in a DCP measurement that is occluded 50% of the time as the vehicle rotates at a constant speed.

The parameters for sensor noise variance and process noise variance in the IEKF were set based on values predicted for our laboratory environment. The sensor noise variance was predicted to be 0.01 cycles^2 and the process noise variance was set at 0.01 N–m.

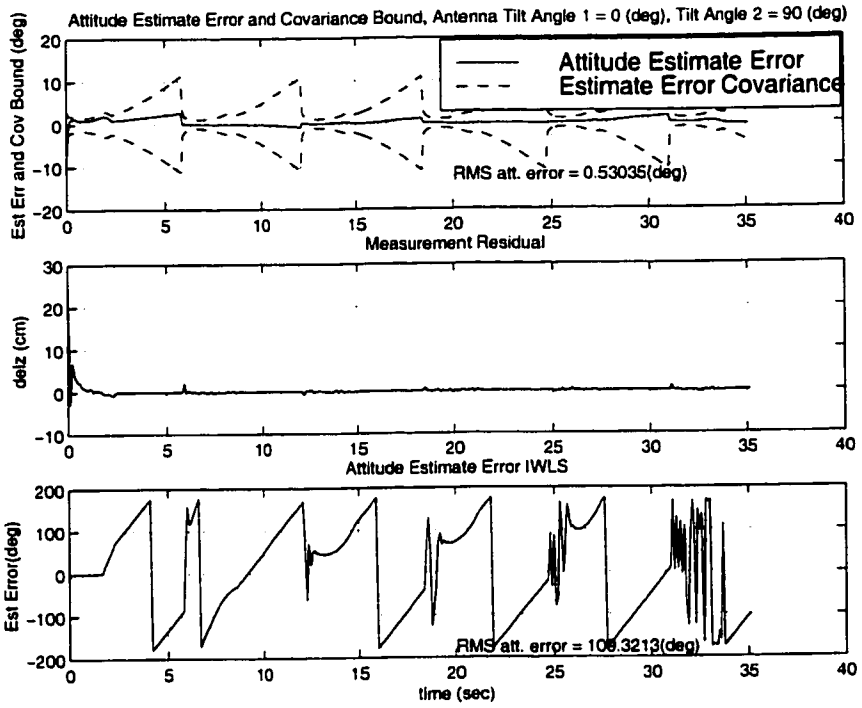

Figure 3.7: Planar attitude estimation - Tilt angle antenna 1 = 0°, tilt angle antenna 2 = 90°. Estimate error with covariance bounds, measurement residual, and the estimate error for the IWLS case.

The time history of a typical estimation run is presented in Figure 3.7, for a vehicle rotating at 1 rad/sec. The results are shown for the worst polarization bias case of having one antenna with 0° tilt angle, and the other with 90°, as shown in Figure 3.6. The attitude estimate error (top plot) is plotted along with the covariance bound and measurement residual (middle plot). The covariance bound can be seen to rise during periods when the measurement is occluded and drop again when the measurement becomes visible as the vehicle rotates. In the bottom plot, the attitude estimate error for the IWLS estimator is shown. During periods when the measurement is not available, the attitude estimate does not change, and the attitude error grows linearly at the angular rate the vehicle is turning. When a new measurement becomes available, the IWLS estimator diverges and never recovers, rendering the attitude determination

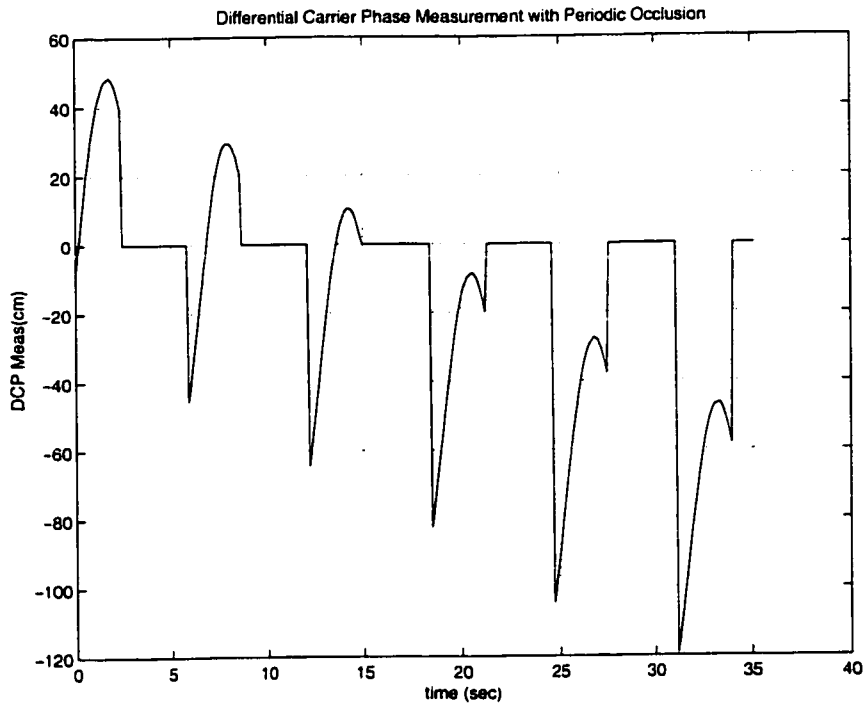

Figure 3.8: Attitude estimation - Tilt angle antenna 1 = 0°, tilt angle antenna 2 = 90°. Simulated DCP measurement with periodic dropout and RHCP bias increasing with each rotation.

a complete failure. This shows dramatically the benefits of using model information in the dynamic attitude estimation, since the estimate error is still small (0.41° RMS) during the times when the measurement is unavailable. The DCP measurement is plotted in Figure 3.8, and can be seen to have the periodic dropouts and increasing bias that was evident in the test data presented in Figure 2.7 (Section 2.2).

3.2.4 Continuous Bias Re-acquisition

Another challenge of performing attitude estimation on a generally rotating platform is that the rapidly changing measurement visibility requires continuous measurement bias re-acquisition. As shown in Chapter 2, the DCP measurement can be written in terms of the nonlinear measurement function h, and the combined non-integer

measurement bias B_{ijk} (see Equation 2.6).

$$\Delta\phi_{ijk} = h(\underline{X}, \underline{b}_i, \underline{b}_j, \underline{Q}_k) + B_{ijk} + \nu_{ijk} \tag{3.53}$$

The total bias B_{ijk} is the combination of the non-integer line bias β_{ijk}, geometric integer bias K_{ijk}, and polarization integer bias P_{ijk}. P_{ijk} is a function of the visibility of an antenna pair to a common transmitter over time. β_{ijk} and K_{ijk} can be resolved using known bias resolution techniques, such as batch least squares techniques that use vehicle motion, or search techniques in the case of integer biases.

Issues involving the resolution of the biases in the DCP measurement have been well researched in other work [DK94] [CC92] [GL97], and are not addressed in this thesis. Initial measurement bias resolution was accomplished in the experimental portions of this research by placing the vehicle in a known attitude relative to the transmitters. Subsequent bias re-acquisition was accomplished each time a DCP measurement became available by differencing the actual and predicted measurement (see Equation 3.54), using either a truth measurement of the vehicle state from an overhead vision system (2D experiments) or the previous best estimate of the vehicle attitude state (3D experiments).

$$B_{ijk} \approx \Delta\phi_{ijk} - h(\hat{\underline{X}}, \underline{b}_i, \underline{b}_j, \underline{Q}_k) \tag{3.54}$$

As demonstrated by Olsen [EO98], this re-acquired bias estimate can be improved by averaging the B_{ijk} value over several time steps before declaring a visible DCP baseline measurement to be valid. This method is effective at removing the random receiver noise component from the bias estimate, but requires that there be no significant vehicle motion during the averaging period which will cause the measurement bias to change. A trade-off, depending on vehicle rotation rate, exists between averaging the bias estimate for longer periods of time to smooth the random component of receiver

noise, and averaging for shorter periods of time to avoid introducing errors in the bias estimate due to vehicle motion.

3.3 LOS Dependent Phase Compensation

Once a model for the RHCP contribution to the DCP measurement has been derived, there are different methods that can be used to compensate for this phase term in the attitude estimation. One method is to include the new polarization phase term as part of the measurement model [KZ96] and the linearized measurement used in the estimation process as well. Another more straightforward method that is often employed [EGL96] is to simply subtract the modeled RHCP phase from the current measurement using the current estimate of vehicle attitude, and proceed using these calibrated measurements. The linearized measurement is then just the more simple linearization based on the model of DCP that is only a function of the relative distances between transmit and receive antennas, which, as was shown in Table 3.1, is significantly easier to compute than the linearized model which includes the polarization terms (especially for the case of near transmitters). However, it is not clear that if the polarization component is ignored in the linearization the state estimate will still converge to the correct value, or converge at all. Not including the polarization component in the linearized measurement model is equivalent to assuming that the error in the calibration of this term is random and is uncorrelated with the system state, which is not the case. Errors in the RHCP calibrated measurement are correlated with both the system state and parameter error.

To verify the estimation stability when using the calibration technique, it is necessary to derive a stability condition based on vehicle state and the geometry of

the antenna baselines. In this section, the sufficient stability condition is presented for the estimation problem where the Jacobian of the polarization model ($H_{\text{RHCP}} = \partial \underline{h}_{\text{RHCP}}/\partial \underline{X}$) is neglected, and the RHCP is instead calibrated out of the total measurement.

3.3.1 Stability of Estimation Algorithm

A stability condition for attitude estimation was derived jointly by Adams and Olsen [EO99], and is presented in this section. The sufficient conditions for stability of a gradient descent search, or iterated weighted least squares estimation, wherein a portion of the Jacobian is neglected when computing the descent direction [JCA298] is derived. Starting with the definition of the DCP measurement

$$\underline{z}(\underline{X}) = \underline{z}_D(\underline{X}) + \underline{z}_{\text{RHCP}}(\underline{X}) = \underline{h}_D(\underline{X}) + \underline{h}_{\text{RHCP}}(\underline{X}) \tag{3.55}$$

where $\underline{z}_D(\underline{X})$ is that portion of the DCP measurement due to relative distance, and $\underline{z}_{\text{RHCP}}(\underline{X})$ is that portion of the measurement due to polarization. The bias is assumed known, and arbitrarily set to zero. The Taylor series expansion of $\underline{z}_D(\underline{X}) = \underline{h}_D(\underline{X})$ and $\underline{z}_{\text{RHCP}}(\underline{X}) = \underline{h}_{\text{RHCP}}(\underline{X})$ about the solution $\underline{X}_1$ is

$$\begin{aligned}
\underline{z}_D(\underline{X}) &= \underline{z}_D(\underline{X}_1) + \Delta \underline{z}_D \\
&= \underline{h}_D(\underline{X}_1) + H_D(\underline{X}_1)\Delta \underline{X} + \mathcal{O}(\Delta \underline{X})\Delta \underline{X} \\
&= \underline{h}_D(\underline{X}_1) + \overline{H_D}\Delta \underline{X} \\
\underline{z}_{\text{RHCP}}(\underline{X}) &= \underline{z}_{\text{RHCP}}(\underline{X}_1) + \Delta \underline{z}_{\text{RHCP}} \\
&= \underline{h}_{\text{RHCP}}(\underline{X}_1) + H_{\text{RHCP}}(\underline{X}_1)\Delta \underline{X} + \mathcal{O}(\Delta \underline{X})\Delta \underline{X} \\
&= \underline{h}_{\text{RHCP}}(\underline{X}_1) + \overline{H_{\text{RHCP}}}\Delta \underline{X}
\end{aligned} \tag{3.56}$$

where $H_D = \partial \underline{h}_D/\partial \underline{X}$, $H_{\text{RHCP}} = \partial \underline{h}_{\text{RHCP}}/\partial \underline{X}$, and $\Delta \underline{X} = \underline{X} - \underline{X}_1$. Using just the expansion of the distance component of the measurement, $\underline{z}_D(\underline{X})$, the least squares

solution is

$$\begin{aligned}\Delta\underline{X} &= ([H_D + \mathcal{O}(\Delta\underline{X})]^T[H_D + \mathcal{O}(\Delta\underline{X})])^{-1}[H_D + \mathcal{O}(\Delta\underline{X})]^T\Delta\underline{z}_D \\ &= (\overline{H_D}^T\overline{H_D})^{-1}\overline{H_D}^T\Delta\underline{z}_D\end{aligned} \tag{3.57}$$

Let $\hat{\underline{X}}_i$ denote the estimated state at the ith iteration. We now the perform the calibration step, so that

$$\Delta\underline{z}_i = [\underline{z}_D(\hat{\underline{X}}_i) + \underline{z}_{\text{RHCP}}(\hat{\underline{X}}_i)] - \underline{z}(\underline{X}_1) = \Delta\underline{z}_{Di} + \Delta\underline{z}_{\text{RHCPi}} \tag{3.58}$$

In this case, the updated estimate is given by the following, where $\overline{\Delta\underline{X}_i}$ is the change in the state estimate computed at iteration i.

$$\begin{aligned}\hat{\underline{X}}_{i+1} &= \hat{\underline{X}}_i + \overline{\Delta\underline{X}_i} = \hat{\underline{X}}_i - (\overline{H_D}^T\overline{H_D})^{-1}\overline{H_D}^T\Delta\underline{z}_i \\ &= \hat{\underline{X}}_i - (\overline{H_D}^T\overline{H_D})^{-1}\overline{H_D}^T(\Delta\underline{z}_{Di} + \Delta\underline{z}_{\text{RHCPi}})\end{aligned} \tag{3.59}$$

$$\begin{aligned}\Rightarrow \Delta\underline{X}_{i+1} &= \hat{\underline{X}}_{i+1} - \underline{X}_1 \\ &= \hat{\underline{X}}_i - (\overline{H_D}^T\overline{H_D})^{-1}\overline{H_D}^T(\Delta\underline{z}_{Di} + \Delta\underline{z}_{\text{RHCPi}}) - \underline{X}_1 \\ &= \Delta\underline{X}_i - (\overline{H_D}^T\overline{H_D})^{-1}\overline{H_D}^T(\Delta\underline{z}_{Di} + \Delta\underline{z}_{\text{RHCPi}})\end{aligned} \tag{3.60}$$

The estimation converges if the sequence $\|\Delta\underline{X}_i\|$ converges. This convergence can be demonstrated if $\|\Delta\underline{X}_i\| > \|\Delta\underline{X}_{i+1}\| \quad \forall\ i > n$. This condition is equivalent to requiring that

$$\|\Delta\underline{X}_i\| > \|\Delta\underline{X}_i - (\overline{H_D}^T\overline{H_D})^{-1}\overline{H_D}^T(\Delta\underline{z}_{Di} + \Delta\underline{z}_{\text{RHCPi}})\| \quad \forall\ i > n \tag{3.61}$$

for some n. If we define $\Delta\underline{z}_{Di}$ so that $\Delta\underline{z}_{Di} = \overline{H_D}\Delta\underline{X}_i$, this condition can be rewritten as

$$\|\Delta\underline{X}_i\| > \|(\overline{H_D}^T\overline{H_D})^{-1}\overline{H_D}^T\Delta\underline{z}_{\text{RHCPi}}\| \tag{3.62}$$

Using Equation 3.56, then Equation 3.62 becomes

$$\|\Delta\underline{X}_i\| > \|(\overline{H_D}^T\overline{H_D})^{-1}\overline{H_D}^T\overline{H_{\text{RHCP}}}\Delta\underline{X}_i\| \tag{3.63}$$

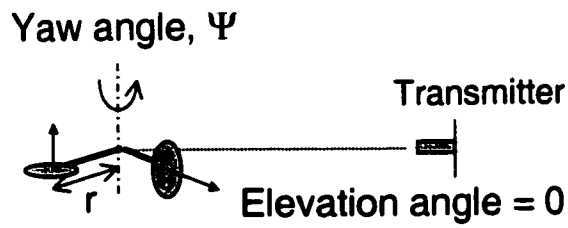

Figure 3.9: Single antenna baseline with single transmitter - planar case for estimation stability analysis. Antenna radial distance, r, and baseline yaw angle, Ψ.

using standard properties of the norm, the sufficient condition then becomes

$$\|\Delta \underline{X}_i\| > \|(\overline{H_D}^T \overline{H_D})^{-1} \overline{H_D}^T \overline{H_{\text{RHCP}}}\| \cdot \|\Delta \underline{X}_i\| \tag{3.64}$$

$$\|(\overline{H_D}^T \overline{H_D})^{-1} \overline{H_D}^T \overline{H_{\text{RHCP}}}\| < 1 \tag{3.65}$$

In the limit, as $\Delta \underline{X}_i \rightarrow 0$, the sufficient condition for stability becomes

$$\|(H_D^T H_D)^{-1} H_D^T H_{\text{RHCP}}\| < 1 \tag{3.66}$$

At any point where Equation 3.66 is satisfied, there is some region in the vehicle state space about the linearization point where the estimation algorithm is stable. The effect of antenna pointing geometry, baseline separation, and vehicle attitude on the stability boundary for attitude estimation is examined in the next section.

3.3.2 Single Baseline Example

To examine the implications of this stability criterion, we again look at the single baseline case (see Figure 3.9), with two antennas angled at 90°, and rotated 360° in yaw, and with a transmitter elevation of zero degrees to make the problem planar. In that case the linearized measurement components can be defined as shown.

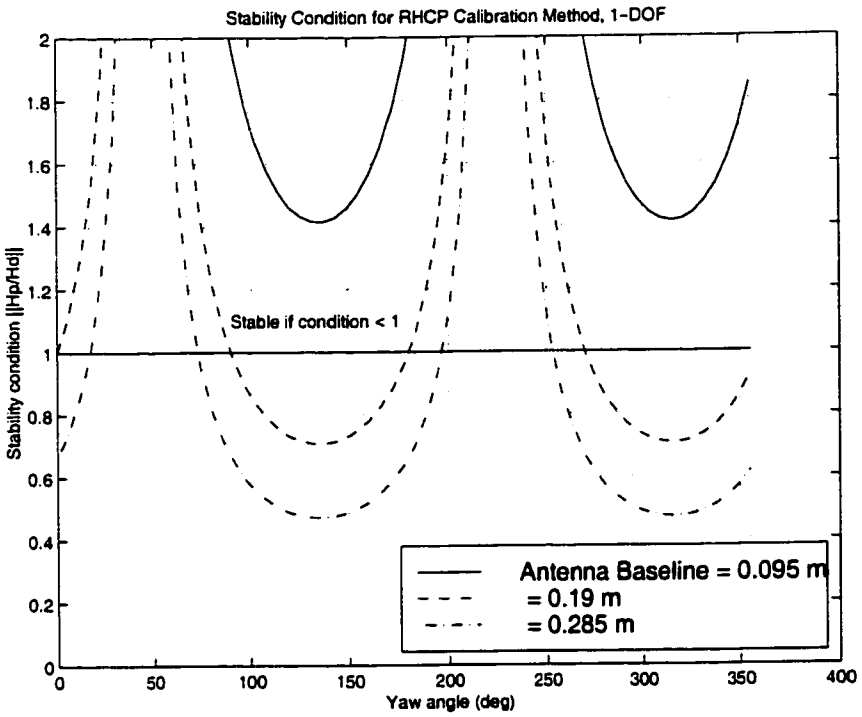

Figure 3.10: Stability bound for attitude estimation - *Single Transmitter.*

With r and Ψ as defined in Figure 3.9, and assuming large distances to the transmitter, the DCP and the linearized DCP can be calculated analytically to be,

$$\underline{h}_D = -\frac{r}{\lambda}(\cos(\Psi) + \sin(\Psi)) \quad \text{and} \quad \underline{h}_{\text{RHCP}} = -\Psi \tag{3.67}$$

where λ is the GPS signal L_1 carrier wavelength, and,

$$H_D = -\frac{r}{\lambda}(\cos(\Psi) - \sin(\Psi)) \quad \text{and} \quad H_{\text{RHCP}} = -1 \tag{3.68}$$

For the single transmitter case, the linearized measurement matrix is just a scalar and the stability conditions for the attitude estimation given in Equation 3.66 reduces to the condition,

$$\left| \frac{-1}{\left(-\frac{r}{\lambda}(\cos(\Psi) - \sin(\Psi))\right)} \right| < 1 \tag{3.69}$$

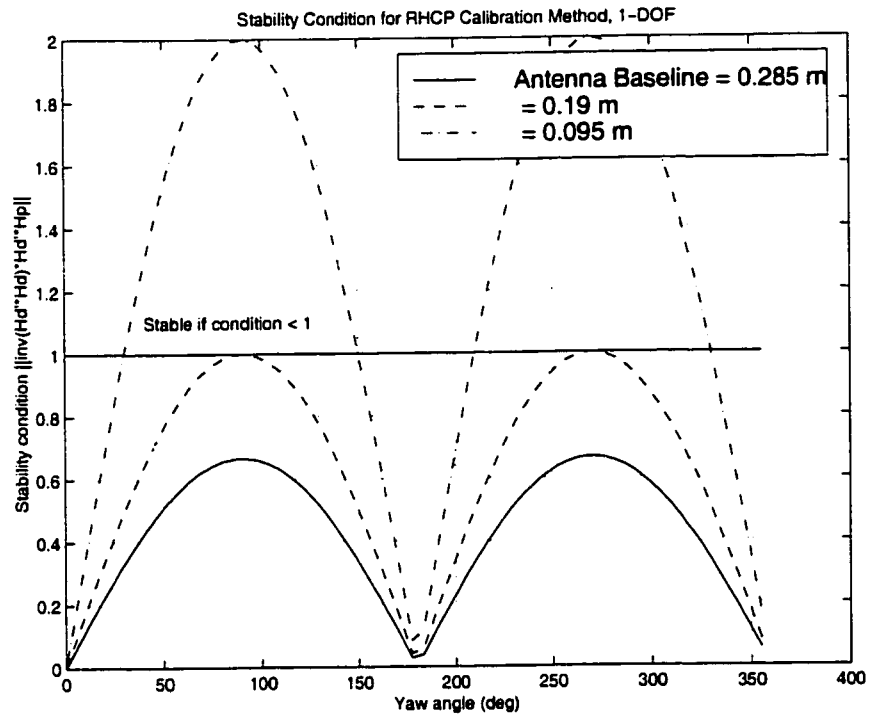

Figure 3.11: Stability bound for attitude estimation - *Two Transmitters.*

The stability condition is not met for vehicle yaw angles where H_D goes to zero, or for sufficiently small antenna baselines, where $\frac{r}{\lambda}$ becomes large. There is no antenna baseline large enough that the estimation is stable for all vehicle yaw angles. This is shown in Figure 3.10, which plots the stability bound for different antenna baselines and varying vehicle rotation angle. It can be seen that for one transmitter, there are ranges of yaw angle for which the stability criteria is greater than one, and thus the attitude estimation is unstable, for any antenna baseline. In fact, for baselines less than half a wavelength, the estimation is unstable for all yaw angles.

If a second transmitter is added, there is a threshold for the antenna baseline above which the estimation stability is guaranteed. This can be seen in Figure 3.11, where the stability condition in Equation 3.66 is plotted for the two transmitter case. This plot shows that for two transmitters, with line-of-sights oriented at 90° to each other,

estimation stability is guaranteed for antenna baselines greater than λ. When the number of transmitters is increased to two or more, a minimum baseline separation can be found for which the attitude estimation is stable for all yaw angles. In this case, that separation was one wavelength or 19 cm. This lower limit decreases as the number of transmitters is increased.

For the vehicle attitude problem, there are usually many more than two transmitters in view at any given time, and the antenna baselines are usually large compared to the carrier wavelength λ (typically 1 m, or 5λ, for spacecraft applications), ensuring stable estimation if the LOS dependent disturbances on the DCP measurement are ignored in the linearization. The difficulty remains to obtain an estimate which ensures that $\Delta\underline{X}_1$, the initial estimate error, will be sufficiently small to allow convergence of the estimation.

3.4 Attitude Simulation Results

In this section, simulation results are presented for the modified attitude estimation algorithms outlined in Section 3.2. The purpose of these simulations is to validate the improvements in performance and robustness intended by these modifications. These simulations cover the 2D and 3D laboratory experiments undertaken in this work. The experimental results will be presented in Chapter 6. Also, simulation results are presented for attitude determination including compensation for the phase center variation in the DCP measurement, which was not done in the laboratory experiments.

Four sets of results are included here. The first set of simulations is for a single antenna baseline on a 2D test vehicle, comparing the attitude estimation error when the RHCP component of the measurement is either included or not included in the

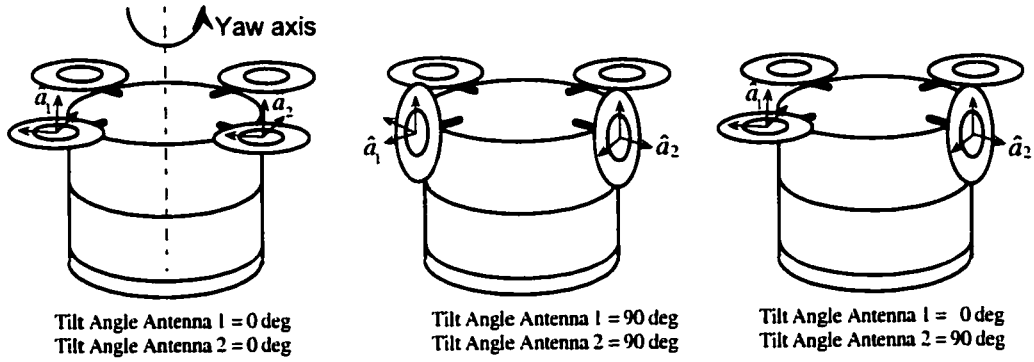

Figure 3.12: Antenna array geometries simulated in 2D simulation results table. Antenna baseline separation is 0.5 meters.

estimation algorithm. These comparisons are made for three representative antenna array geometries. The second set of simulations makes the same comparison, but for the case where antenna pointing angle is varied over a continuous range from 0° to 90°. The third series of simulations also makes the attitude estimate error comparison for RHCP compensation, but for a vehicle with full 3D attitude motion. And the last simulation results show the performance improvement achievable through compensation for the antenna phase center variation based on a pre-calibrated model.

3.4.1 2D Simulations

A diagram of the 2D antenna test platform simulated in this first set of tests is shown in Figure 3.12. The three cases, which cover the range of antenna visibility for the 2D test platform, are: aligned antennas (both tilt angles = 0°); non-aligned, same tilt angle (both tilt angles = 90°); and non-aligned, different tilt angles (tilt angle 1 = 0°, tilt angle 2 = 90°). These three cases were tested in simulation, with single-axis yaw rotation, and the results are summarized in Table 3.2.

Table 3.2: Simulation results for attitude estimation - Planar 1-DOF Rotation

Attitude Estimate Error (Yaw - degrees)	No RHCP Mean	No RHCP STD	RHCP Uncompensated Mean	RHCP Uncompensated STD	RHCP Compensated Mean	RHCP Compensated STD
1) Aligned antenna array tilt angle1 = 0° tilt angle2 = 0°	0.05	1.94	0.05	1.96	0.05	1.94
2) Non-aligned Antennas tilt angle1 = 90° tilt angle2 = 90°	0.32	7.5	**2.81**	7.81	**0.35**	7.50
3) Non-aligned Antennas tilt angle1 = 0° tilt angle2 = 90°	0.15	5.17	**estimation failed**		**0.12**	5.11

A comparison is made between the cases where; no RHCP component is included in the truth model or estimator, the RHCP is included in the truth model but not the estimator, and the RHCP is included in both the truth model and estimator. For the aligned array, case 1) in Table 3.2, the RMS attitude error is relatively unaffected by the polarization component of the model, with or without compensation in the estimator, because the LOS dependent phase effects are removed in the differencing between antennas. For the non-aligned array with both tilt angles at 90°, case 2), the estimate error increases because each DCP measurement is available only 25% of the time as the vehicle rotates, and increases by a factor of 9 if there is no compensation for the polarization phase. This error can be removed using the new measurement model. In case 3), if the polarization bias is present and not compensated for, the estimation fails entirely, due to the increasing polarization bias term (shown in Figure 2.7). As shown, this effect can be removed using the new estimation algorithm. If the polarization is compensated for in the estimation, the mean attitude error is less than that for case 2) because each DCP measurement is available 50% of the time as the vehicle rotates.

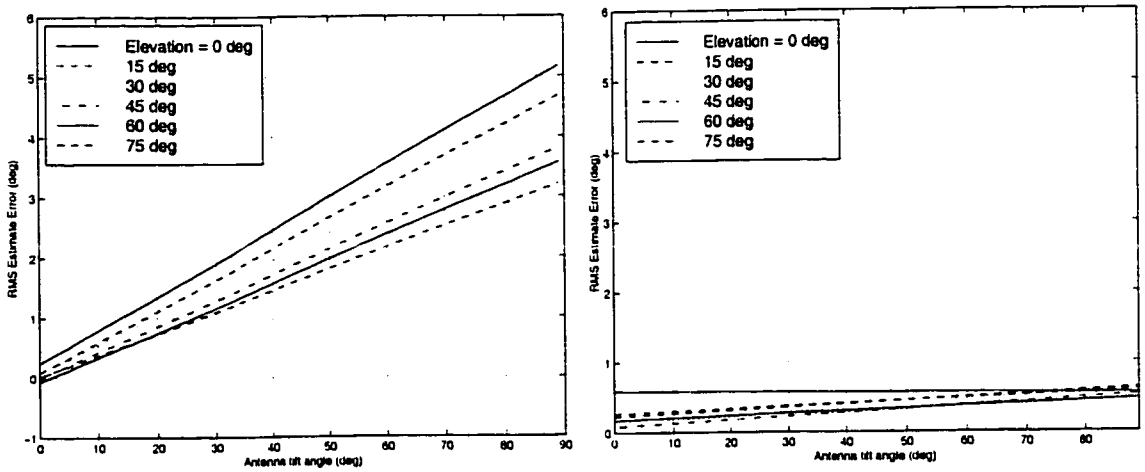

Figure 3.13: Attitude Estimate Error vs. Antenna Tilt Angle, 2D case - *without* RHCP Compensation on the left, and *with* RHCP Compensation on the right.

Another set of simulations focused on antenna array case 2), but varied the antenna tilt angles from 0° to 90°. Figure 3.13 shows the resulting attitude estimate error for the single transmitter case, with different transmitter elevations. In the plot on the left, RMS attitude error is plotted versus antenna tilt angle for the case where the polarization in the differential carrier phase measurement is present but ignored. This can be compared with the plot on the right where the estimated polarization effect is being calibrated out. These curves give a good indication of the problem when the antennas have the same visibility to the transmitter (*i.e.* the polarization bias component of the measurement is not an issue). For the largest antenna tilt angles, the RMS error in attitude estimation is between 3°–5° if the polarization in the measurement is ignored. This error can be reduced by a factor of 10 by including the polarization in the estimator.

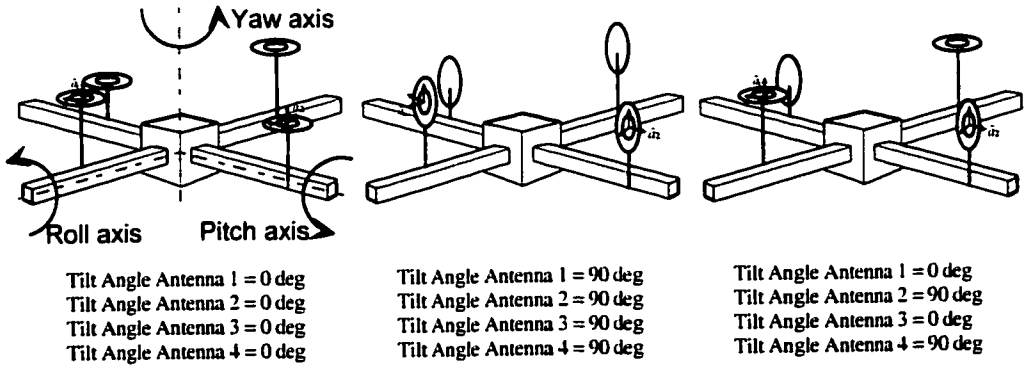

Figure 3.14: Antenna array geometries simulated in 3D simulation results table.

3.4.2 3D Simulations

A diagram of the 3D antenna test platform simulated in this next set of tests is shown in Figure 3.14. For the 3D testbed, attitude motion consisting of continuous yaw rotation, with sinusoidal oscillations in pitch and roll with a magnitude 15° was simulated. This attitude motion was typical of that used in subsequent laboratory experiments.

As in the 2D simulations, three antenna configuration cases were chosen to cover the range of antenna visibility:

- Aligned antennas (all tilt angles = 0°)
- Non-aligned, same tilt angle (all tilt angles = 90°)
- Non-aligned, different tilt angles (tilt angle 1 = tilt angle 3 = 0°, tilt angle 2 = tilt angle 4 = 90°)

These three cases were tested in simulation and the results are summarized in Tables 3.3 and 3.4. In Table 3.3, a comparison is made between the cases where: (1) no RHCP component is included in the truth model or estimator, (2) the RHCP is included in the truth model but not the estimator, and (3) the RHCP is included in

Table 3.3: Simulation results for attitude estimation, 3D General Rotation - *RHCP compensation.*

Attitude Estimate Error (Yaw - degrees)	No RHCP Mean	No RHCP STD	RHCP Uncompensated Mean	RHCP Uncompensated STD	RHCP Compensated Mean	RHCP Compensated STD
1) Aligned antenna array tilt angles = 0°	0.24°	1.11°	0.57°	1.11°	0.27°	1.10°
2) Non-aligned Antennas tilt angles = 90°	1.01°	6.49°	**4.12°**	6.41°	**0.92°**	6.68°
3) Non-aligned Antennas tilt angles 1,3 = 0° tilt angles 2,4 = 90°	0.26°	3.92°	**estimation failed**		**0.27°**	3.89°

both the truth model and estimator. For the aligned array, case 1), the RMS attitude error for the 3D case is again unaffected by the polarization component of the model, with or without compensation in the estimator, because the effect is removed in the phase differencing between antennas. For the non-aligned array with all tilt angles at 90°, case 2), the estimate error increases by a factor of 8 (0.57° versus 4.12°) because the measurement is only available 25% of the time, and the polarization phase is not accounted for in the estimation. The results show that this error can be decreased (from 4.12° to 0.92°) using the new DCP measurement model. In case 3), if the polarization bias is present and not compensated for the estimation fails entirely, as in the 2D case, due to the increasing polarization bias term, but this can be compensated for by using the new estimation algorithm (0.27° estimate error).

Similar results can be seen in Table 3.4 for the case where phase center variation (as defined in Section 2.5) is included in the measurement and compensated for in the estimation. The worst case attitude estimate error is only one third that for the RHCP simulation case (1.63° versus 4.12°). The estimation does not fail for the uncompensated (case 3) because there is no unmodeled measurement bias contributed by

Table 3.4: Simulation results for attitude estimation, 3D General Rotation - *PCV compensation.*

Attitude Estimate Error (Yaw - degrees)	No PCV Mean	No PCV STD	PCV Uncompensated Mean	PCV Uncompensated STD	PCV Compensated Mean	PCV Compensated STD
1) Aligned antenna array tilt angles = 0°	0.31°	1.11°	0.42°	1.09°	0.25°	1.10°
2) Non-aligned Antennas tilt angles = 90°	0.92°	6.28°	**1.63°**	6.61°	**1.17°**	6.11°
3) Non-aligned Antennas tilt angles 1,3 = 0° tilt angles 2,4 = 90°	0.73°	3.75°	**1.72°**	3.72°	**0.79°**	3.55°

the PCV component, as there is in the case of the RHCP. This method assumes that a pre-calibrated model of PCV versus transmitter LOS, from an anechoic chamber test [CC92], is available for a receive antenna/groundplane combination.

In conclusion, these simulations have demonstrated the performance improvements of using the modified DCP measurement model and attitude estimation algorithms for performing attitude determination using a set of measurements from a NAA. The RHCP component has been shown to cause the attitude estimation to fail for certain non-aligned antenna configurations due to the rapidly increasing polarization measurement bias that occurs when the vehicle is rotating. The effect on attitude estimation accuracy of ignoring LOS dependent phase effects gets worse as the antennas are pointed further away from the aligned case, and the attitude estimation accuracy is also greatly affected by transmitter visibility. In addition, it was shown that the next largest LOS dependent phase effect, the PCV, can be compensated for in the event that calibration data is available for modeling the effect as a function of transmitter LOS. These simulation results will be compared to the results of the 2D and 3D testbed experimental results in Chapter 6.

Chapter 4

On-Orbit Simulations

The attitude estimation simulation results shown in Chapter 3 were for cases that modeled our laboratory vehicle antenna array geometries and attitude motion profiles. While this was good for comparison to (and verification of) the laboratory experiment data, it is also necessary to simulate the performance of the modified attitude estimation algorithms for on-orbit spacecraft conditions. In simulation, the larger range of attitude motions possible in orbit can be examined. Also, more realistic conditions for GPS transmitter visibility, including the rapid line-of-sight changes that occur on-orbit and large number of visible transmitters in LEO, can be examined in simulation more easily than in experiment.

In this chapter, results are presented from three simulation studies that were used to validate the new attitude estimation algorithms under realistic space mission conditions. The first simulation study was based on the work of Lightsey [GL97] who performed a transmitter observability analysis for a generic LEO spacecraft mission that used GPS measurements from a non-aligned antenna array. A similar general

LEO spacecraft GPS attitude application was simulated here to extend the previous work to include attitude determination accuracy.

The second simulation study investigated the impact of using measurements from a non-aligned antenna array on the tracking channel requirements for a spacecraft attitude receiver. The increased number of measurements available in orbit when using an all-baselines-in-view tracking strategy requires either more correlator tracking channels be designed into the spacecraft receiver, or a satellite/channel allocation scheme that uses the best subset of the current DCP measurements for determining attitude. A comparison of the attitude determination performance and maximum tracking channel requirements for three different satellite/channel allocation methods is presented for an example LEO spacecraft mission.

The last spacecraft mission simulation is based on the ORION spacecraft formation flying mission currently in development at Stanford [JH99]. In this study, a comparison is made of different non-aligned antenna array geometries for the ORION spacecraft to determine the impact of making DCP measurements from a NAA on the signal re-acquisition time, maximum spinrate requirement during deployment, and attitude determination performance. The results of this study were used to select the current baseline GPS antenna array design.

4.1 General LEO Mission Study

The goals of the general LEO mission simulation study were to validate the new attitude estimation algorithms, and to extend the visibility simulation results in [GL97] to include attitude estimation accuracy. The parameter space for simulating a GPS spacecraft attitude determination mission includes different:

- Antenna array configurations
- Vehicle attitude motion profiles
- Spacecraft orbits

For ease of comparison to the Lightsey's results, similar choices were made for the vehicle orbit parameters, attitude motion, and NAA geometries, with some extensions that will now be discussed.

The choice for a representative spacecraft orbit should challenge the receiver capabilities in terms of tracking a large number of measurements. A circular, low earth orbit with altitude of 700 km was chosen, with both polar and equatorial inclinations. The chosen altitude corresponds to the planned altitude for the Gravity Probe-B mission, a good candidate GPS attitude mission using measurements from a NAA, and was also chosen by Lightsey [EGL96].

The spacecraft attitude motion simulated should demonstrate the robustness of the new attitude determination algorithms. The study should include motions that, given measurements from an aligned antenna array, the transmitters will be periodically occluded from the receive antennas, so that continuous attitude solution availability requires measurements from a NAA. The attitude motion profile should also test the robustness of the attitude determination in terms of signal re-acquisition lock-on times, so a spinning attitude motion of 1–10 RPM is desirable. As a result, three motion profiles were examined:

- Local Vertical-Local Horizontal (LVLH) fixed attitude
- Inertially fixed attitude
- Rotation - inertially fixed axis (1 RPM)

The first attitude motion fixes the vehicle in a local orbit frame and is used for comparison between aligned and non-aligned array measurement availability. In this

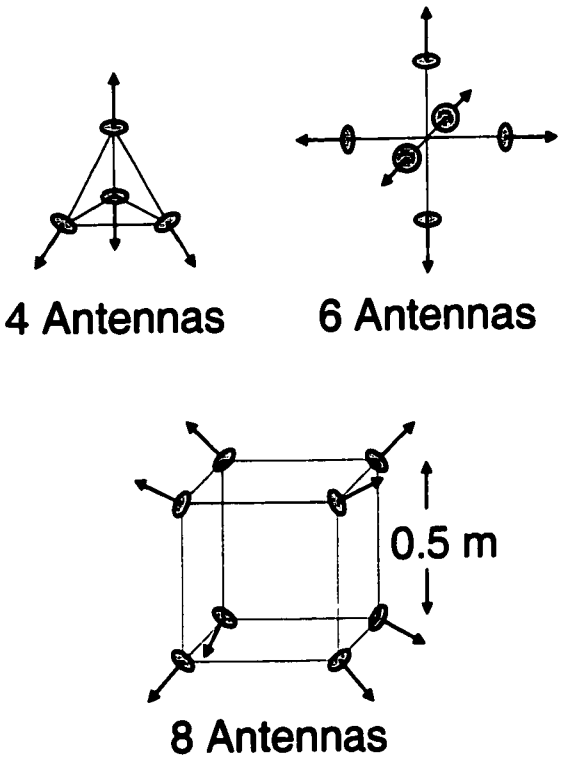

Figure 4.1: GPS antenna array geometries for LEO mission study. Symmetric design for maximizing sky coverage. The 4 and 6 antenna designs are similar to those used in Lightsey [GL97] study. 8 antenna array is new.

case, as was described in the outline of the research problem in Chapter 1, an aligned antenna array with the antenna boresights pointed towards the orbit zenith should provide continuous attitude solutions. The second attitude motion fixes the vehicle axes with respect to inertial coordinates. This motion will occlude the antennas periodically at the relatively slow orbit frequency. And the third motion profile is a rotation about the vehicle pitch axis, with the axis fixed with respect to inertial coordinates. This motion causes the pitch axis to rotate about the orbit normal as the vehicle orbits the Earth (vehicle axes as defined in Figure 4.5).

The antenna geometries studied in these simulations are shown in Figure 4.1. The three non-aligned antenna array geometries simulated are:

- 4 antennas - tetrahedron
- 6 antennas - cube faces
- 8 antennas - cube vertices

The first two antenna arrays are similar to those simulated in Lightsey's study [GL97]. In that work, he showed that a 4 antenna non-aligned array improved visibility to the NAVSTAR constellation for a rotating spacecraft over an aligned array. However, with only 4 antennas the common visibility of any two antennas to a transmitter was still low, and did not provide enough measurements to guarantee 100% attitude solution availability over the spacecraft orbit. It was shown that expanding the array to 6 antennas does provide sufficient common visibility for continuous attitude solution availability, for the inertially spinning case. This study extends the analysis to an 8 antenna configuration to examine the benefits of this increased number of antennas on the accuracy of the attitude estimate and availability of attitude estimates on a more rapidly rotating spacecraft than was simulated by Lightsey [GL97].

The results from the on-orbit simulation have been extended from just the attitude estimate availability (based on the number of visible DCP measurements) to include the attitude determination performance, in terms of the attitude estimate error STD (for one axis) and the attitude dilution of precision as defined in Section 3.1.3 [CC96].

The errors modeled in these simulations include the receiver phase noise and and vehicle self-reflected multipath. Also, the receiver lock-on delay for signal re-acquisition is modeled, which is important for a rotating vehicle. The differential carrier phase noise is assumed on the order of 0.6 cm STD, and the signal re-acquisition lock-on delay is set at 8 sec, which is consistent with tests on our laboratory receiver.

Table 4.1: LEO simulation study results summary - equatorial orbit. Large improvement in attitude estimation continuity and accuracy when antennas increased from 4 to 6. Smaller improvement when the number of antennas is increased from 6 to 8. Assumes 0.5 m antenna baselines.

Antenna Geometry	4 Antenna NAA		6 Antenna NAA		8 Antenna NAA	
Attitude Motion Profile	STD Err	Mean ADOP	STD Err	Mean ADOP	STD Err	Mean ADOP
LVLH Fixed (Availability)	0.46°	3.08 (61%)	0.36°	1.44 (100%)	0.18°	0.94 (100%)
Inertial Fixed	0.37°	2.80 (55%)	0.33°	1.30 (100%)	0.19°	0.99 (100%)
Rotation Fixed Axis - 1 RPM	1.18°	5.06 (60%)	0.33°	1.36 (100%)	0.17°	0.92 (100%)

The simulation results for the equatorial LEO orbit case are summarized in Table 4.1. The results of each simulation in the matrix are presented in terms of the STD of the attitude pitch error and mean ADOP over multiple orbits, for each of the antenna geometries and attitude motion profiles. As was seen by Lightsey, there is an improvement in attitude solution availability in going from a 4 antenna NAA to a 6 antenna NAA. When the number of antennas is increased to 8, there is no improvement in attitude solution availability, but there is a decrease in the STD of the attitude error (50 % for the 1 RPM rotation case) and the mean ADOP (25 %). This decrease is due to increased number of measurements available with eight antennas. From these results, there is a dramatic improvement in the attitude solution availability by going from 4 to 6 antennas. Further if the number of antennas

is increased to 8, there is an additional improvement in attitude determination performance. This improvement in performance must be balanced against the increased weight and power requirements of the additional antennas.

4.2 Satellite/Channel Allocation Simulations

The next simulation study examines the problem of determining the tracking channel requirements for a spacecraft GPS attitude receiver, and how it is affected by signal tracking architecture and DCP measurement strategy.

There are different signal processing architectures that can be used for GPS carrier phase tracking in the receiver, each with different limitations. Three common carrier phase tracking architectures are:

- Master/Slave carrier phase tracking
- Roving master carrier phase tracking
- Channel independent carrier phase tracking

One method is the 'master/slave' channel tracking architecture, where for a given transmitter, a single antenna and correlator are designated the 'master' channel for that DCP measurement [CC92]. The feedback signal for the master channel PLL is used to slave the other antenna PLL tracking loops, and the subsequent phase difference between master and slave antenna is observable as the phase difference between the replica carrier signals used in the master and slave channel correlators. This architecture is a natural extension for single antenna input GPS receivers that are multiplexed between multiple antennas for attitude applications.

A similar approach to the 'master/slave' carrier phase tracking architecture is the 'roving master' method [HU95], which uses the same method of determining the

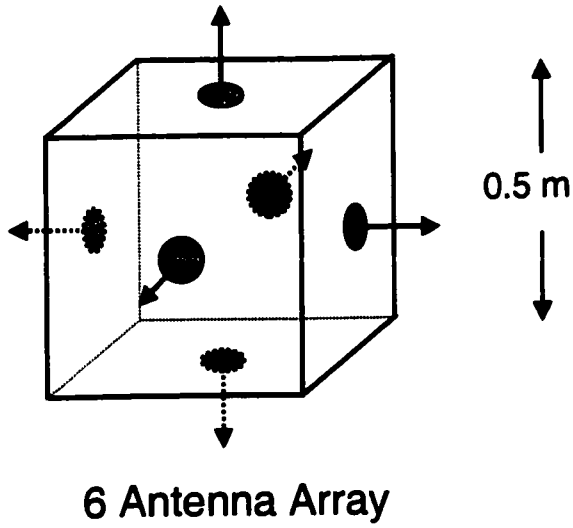

Figure 4.2: Satellite/channel allocation simulation antenna array configuration. 6 antennas arranged on the face of a cube on 0.5 m baselines, similar to 6 antenna configuration used in LEO mission study.

DCP between master and slave antenna, but allows a different master antenna to be assigned for each transmitter tracked. The master antenna can be designated separately for each transmitter, depending on criteria such as maximum received signal SNR.

The most flexible and general architecture for carrier phase tracking is to allow independent GPS carrier phase tracking on each antenna for any given transmitter. To make coherent DCP measurements, this method requires careful synchronization between the correlator channels used on separate antenna inputs. This is usually achieved through using a common frequency reference between multiple antenna RF downconverters and tracking channel correlators.

The choice of carrier phase tracking architecture depends on the particular receiver hardware and software architecture, and the antenna array geometry. A NAA requires

the use of either the roving master or independent phase tracking to produce enough DCP measurements for effective attitude estimation.

Because a generally rotating vehicle will have to some degree reduced transmitter visibility, and because receivers have a finite number of channels, it is necessary to make the best use of that limited number of channels by tracking only the subset of visible transmitters that are the best for attitude estimation. This is the satellite/channel allocation problem. There are many different methods for picking this subset of available transmitters. Three which are examined in this study are:

- Highest elevation satellite subset
- Minimum ADOP satellite subset
- ABIV satellite set

The first method picks the subset of visible GPS satellites with the highest elevations above the horizon, to limit the effect of ionospheric disturbances on the DCP measurement. Another method is to run a real-time minimization calculation that picks the subset of visible satellites that yields the lowest attitude dilution of precision (ADOP). And the last method examined is the default case where all baseline measurements in view (ABIV) are tracked.

Determining which method of satellite/channel allocation is best for a particular attitude application depends on the maximum number of tracking channels required for a given antenna configuration and the attitude motion profile of the vehicle in a LEO orbit. This maximum tracking channel requirement must also be compared to the number of available tracking channels in currently envisioned receivers. A trade-off will have to be made between increasing the number of tracking channels on the spacecraft receiver and the performance improvement involved in going to an ABIV receiver.

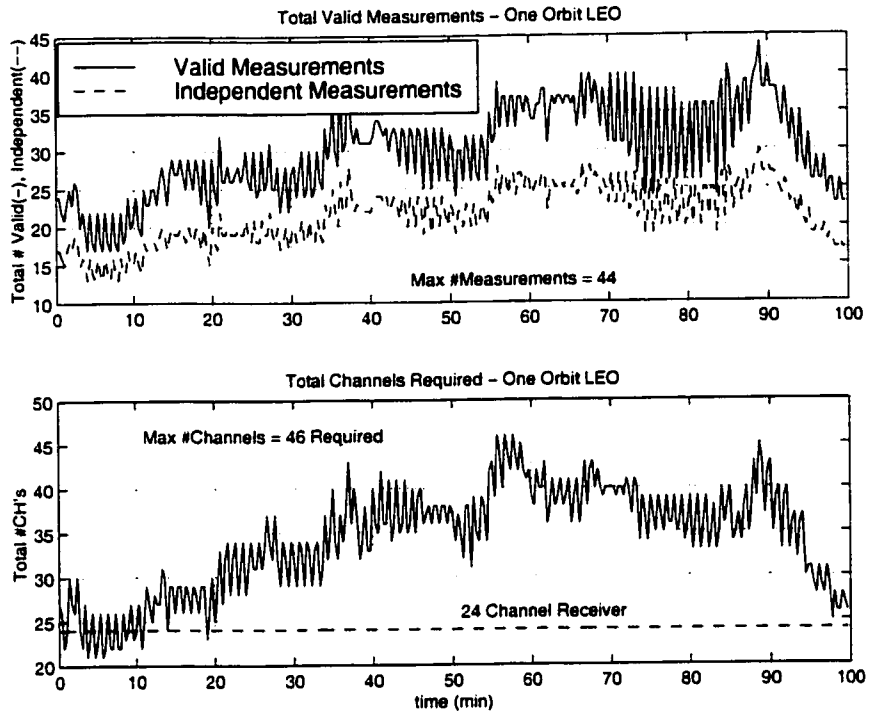

Figure 4.3: Total valid and independent DCP measurements over one orbit (top), and total tracking channel requirements for ABIV satellite/channel allocation (bottom). Maximum number of channels required for ABIV is 46, versus 24 channels provided by current receiver design.

Uematsu [HU95], in his work on the GPB mission, looked at the satellite/channel allocation problem for a spacecraft making DCP measurements from a non-aligned antenna array. For the GPB case, there are only 4 antennas for the chosen flight receiver, so the number of available measurements is particularly limited. The spacecraft is slowly rotating (0.1–1 RPM) about an inertially fixed axis pointing at a distant guide star, which is an attitude motion profile similar to the last case shown in the LEO study, but at a slower rate.

Table 4.2: Satellite/channel allocation simulation results. A comparison of the total tracking channels required and mean pitch estimate error STD for three different methods of channel allocation.

(pitch - deg)	Case 1: Highest Elevation Satellites	Case 2: Minimum ADOP	Case3: ABIV
Maximum Req'd Tracking Channels	24	24	46
σ error	1.13°	0.54°	0.36°

The antenna geometry used for this simulation study case was chosen to be the same as the 6 antenna array from LEO mission study, shown in Figure 4.2, to guarantee 100% attitude availability over the orbit. The orbit was the same as the LEO mission results, a circular, 700 km, equatorial orbit. An on-orbit simulation of this six antenna symmetric array was done for an attitude motion with a 1 RPM pitch roll about a fixed inertial axis. In Figure 4.3, the total number of available baseline measurements and the total number of required tracking channels to track all of these measurements over one orbit are plotted. The high frequency oscillations that can be seen are due to the 1 RPM rotation of the vehicle, while the longer period variations are due to the changing NAVSTAR constellation visibility as the vehicle moves through its orbit. Also plotted is the tracking channel limit of a receiver (similar to the test receiver we use in our laboratory) that has a total of 24 channels. It can seen that there are only limited periods during the orbit that this number of channels is enough for tracking all the baseline measurements that are in view, even when the measurement vector is restricted to independent measurements alone.

A comparison of the maximum required tracking channels and mean pitch estimate error STD for the three satellite channel allocation methods is shown in Table 4.2. It can be seen that there is an improvement in the standard deviation of the pitch angle estimate error by going to an all-baselines-in-view channel allocation, but that change

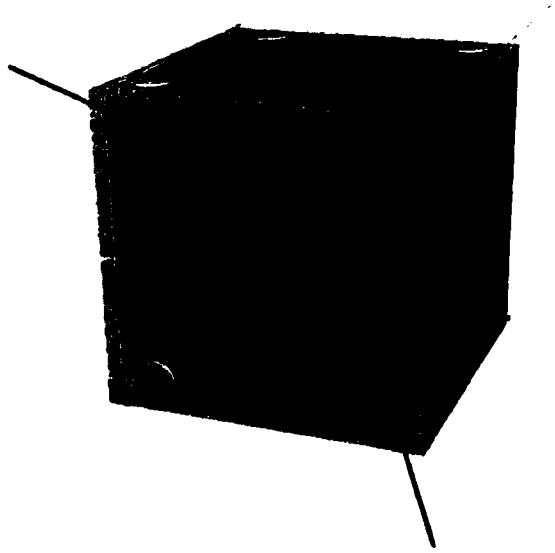

Figure 4.4: ORION spacecraft formation flying mission. Preliminary design configuration for spacecraft, 6 antenna array.

requires a near doubling of the receiver channel capacity, from 24 to 46. However, as the receiver development effort for this research project has indicated, 48 channels is not an unreasonable goal for future spacecraft receiver designs. Also, calculating the optimum subset of DCP measurements that result in the minimum ADOP in real-time is a significant computational burden. This computation can be avoided, with improved attitude accuracy, by expanding the channel of the capacity of the receiver to allow ABIV tracking.

4.3 ORION Mission Simulations

A third test case simulated various preliminary design configurations for the ORION spacecraft, currently being developed in a joint project between the Stanford Formation Flying Laboratory and the Stanford Satellite Systems Design Laboratory [JH99]. This vehicle is part of a LEO precision spacecraft formation flying experiment, the

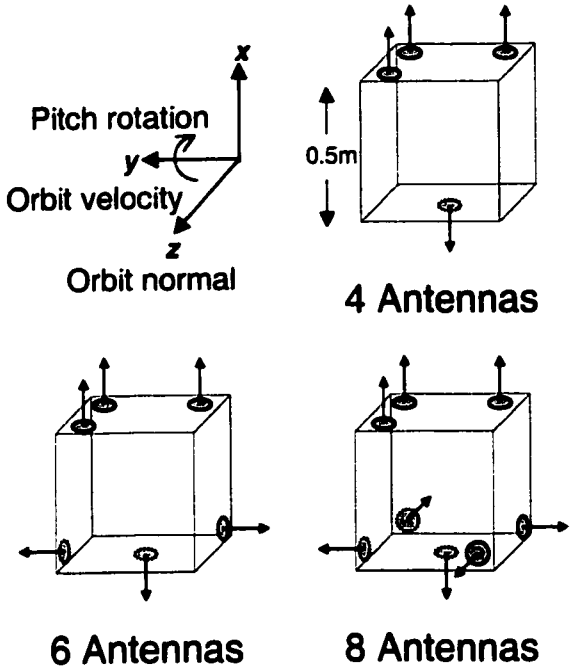

Figure 4.5: Antenna array geometries for ORION mission study, and simulated attitude pitch rotation.

objective of which is to validate the use of DCP GPS for precise relative ranging between spacecraft [EO98].

Using the preliminary spacecraft design (see Figure 4.4) and potential GPS antenna array configurations (see Figure 4.5), there were two important questions that were addressed by this simulation study. The first question looked at the impact of vehicle attitude motion on the requirements for signal re-acquisition lock-on time. This timing is particularly important during vehicle deployment, where vehicle attitude tip-off rates must be below what is required for successful re-acquisition of the GPS satellite signals on each rotation. If the tip-off rates are below this limit, GPS attitude solutions will still be possible, even as the vehicle is tumbling.

The second question addressed by this simulation study is the effect of the different potential non-aligned GPS antenna array configurations on the attitude determination

performance. The impact of different numbers of antennas and different antenna boresight pointing geometries was examined.

4.3.1 Signal Acquisition Requirements

After deployment from the launch vehicle, the ORION vehicle will be rotating about an indeterminate axis with some maximum tip-off rate. This rotation will limit the GPS antenna array visibility to the NAVSTAR constellation by decreasing the time that any given antenna has view to a transmitter. The rotation will also increase the Doppler shift disturbance in the received GPS signal, impacting the receiver lock-on time. This effect is exacerbated by initial spacecraft ephemeris errors, which increase the error in the initial estimates of relative velocity between the spacecraft and transmitter.

There are two ways that vehicle rotation can affect signal acquisition, as is shown in the plot in Figure 4.6. First, the vehicle rotation will decrease the time that a transmitter is visible, and this time decreases inversely with rotation rate. This is shown by the solid line plot of required lock-on time versus vehicle rotation rate, marked as 'Lockon Time Requirement Curve'. The second effect is that the receiver lock-on time increases with rotation rate due to increased Doppler error for the signal tracking loops. This increase is relatively flat, as is shown in the line marked 'Lockon Time Capability Curve', but becomes steeper (each dotted line) with greater orbit ephemeris error. Larger ephemeris errors increase the error in knowledge of relative velocity between the vehicle and transmitter, which means a larger initial signal Doppler error for signal acquisition. Where these two curves cross is the maximum rotation rate that the vehicle can have and still re-acquire a satellite on each rotation. The ephemeris errors are expressed in these curves in terms of percentage error in

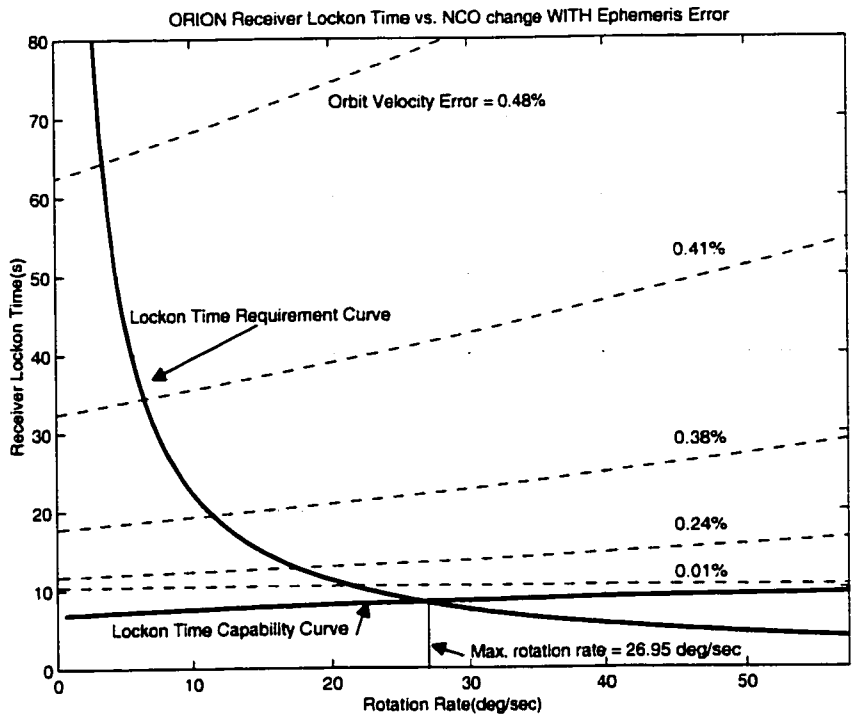

Figure 4.6: Lock-on time requirements for re-acquisition and lock-on time capability for ORION receiver versus Doppler shift due to rotation rate and orbit ephemeris error.

the predicted carrier phase Doppler. This can be deduced from the predicted error in intrack orbit position accuracy after launch. The curves plotted here are for a range of errors in insertion from 0° to 5° in orbit anomaly, which give a range of predicted carrier Doppler error from 0.01% to 0.5%. With orbit position knowledge accuracy on the order of GPS code phase positioning, the solid curve is the best representation of receiver performance.

The antenna array used in this lock-on simulation was the six antenna array shown in Figure 4.5. The orbit was similar to the previous two simulation studies, an equatorial, circular orbit with 700 km altitude. For this configuration, a maximum rotation rate of 26 deg/sec is possible at deployment before the satellites cannot be

re-acquired on each revolution, and attitude estimation from the GPS signals is not possible. This maximum rotation rate is quite fast and is well within the attitude rate nulling methods using additional rate sensors, such as rate gyros, that are currently planned for the ORION spacecraft.

4.3.2 Antenna Array Requirements

The impact of the different antenna array geometries shown in Figure 4.1 on the GPS attitude determination accuracy was also examined. The vehicle was simulated over one orbit with a 1 RPM pitch rotation about an inertially fixed axis. The relative attitude determination accuracy for the three antenna array configurations is quantified as the mean ADOP over the orbit.

The results for the simulations are summarized in Table 4.3. Since the ORION spacecraft will nominally be stabilized in a local vertical, local horizontal frame, 3 antennas on the zenith face of the vehicle is sufficient for good constellation visibility for this attitude profile. For this reason, the three preliminary antenna array designs all have at least 3 antennas on the nominally zenith pointing face of the spacecraft.

For the inertially rotating attitude profile, attitude solutions are available over 91% of the orbit for the 4 antenna ORION array, versus 60% of the orbit for the tetrahedron antenna array configuration in Figure 4.1 (used in the LEO mission study in Section 4.1). The mean ADOP over the orbit is also improved from 5.06 for the 4 antenna tetrahedron array to 3.10 for the 4 antenna ORION array. This attitude solution availability is increased to 100% for the 6 and 8 antenna ORION designs.

A significant improvement in attitude determination performance is achieved by going from the 4 antenna to 6 antenna array, as was also shown in the LEO mission simulation study. The mean ADOP for the ORION vehicle attitude determination

Table 4.3: ORION formation flying mission spacecraft simulation results.

	4 Antenna Array	6 Antenna Array	8 Antenna Array
% Availability	91%	100%	100%
Mean ADOP	3.10	1.25	0.88
Max. Channels Required	36	52	72

was reduced from 3.10 to 1.25. And again, as in the LEO study, there is less of an improvement in going to 8 antennas (1.25 to 0.88 mean ADOP) with an increase of 40% in the number of required receiver channels (52 to 72) to track all baseline measurements in view. This comparison shows that going to an 8 antenna array on the ORION spacecraft increases the power, weight, and tracking channel requirements for the GPS attitude receiver without significantly improving the attitude determination performance.

The simulation results presented in this chapter provide a necessary validation of the robust attitude determination algorithms using GPS DCP measurements from a NAA for on-orbit spacecraft conditions. While the eventual goal is to prove this attitude estimation performance on-orbit during the ORION mission, an initial experimental validation was done in a series of ground based experiments. The laboratory apparatus and experiments will be described in the following Chapters 5 and 6.

$\sim$

Chapter 5

Laboratory Test Setup

The final validation of the new robust attitude estimation algorithms was done in two sets of laboratory experiments. The optimal conditions for testing a GPS spacecraft attitude system would be on a spacecraft in orbit. Due to constraints on the availability of a spacecraft mission using GPS for attitude determination during the time frame of this research project, a compromise was made to test the new attitude determination algorithms in a laboratory setting. Ground-based laboratory tests are a valid approach to verify the performance of a GPS attitude system. Spacecraft attitude motion can be simulated in both 2D and 3D using suspended test platforms. A functional equivalent to the NAVSTAR constellation can be created with the use of GPS pseudolite transmitters. There are two important differences from the actual constellation. The first difference is transmitter distance, which is much smaller in a laboratory setting and may require the assumption of near transmitters and spherical carrier wavefronts in the DCP measurement model. This assumption is a function of the transmitter distance, the receive antenna baseline separation, and level of receiver carrier phase noise in the measurement. As shown in Figure 5.1, the boundary

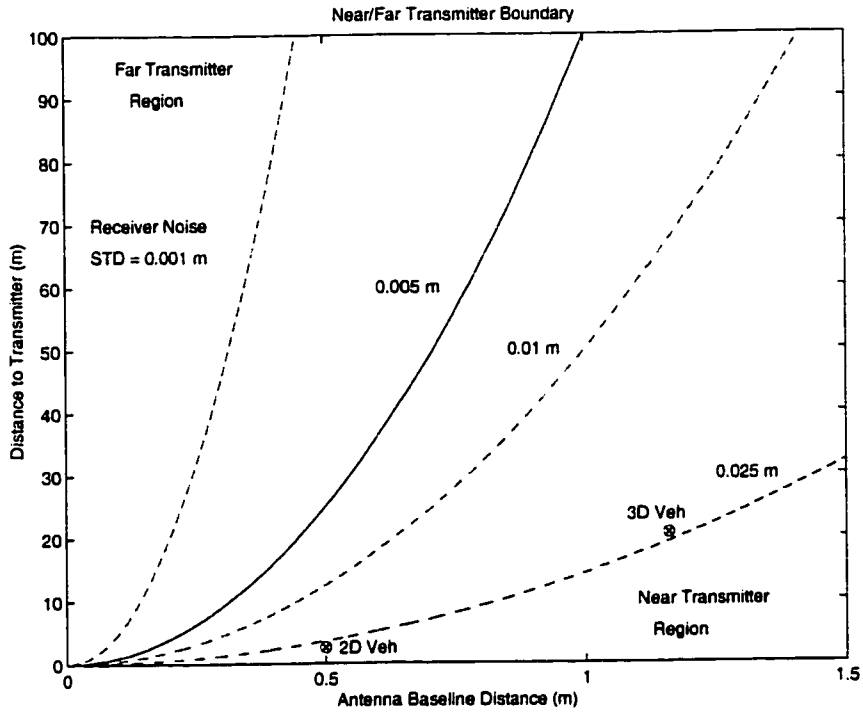

Figure 5.1: Plot of near versus far transmitter definition boundary for various receiver noise STD. The boundary between the near and far transmitter assumption is where the receiver noise is greater than the difference between the near and far transmitter modeled DCP measurement.

between the near and far transmitter assumptions can be plotted based on these three system parameters. The boundary is defined as where, for a given transmitter distance and antenna baseline separation, the difference in DCP between spherical and planar wavefront assumptions is equal to the expected values of receiver phase noise. If D is defined as the transmitter distance, b as the baseline separation between antennas, and σ_{REC} is the standard deviation of the receiver DCP noise, then the boundary between near and far transmitter assumption is where;

$$\sigma_{\text{REC}} = \sqrt{D^2 + b^2} - D \tag{5.1}$$

Also plotted is the location of the two laboratory test environments developed for this work; a 2D vehicle near transmitter laboratory and a 3D vehicle far transmitter laboratory. This plot shows that for our choices of transmitter distance and antenna baseline separation, it is reasonable to assume that valid far transmitter experiments were possible in our 3D vehicle indoor laboratory, given our assumption of 2.5 cm STD DCP noise.

The second difference between the NAVSTAR satellite constellation and an indoor pseudolite constellation is the lack of a significant Doppler shift due to relative orbit velocities in the indoor case. As this is a concern only for GPS signal acquisition and tracking performance, it does not significantly impact the validity of indoor tests in verifying attitude determination performance.

Indoor laboratory tests of GPS attitude performance have another advantage in comparison to on-orbit testing. A reference truth measurement of attitude from a calibrated vision system or other sensing system can be used in a laboratory setting to verify GPS performance. Because the pseudolite transmitter positions are stationary, they can be accurately surveyed to remove systematic errors in measurement modeling. The lack of large Doppler shifts due to relative orbit velocities between the transmitters and the test vehicle decreases the signal acquisition time. And in general the indoor environment presents a more controlled situation in terms of weather and environment for testing of a GPS sensing system. The limitations of indoor GPS system testing, primarily due to multipath reflected signals and signal power variations, are discussed further in Sections 5.1 and 5.3.

In this chapter, the laboratory environments and test vehicle platforms for two indoor laboratories are described. The first indoor laboratory used pseudolite transmitters mounted very near the test vehicle. The vehicle platform was a 2D planar

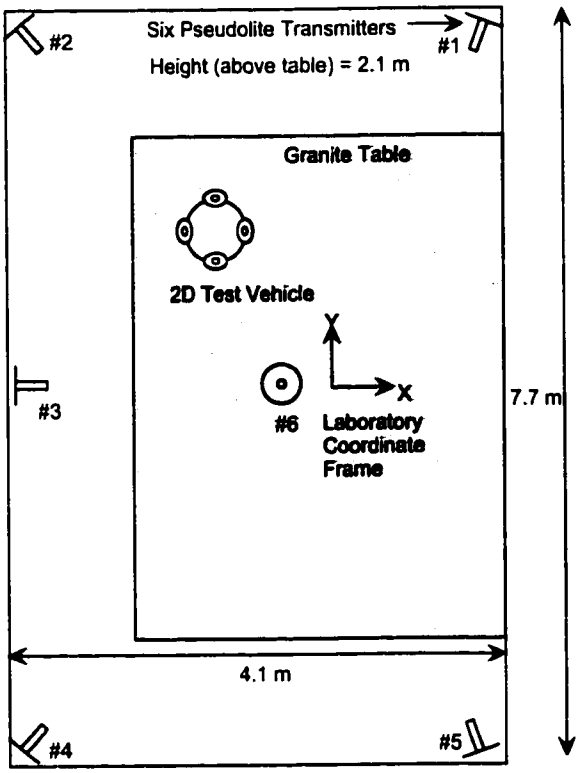

Figure 5.2: GPS pseudolite transmitter layout in near transmitter indoor laboratory.

test vehicle with single degree of freedom rotation. The second indoor laboratory had transmitter distances that were much larger, and used a 3D test vehicle platform with full three degree of freedom rotation.

5.1 Near Transmitter Laboratory

The near transmitter indoor GPS environment was originally constructed for the spacecraft rendezvous and capture experiments done by Zimmerman [KZ95]. This laboratory consists of six ceiling mounted pseudolite transmitters broadcasting the L_1 carrier phase signal modulated by a unique C/A code, with no navigation data (see right side of Figure 5.3). All the pseudolites are mounted at a height of 2.1 m above

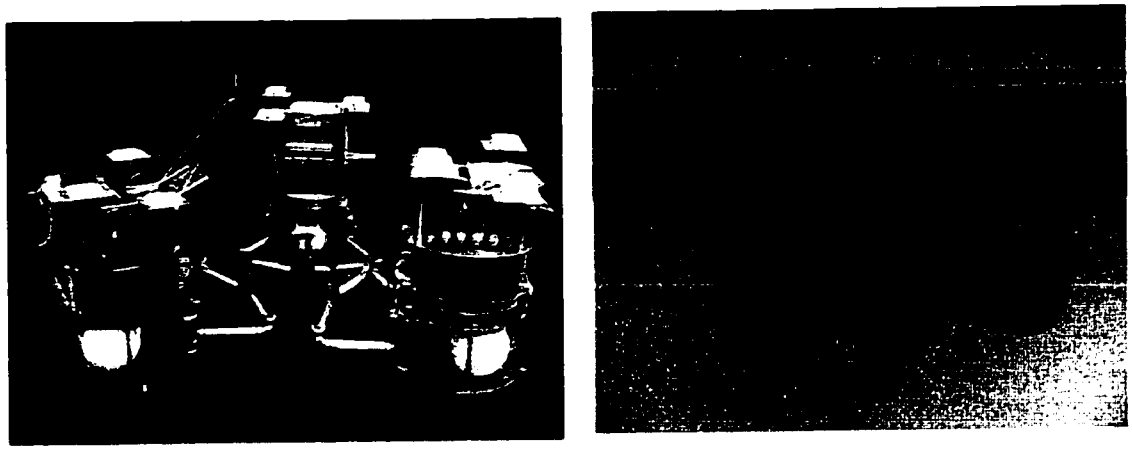

Figure 5.3: 2D Testbed - Air-bearing granite table top, air-bearing vehicles, ceiling mounted pseudolites and overhead vision system (left). Ceiling mounted GPS pseudolite transmitter, L1 C/A code(right).

the workspace in the laboratory, with an average transmitter distance of 2–3 m. The configuration of these transmitters is shown in Figure 5.2. As shown in Figure 5.1, for the 2.5 cm STD of random DCP receiver noise experienced in this laboratory, and a 0.5 m antenna baseline separation, this 2D vehicle laboratory requires modeling the non-planar wavefront near transmitter DCP measurement phase effects. This was initially reported by Zimmerman [KZ96] during his thesis experiments.

An airbearing granite table top supports between one and four floating test vehicles (see left side of Figure 5.3). The table is 9 ft by 12 ft in area and is used to simulate unforced zero-G vehicle dynamics in two dimensions. The are two types of vehicles; actively controlled vehicles using onboard thrusters, and passively floating vehicles.

As stated before, an indoor GPS environment has many advantages. One advantage of performing GPS sensing tests in an indoor laboratory is the capability of having precise reference truth sensors for attitude and position of the test vehicle.

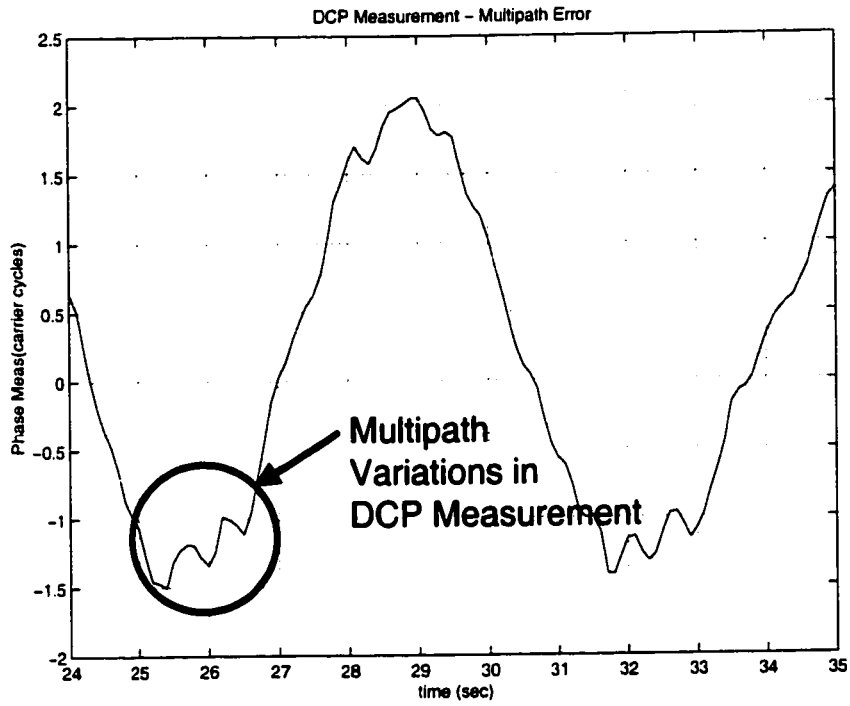

Figure 5.4: Example DCP measurement for rotating 2D vehicle - unmodeled multipath component on order of 0.25 wavelength.

In this case, an overhead vision system provides truth measurements of the vehicle position to within 0.5 cm, and rotation angle to within 0.25°. The vision system tracks an LED target with a unique pattern attached to each vehicle.

The static laboratory environment allows for a precise calibration of the pseudolite transmitter phase center positions. Calibration of these positions to centimeter level is possible, compared to NAVSTAR satellite ephemeris errors that can yield ranging errors on the order of 2 m. Since the relative velocity between the vehicle and transmitters is small, the Doppler shift in the GPS carrier is small, in most cases less than 2.5 Hz due to vehicle motion as compared to anywhere from 5–40 KHz for the NAVSTAR satellite relative motion. This greatly improves signal acquisition speed, reducing lock-on time to a matter of 2–3 seconds in most cases. When performing

many repeated attitude determination experiments, this faster acquisition speed is a necessity.

There are also additional challenges when testing GPS systems in a near transmitter laboratory environment, particularly when the transmitter distances are small (2–4 m). There are large near/far signal power variations as the vehicle range to the transmitters varies across the workspace. These signal power variations cause problems during signal acquisition and can also lead to signal cross correlation between pseudolites, as well as aliasing and jamming problems. Also, the multipath reflected signals from the walls are severe, as can be seen in Figure 5.4. The plot shows a typical DCP measurement for 1.5 rotations of a single antenna baseline in the near transmitter laboratory. The high frequency variations in the measurement at each peak are evidence of an unmodeled measurement disturbance, most likely due to multipath reflected signals, on the order of 0.25 carrier cycles.

5.2 2D Laboratory Platform

The 2D laboratory platform includes the planar test vehicle, antenna array, and groundstation electronics for attitude sensing. The vehicle and groundstation components are described in the following sections.

5.2.1 Air-bearing Table Vehicle

A passive airbearing 2D platform, shown in Figure 5.5, was used to simulate the zero-G attitude dynamics of a rotating spacecraft. The vehicle motion was single axis yaw rotation and two degrees of freedom translation. The antenna array mounted on the vehicle had four antennas, mounted in a plane, with tilt angles that could be

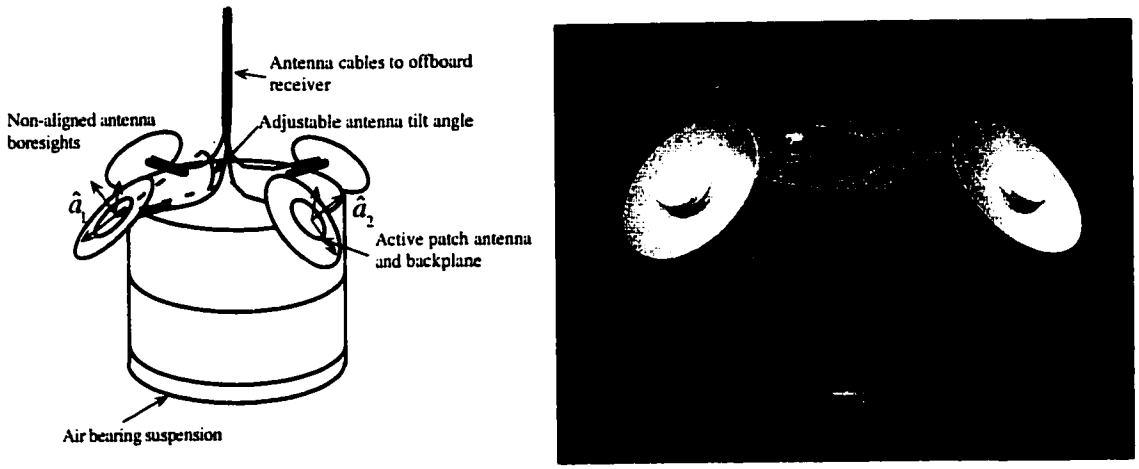

Figure 5.5: 2D air-bearing test vehicle.

adjusted between 0° and 90°. The antenna baseline separation distances were on the order of 0.5 m. There is an onboard power and communication system, and pressurized gas supply. For these tests, the antenna signals were routed to a GPS receiver offboard the vehicle. This provided a flexible development environment for testing new estimation algorithms, but also limited the vehicle from having continuous rotation due to antenna cable windup. This vehicle simulates, in 2D, the two important aspects of the robust attitude problem necessary to test the new attitude estimation algorithms; DCP measurements from a non-aligned antenna array that are rapidly and periodically occluded.

5.2.2 Modular GPS Receiver - GPSOAC

A development GPS attitude receiver, shown on the left side of Figure 5.6 was constructed for the 2D experiments. The attitude receiver consists of four commercial receiver cards, the Mitel Plessey Builder 2, installed in a single ISA card cage, along with a target processor, a single board Pentium Pro 200 computer card. Each receiver

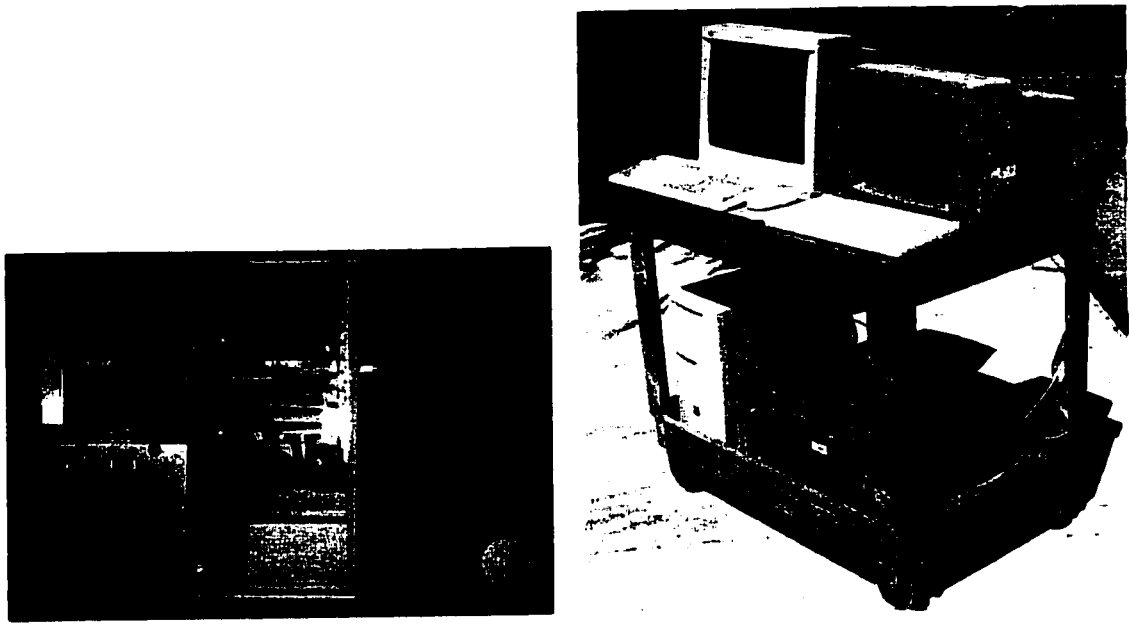

Figure 5.6: Development attitude receiver based on GEC Plessey Builder 2 receiver cards (left), and 2D attitude determination experiment ground station computer (right).

card has dual antenna inputs and 12 correlator tracking channels. Starting in the fall of 1996, hardware and software modifications were made to the Plessey receiver cards to produce coherent DCP measurements between any two antenna inputs among the four cards, giving the receiver a total of 8 antenna inputs and 48 satellite tracking channels [TC94] [CA96] [JS98]. Each receiver card has the capability of being synchronized to an external 10 MHz oscillator. By synchronizing all the cards to a single clock source, differential carrier measurements can be made between any two antenna inputs.

The attitude receiver and target computer were linked through an ethernet connection to a development host computer, shown on the right side of Figure 5.6. The host computer served as the software development platform and graphical display for the attitude determination tests. It was also used for data post-processing of the

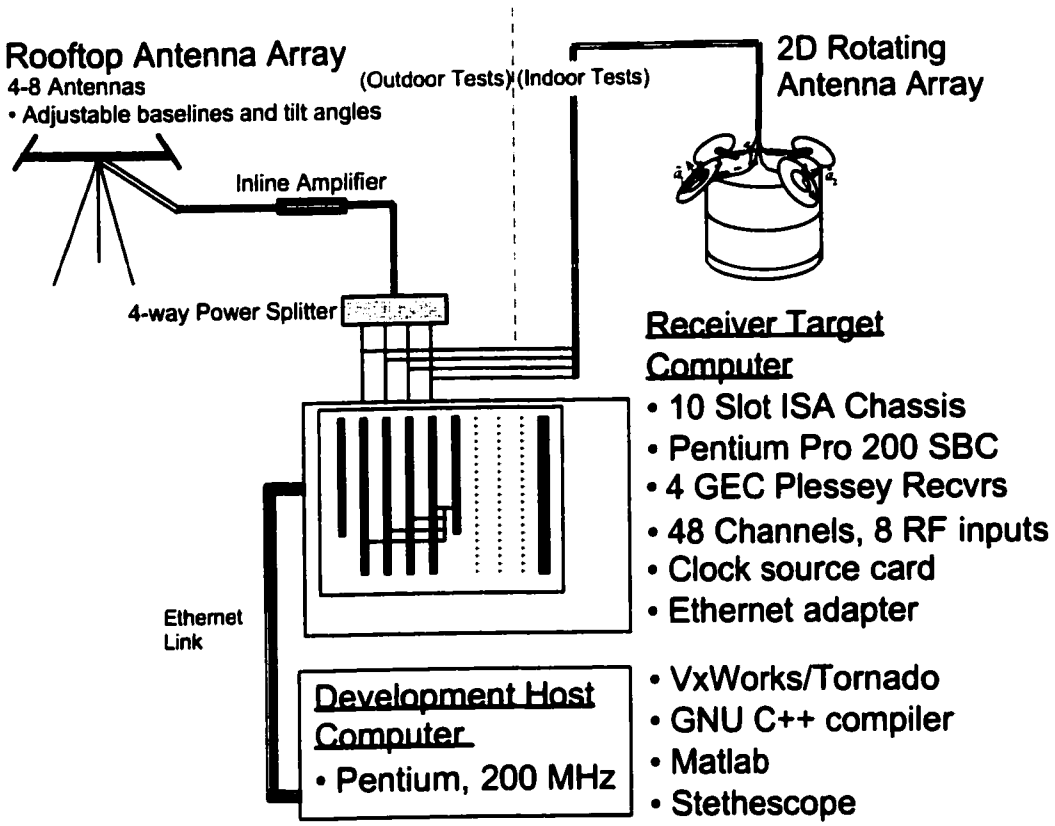

Figure 5.7: Functional block diagram of 2D vehicle experiment lab setup.

DCP measurements to produce vehicle attitude estimates, and for analysis of these results (see Figure 5.7).

The receiver target/host system is on a mobile platform for easy relocation between the laboratory and outdoor testing areas. The receiver can be used in the indoor 2D near transmitter laboratory using signals from the pseudolite constellation, or outdoors with a static, tripod mounted, adjustable antenna array (see Figure 5.8), For this static antenna array, cabling and inline amplifiers were routed outside to acquire the NAVSTAR signals. This array has each antenna hinged so that it is possible to orient the antenna boresights at 90° to each other, and was used in static tests of the attitude determination algorithms.

Figure 5.8: Four antenna array - Boresights aligned and at 90° tilt angles. This antenna array was used for static outdoor testing of the new attitude estimation algorithms.

Since many of the software functions of a GPS attitude receiver occur at regular time intervals, the problem lends itself to the application of a real-time operating system to the embedded target processor in the receiver. As part of this development, the Builder 2 operating code was ported to the VxWorks real-time operating system, and the VxWorks/Tornado code development environment was used on the host processor for cross compiling and downloading the receiver code. A separate implementation for the Windows NT operating system using a Borland 'C++' compiler was also maintained.

This development receiver architecture represents the desired qualities of a next generation spacecraft receiver, in terms of modular, expandable hardware and open architecture software. The GPS applications designer can use a flexible development system to match the desired number of tracking channels and antenna inputs to the particular sensing application. The development of this receiver was part of the NASA 'GPS-on-a-Chip' (GPSOAC) project, a collaborative effort between NASA JPL, NASA GSFC and Stanford University to create the modular hardware architecture, advanced algorithms, and software necessary for the next generation of spacecraft GPS receivers. This receiver testbed is a versatile platform for developing

software for future spacecraft GPS applications, in particular for developing new GPS attitude determination algorithms.

Modifications to the software and hardware of the Plessey Builder 2 receiver were required to create an attitude capable receiver. The main hardware and software changes will now be discussed, and data from tracking loop tests of the receiver will be presented.

Synchronization of Receiver Cards

An important modification to the Builder 2 receiver was synchronizing it with an external clock source. This made DCP measurements between antennas on separate cards possible. As was first suggested by Clark [TC94], and then by Stone [JS98], the separate receivers were synchronized at the level of the 10 MHz crystal oscillator. The Builder 2 cards are designed to accept an external 10 MHz oscillator signal. This signal is used to synthesize the 40MHz signal used in the down conversion of the incoming GPS signal in the RF front end chip, and also used in the digital correlator ASIC. The SMA connectors necessary to input an external clock input to the daughter cards on the receivers were installed, and a modification to one of the receiver cards allowed it to be used as the source of the 10MHz signal for the other three, as shown in the diagram of the test receiver in Figure 5.7.

During initial testing, two cards were synchronized to the same oscillator and no degradation in DCP measurement performance was noted. Subsequent tests that connected three and then four cards to the same oscillator in a daisy chained configuration showed that there was a problem due to a noticeable increase in the clock noise. In fact, with four cards connected, the signal was degraded to the point where no satellites could be tracked.

Three solutions were pursued for this problem. Since the 10MHz signal is on the border of what is considered high frequency in terms of circuit design, the first thought was that the added noise in the signal might be coming from impedance mismatches in the 'T' connections used in the daisy chain. These were replaced with a parallel routing of the clock signal, but the noise problems persisted.

The next solution approach was an attempt to buffer the digital signal so that the current drawn by the three other RF front ends would not exceed the current capabilities of the oscillator and draw down the voltage. A simple bread board circuit was created to buffer the 10MHz signal using an LM310 voltage follower, but this circuit proved to have too low a bandwidth. A wideband op-amp such as the CLC428 was procured and successfully used in the line driving circuit. This isolation circuit was used with an external frequency source in subsequent receiver designs, such as the ORION attitude receiver [EO98] designed by Olsen. Subsequent receiver tracking loop software modifications and timing tests for DCP measurements between the multiple, synchronized GPS receiver cards are presented in Appendix A.1.

The tests done in the near transmitter laboratory with the 2D planar vehicle provided initial attitude estimation results that could be compared with a precise truth sensor for attitude. The next part of this research effort extends those results to the more realistic conditions of a laboratory with far transmitters, and a vehicle capable of general 3D attitude motion.

5.3 Far Transmitter Laboratory

An indoor GPS environment was constructed for the 3D vehicle experiments in a Stanford highbay facility, building on the work of Teague [HT97]. The laboratory has

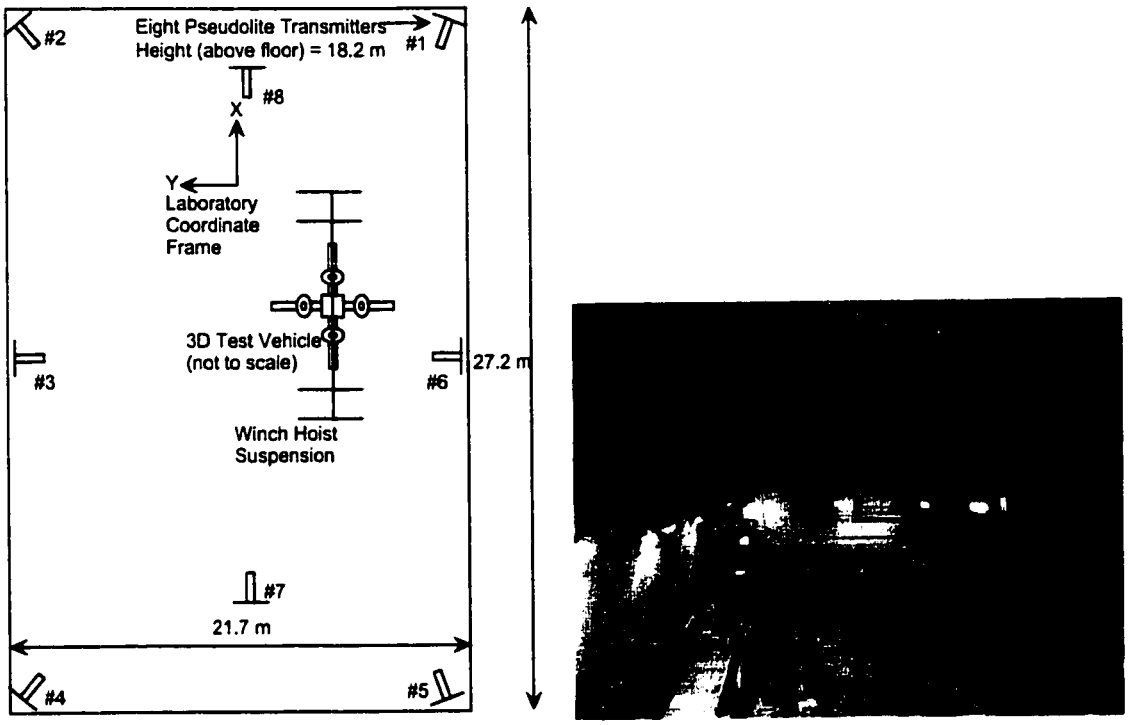

Figure 5.9: GPS pseudolite transmitter layout in far transmitter laboratory highbay, top view on the left and end view of the Stanford HEPL End Station III on the right.

eight ceiling mounted pseudolite transmitters broadcasting the L_1, C/A code, GPS signal with no navigation data. These pseudolites are at a much larger distance from the test vehicle (15 – 20 meters), than the previous 2D experiments (2 – 4 meters). The pseudolite positions and laboratory dimensions are shown in Figure 5.9, along with the position of the test vehicle in the laboratory. Assuming a DCP noise with standard deviation of 2.5 cm, which is consistent with experimentally collected data, and antenna baseline separation distances on the order of 1 m, these laboratory dimensions mean that the transmitters can be assumed to be far away, and the incoming wavefronts modeled as plane waves, for the attitude problem. This can be seen in the plot shown in Figure 5.1. This also means that the attitude determination

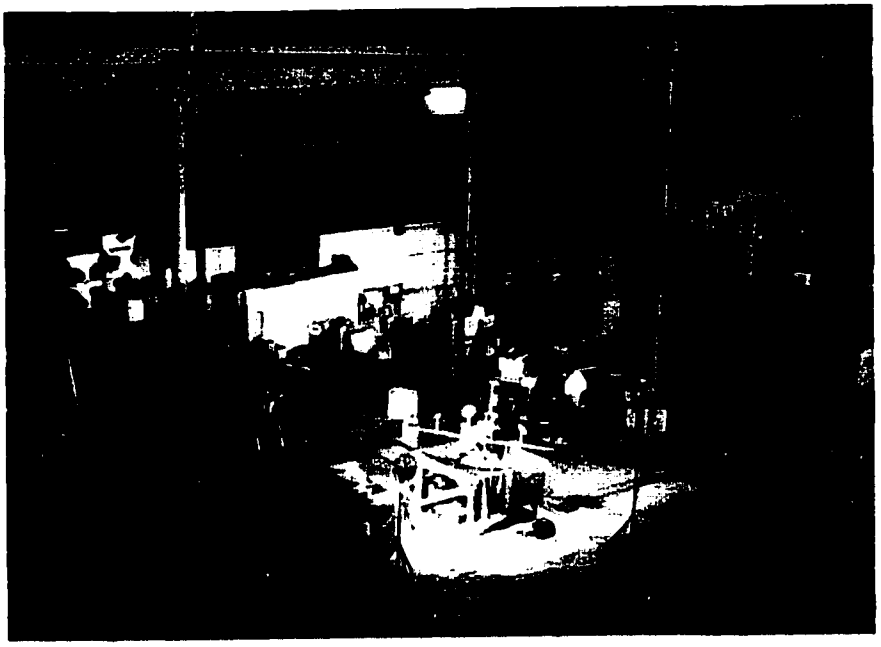

Figure 5.10: Highbay laboratory - cable suspended vehicle in center with winch hoists on each side and suspension cross member at the top.

problem can be uncoupled from the position of the vehicle, as there is less coupling between vehicle position and attitude in the DCP measurements.

A pair of winch hoists is used to raise and lower a cable supported 3D test vehicle, with the vehicle balanced such that the center of mass is very close to the cable attach point, as shown in Figure 5.10. The supporting cable is 1/16in wire rope and is 5 meters in length. This provides for relatively torque free rotation of the vehicle about three axes. The vehicle is capable of continuous rotation in yaw, and ±30° rotation in pitch and roll. This attitude motion is used to simulate the rotational dynamics of a spacecraft in zero-g.

This far transmitter GPS environment has many of the same advantages for testing GPS sensing applications as the near transmitter environment did, such as, a controlled environment and small signal Doppler shifts. However, there is no vision

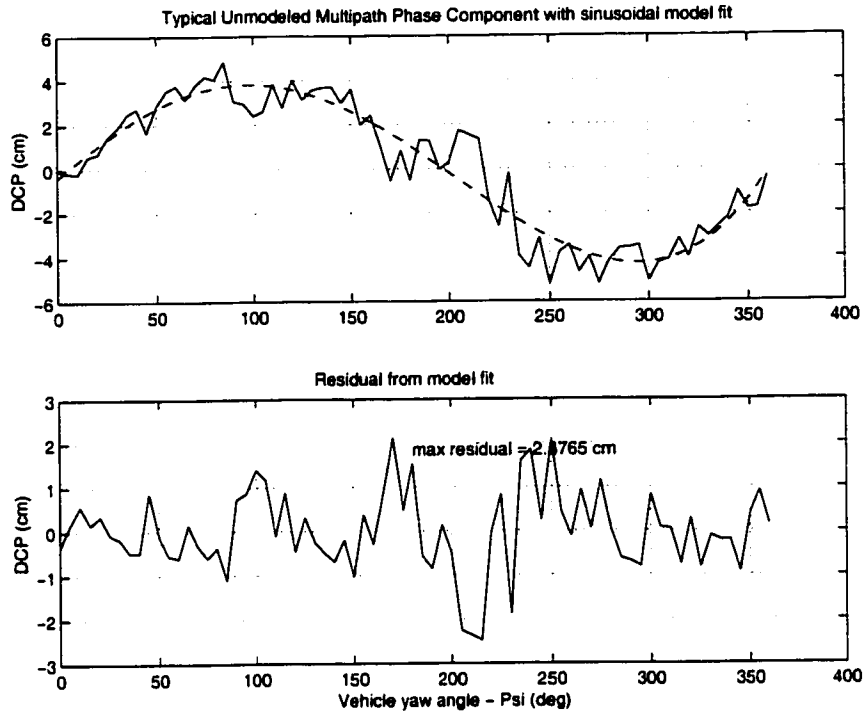

Figure 5.11: Typical multipath component of a single DCP measurement vs. vehicle yaw angle for the 3D vehicle. The unmodeled measurement component is plotted in the top graph along with a sinusoidal model fit. The bottom graph shows the residual between the data and this model fit, which is less than 2.5 cm.

system for truth sensing of vehicle attitude. An attitude solution based on vehicle mounted rate gyros was used for comparison to the GPS derived attitude solutions in the 3D case.

There were also large multipath reflected signals in this laboratory environment, as can be seen in Figure 5.11. The plot shows a typical multipath component of a DCP measurement for one rotation of the test vehicle. This was obtained by rotating the vehicle to a series of calibrated yaw angles, collecting data, and comparing it to the modeled measurement. The unmodeled multipath component of the measurement is plotted along with a fitted sinusoidal model as a function of vehicle yaw angle, and

the residual between the data and the fitted model is shown in the lower plot. The unmodeled measurement component also includes errors in the system parameters, such as antenna baselines, vehicle location, and antenna location, but it is primarily due to the multipath in the laboratory. The multipath component of the DCP measurement can be as large as 5 cm, but when a model of the multipath versus yaw angle is used to remove this measurement disturbance, a phase error residual with magnitude of less than 2.5 cm is left in the measurement.

While the multipath characteristics of the far transmitter laboratory were not a significant improvement over the near transmitter laboratory, there was a significant improvement in the near/far signal power variations experienced due to vehicle motion. This helped improve signal tracking performance in terms of signal re-acquisition speed and cycle slip rejection.

5.4 3D Laboratory Platform

The 3D laboratory platform includes the test vehicle, antenna array, and both onboard and groundstation electronics for attitude sensing, control processing, and closed-loop control actuation. The vehicle components are described in the following sections.

5.4.1 Cable Supported Vehicle

The 3D test vehicle constructed for the 3D attitude determination experiments consists of a central attachment node [HT97] with four booms that support a four antenna array with adjustable tilt angles on 1.2 m baselines (see Figure 5.12). The test vehicle GPS antenna array has four antennas, each with adjustable boresight tilt angles. Attached to the central node are most of the vehicle electronic components, including

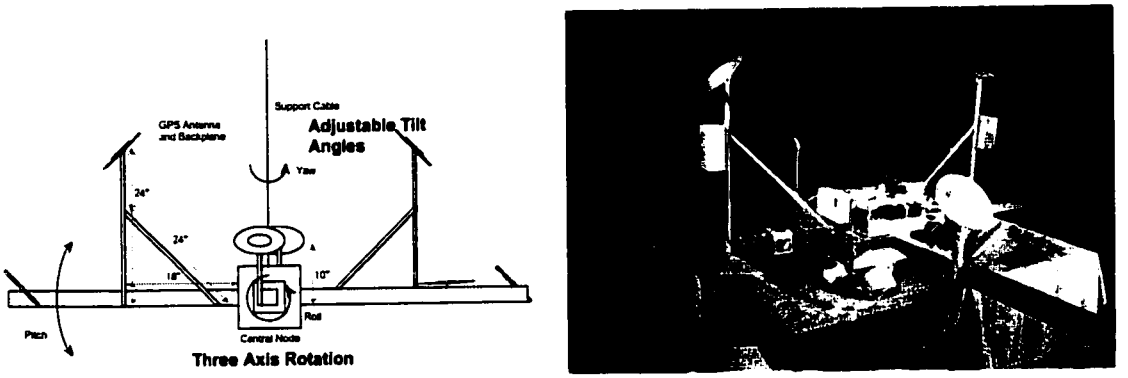

Figure 5.12: 3D cable suspended test vehicle.

an onboard GPS attitude receiver, battery power supply, actuator speed controllers, a radio modem communication system, and a computer and data acquisition system (see Figure 5.14). Also, mounted on the vehicle booms along with the GPS antenna array are four propeller thruster actuators and three single axis rate gyros. The vehicle is free spinning with an onboard GPS receiver, avoiding the antenna cable windup limitations encountered with the 2D testbed. It also includes actuators for closed-loop attitude control that were not present on the passive 2D test vehicle. A block diagram of the major subsystems and data paths for the 3D experiment is shown in Figure 5.13. The vehicle is un-tethered and provides continuous rotation and a flexible development environment for testing the new estimation algorithms under general attitude motion.

There are two main sensors onboard the 3D test vehicle; an in-house developed four-antenna GPS attitude receiver, and three single-axis rate gyros. The GPS attitude receiver is discussed in more detail in Section 5.4.2. The receiver and battery power pack can be seen mounted on the vehicle center node in the photo on the right side of Figure 5.14. The rate gyros are mounted along three orthogonal axes on the vehicle, as can be seen on the left side of Figure 5.14, and are used to give a reference

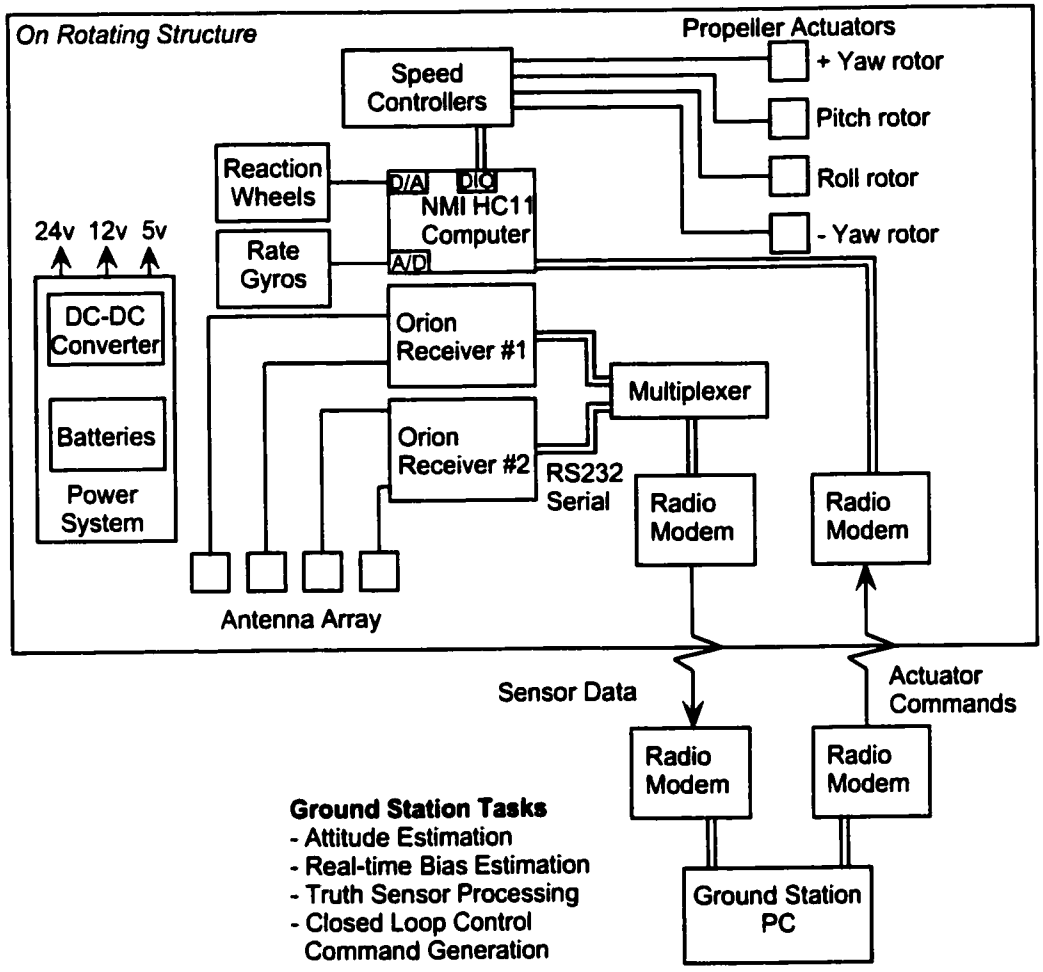

Figure 5.13: Functional block diagram of 3D vehicle experiment lab setup.

attitude measurement for comparison with the GPS derived attitude solutions. The rate gyros used were the Murata Gyrostar, a vibrating beam gyroscope developed for car navigation systems. These gyros are not aircraft navigation class, having an angular rate drift rate of 6 deg/sec/hour. Since the GPS attitude tests performed here typically lasted between 1–2 minutes, this gyro drift was easily compensated for through filtering in the gyro sensing software. Typical attitude results based on gyro data were much smoother than those obtained with from GPS DCP measurements, and are presented in the next chapter.

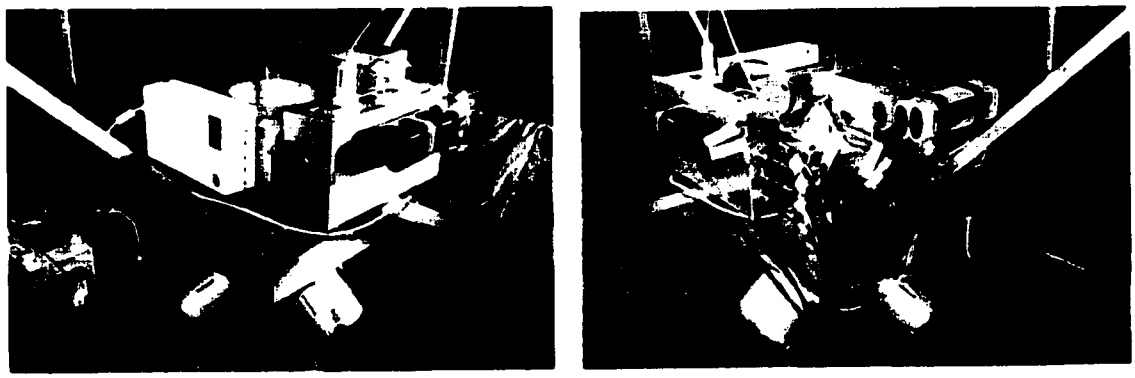

Figure 5.14: Central node electronics. Radio modem, rate gyros, GPS attitude receiver (left). GPS attitude receiver, onboard computer and power regulation and distribution (right).

For the 3D vehicle, propeller thrusters are used for closed-loop attitude control. Four thrusters, consisting of an 8 in. propeller mounted on a Graupner Speed 400 RC motor, are mounted on the vehicle, as shown in the photo on the left side of Figure 5.15. Two opposing thrusters are used for yaw angle control, as the vehicle has the highest moment of inertia about this axis, and single thrusters are used for pitch and roll control respectively. The power and control inputs for the thruster actuators are generated by four RC speed controllers, shown mounted on the vehicle central node in the photo on the right side of Figure 5.15. These speed controllers take a pulse width modulated input and output a corresponding motor current. A set of three-axis reaction wheels, visible attached to the bottom of the central node in Figure 5.14, were not used due to their limited control authority.

The onboard computer is a Motorola HC11 single board computer, shown in its enclosure mounted on the vehicle in the photo on the right side of Figure 5.14, and in Figure 5.17. The HC11 computer is used for performing the digital to analog conversion on the rate gyro measurements, and to generate the PWM motor actuator

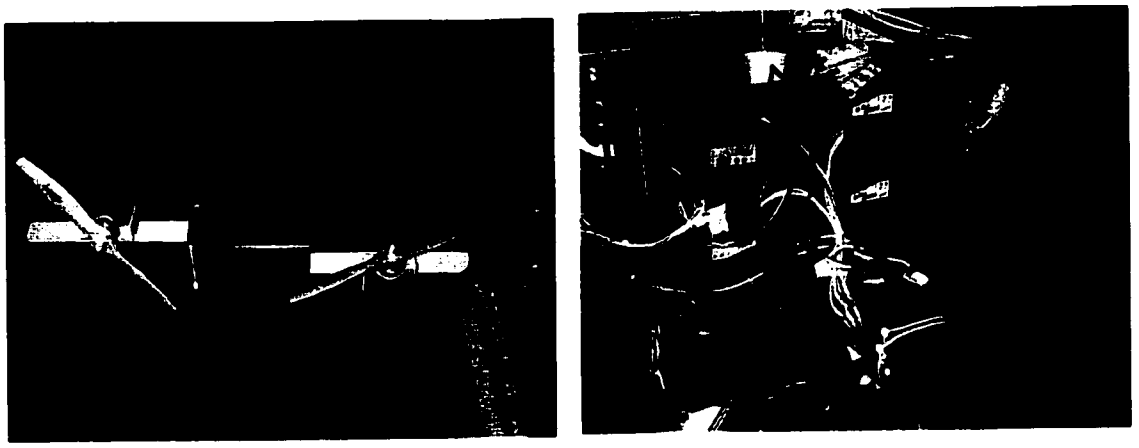

Figure 5.15: Yaw and roll axis propeller actuators (left) and actuator speed controllers (right).

commands for the thrusters. A custom lower board in the onboard computer enclosure was built to provide power regulation and serial communications functions (see Figure 5.16).

Wireless communication between the vehicle and the ground station is achieved using two pairs of radio modems, set to separate channel frequencies, to create two RS232 serial links, one for downlinking GPS attitude receiver data and one for uplinking attitude control commands and downlinking rate gyro measurements. These radio modems are theoretically capable of baud rates up to 76.8 Kbaud, but due to interference concerns are run at 19.2 Kbaud. For the size of data messages transmitted between the vehicle and groundstation, this data rate allowed for a 5 Hz update rate on the real-time closed-loop attitude determination and control.

There are four required functions to be performed by the ground station computer. First, the software for implementing the IEKF and IWLS filters for attitude determination given the downlinked DCP measurements from the GPS attitude receiver is executed on the groundstation. As part of this task, the real-time bias

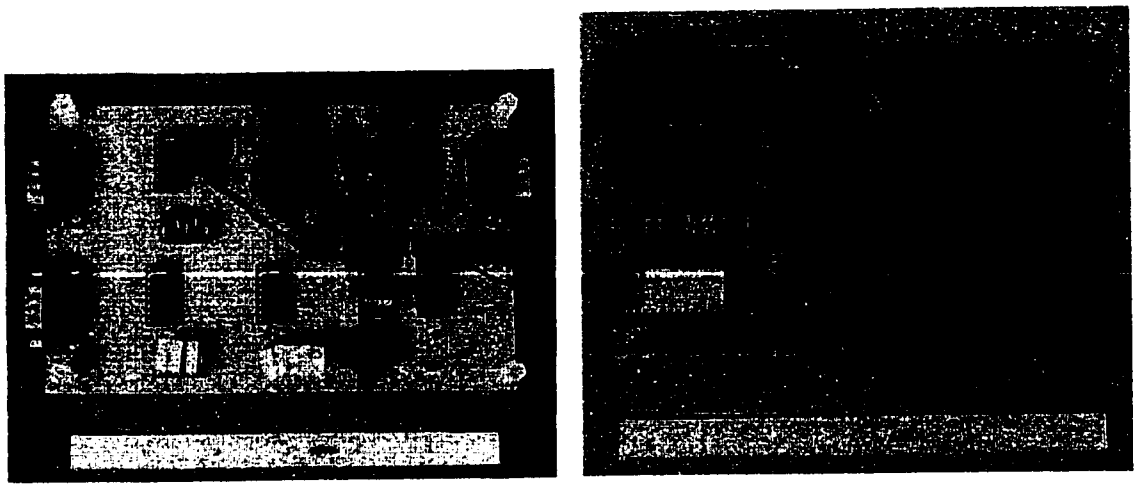

Figure 5.16: Onboard computer components. The top board, the HC11 computer, is shown on the right. The bottom board, custom built card for multiplexing, communication, and power regulation, is shown on the left.

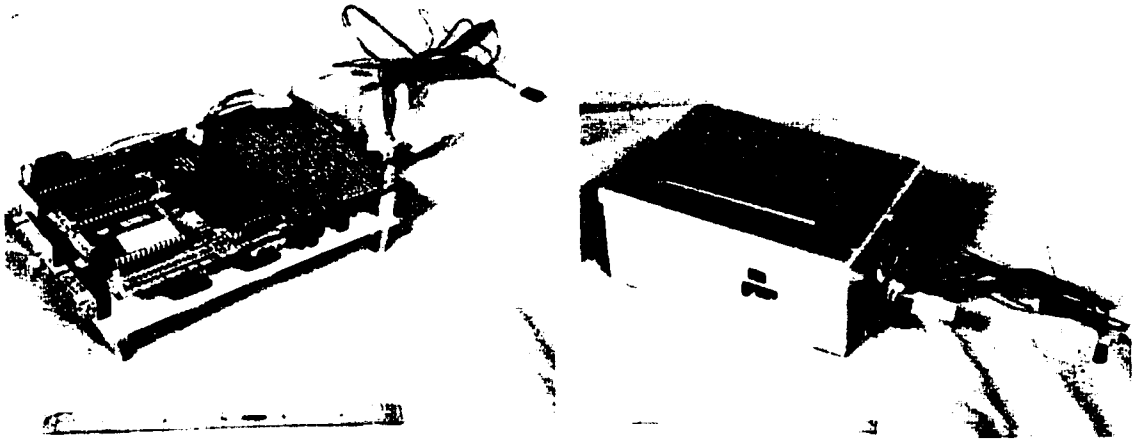

Figure 5.17: Onboard Motorola HC11 embedded computer card, and power distribution and serial communications card, stacked components left, and in enclosure, right.

re-acquisition process must also be run as measurements are constantly being lost and brought back online. The rate gyro data is filtered and integrated in real-time to produce an attitude estimate for comparison to the GPS derived attitude. And

finally, the closed-loop control commands are determined based on the current attitude estimate, desired reference attitude, and a set of pre-derived LQR control gains., The commands are then uplinked to the onboard vehicle computer for execution.

To achieve the desired 5 Hz sample rate for sensing and control, the ground station computer needed significant processing capability to perform the required functions. The ground station computer is a single board system with a Pentium II 450 MHz processor, mounted in an industrial computer ISA chassis, along with a serial communications card and ethernet card. The entire system is on a mobile platform.

The ground station software environment included a Borland 'C++' development environment for the sensing and control software, an ICC11 cross-compiler for the embedded application that ran on the vehicle's onboard computer, and Matlab/Simulink for data analysis and visualization. All code was written in 'C' for portability and efficiency.

5.4.2 Onboard GPS Receiver - ORION

The GPS ORION attitude receiver was developed using multiple Mitel Plessey 'Orion' receiver cards and a custom made clock reference and communications card. The Mitel Plessey 'Orion' receiver board was designed to enable stand-alone operation of the receiver on a small moving platform. The original Orion receiver design, a single antenna input L1 C/A code design, was modified by Olsen [EO98] to provide two RF antenna inputs and an external clock input.

The ORION receiver has the flexible, modular hardware architecture and open architecture software design necessary for attitude algorithm research and testing. The receiver has 4 RF inputs and 24 satellite tracking channels. Two dual input receiver cards are synchronized to a single 10 MHz oscillator, allowing differential

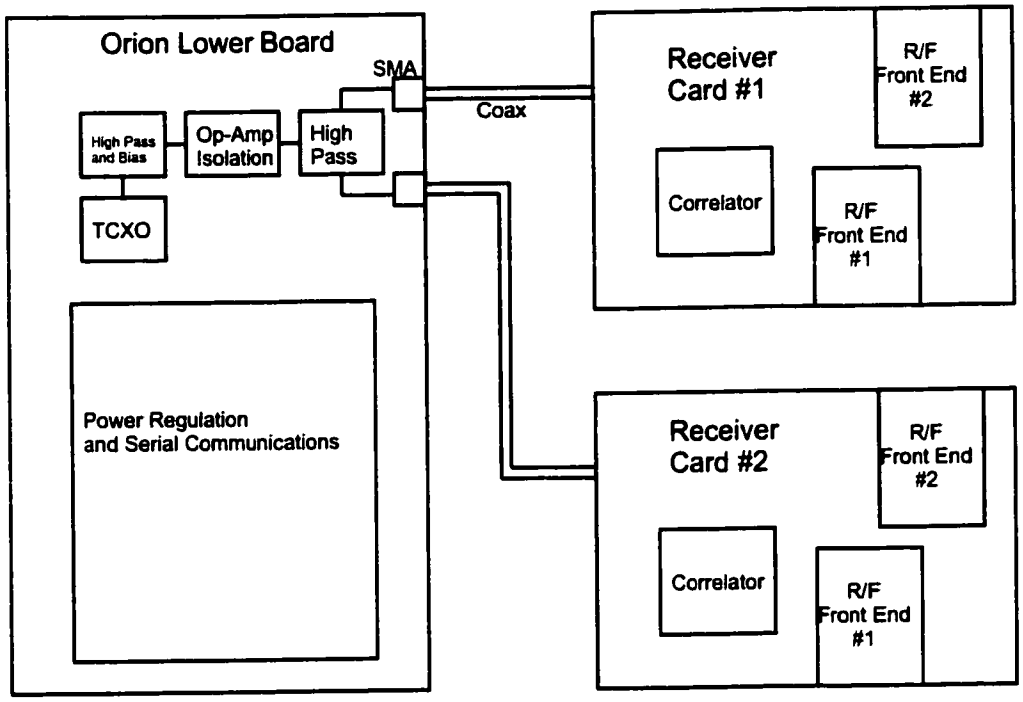

Figure 5.18: Receiver clock synchronization functional block diagram for the ORION receiver. Multiple ORION cards, each with 2 antenna inputs and 12 correlator tracking channels, are synchronized to a common 10 MHz oscillator on a custom built lower board.

carrier measurements to be made between any two antenna inputs (see Figure 5.18). Each receiver card has an onboard ARM60 microprocessor for implementing the software PLL satellite tracking loops, navigation processing, and attitude determination. The lower board also provides power regulation and serial communications for the receiver.

The Mitel Plessey 'Orion' receiver card, as modified by Olsen, is shown in Figure 5.19. The photo on the left side shows the receiver ARM60 microprocessor, onboard RAM, dual antenna input connections, and external clock input. The photo on the right shows the GPS correlator ASIC and dual antenna RF front-end circuitry. The integrated, 4 antenna, ORION attitude receiver is shown in Figure 5.20, with

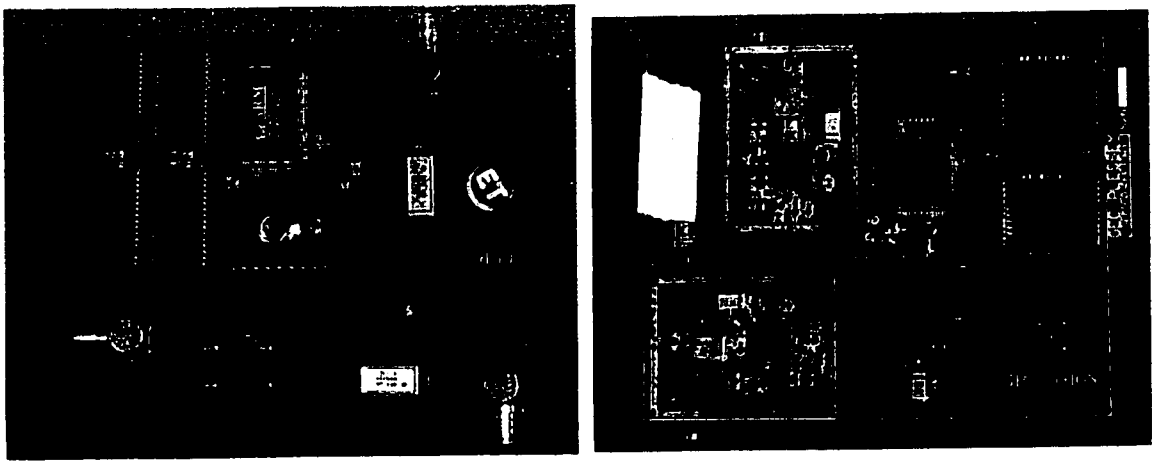

Figure 5.19: Mitel Plessey 'Orion' receiver board photo (Top side - right, Bottom side - left). This card was modified from a version of the Mitel ORION design by Olsen [EO98] to include 2 antenna inputs and an external clock input.

Figure 5.20: 4 antenna GPS attitude receiver based on dual Orion receiver cards(left) and in enclosure with battery power and output attenuators (right).

the top off the enclosure in the photo on the left, and enclosed with attached battery power supply on the right.

This receiver architecture represents the desired qualities of a next generation spacecraft receiver. It has the modular expandable hardware and open architecture

software that a GPS sensing system designer can use to match the desired number of tracking channels and antenna inputs to different sensing applications. The ORION is particularly useful for embedded receiver applications, due to its small weight (1.8 Kg), relatively low power consumption (5.5 W avg), and small volume (3"x5"x9").

The ORION receiver DCP tracking accuracy is a function of board synchronization and clock stability. This is discussed in more detail in Appendix A.2, where the results of a zero baseline DCP test are presented.

Now that the laboratory test environments and experimental vehicles have been described, the series of attitude determination experiments performed and the results obtained from these experiments will be described in Chapter 6.

Chapter 6

Laboratory Experiment Results

After describing the indoor GPS laboratory test setup and the different test vehicle platforms in Chapter 5, the results of a series of experimental tests will now be presented. These laboratory experiments, along with the on-orbit simulation studies presented in Chapter 4, were a final validation of the new robust attitude estimation algorithms. The tests were done in three sets of laboratory experiments; one set of tests on the 2D, planar, air-bearing test vehicle and two sets of tests on the 3D, cable-suspended, test vehicle. The first set of 2D planar experiments were open-loop attitude estimation and were done in the near transmitter laboratory. The second set were again a test of open-loop attitude estimation, but this time on the 3D test vehicle in the far transmitter highbay laboratory. In these tests, the vehicle had continuous yaw rotation with simultaneous limited pitch and roll motion. While the truly arbitrary attitude motion that is expected on orbit is difficult to achieve, these tests were done for a rapidly rotating 3D attitude motion that presented challenging conditions for GPS attitude determination. And the last set of experiments were a

test of closed-loop attitude determination and control on the 3D vehicle in highbay laboratory. The results of these experiments are summarized in the following chapter.

6.1 2D Laboratory Experiments

The 2D planar experiments were done for test parameters that are similar to the 2D simulation results presented in Section 3.4. In addition, an antenna configuration similar to that used on the RADCAL spacecraft was also tested [CL94]. The 2D air-bearing laboratory vehicle was spun on the granite table at rotation rates up to 1 rad/sec, and measurements were made of the DCP between two receive antennas for each of six ceiling mounted pseudolite transmitters. Data was collected simultaneously from the overhead vision system of the position and rotation of the vehicle on the table to serve as a truth measurement. For the 2D cases, the DCP measurements were post-processed to determine the attitude of the vehicle, which in this case was just the single-axis yaw rotation angle about vertical.

An IEKF estimator that compensated for the LOS dependent DCP measurement components was implemented in the post-processing attitude determination. A typical time history of the post-processed attitude estimation is shown in Figure 6.1, for three different antenna configurations. In these plots, the yaw estimate error for the three antenna array tilt angle configurations shown in Figure 3.12 are plotted over time, along with the estimate error covariance bound. The number of DCP measurements periodically decreases and increases, which can be seen in the increases in the covariance bound on the attitude estimate error. The estimate errors are not zero mean over time, indicating that an unmodeled measurement component or input

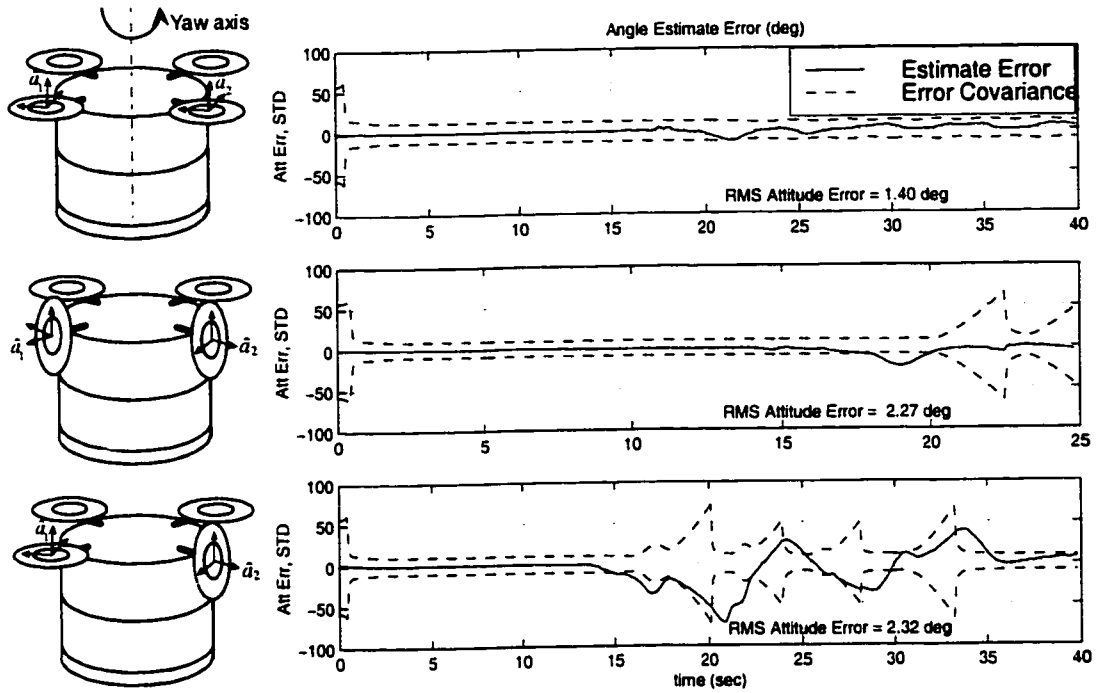

Figure 6.1: Yaw angle estimate error time history for 2D spinning test vehicle. Three antenna tilt angle cases are presented (see Figure 3.12); Aligned antennas (top), Non-aligned antennas with the same tilt angle (middle), Non-aligned antennas with different tilt angles (bottom).

disturbance torque is present. The unmodeled DCP measurement components, as described in Section 2.6, include reflected multipath, antenna phase center variation, and model parameter errors, such as the geometric location of the antennas centers. An unmodeled disturbance torque on the system was present due the windup in the GPS antenna array cables. The antenna boresight tilt angles increase from the top to the bottom in the plots shown in Figure 6.1. It can be seen from these plots that the yaw estimate error STD increases for the two NAA cases.

The experimental results for the antenna array geometries cases shown in Figure 3.12 are summarized in Table 6.1. This table compares the attitude estimation

Table 6.1: Experimental results for 2D attitude estimation. Results when compensating for RHCP in measurement versus results when not compensating for RHCP.

Attitude Estimate Error (Yaw - degrees)	Uncompensated Mean	Uncompensated STD	Compensated Mean	Compensated STD
1) Aligned Antenna Array tilt angle1 = 0° tilt angle2 = 0°	0.37	1.42	0.36	1.40
Non-aligned Antennas tilt angle1 = 17.5° tilt angle2 = 17.5° RADCAL Configuration	0.58	4.24	0.51	1.30
2) Non-aligned Antennas tilt angle1 = 90° tilt angle2 = 90°	**8.46**	2.71	**3.27**	2.27
3) Non-aligned Antennas tilt angle1 = 0° tilt angle2 = 90°	**estimation**	**failed**	**3.29**	2.32

errors for the different antenna configurations for the case where the polarization component of the phase measurement is included in the measurement model in the attitude estimation algorithms, and the case where it is ignored in the estimation. This table of experimental results can be compared to the 2D simulation results summarized in Table 3.2.

The resulting yaw angle estimate mean errors seen in Table 6.1 are larger than those found in the 2D simulations in Section 3.4, but show the same trends. In the simulations, an assumption of 0.5 cm DCP noise was assumed, which for a 1 m baseline yields attitude estimates with accuracies on the order of 0.25°. For the indoor tests, the DCP noise was a factor of 5 larger, with a corresponding decrease in attitude determination accuracy.

For the aligned antenna case 1), the attitude estimate error is the same for the compensated and uncompensated cases, showing that the effects of the LOS dependent phase components in the measurement have been removed in the differencing of carrier phase between antennas. For the non-aligned antenna array in case 2), there is an increase in the estimate error if the RHCP phase is not included in the estimator measurement model, but the error can be reduced when the modeled RHCP is calibrated out of the DCP measurements in the attitude estimator, using the algorithm in Chapter 3. The mean attitude error was reduced by more than a factor of 2 (8.46° to 3.27°) when the polarization is accounted for in the estimation. And for antenna array case 3), where the increasing measurement bias due to the RHCP phase is present, the attitude estimation fails if the RHCP is not accounted for in the estimation, but similar estimate accuracy results to case 2) can be achieved if the RHCP is included in the estimation algorithm.

The overall accuracy of these attitude estimates is worse than predicted in simulation due to the unmodeled measurement effects found in our test environment. The most significant are the multipath reflected signals. The phase center variations of the GPS antennas with transmitter LOS, as shown in Section 2.5, are predicted to be less than 0.8 cm. The effect of the antenna cable windup torques was not modeled in the IEKF, leading to an unmodeled process noise. The 3D test results presented in the next section try to mitigate the impact of this effect by using a test vehicle that is completely free-spinning.

The 2D tests experimentally validated the need to compensate for the LOS dependent DCP components in the attitude estimation. In particular, the DCP component due to RHCP must be accounted for, especially in the case where one antenna is in constant view of the transmitters while the other is periodically occluded (case 3),

in which case the estimation fails if the RHCP is ignored, due to the ramp-up in measurement bias that occurs with each rotation of the vehicle.

And finally, the test results for the RADCAL antenna array configuration show that the error in attitude estimation increases slightly (0.37° to 0.58°) when the LOS dependent components of the DCP measurement are not accounted for in the estimation. This is supported by the experimental results from the RADCAL mission [CL94], where accurate attitude estimates were obtained while ignoring the non-aligned antenna boresights.

These 2D tests show the importance of including the LOS dependent phase components in the measurement model for the attitude estimator. 3D tests are required to fully evaluate the importance of antenna array geometry and visibility on the robustness of the new attitude estimation algorithms. A set of experiments using the 3D cable-supported vehicle are described in the next section.

6.2 3D Laboratory Experiments

6.2.1 Open-loop Attitude Estimation - IWLS

Attitude estimation experiments using the 3D test platform were done in the Stanford HEPL highbay. These experiments were similar to the previous 3D simulations in Section 3.4. The antenna array configurations used in these experiments were those shown in Figure 3.14, with an additional case where all the antenna tilt angles are at 45°. The 3D cable-supported laboratory vehicle was spun in both planar and non-planar configurations, at rotation rates of up to 1 rad/sec, and measurements were made of the DCP between all four GPS antennas for six of the eight ceiling mounted pseudolite transmitters in the HEPL highbay. The DCP measurements were used in

Table 6.2: Experimental results for 3D attitude estimation. Results when compensating for RHCP in estimation versus results when RHCP is not accounted for in measurement.

Attitude Estimate Error (Pitch-degrees)	Uncompensated Mean	Uncompensated STD	Compensated Mean	Compensated STD
1) Aligned Antenna Array tilt angle1 = 0° tilt angle2 = 0°	0.32	1.84	0.22	1.77
2) Non-aligned Antennas tilt angles 1-4 = 90°	1.13	13.8	0.53	2.84
3) Non-aligned Antennas tilt angles 1&3 = 0° tilt angles 2&4 = 90°	0.89	6.75	0.31	2.17
4) Non-aligned Antennas tilt angles 1-4 = 45°	0.75	2.32	0.25	1.80

real-time to estimate the attitude Euler angles of the vehicle; yaw, pitch and roll. Attitude estimation experiments were done using both an iterated weighted least squares and an iterated extended Kalman filter algorithm.

The results for the open-loop test results for the 3D vehicle where the polarization component of the measurement is first ignored, and then accounted for in the estimator measurement model, are summarized in Table 6.2. These accuracy numbers were based on the pitch angle estimate for the vehicle in a planar spinning motion where pitch motion was negligible (so the pitch angle estimate should be near zero). These tests were done with a 2 RPM yaw spin rate. Again, as in the 2D case, the results for the aligned antenna case are very close (0.32° vs. 0.22°). As the tilt angles of the antennas are increased, the STD of the pitch angle estimate error increases dramatically, particularly for the case where all the antennas are at 90°. This increase in attitude estimate error was due to the very limited number of measurements available at these high antenna boresight tilt angles. There is a slight rise in the STD of the

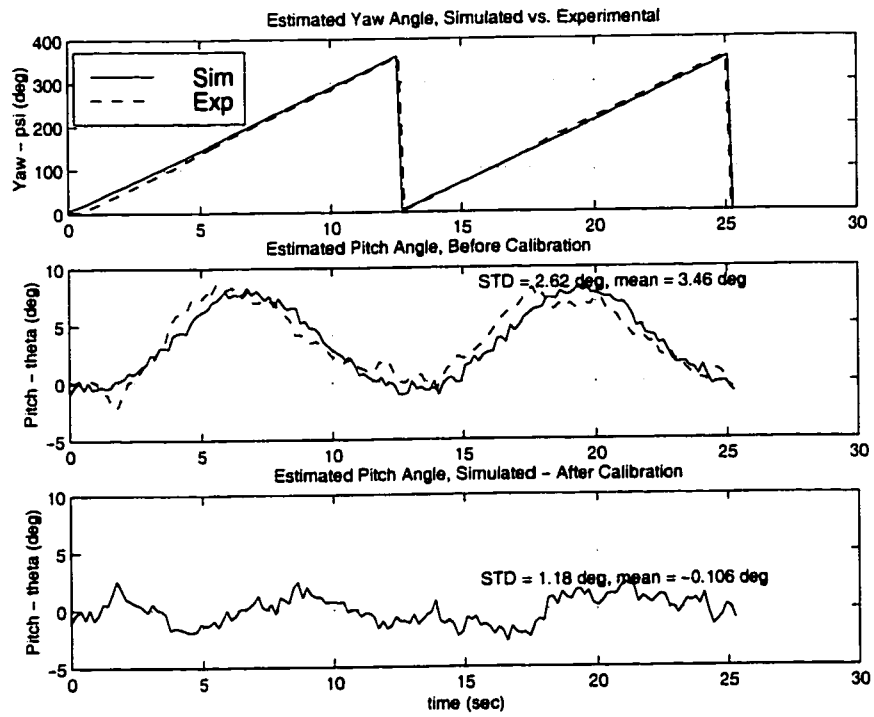

Figure 6.2: 3D attitude estimation using IWLS; yaw estimate, pitch estimate, and pitch estimate after multipath calibration. Antenna tilt angles = 45°.

attitude estimate error for increasing antenna tilt angle for the compensated case, due in part to unmodeled phase center variation and multipath errors, but in general the errors were corrected for by including the signal polarization component in the DCP measurement model. In case 3), the estimation does not fail for the case where RHCP is not accounted for in the estimation as it did in the 2D case because the polarization bias term is compensated for in the real-time bias re-acquisition for the 3D experiments.

Figure 6.2 shows that the apparent effects of multipath on the pitch estimate increases the pitch angle estimate error to a maximum of 8 degrees. A multipath error that varies sinusoidally with vehicle yaw angle and has an amplitude of ±4 cm was simulated (dashed lines in Figure 6.2) and gives a reasonably good match to the

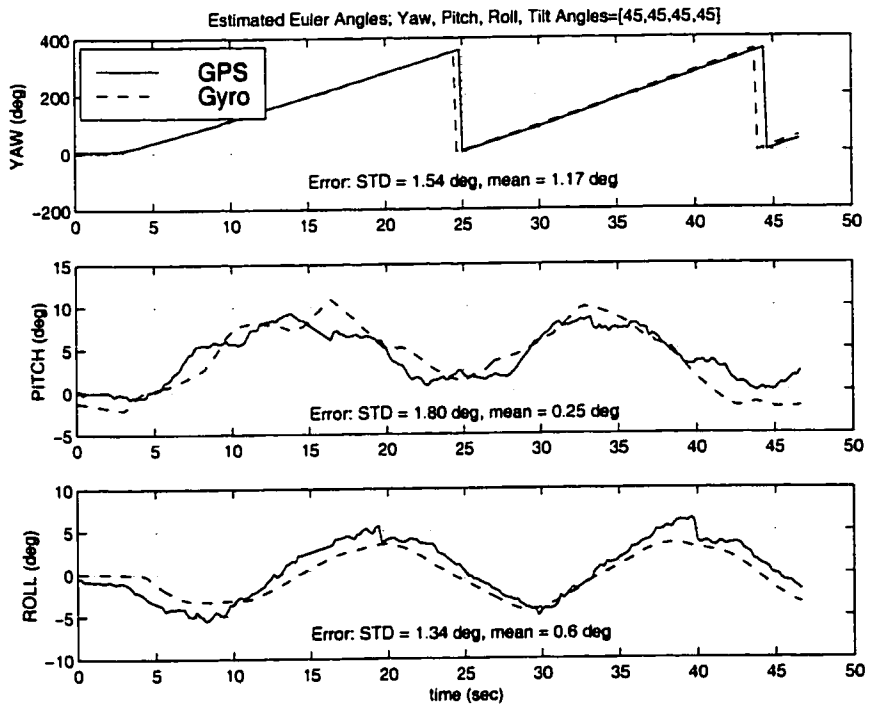

Figure 6.3: 3D attitude estimation using IWLS; vehicle Euler angles, yaw, pitch and roll. The attitude derived from rate gyro data (dashed lines) is compared with GPS determined attitude (solid lines). Antenna tilt angles = 45°.

experimental data for a 2 RPM yaw spin test on the 3D vehicle, leaving residual errors between the simulated and actual pitch angle estimates on the order of only 1–2°. A simple calibration curve based on previously measured multipath data presented in Figure 5.11 was used to partially remove the multipath from the DCP measurements. This improved the accuracy of the 3D attitude estimation to the extent where a comparison of RHCP compensation techniques could be made.

Just as in the 2D case, the resulting attitude estimate errors for the 3D case are larger than those found in simulation, but the attitude estimate errors have a similar trend for changes in transmitter visibility due to the different antenna array configurations. For the aligned antenna case 1), the attitude estimate error is the same

for the aligned and non-aligned cases, showing that the effects of the LOS dependent phase components in the measurement have been removed by the differencing between the receive antennas. For the non-aligned case 2), there is an increase in the estimate error if the RHCP phase is not included in the estimation, but the error can be reduced through compensation, as is shown in the righthand column of Table 6.2.

The highbay laboratory did not include the overhead vision system that was available as a truth sensor for vehicle attitude for the 2D laboratory experiments. For this reason, three axes of rate gyro data were collected during the 3D tests, to derive an attitude estimate that could be used to compare with the GPS attitude solution. In Figure 6.3, an example of an open-loop test result for spinning the 3D vehicle in yaw at 2-3 RPM, with a simultaneous 10 degree pitch motion is presented. In this plot the attitude solution from GPS measurements is plotted along with the attitude estimate from the rate gyro measurements. The pitch estimate error compared to the rate gyro derived solution has an STD of 1.80°, and a mean pitch error of 0.25°. As can be seen in the roll angle estimate shown in bottom plot of Figure 6.3, the rate gyro measurement derived attitude solution is much smoother than the GPS derived attitude solution, particularly when using the IWLS estimator for the GPS-based attitude determination.

These tests showed the importance of compensating for the LOS dependent RHCP component of the measurement for the 3D attitude estimation case using an IWLS filter. They also show that the gyro derived attitude solution, over short time spans, can be used as a comparison to the GPS derived attitude solution for accuracy. In the next section, the results of tests using an extended Kalman filter for attitude estimation are shown.

Table 6.3: Experimental results for 3D attitude estimation. Kinematic weighted least squares estimator results versus dynamic extended Kalman estimator results. In both cases, the RHCP measurement components are accounted for in the estimation.

Attitude Estimate Error (Pitch-degrees)	IWLS		IEKF	
	Mean	STD	Mean	STD
1) Aligned Antenna Array tilt angle1 = 0° tilt angle2 = 0°	0.22	1.77	0.13	0.57
2) Non-aligned Antennas tilt angles 1-4 = 90°	0.53	2.84	0.41	1.44
3) Non-aligned Antennas tilt angles 1&3 = 0° tilt angles 2&4 = 90°	0.31	2.17	0.33	1.21
4) Non-aligned Antennas tilt angles 1-4 = 45°	0.25	1.80	0.20	0.60

6.2.2 Open-loop Attitude Estimation - IEKF

A second set of 3D vehicle experiments were performed, similar to set of open-loop tests presented in Section 6.2.1. In these experiments the signal polarization was included in the DCP measurement model for all the tests, while the estimator algorithm was varied from the kinematic iterated weighted least squares to the dynamic iterated extended Kalman filter. The same antenna array configurations that were tested in the IWLS test cases were examined in the IEKF tests, and the results are summarized in Table 6.3. In this case there was no significant decrease in the mean pitch error, but there was a decrease in the STD of the pitch error by a factor of 2–3 due to including the dynamic model in the estimation.

A time history of the pitch angle estimate using the IEKF filter for case 4 in Table 6.3 is shown in Figure 6.4. Both the pitch angle estimate from the GPS derived attitude solution and the gyro derived truth measurement of attitude are plotted, as

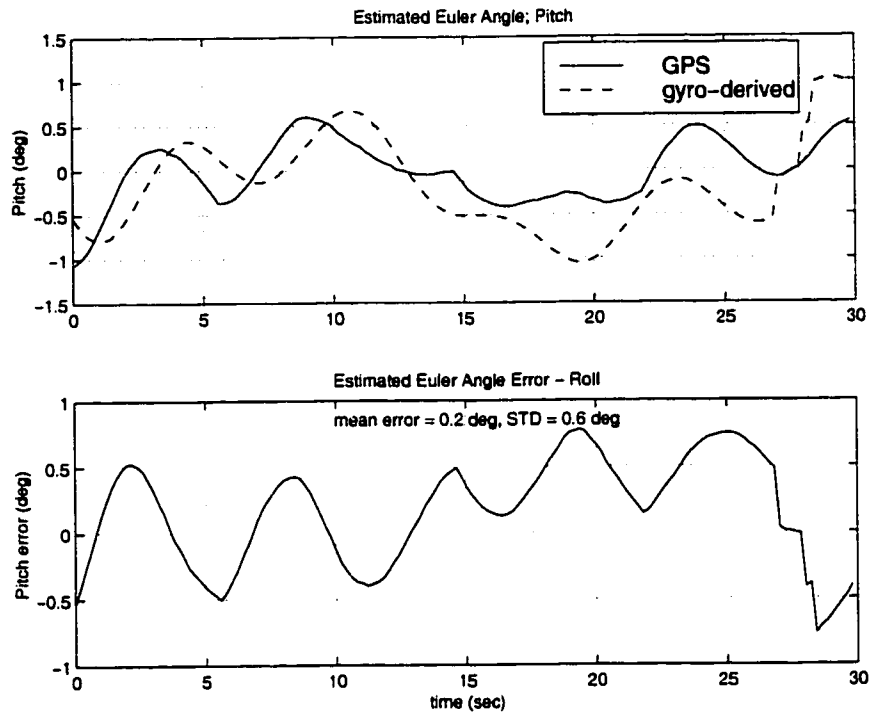

Figure 6.4: 3D attitude estimation using IEKF; Comparing vehicle pitch estimate for GPS and gyro derived attitude. Antenna tilt angles = 45°.

well as the difference between these two estimates. In comparing these results with the IWLS filtered pitch angle estimate time history in Figure 6.3, it can be seen that the dynamic IEKF estimator provides a much smoother attitude estimate than the kinematic IWLS estimator (0.60 vs. 1.80 STD).

An attitude estimation algorithm that takes advantage of knowledge of the vehicle dynamics is not typically used on spacecraft GPS attitude receivers because the receivers are normally developed without any dynamic model information about the vehicle on which they will be used. Implementing an IEKF for attitude determination also requires communicating the vehicle thruster profile to the receiver, along with an accurate calibration of the torques produced by each thruster, to insure accurate attitude estimation when using a dynamic filter. In cases where this information is

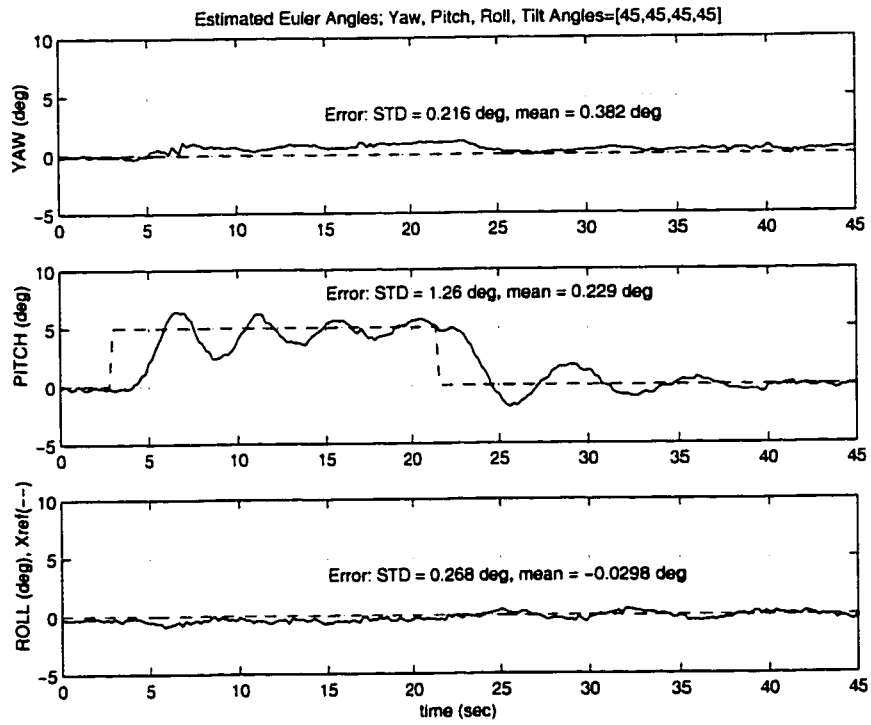

Figure 6.5: Closed-loop attitude control, step pitch command of 5°.

available, these results show that the attitude estimates can be smoothed significantly by using a dynamic filter for attitude estimation.

6.2.3 Closed-loop Attitude Control

Finally, some results for a closed-loop attitude test are presented in Figure 6.5. In this plot, the commanded attitude and attitude estimate based on DCP measurements are shown for a step command of 5° in pitch. The controller is a linear state feedback controller using LQR feedback on the estimated state. The model used in the control design is the same model used for the extended Kalman filter attitude estimator. The controller can be seen to damp out the oscillations of the vehicle and has a steady state pitch error of 0.22° and a damping ratio of 0.51. The controller performance is

limited by the nonlinearities in the thruster actuators. An inverse mapping between motor speed command and output thrust was used to partially linearize the output of the thruster actuators. Additional control error is introduced by the switching delay inherent in the thruster when changing commanded thrust direction. There is also some slight cross coupling in the yaw and roll axes, due to thruster misalignments and the fact that the Euler coupling torques in the vehicle dynamics were ignored in the model.

These 2D and 3D attitude determination experiments, both open-loop and with closed-loop attitude control, present a validation of the robust attitude determination algorithms developed for use with DCP measurements from a non-aligned array of antennas. In the following chapter, some conclusions and recommendations will be drawn based on this experimental work.

Chapter 7

Conclusions and Future Work

In this last chapter, some conclusions are made about the potential for improved performance of future spacecraft GPS attitude systems based on the theoretical and experimental work done in this dissertation research. The contributions provided by this work in terms of the attitude estimation algorithm development, experimental attitude determination validation, and on-orbit spacecraft mission simulations are briefly summarized. Also, some suggestions for how the current research work can be extended are presented. Finally, two space missions planned for the near term that will use measurements from a non-aligned array of GPS antennas for attitude determination are discussed, and how these missions can benefit from the research results presented here.

7.1 Conclusions

This research has demonstrated in simulation and in laboratory experiments the benefits of using measurements from a non-aligned array of antennas for spacecraft attitude determination, in terms of increased attitude solution availability and improved

robustness of the attitude determination to general spacecraft attitude motion. It was also shown that problems will arise if LOS dependent effects on the differential carrier phase measurement, such as the right hand circular polarization (RHCP) and the antenna phase center variation, are ignored. The most important effect is the additional DCP component due to the RHCP of the GPS signal. A new measurement model and attitude estimation algorithm were derived to handle these problems. Attitude estimation was done with the LOS dependent phase effects calibrated out of the measurement, and a proof of the stability of the estimation algorithm in this case was presented.

The next generation spacecraft GPS receiver will require new hardware and software architectures to provide the versatile, flexible development tools necessary for the GPS applications designer to match the receiver design to the mission requirements. A prototype development receiver with these characteristics was built for this research.

Proof-of-concept laboratory tests were performed using measurements from a non-aligned GPS antenna array on both 2D and 3D rotating test vehicles, using a set of pseudolite transmitters in a laboratory environment. Attitude estimation for a rapidly rotating vehicle was successfully accomplished. It appears that the attitude determination accuracy that has been demonstrated in this research ($\approx 0.5°$, see Table 6.3) will support the use of DCP GPS measurements for spacecraft attitude sensing for many upcoming missions, in particular the large volume LEO communications constellation missions described in Section 1.1.1. Improvements in estimation accuracy can be achieved in future applications through the use of additional aiding sensors [RH98], increasing antenna baseline separation, or potentially increasing the

ranging signal carrier frequency, as is planned for some self-constellation missions such as the New Millennium Interferometer [KL97].

The attitude estimation techniques described in this work will become increasingly important in the future as mission requirements on attitude motion and versatility drive the GPS applications designer to use non-aligned antenna arrays and near transmitters. Missions with these characteristics are currently under development, such as Gravity Probe B, the ORION spacecraft formation flying experiment, and the AERCAM/Sprint inspection vehicle proposed for the Space Station.

7.2 Summary of Contributions

This section summarizes the main contributions of this dissertation research. The most important contributions of this research are the extensions to the attitude estimation algorithms developed for determining vehicle attitude based on GPS carrier phase measurements from an array of antennas with non-aligned boresights. This involved modifications to the attitude estimation algorithms to improve their robustness under general 3D spacecraft attitude motion. An improved, near/far transmitter differential carrier phase measurement model that includes the effect of the right hand circular polarization of the GPS signal was derived. These new, robust attitude estimation algorithms were able to compensate for periodically and rapidly occluded DCP measurements.

Once the LOS dependent DCP effects that are present when making measurements from a NAA were defined, the difficulty of using a linearized model of these measurement terms was clearly evident. A simpler alternative based on calibrating the LOS dependent DCP measurement components out of the DCP measurements

was tested. A stability proof for attitude estimation when using the technique of calibrating out the LOS dependent phase components from the DCP measurement was derived and tested in simulation for the single antenna baseline case.

In three sets of laboratory experiments, attitude estimation was performed using DCP measurements from a NAA, for both the near and far transmitter distance cases. These experiments were performed in real-time, on dynamic, rotating test vehicle platforms in an indoor GPS laboratory environment, for both 2D and 3D vehicle attitude motion. These experiments validated the improved, robust attitude determination algorithms that were developed, under rapid, 3D attitude motion.

And the last contribution of this research was a set of simulation studies that validated the new robust spacecraft GPS attitude determination techniques under realistic space mission conditions. The antenna configurations and attitude motion profiles for three candidate LEO spacecraft missions using GPS determination were simulated. The signal acquisition and satellite/channel allocation problems associated with determining attitude on an arbitrarily rotating vehicle using DCP measurements from a NAA were examined.

7.3 Recommendations for Future Work

The experimental work presented here can be extended to include DCP measurements from more antennas. As our experiments were somewhat limited by the in-house developed GPS test receiver, the results presented here are all for four antenna arrays, but in simulation it was shown that the optimum number of antennas for providing robust attitude determination is in the range of six to eight. This is also the number planned for upcoming spacecraft missions such as the ORION spacecraft.

A laboratory experiment with an array that uses 6 or 8 antennas will provide valuable ground-based test results during the development of these types of missions. This experiment will require a more complicated vehicle suspension system, and new pseudolite transmitter geometry in the laboratory.

Another extension to this research would be to provide even more general, 6-DOF attitude motion in the test vehicle platform. The cable supported vehicle had continuous rotation about the yaw axis only. A new testbed design could extend this continuous motion to all three vehicle axes.

Also, since the ORION spacecraft formation flying mission is planning to perform attitude estimation on a group of three vehicles with both onboard pseudolites and view to the NAVSTAR constellation, an indoor testbed that involves multiple vehicles would be a useful extension to this work. A three vehicle ORION formation testbed should be planned, where attitude estimation and DCP measurement bias resolution using near pseudolite transmitters and vehicle motion can be tested.

Any validation of these extensions to present attitude estimation algorithms will eventually require testing using measurements from the NAVSTAR satellite transmitters. Outdoor, ground-based validation tests of the attitude estimation algorithms can be done for this validation step.

7.4 Upcoming Spacecraft GPS Missions

There are two impending spacecraft missions that are planning on using measurements from a non-aligned antenna array for GPS attitude determination. During the development of the GPS attitude sensing system for these missions, the algorithmic and experimental issues outlined in this dissertation will need to be addressed. The

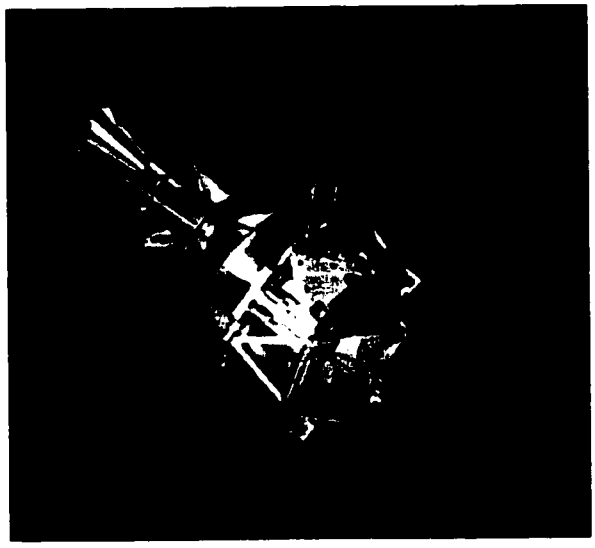

Figure 7.1: Gravity Probe-B spacecraft. NAA mission scheduled to fly Sept. 2001.

data from these flights will provide a valuable flight validation of the concepts derived here.

7.4.1 Gravity Probe-B Mission

One spacecraft planned to fly with a non-aligned antenna array for GPS attitude is the Gravity Probe-B spacecraft (see Figure 7.1). Currently, GP-B is scheduled to fly in September of 2001. The GPB spacecraft will be slowly rotating about an inertial axis fixed on a distant guide star. The spacecraft will use telescope measurements of this guide star position and measurements from an accelerating proof mass, to fly in a drag free orbit. The GPB mission is planning on performing an attitude determination experiment using downlinked GPS carrier phase measurements in post-processing. Because of the slow inertial rotation of the vehicle about the telescope axis, an aligned array of GPS antennas will not provide continuous DCP measurements for attitude

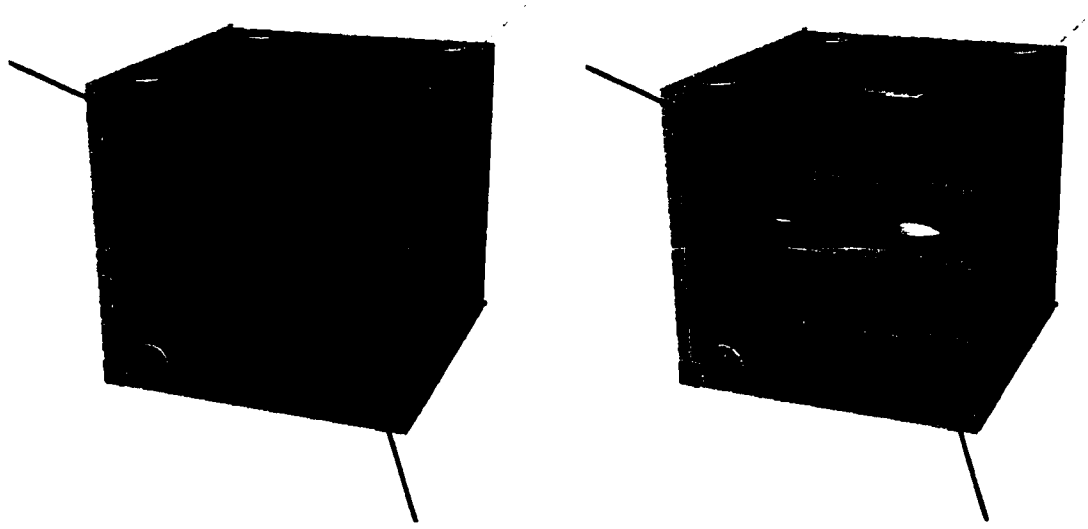

Figure 7.2: ORION spacecraft for LEO formation flying experiment. NAA mission scheduled to fly ≈ Jan. 2001. Interior and exterior views.

determination. For this reason, a non-aligned antenna array is planned, as was shown in Figure 1.7.

7.4.2 ORION Formation Flying Mission

The ORION spacecraft formation flying experiment will use a cluster of microsats, developed and built at Stanford, to test the use of DCP GPS measurements for precise relative spacecraft position sensing and control. The mission is scheduled to fly in early 2001. As part of this mission, a real-time GPS attitude receiver that uses measurements from a non-aligned antenna array will be flown. This receiver will also be developed at Stanford. One of the planned antenna array configurations, with 6 GPS antennas, is shown from two viewpoints in Figure 7.2. Because the planned attitude motion profile for this vehicle includes general spacecraft attitude motion,

the GPS attitude receiver will require robust performance through the use of the algorithmic extensions to the GPS attitude problem provided by this research.

Appendix A

GPS Receiver Test Data

A.1 GPSOAC Receiver Tracking Loop Software

After synchronizing the multiple Mitel Plessey Builder 2 GPS receiver cards and porting the operating software to the VxWorks operating system and Tornado development environment, the biggest modification to the receiver software was changing from non-coherent frequency-locked loop (FLL) signal tracking to coherent phase-locked loop (PLL) tracking. The original Builder 2 code was designed for rapid signal acquisition in highly dynamic environments, but not for carrier phase measurement, which requires coherent phase tracking. Olsen [EO98] modified the carrier phase tracking loop to produce coherent phase measurements. These modifications and some test results are summarized here.

A.1.1 Tracking Loop Modifications

To measure the differential carrier phase between two channels on the receiver, the two channels must provide a coherent measurement of the same incoming GPS carrier signal. Building on previous work done with the Trimble TANS Quadrex receiver [CC92], it was initially thought that the best method for getting carrier phase measurements would be to modify the tracking loop code provided with the Builder 2 development system from an FLL to a first order coherent phase-locked loop.

The carrier phase tracking loop was rewritten to implement a third order PLL, similar to the work of Cohen [CC92], who demonstrated with the TANS Quadrex receiver that the higher order PLL tracking loop is more robust to antenna motion. A higher order PLL was designed and tested in simulation by Olsen, and the desired performance was achieved in simulation.

This coherent tracking loop was augmented by making use of the current FLL structure of the Builder 2 code. The FLL tracking loop code provided with the Builder 2 is hierarchical, with a coarse frequency discriminator being used to rapidly bring the carrier frequency tracking error down from about 500Hz to 10Hz, and a fine second order FLL to track the carrier frequency after that. A new tracking loop filter was implemented that had a third inner loop such that, when the carrier frequency error was less that 1Hz, the filter would switch to a first order PLL. This was an attempt to maintain the robustness in tracking exhibited by the original FLL, and still get coherent carrier phase tracking. A filter that switches between an FLL and a PLL is conceptually similar to a higher order PLL, but requires less modification of the original, functional, Builder 2 tracking loop code.

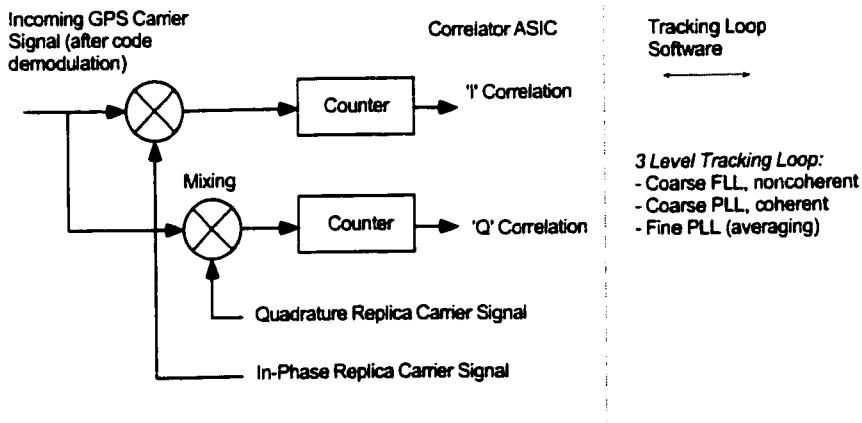

Figure A.1: Carrier phase correlation process block diagram.

A.1.2 Tracking Loop Tests

To assess the performance of these various tracking loop designs, first consider the carrier signal correlation process, as outlined in Figure A.1. The incoming GPS signal is first correlated with the corresponding satellite gold code, and this demodulated signal is input to the carrier phase correlator. The incoming signal is mixed with an inphase and quadrature replica of the incoming signal carrier, based on the frequency of the correlator digitally controlled oscillator (DCO). These demodulated inphase and quadrature signals are then counted in an accumulator, which averages the correlation value over each sample period. The output of the counter provides an average value of the inphase (I) and quadrature (Q) correlation of the incoming and replica signals, which are filtered in the tracking loop software and used to drive the correlator DCO.

For an FLL tracking loop, the I and Q values are used in a frequency discriminator to drive the replica signals such that their frequency matches the incoming carrier frequency. So for an FLL, if the frequency error is zero, the I and Q values should be stationary, but the phasor described I and Q can be pointed in any direction depending

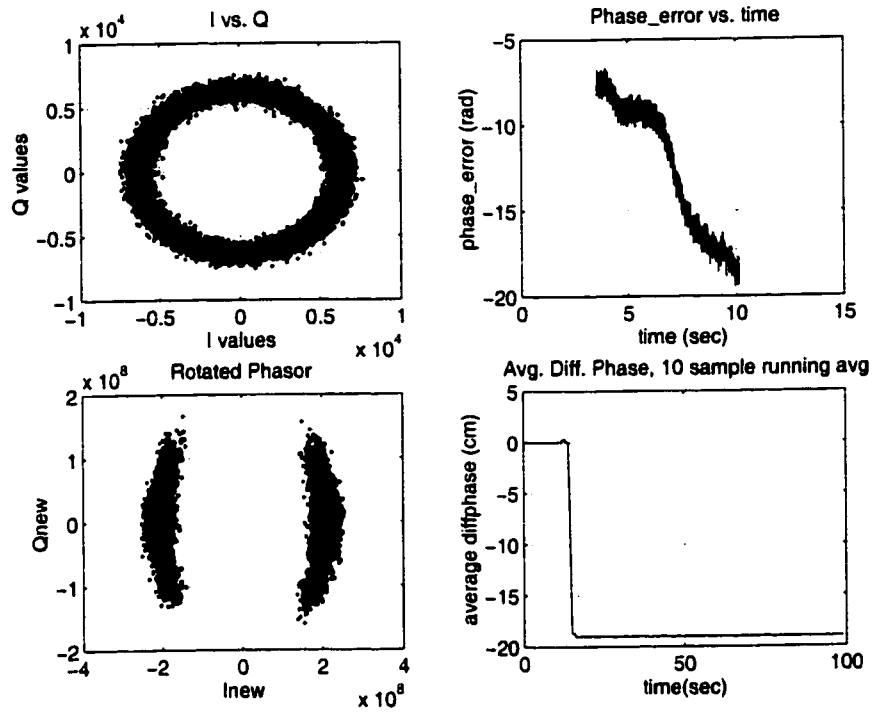

Figure A.2: Zero baseline, single receiver card, FLL tracking loop in-phase (I) and quadrature phase (Q) correlation components, and differential phase.

on the phase difference between the incoming and replica signals. In practice, the frequency error is never exactly zero, so the correlation phasor continually rotates in the I and Q plane. This is demonstrated in the tracking loop test results in Figure A.2, for a static zero-baseline case. There are four subplots of these test results. The plot on the upper left is the inphase and quadrature carrier signal correlation values, I and Q, plotted against each other to show the rotation of the correlation phasor of the incoming and replica carrier signals. The upper right plot shows the phase error of the replica versus the incoming carrier signal. The lower left plot is the new, coherent inphase and quadrature correlation values, Inew and Qnew, determined by compensating I and Q for the phase error value. And finally, the bottom right plot is

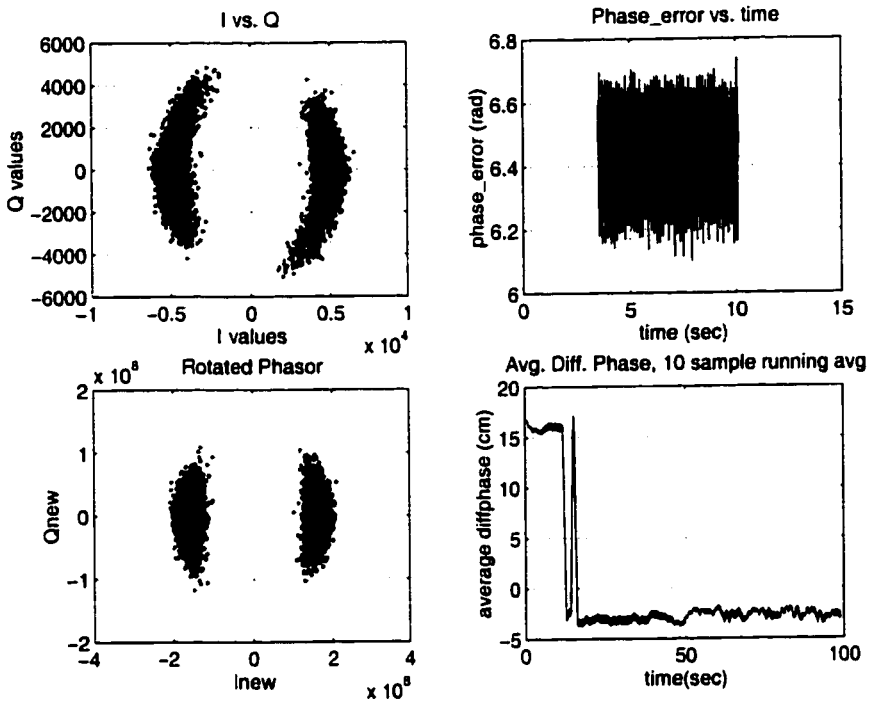

Figure A.3: Zero baseline, single receiver card, combined FLL/PLL tracking loop in-phase (I) and quadrature phase (Q) correlation components, and differential phase.

of the DCP measurement. Now that the I and Q values are controlled such that the phasor is not continually rotating, coherent carrier phase measurements are possible.

For a PLL, the I and Q values are used in a phase discriminator, and the phase error between the incoming and replica signals is driven to zero. In this case, the Q value should be driven to zero, and the I value should be driven to a large number that depends on the sample period of the accumulator and signal to noise ratio. This behavior of the correlation values in the PLL is evident in the test results presented in Figure A.3. The Q value can be seen to cluster near zero, while the I value jumps between positive and negative values. This change in sign for the I correlation value is due to the 50 baud data message modulated on top of the carrier signal. Since it is not desirable to treat a databit transition as a change in carrier phase, the PLL

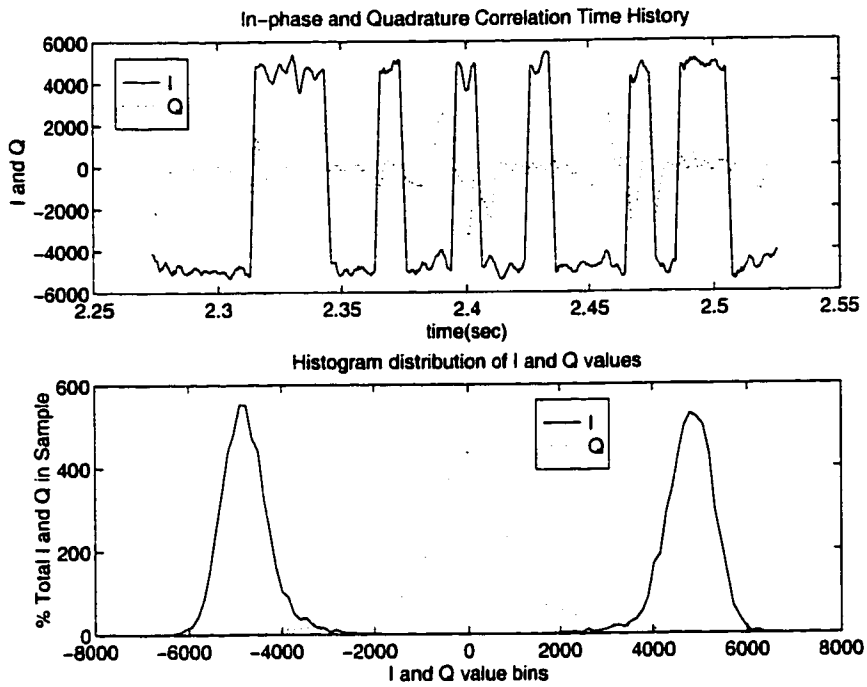

Figure A.4: Time history and histogram of I and Q correlation values for new coherent PLL tracking loop.

detects the data bit flip and tracks the phase of the carrier in alternating 180° shifts.

The time history of the I and Q correlation values from a locked PLL are shown in Figure A.4. This was the desired performance that the modified tracking loop was aiming for, with the replica carrier signal tracking the incoming carrier signal with the data bit flips. The histogram of I and Q values shown in the plot indicates that the phasor is hovering near the phase lock condition. These static tests have demonstrated that a coherent phase measurement is possible after making modifications to the channel tracking loop software.

A.2 ORION Receiver Timing Tests

A.2.1 Receiver Synchronization

The ORION receiver design is based on separate, 2 antenna input, 12 correlator channel GPS receiver cards synchronized to a common, external, 10 MHz clock source (as shown in the diagram in Figure 5.18). In this section, the results of tests of the synchronization of two GPS receiver cards on the overall DCP measurement performance are presented. These tests are a follow on to initial work done using the Mitel Plessey GPS Builder 2 receiver design. Using the Builder 2 cards, differential carrier phase measurements were successfully collected between two receivers by synchronizing the 10 MHz oscillator between the cards, as part of the 'GPS-on-a-Chip' (GPSOAC) receiver algorithm development effort. The goal of having a modular, expandable hardware architecture lead us to attempt to use the onboard oscillator on one Builder 2 card to drive the external clock input on three other cards, thus synchronizing all four cards. It was found that insufficient isolation of the onboard oscillator lead to unstable performance and loss of lock when more than two cards were linked in this manner. To remedy this, an external clock circuit with high bandwidth isolation was designed to drive all four cards from their external inputs. However, initial versions of this external clock circuit fabricated using perf board and wirewrap did not perform well due to the limitations of using wirewrap connections at higher frequencies.

To synchronize multiple Mitel Plessey 'Orion' receiver cards, the same clock circuit design used with the Builder 2 cards was implemented, but this time using etched traces on a copper clad board to achieve the necessary high frequency performance. After tuning the oscillator circuit for stable operation, the clock generation circuit was transferred to a printed circuit board designed to provide communications and

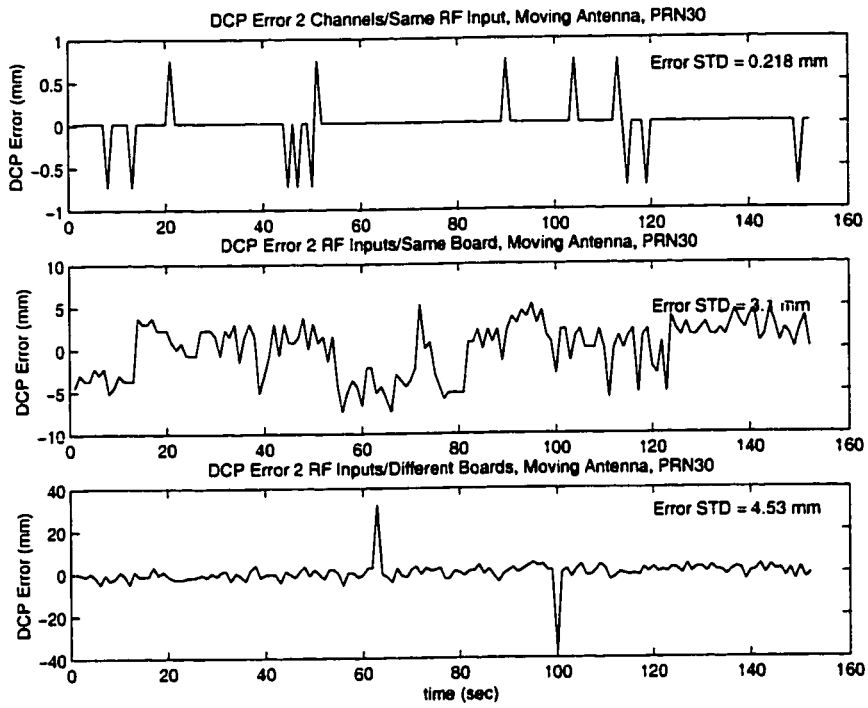

Figure A.5: Moving zero baseline DCP error test results for the ORION receiver. 3–4 mm DCP noise for after synchronization.

power conditioning to multiple receiver cards. A 2 card, 4 antenna input, 24 tracking channel version of this receiver was created, giving the capability of producing 3D attitude solutions. This receiver was suitable for use as the vehicle onboard receiver for the test of attitude determination algorithms using measurements from an array of non-aligned antennas.

A.2.2 Timing Test Results

A series of tests were conducted to determine the contribution to the differential carrier phase (DCP) measurement noise due to the synchronization method. The error in DCP measurement was measured for the zero antenna baseline case, with the receive antenna in motion. A splitter was used to route the antenna signal into all

four RF inputs on the receiver and integrated carrier phase was tracked for a period of roughly two minutes at a 1 Hz data rate, and the measurements were made using the array of indoor pseudolite transmitters in the far transmitter laboratory.

Test results for the stationary case showed that error in the DCP measurement between multiple boards synchronized at the 10 MHz clock level is very small (STD 2–3 mm), which are comparable error characteristics to single board receivers (such as the Trimble TANS Vector) . Previous issues concerning the stability of the synthesized 40 MHz sample clock on separate cards due to thermal gradients have proven not to be a problem, probably due to the constant thermal environment for all cards inside a single enclosure. The problem of having a phase bias contribution due to the length of the clock transfer line can be resolved using floating point bias resolution techniques, and is no different than resolving a non-integer line bias.

The results for the moving antenna case are shown in Figure A.5, and show 3–4 mm DCP noise. The bias in the DCP data has been removed to show only the error. The error is increased slightly by the presence of two cycle slips during the data collection period. These slips occurred when the antenna was moved quite rapidly from side to side, but the receiver cycle slip detection algorithm was able to detect and correct for the integer wavelength jump in the DCP data.

~

Appendix B

Linearized Measurement Matrix with RHCP

These are representative equations are for the linearized measurement matrix for a single baseline DCP measurement with the RHCP component included. The vehicle state is position, $\underline{P} = [p_x, p_y, p_z]^T$, and attitude, expressed as an attitude quaternion, $\underline{q} = [e_1, e_2, e_3, e_4]^T$. The transmitter position is $\underline{Q} = [q_x, q_y, q_z]^T$, and the antenna baseline vectors are $\underline{b}_1 = [b_{1x}, b_{1y}, b_{1z}]^T$ and $\underline{b}_2 = [b_{2x}, b_{2y}, b_{2z}]^T$. The rotation matrices from the receive antenna frames to the vehicle frame are R_{A1} and R_{A2}. These equations were generated and linearized using the Matlab/Maple symbolic math toolbox.

Temporary Variable Definition:

$$T(1) = (p_y - q_y)^2 + (p_z - q_z)^2 \tag{B.1}$$

$$T(2) = 2e_2e_3 + 2e_1e_4 \tag{B.2}$$

$$T(3) = 2e_1e_3 - 2e_2e_4 \tag{B.3}$$

$$T(4) = (2e_1e_3 - 2e_2e_4)R_{A2}(1,2) + (2e_2e_3 + 2e_1e_4)R_{A2}(2,2) +$$

$$(1-2e_1^2-2e_2^2)R_{A2}(3,2) \tag{B.4}$$

$$T(5) = 2e_2e_3-2e_1e_4 \tag{B.5}$$

$$T(6) = 2e_1e_2+2e_3e_4 \tag{B.6}$$

$$T(7) = (2e_1e_2+2e_3e_4)R_{A2}(1,2)+(1-2e_1^2-2e_3^2)R_{A2}(2,2)+ (2e_2e_3-2e_1e_4)R_{A2}(3,2) \tag{B.7}$$

$$T(8) = (p_x-q_x)^2+(p_y-q_y)^2+(p_z-q_z)^2 \tag{B.8}$$

$$T(9) = (2e_1e_3-2e_2e_4)R_{A2}(1,1)+(2e_2e_3+2e_1e_4)R_{A2}(2,1)+ (1-2e_1^2-2e_2^2)R_{A2}(3,1) \tag{B.9}$$

$$T(10) = (2e_1e_2+2e_3e_4)R_{A2}(1,1)+(1-2e_1^2-2e_3^2)R_{A2}(2,1)+ (2e_2e_3-2e_1e_4)R_{A2}(3,1) \tag{B.10}$$

$$T(11) = 2e_1e_3+2e_2e_4 \tag{B.11}$$

$$T(12) = 2e_1e_2-2e_3e_4 \tag{B.12}$$

$$T(13) = (1-2e_2^2-2e_3^2)R_{A2}(1,1)+(2e_1e_2-2e_3e_4)R_{A2}(2,1)+(2e_1e_3+ 2e_2e_4)R_{A2}(3,1) \tag{B.13}$$

$$\begin{aligned} T(14) = {} & ((1-2e_2^2-2e_3^2)R_{A2}(1,1)+(2e_1e_2-2e_3e_4)R_{A2}(2,1)+ \\ & (2e_1e_3+2e_2e_4)R_{A2}(3,1))((p_y-q_y)^2+(p_z-q_z)^2)^{\frac{1}{2}}/((p_x-q_x)^2+ \\ & (p_y-q_y)^2+(p_z-q_z)^2)^{\frac{1}{2}}+((2e_1e_2+2e_3e_4)R_{A2}(1,1)+ \\ & (1-2e_1^2-2e_3^2)R_{A2}(2,1)+(2e_2e_3-2e_1e_4)R_{A2}(3,1))(-p_x+ \\ & q_x)(p_y-q_y)/((p_x-q_x)^2+(p_y-q_y)^2+(p_z-q_z)^2)^{\frac{1}{2}}/((p_y- \\ & q_y)^2+(p_z-q_z)^2)^{\frac{1}{2}}+((2e_1e_3-2e_2e_4)R_{A2}(1,1)+(2e_2e_3+ \\ & 2e_1e_4)R_{A2}(2,1)+(1-2e_1^2-2e_2^2)R_{A2}(3,1))(-p_x+q_x)(p_z- \\ & q_z)/((p_x-q_x)^2+(p_y-q_y)^2+(p_z-q_z)^2)^{\frac{1}{2}}/((p_y-q_y)^2+ \\ & (p_z-q_z)^2)^{\frac{1}{2}}-(((2e_1e_2+2e_3e_4)R_{A2}(1,2)+(1-2e_1^2- \\ & 2e_3^2)R_{A2}(2,2)+(2e_2e_3-2e_1e_4)R_{A2}(3,2))(p_z-q_z)/((p_y- \\ & q_y)^2+(p_z-q_z)^2)^{\frac{1}{2}}+((2e_1e_3-2e_2e_4)R_{A2}(1,2)+(2e_2e_3+ \\ & 2e_1e_4)R_{A2}(2,2)+(1-2e_1^2-2e_2^2)R_{A2}(3,2))(-p_y+q_y)/((p_y- \\ & q_y)^2+(p_z-q_z)^2)^{\frac{1}{2}})\mathrm{e} \end{aligned} \tag{B.14}$$

$$T(15) = (1-2e_2^2-2e_3^2)R_{A2}(1,2)+(2e_1e_2-2e_3e_4)R_{A2}(2,2)+ (2e_1e_3+2e_2e_4)R_{A2}(3,2) \tag{B.15}$$

$$\begin{aligned} T(16) = {} & (((2e_1e_2+2e_3e_4)R_{A2}(1,1)+(1-2e_1^2-2e_3^2)R_{A2}(2,1)+ \\ & (2e_2e_3-2e_1e_4)R_{A2}(3,1))(p_z-q_z)/((p_y-q_y)^2+ \\ & (p_z-q_z)^2)^{\frac{1}{2}}+((2e_1e_3-2e_2e_4)R_{A2}(1,1)+(2e_2e_3+ \\ & 2e_1e_4)R_{A2}(2,1)+(1-2e_1^2-2e_2^2)R_{A2}(3,1))(-p_y+ \\ & q_y)/((p_y-q_y)^2+(p_z-q_z)^2)^{\frac{1}{2}})\mathrm{e}+((1-2\mathrm{e}_2^2- \\ & 2e_3^2)R_{A2}(1,2)+(2e_1e_2-2e_3e_4)R_{A2}(2,2)+(2e_1e_3+ \\ & 2e_2e_4)R_{A2}(3,2))((p_y-q_y)^2+(p_z-q_z)^2)^{\frac{1}{2}}/((p_x- \\ & q_x)^2+(p_y-q_y)^2+(p_z-q_z)^2)^{\frac{1}{2}}+((2e_1e_2+ \\ & 2e_3e_4)R_{A2}(1,2)+(1-2e_1^2-2e_3^2)R_{A2}(2,2)+(2e_2e_3- \\ & 2e_1e_4)R_{A2}(3,2))(-p_x+q_x)(p_y-q_y)/((p_x-q_x)^2+ \\ & (p_y-q_y)^2+(p_z-q_z)^2)^{\frac{1}{2}}/((p_y-q_y)^2+(p_z-q_z)^2)^{\frac{1}{2}}+ \\ & ((2e_1e_3-2e_2e_4)R_{A2}(1,2)+(2e_2e_3+2e_1e_4)R_{A2}(2,2)+ \\ & (1-2e_1^2-2e_2^2)R_{A2}(3,2))(-p_x+q_x)(p_z-q_z)/((p_x- \\ & q_x)^2+(p_y-q_y)^2+(p_z-q_z)^2)^{\frac{1}{2}}/((p_y-q_y)^2+(p_z- \\ & q_z)^2)^{\frac{1}{2}} \end{aligned} \tag{B.16}$$

$$T(17) = (1-2e_2^2-2e_3^2)b_{2x} \tag{B.17}$$

$$T(18) = (1-2e_1^2-2e_2^2)b_{2z} \tag{B.18}$$

$$T(19) = p_z+(2e_1e_3-2e_2e_4)b_{2x}+(2e_2e_3+2e_1e_4)b_{2y}+ (1-2e_1^2-2e_2^2)b_{2z}-q_z \tag{B.19}$$

$$T(20) = (1-2e_1^2-2e_3^2)b_{2y} \tag{B.20}$$

$$T(21) = p_y+(2e_1e_2+2e_3e_4)b_{2x}+(1-2e_1^2-2e_3^2)b_{2y}+ (2e_2e_3-2e_1e_4)b_{2z}-q_y \tag{B.21}$$

$$T(22) = p_x+(1-2e_2^2-2e_3^2)b_{2x}+(2e_1e_2-2e_3e_4)b_{2y}+ (2e_1e_3+2e_2e_4)b_{2z}-q_x \tag{B.22}$$

$$T(23) = (2e_1e_3-2e_2e_4)R_{A1}(1,2)+(2e_2e_3+2e_1e_4)R_{A1}(2,2)+ (1-2e_1^2-2e_2^2)R_{A1}(3,2) \tag{B.23}$$

$$T(24) = (2e_1e_2 + 2e_3e_4)R_{A1}(1,2) + (1 - 2e_1^2 - 2e_3^2)R_{A1}(2,2) + (2e_2e_3 - 2e_1e_4)R_{A1}(3,2) \tag{B.24}$$

$$T(25) = (2e_1e_3 - 2e_2e_4)R_{A1}(1,1) + (2e_2e_3 + 2e_1e_4)R_{A1}(2,1) + (1 - 2e_1^2 - 2e_2^2)R_{A1}(3,1) \tag{B.25}$$

$$T(26) = (2e_1e_2 + 2e_3e_4)R_{A1}(1,1) + (1 - 2e_1^2 - 2e_3^2)R_{A1}(2,1) + (2e_2e_3 - 2e_1e_4)R_{A1}(3,1) \tag{B.26}$$

$$T(27) = (1 - 2e_2^2 - 2e_3^2)R_{A1}(1,1) + (2e_1e_2 - 2e_3e_4)R_{A1}(2,1) + (2e_1e_3 + 2e_2e_4)R_{A1}(3,1) \tag{B.27}$$

$$\begin{aligned} T(28) = {} & ((1 - 2e_2^2 - 2e_3^2)R_{A1}(1,1) + (2e_1e_2 - 2e_3e_4)R_{A1}(2,1) + \\ & (2e_1e_3 + 2e_2e_4)R_{A1}(3,1))((p_y - q_y)^2 + (p_z - \\ & q_z)^2)^{\frac{1}{2}}/((p_x - q_x)^2 + (p_y - q_y)^2 + (p_z - q_z)^2)^{\frac{1}{2}} + \\ & ((2e_1e_2 + 2e_3e_4)R_{A1}(1,1) + (1 - 2e_1^2 - 2e_3^2)R_{A1}(2,1) + \\ & (2e_2e_3 - 2e_1e_4)R_{A1}(3,1))(-p_x + q_x)(p_y - q_y)/((p_x - \\ & q_x)^2 + (p_y - q_y)^2 + (p_z - q_z)^2)^{\frac{1}{2}}/((p_y - q_y)^2 + \\ & (p_z - q_z)^2)^{\frac{1}{2}} + ((2e_1e_3 - 2e_2e_4)R_{A1}(1,1) + \\ & (2e_2e_3 + 2e_1e_4)R_{A1}(2,1) + (1 - 2e_1^2 - 2e_2^2)R_{A1}(3,1))(-p_x + \\ & q_x)(p_z - q_z)/((p_x - q_x)^2 + (p_y - q_y)^2 + (p_z - \\ & q_z)^2)^{\frac{1}{2}}/((p_y - q_y)^2 + (p_z - q_z)^2)^{\frac{1}{2}} - (((2e_1e_2 + \\ & 2e_3e_4)R_{A1}(1,2) + (1 - 2e_1^2 - 2e_3^2)R_{A1}(2,2) + (2e_2e_3 - \\ & 2e_1e_4)R_{A1}(3,2))(p_z - q_z)/((p_y - q_y)^2 + (p_z - \\ & q_z)^2)^{\frac{1}{2}} + ((2e_1e_3 - 2e_2e_4)R_{A1}(1,2) + (2e_2e_3 + \\ & 2e_1e_4)R_{A1}(2,2) + (1 - 2e_1^2 - 2e_2^2)R_{A1}(3,2))(-p_y + \\ & q_y)/((p_y - q_y)^2 + (p_z - q_z)^2)^{\frac{1}{2}})\mathrm{e} \end{aligned} \tag{B.28}$$

$$T(29) = (1 - 2e_2^2 - 2e_3^2)R_{A1}(1,2) + (2e_1e_2 - 2e_3e_4)R_{A1}(2,2) + (2e_1e_3 + 2e_2e_4)R_{A1}(3,2) \tag{B.29}$$

$$\begin{aligned} T(30) = {} & (((2e_1e_2 + 2e_3e_4)R_{A1}(1,1) + (1 - 2e_1^2 - 2e_3^2)R_{A1}(2,1) + \\ & (2e_2e_3 - 2e_1e_4)R_{A1}(3,1))(p_z - q_z)/((p_y - q_y)^2 + \\ & (p_z - q_z)^2)^{\frac{1}{2}} + ((2e_1e_3 - 2e_2e_4)R_{A1}(1,1) + (2e_2e_3 + \end{aligned}$$

$$
\begin{aligned}
& 2e_1e_4)R_{A1}(2,1) + (1 - 2e_1^2 - 2e_2^2)R_{A1}(3,1))(-p_y + \\
& q_y)/((p_y - q_y)^2 + (p_z - q_z)^2)^{\frac{1}{2}})\mathrm{e} + ((1 - 2\mathrm{e}_2^2 - \\
& 2e_3^2)R_{A1}(1,2) + (2e_1e_2 - 2e_3e_4)R_{A1}(2,2) + (2e_1e_3 + \\
& 2e_2e_4)R_{A1}(3,2))((p_y - q_y)^2 + (p_z - q_z)^2)^{\frac{1}{2}}/((p_x - \\
& q_x)^2 + (p_y - q_y)^2 + (p_z - q_z)^2)^{\frac{1}{2}} + ((2e_1e_2 + \\
& 2e_3e_4)R_{A1}(1,2) + (1 - 2e_1^2 - 2e_3^2)R_{A1}(2,2) + (2e_2e_3 - \\
& 2e_1e_4)R_{A1}(3,2))(-p_x + q_x)(p_y - q_y)/((p_x - q_x)^2 + \\
& (p_y - q_y)^2 + (p_z - q_z)^2)^{\frac{1}{2}}/((p_y - q_y)^2 + (p_z - \\
& q_z)^2)^{\frac{1}{2}} + ((2e_1e_3 - 2e_2e_4)R_{A1}(1,2) + (2e_2e_3 + \\
& 2e_1e_4)R_{A1}(2,2) + (1 - 2e_1^2 - 2e_2^2)R_{A1}(3,2))(-p_x + \\
& q_x)(p_z - q_z)/((p_x - q_x)^2 + (p_y - q_y)^2 + (p_z - \\
& q_z)^2)^{\frac{1}{2}}/((p_y - q_y)^2 + (p_z - q_z)^2)^{\frac{1}{2}} \qquad \text{(B.30)}
\end{aligned}
$$

$$T(31) = (1 - 2e_2^2 - 2e_3^2)b_{1x} \qquad \text{(B.31)}$$

$$T(32) = (1 - 2e_1^2 - 2e_2^2)b_{1z} \qquad \text{(B.32)}$$

$$
\begin{aligned}
T(33) = {} & p_z + (2e_1e_3 - 2e_2e_4)b_{1x} + (2e_2e_3 + 2e_1e_4)b_{1y} + \\
& (1 - 2e_1^2 - 2e_2^2)b_{1z} - q_z \qquad \text{(B.33)}
\end{aligned}
$$

$$T(34) = (1 - 2e_1^2 - 2e_3^2)b_{1y} \qquad \text{(B.34)}$$

$$
\begin{aligned}
T(35) = {} & p_y + (2e_1e_2 + 2e_3e_4)b_{1x} + (1 - 2e_1^2 - 2e_3^2)b_{1y} + \\
& (2e_2e_3 - 2e_1e_4)b_{1z} - q_y \qquad \text{(B.35)}
\end{aligned}
$$

$$
\begin{aligned}
T(36) = {} & p_x + (1 - 2e_2^2 - 2e_3^2)b_{1x} + (2e_1e_2 - 2e_3e_4)b_{1y} + \\
& (2e_1e_3 + 2e_2e_4)b_{1z} - q_x \qquad \text{(B.36)}
\end{aligned}
$$

Linearized Measurement Matrix, Row Definition:

$$
\begin{aligned}
H_{RHCProw}(1,1) = {} & \frac{1}{2}/(T(36))^2 + T(35))^2 + T(33))^2)^{\frac{1}{2}}/\lambda_{L1}(2p_x + \\
& (2(T(31)) + 2T(12)b_{1y} + 2T(11)b_{1z} - 2q_x) + \frac{1}{2}((-\frac{1}{2}T(29) \\
& (T(1)^{\frac{1}{2}}/T(8)^{\frac{3}{2}}(2p_x - 2q_x) - T(24)(p_y - q_y)/ \\
& (T(8)^{\frac{1}{2}}/T(1)^{\frac{1}{2}} - \frac{1}{2}T(24)(-p_x + q_x)(p_y - q_y)/
\end{aligned}
$$

$$
\begin{aligned}
& (T(8)^{\frac{3}{2}}/T(1)^{\frac{1}{2}}(2p_x - 2q_x) - T(23)(p_z - q_z)/ \\
& (T(8)))^{\frac{1}{2}}/T(1)^{\frac{1}{2}} - \frac{1}{2}T(23)(-p_x + q_x)(p_z - q_z)/ \\
& (T(8)^{\frac{3}{2}}/T(1)^{\frac{1}{2}}(2p_x - 2q_x))/T(28) - T(30)/ \\
& (T(28)^2(-\frac{1}{2}T(27)T(1)^{\frac{1}{2}}/T(8)^{\frac{3}{2}}(2p_x - 2q_x) - \\
& (T(26)(p_y - q_y)/T(8)^{\frac{1}{2}}/T(1)^{\frac{1}{2}} - \frac{1}{2}T(26) \\
& ((-p_x + q_x)(p_y - q_y)/T(8)^{\frac{3}{2}}/T(1)^{\frac{1}{2}}(2p_x - 2q_x) - \\
& (T(25)(p_z - q_z)/T(8)^{\frac{1}{2}}/T(1)^{\frac{1}{2}} - \frac{1}{2}T(25)(-p_x + \\
& (q_x)(p_z - q_z)/T(8)^{\frac{3}{2}}/T(1)^{\frac{1}{2}}(2p_x - 2q_x)))/(1 + \\
& (T(30)^2/T(28)^2)/\pi\frac{1}{2}/(T(22)^2 + T(21)^2 + T(19)^2)^{\frac{1}{2}}/ \\
& (\lambda_{L1}(2p_x + 2(T(17)) + 2T(12)b_{2y} + 2T(11)b_{2z} - 2q_x) - \\
& (\frac{1}{2}((-\frac{1}{2}T(15)T(1)^{\frac{1}{2}}/T(8)^{\frac{3}{2}}(2p_x - 2q_x) - T(7) \\
& ((p_y - q_y)/T(8)^{\frac{1}{2}}/T(1)^{\frac{1}{2}} - \frac{1}{2}T(7)(-p_x + q_x) \\
& ((p_y - q_y)/T(8)^{\frac{3}{2}}/T(1)^{\frac{1}{2}}(2p_x - 2q_x) - T(4) \\
& ((p_z - q_z)/T(8)^{\frac{1}{2}}/T(1)^{\frac{1}{2}} - \frac{1}{2}T(4)(-p_x + q_x)(p_z - \\
& (q_z)/T(8)^{\frac{3}{2}}/T(1)^{\frac{1}{2}}(2p_x - 2q_x))/T(14) - T(16)/ \\
& (T(14)^2(-\frac{1}{2}T(13)T(1)^{\frac{1}{2}}/T(8)^{\frac{3}{2}}(2p_x - 2q_x) - \\
& (T(10)(p_y - q_y)/T(8)^{\frac{1}{2}}/T(1)^{\frac{1}{2}} - \frac{1}{2}T(10)(-p_x + \\
& (q_x)(p_y - q_y)/T(8)^{\frac{3}{2}}/T(1)^{\frac{1}{2}}(2p_x - 2q_x) - T(9) \\
& ((p_z - q_z)/T(8)^{\frac{1}{2}}/T(1)^{\frac{1}{2}} - \frac{1}{2}T(9)(-p_x + q_x)(p_z - \\
& (q_z)/T(8)^{\frac{3}{2}}/T(1)^{\frac{1}{2}}(2p_x - 2q_x)))/(1 + T(16)^2/ \\
& (T(14)^2)/\pi
\end{aligned}
\tag{B.37}
$$

$$
\begin{aligned}
H_{RHCProw}(1,2) \;=\; & \frac{1}{2}/(T(36))^2 + T(35))^2 + T(33))^2)^{\frac{1}{2}}/\lambda_{L1}(2p_y + \\
& 2T(6)b_{1x} + 2(T(34)) + 2T(5)b_{1z} - 2q_y) + \frac{1}{2}(((-\frac{1}{2}T(26)(p_z - \\
& q_z)/T(1)^{\frac{3}{2}}(2p_y - 2q_y) - T(25)/T(1)^{\frac{1}{2}} - \\
& \frac{1}{2}T(25)(-p_y + q_y)/T(1)^{\frac{3}{2}}(2p_y - 2q_y))\mathrm{e} + \frac{1}{2}\mathrm{T}(29)/ \\
& T(1)^{\frac{1}{2}}/T(8)^{\frac{1}{2}}(2p_y - 2q_y)\frac{1}{2}T(29)T(1)^{\frac{1}{2}}/ \\
& T(8)^{\frac{3}{2}}(2p_y - 2q_y) + T(24)(-p_x + q_x)/T(8)^{\frac{1}{2}}/ \\
& T(1)^{\frac{1}{2}} - \frac{1}{2}T(24)(-p_x + q_x)(p_y - q_y)/T(8)^{\frac{3}{2}}/ \\
& T(1)^{\frac{1}{2}}(2p_y - 2q_y) - \frac{1}{2}T(24)(-p_x + q_x)(p_y - \\
& q_y)/T(8)^{\frac{1}{2}}/T(1)^{\frac{3}{2}}(2p_y - 2q_y) - \frac{1}{2}T(23)
\end{aligned}
$$

$(-p_x + q_x)(p_z - q_z)/T(8)^{\frac{3}{2}}/T(1)^{\frac{1}{2}}(2p_y - 2q_y) -$
$\frac{1}{2}T(23)(-p_x + q_x)(p_z - q_z)/T(8)^{\frac{1}{2}}/T(1)^{\frac{3}{2}}(2p_y -$
$2q_y))/T(28) - T(30)/T(28)^2(\frac{1}{2}T(27)/T(1)^{\frac{1}{2}}/T(8)^{\frac{1}{2}}(2p_y -$
$2q_y) - \frac{1}{2}T(27)T(1)^{\frac{1}{2}}/T(8)^{\frac{3}{2}}(2p_y - 2q_y) +$
$T(26)(-p_x + q_x)/T(8)^{\frac{1}{2}}/T(1)^{\frac{1}{2}} - \frac{1}{2}T(26)(-p_x + q_x)$
$(p_y - q_y)/T(8)^{\frac{3}{2}}/T(1)^{\frac{1}{2}}(2p_y - 2q_y) - \frac{1}{2}T(26)$
$(-p_x + q_x)(p_y - q_y)/T(8)^{\frac{1}{2}}/T(1)^{\frac{3}{2}}(2p_y - 2q_y) -$
$\frac{1}{2}T(25)(-p_x + q_x)(p_z - q_z)/T(8)^{\frac{3}{2}}/T(1)^{\frac{1}{2}}$
$(2p_y - 2q_y) - \frac{1}{2}T(25)(-p_x + q_x)(p_z - q_z)/T(8)^{\frac{1}{2}}/$
$T(1)^{\frac{3}{2}}(2p_y - 2q_y) - (-\frac{1}{2}T(24)(p_z - q_z)/T(1)^{\frac{3}{2}}$
$(2p_y - 2q_y) - T(23)/T(1)^{\frac{1}{2}} - \frac{1}{2}T(23)(-p_y + q_y)/T(1)^{\frac{3}{2}}$
$(2p_y - 2q_y))\mathrm{e}))/(1 + \mathrm{T}(30)^2/\mathrm{T}(28)^2)/\pi - \frac{1}{2}/(\mathrm{T}(22)^2 + \mathrm{T}(21)^2 +$
$T(19)^2)^{\frac{1}{2}}/\lambda_{L1}(2p_y + 2T(6)b_{2x} + 2(T(20)) + 2T(5)b_{2z} - 2q_y) -$
$\frac{1}{2}(((-\frac{1}{2}T(10)(p_z - q_z)/T(1)^{\frac{3}{2}}(2p_y - 2q_y) - T(9)/$
$T(1)^{\frac{1}{2}} - \frac{1}{2}T(9)(-p_y + q_y)/T(1)^{\frac{3}{2}}(2p_y - 2q_y))\mathrm{e} +$
$\frac{1}{2}T(15)/T(1)^{\frac{1}{2}}/T(8)^{\frac{1}{2}}(2p_y - 2q_y) - \frac{1}{2}T(15)$
$T(1)^{\frac{1}{2}}/T(8)^{\frac{3}{2}}(2p_y - 2q_y) + T(7)(-p_x + q_x)/T(8)^{\frac{1}{2}}/$
$T(1)^{\frac{1}{2}} - \frac{1}{2}T(7)(-p_x + q_x)(p_y - q_y)/T(8)^{\frac{3}{2}}/$
$T(1)^{\frac{1}{2}}(2p_y - 2q_y) - \frac{1}{2}T(7)(-p_x + q_x)(p_y - q_y)/$
$T(8)^{\frac{1}{2}}/T(1)^{\frac{3}{2}}(2p_y - 2q_y) - \frac{1}{2}T(4)(-p_x +$
$q_x)(p_z - q_z)/T(8)^{\frac{3}{2}}/T(1)^{\frac{1}{2}}(2p_y - 2q_y) -$
$\frac{1}{2}T(4)(-p_x + q_x)(p_z - q_z)/T(8)^{\frac{1}{2}}/T(1)^{\frac{3}{2}}$
$(2p_y - 2q_y))/T(14) - T(16)/T(14)^2(\frac{1}{2}T(13)/T(1)^{\frac{1}{2}}/$
$T(8)^{\frac{1}{2}}(2p_y - 2q_y) - \frac{1}{2}T(13)T(1)^{\frac{1}{2}}/$
$T(8)^{\frac{3}{2}}(2p_y - 2q_y) + T(10)(-p_x + q_x)/T(8)^{\frac{1}{2}}/T(1)^{\frac{1}{2}} -$
$\frac{1}{2}T(10)(-p_x + q_x)(p_y - q_y)/T(8)^{\frac{3}{2}}/T(1)^{\frac{1}{2}}$
$(2p_y - 2q_y) - \frac{1}{2}T(10)(-p_x + q_x)(p_y - q_y)/T(8)^{\frac{1}{2}}/$
$T(1)^{\frac{3}{2}}(2p_y - 2q_y) - \frac{1}{2}T(9)(-p_x + q_x)(p_z - q_z)/$
$T(8)^{\frac{3}{2}}/T(1)^{\frac{1}{2}}(2p_y - 2q_y) - \frac{1}{2}T(9)(-p_x +$

$$
\begin{aligned}
& q_x)(p_z - q_z)/T(8)^{\frac{1}{2}}/T(1)^{\frac{3}{2}}(2p_y - 2q_y) - (-\frac{1}{2}T(7) \\
& (p_z - q_z)/T(1)^{\frac{3}{2}}(2p_y - 2q_y) - T(4)/T(1)^{\frac{1}{2}} - \frac{1}{2}T(4) \\
& (-p_y + q_y)/T(1)^{\frac{3}{2}}(2p_y - 2q_y))\mathrm{e}))/(1 + \mathrm{T}(16)^2/\mathrm{T}(14)^2)/\pi \qquad \text{(B.38)}
\end{aligned}
$$

$$
\begin{aligned}
H_{RHCProw}(1,3) \;=\; & \frac{1}{2}/(T(36))^2 + T(35))^2 + T(33))^2)^{\frac{1}{2}}/\lambda_{L1}(2p_z + \\
& 2T(3)b_{1x} + 2T(2)b_{1y} + 2(T(32)) - 2q_z) + \frac{1}{2}(((T(26)/T(1)^{\frac{1}{2}} - \\
& \frac{1}{2}T(26)(p_z - q_z)/T(1)^{\frac{3}{2}}(2p_z - 2q_z) - \frac{1}{2}T(25) \\
& (-p_y + q_y)/T(1)^{\frac{3}{2}}(2p_z - 2q_z))\mathrm{e} + \frac{1}{2}\mathrm{T}(29)/ \\
& T(1)^{\frac{1}{2}}/T(8)^{\frac{1}{2}}(2p_z - 2q_z)\frac{1}{2}T(29)T(1)^{\frac{1}{2}}/ \\
& T(8)^{\frac{3}{2}}(2p_z - 2q_z) - \frac{1}{2}T(24)(-p_x + q_x)(p_y - q_y)/ \\
& T(8)^{\frac{3}{2}}/T(1)^{\frac{1}{2}}(2p_z - 2q_z) - \frac{1}{2}T(24)(-p_x + q_x) \\
& (p_y - q_y)/T(8)^{\frac{1}{2}}/T(1)^{\frac{3}{2}}(2p_z - 2q_z) + T(23)(-p_x + \\
& q_x)/T(8)^{\frac{1}{2}}/T(1)^{\frac{1}{2}} - \frac{1}{2}T(23)(-p_x + q_x)(p_z - \\
& q_z)/T(8)^{\frac{3}{2}}/T(1)^{\frac{1}{2}}(2p_z - 2q_z) - \frac{1}{2}T(23)(-p_x + \\
& q_x)(p_z - q_z)/T(8)^{\frac{1}{2}}/T(1)^{\frac{3}{2}}(2p_z - 2q_z))/T(28) - T(30)/T(28)^2 \\
& (\frac{1}{2}T(27)/T(1)^{\frac{1}{2}}/T(8)^{\frac{1}{2}}(2p_z - 2q_z) - \frac{1}{2}T(27) \\
& T(1)^{\frac{1}{2}}/T(8)^{\frac{3}{2}}(2p_z - 2q_z) - \frac{1}{2}T(26)(-p_x + q_x) \\
& (p_y - q_y)/T(8)^{\frac{3}{2}}/T(1)^{\frac{1}{2}}(2p_z - 2q_z) - \frac{1}{2}T(26) \\
& (-p_x + q_x)(p_y - q_y)/T(8)^{\frac{1}{2}}/T(1)^{\frac{3}{2}}(2p_z - 2q_z) + \\
& T(25)(-p_x + q_x)/T(8)^{\frac{1}{2}}/T(1)^{\frac{1}{2}} - \frac{1}{2}T(25)(-p_x + q_x) \\
& (p_z - q_z)/T(8)^{\frac{3}{2}}/T(1)^{\frac{1}{2}}(2p_z - 2q_z) - \frac{1}{2}T(25)(-p_x + \\
& q_x)(p_z - q_z)/T(8)^{\frac{1}{2}}/T(1)^{\frac{3}{2}}(2p_z - 2q_z) - (T(24)/ \\
& T(1)^{\frac{1}{2}} - \frac{1}{2}T(24)(p_z - q_z)/T(1)^{\frac{3}{2}}(2p_z - 2q_z) - \\
& \frac{1}{2}T(23)(-p_y + q_y)/T(1)^{\frac{3}{2}}(2p_z - 2q_z))\mathrm{e}))/(1 + \mathrm{T}(30)^2/ \\
& T(28)^2)/\pi - \frac{1}{2}/(T(22)^2 + T(21)^2 + T(19)^2)^{\frac{1}{2}}/\lambda_{L1}(2p_z + \\
& 2T(3)b_{2x} + 2T(2)b_{2y} + 2(T(18)) - 2q_z) - \frac{1}{2}(((T(10)/T(1)^{\frac{1}{2}} - \\
& \frac{1}{2}T(10)(p_z - q_z)/T(1)^{\frac{3}{2}}(2p_z - 2q_z) - \frac{1}{2}T(9)(-p_y + \\
& q_y)/T(1)^{\frac{3}{2}}(2p_z - 2q_z))\mathrm{e} + \frac{1}{2}\mathrm{T}(15)/\mathrm{T}(1)^{\frac{1}{2}}/ \\
& T(8)^{\frac{1}{2}}(2p_z - 2q_z) - \frac{1}{2}T(15)T(1)^{\frac{1}{2}}/T(8)^{\frac{3}{2}}
\end{aligned}
$$

$$
\begin{aligned}
& (2p_z - 2q_z) - \frac{1}{2}T(7)(-p_x + q_x)(p_y - q_y)/T(8)^{\frac{3}{2}}/ \\
& T(1)^{\frac{1}{2}}(2p_z - 2q_z) - \frac{1}{2}T(7)(-p_x + q_x)(p_y - q_y)/ \\
& T(8)^{\frac{1}{2}}/T(1)^{\frac{3}{2}}(2p_z - 2q_z) + T(4)(-p_x + q_x)/T(8)^{\frac{1}{2}}/ \\
& T(1)^{\frac{1}{2}} - \frac{1}{2}T(4)(-p_x + q_x)(p_z - q_z)/T(8)^{\frac{3}{2}}/ \\
& T(1)^{\frac{1}{2}}(2p_z - 2q_z) - \frac{1}{2}T(4)(-p_x + q_x)(p_z - q_z)/ \\
& T(8)^{\frac{1}{2}}/T(1)^{\frac{3}{2}}(2p_z - 2q_z))/T(14) - T(16)/T(14)^2 \\
& (\frac{1}{2}T(13)/T(1)^{\frac{1}{2}}/T(8)^{\frac{1}{2}}(2p_z - 2q_z) - \frac{1}{2}T(13) \\
& T(1)^{\frac{1}{2}}/T(8)^{\frac{3}{2}}(2p_z - 2q_z) - \frac{1}{2}T(10)(-p_x + q_x)(p_y - \\
& q_y)/T(8)^{\frac{3}{2}}/T(1)^{\frac{1}{2}}(2p_z - 2q_z) - \frac{1}{2}T(10)(-p_x + q_x) \\
& (p_y - q_y)/T(8)^{\frac{1}{2}}/T(1)^{\frac{3}{2}}(2p_z - 2q_z) + T(9)(-p_x + q_x)/ \\
& T(8)^{\frac{1}{2}}/T(1)^{\frac{1}{2}} - \frac{1}{2}T(9)(-p_x + q_x)(p_z - q_z)/ \\
& T(8)^{\frac{3}{2}}/T(1)^{\frac{1}{2}}(2p_z - 2q_z) - \frac{1}{2}T(9)(-p_x + q_x)(p_z - \\
& q_z)/T(8)^{\frac{1}{2}}/T(1)^{\frac{3}{2}}(2p_z - 2q_z) - (T(7)/T(1)^{\frac{1}{2}} - \\
& \frac{1}{2}T(7)(p_z - q_z)/T(1)^{\frac{3}{2}}(2p_z - 2q_z) - \frac{1}{2}T(4)(-p_y + \\
& q_y)/T(1)^{\frac{3}{2}}(2p_z - 2q_z))\mathrm{e}))/(1 + \mathrm{T}(16)^2/\mathrm{T}(14)^2)/\pi
\end{aligned}
\tag{B.39}
$$

$$
\begin{aligned}
H_{RHCProw}(1,4) \;=\; & \frac{1}{2}/(T(36))^2 + T(35))^2 + T(33))^2)^{\frac{1}{2}}/\lambda_{L1}(2T(36)) \\
& (2e_2b_{1y} + 2e_3b_{1z}) + 2T(35))(2e_2b_{1x} - 4e_1b_{1y} - 2e_4b_{1z}) + \\
& 2T(33))(2e_3b_{1x} + 2e_4b_{1y} - 4e_1b_{1z})) + \frac{1}{2}((((2e_2R_{A1}(1,1) - \\
& 4e_1R_{A1}(2,1) - 2e_4R_{A1}(3,1))(p_z - q_z)/T(1)^{\frac{1}{2}} + (2e_3R_{A1}(1,1) \\
& + 2e_4R_{A1}(2,1) - 4e_1R_{A1}(3,1))(-p_y + q_y)/T(1)^{\frac{1}{2}})\mathrm{e} + (2\mathrm{e}_2 \\
& R_{A1}(2,2) + 2e_3R_{A1}(3,2))T(1)^{\frac{1}{2}}/T(8)^{\frac{1}{2}} + (2e_2R_{A1}(1,2) - 4e_1 \\
& R_{A1}(2,2) - 2e_4R_{A1}(3,2))(-p_x + q_x)(p_y - q_y)/T(8)^{\frac{1}{2}}/ \\
& T(1)^{\frac{1}{2}} + (2e_3R_{A1}(1,2) + 2e_4R_{A1}(2,2) - 4e_1R_{A1}(3,2))(-p_x + q_x) \\
& (p_z - q_z)/T(8)^{\frac{1}{2}}/T(1)^{\frac{1}{2}})/T(28) - T(30)/T(28)^2((2e_2R_{A1}(2,1) + \\
& 2e_3R_{A1}(3,1))T(1)^{\frac{1}{2}}/T(8)^{\frac{1}{2}} + (2e_2R_{A1}(1,1) - 4e_1R_{A1}(2,1) - \\
& 2e_4R_{A1}(3,1))(-p_x + q_x)(p_y - q_y)/T(8)^{\frac{1}{2}}/T(1)^{\frac{1}{2}} + \\
& (2e_3R_{A1}(1,1) + 2e_4R_{A1}(2,1) - 4e_1R_{A1}(3,1))(-p_x + q_x)(p_z - q_z)/ \\
& T(8)^{\frac{1}{2}}/T(1)^{\frac{1}{2}} - ((2e_2R_{A1}(1,2) - 4e_1R_{A1}(2,2) - \\
& 2e_4R_{A1}(3,2))(p_z - q_z)/T(1)^{\frac{1}{2}} + (2e_3R_{A1}(1,2) + 2e_4R_{A1}(2,2) - \\
& 4e_1R_{A1}(3,2))(-p_y + q_y)/T(1)^{\frac{1}{2}})\mathrm{e}))/(1 + \mathrm{T}(30)^2/\mathrm{T}(28)^2)/\pi -
\end{aligned}
$$

$$\frac{1}{2}/(T(22)^2 + T(21)^2 + T(19)^2)^{\frac{1}{2}}/\lambda_{L1}(2T(22)(2e_2b_{2y} + 2e_3b_{2z}) + 2T(21)(2e_2b_{2x} - 4e_1b_{2y} - 2e_4b_{2z}) + 2T(19)(2e_3b_{2x} + 2e_4b_{2y} - 4e_1b_{2z})) - \frac{1}{2}((((2e_2R_{A2}(1,1) - 4e_1R_{A2}(2,1) - 2e_4R_{A2}(3,1))(p_z - q_z)/T(1)^{\frac{1}{2}} + (2e_3R_{A2}(1,1) + 2e_4R_{A2}(2,1) - 4e_1R_{A2}(3,1))(-p_y + q_y)/T(1)^{\frac{1}{2}})\mathrm{e} + (2\mathrm{e}_2\mathrm{R}_{\mathrm{A2}}(2,2) + 2e_3R_{A2}(3,2))T(1)^{\frac{1}{2}}/T(8)^{\frac{1}{2}} + (2e_2R_{A2}(1,2) - 4e_1R_{A2}(2,2) - 2e_4R_{A2}(3,2))(-p_x + q_x)(p_y - q_y)/T(8)^{\frac{1}{2}}/T(1)^{\frac{1}{2}} + (2e_3R_{A2}(1,2) + 2e_4R_{A2}(2,2) - 4e_1R_{A2}(3,2))(-p_x + q_x)(p_z - q_z)/T(8)^{\frac{1}{2}}/T(1)^{\frac{1}{2}})/T(14) - T(16)/T(14)^2((2e_2R_{A2}(2,1) + 2e_3R_{A2}(3,1))T(1)^{\frac{1}{2}}/T(8)^{\frac{1}{2}} + (2e_2R_{A2}(1,1) - 4e_1R_{A2}(2,1) - 2e_4R_{A2}(3,1))(-p_x + q_x)(p_y - q_y)/T(8)^{\frac{1}{2}}/T(1)^{\frac{1}{2}} + (2e_3R_{A2}(1,1) + 2e_4R_{A2}(2,1) - 4e_1R_{A2}(3,1))(-p_x + q_x)(p_z - q_z)/T(8)^{\frac{1}{2}}/T(1)^{\frac{1}{2}} - ((2e_2R_{A2}(1,2) - 4e_1R_{A2}(2,2) - 2e_4R_{A2}(3,2))(p_z - q_z)/T(1)^{\frac{1}{2}} + (2e_3R_{A2}(1,2) + 2e_4R_{A2}(2,2) - 4e_1R_{A2}(3,2))(-p_y + q_y)/T(1)^{\frac{1}{2}})\mathrm{e}))/(1 + T(16)^2/T(14)^2)/\pi \tag{B.40}$$

$$H_{RHCProw}(1,5) = \frac{1}{2}/(T(36))^2 + T(35))^2 + T(33))^2)^{\frac{1}{2}}/\lambda_{L1}(2T(36))(-4e_2b_{1x} + 2e_1b_{1y} + 2e_4b_{1z}) + 2T(35))(2e_1b_{1x} + 2e_3b_{1z}) + 2T(33))(-2e_4b_{1x} + 2e_3b_{1y} - 4e_2b_{1z})) + \frac{1}{2}((((2e_1R_{A1}(1,1) + 2e_3R_{A1}(3,1))(p_z - q_z)/T(1)^{\frac{1}{2}} + (-2e_4R_{A1}(1,1) + 2e_3R_{A1}(2,1) - 4e_2R_{A1}(3,1))(-p_y + q_y)/T(1)^{\frac{1}{2}})\mathrm{e} + (-4\mathrm{e}_2\mathrm{R}_{\mathrm{A1}}(1,2) + 2\mathrm{e}_1\mathrm{R}_{\mathrm{A1}}(2,2) + 2\mathrm{e}_4 R_{A1}(3,2))T(1)^{\frac{1}{2}}/T(8)^{\frac{1}{2}} + (2e_1R_{A1}(1,2) + 2e_3R_{A1}(3,2))(-p_x + q_x)(p_y - q_y)/T(8)^{\frac{1}{2}}/T(1)^{\frac{1}{2}} + (-2e_4R_{A1}(1,2) + 2e_3R_{A1}(2,2) - 4e_2R_{A1}(3,2))(-p_x + q_x)(p_z - q_z)/T(8)^{\frac{1}{2}}/T(1)^{\frac{1}{2}})/T(28) - T(30)/T(28)^2((-4e_2R_{A1}(1,1) + 2e_1R_{A1}(2,1) + 2e_4R_{A1}(3,1))T(1)^{\frac{1}{2}}/T(8)^{\frac{1}{2}} + (2e_1R_{A1}(1,1) + 2e_3R_{A1}(3,1))(-p_x + q_x)(p_y - q_y)/T(8)^{\frac{1}{2}}/T(1)^{\frac{1}{2}} + (-2e_4R_{A1}(1,1) + 2e_3R_{A1}(2,1) - 4e_2R_{A1}(3,1))(-p_x + q_x)(p_z - q_z)/T(8)^{\frac{1}{2}}/T(1)^{\frac{1}{2}} - ((2e_1R_{A1}(1,2) + 2e_3R_{A1}(3,2))(p_z -$$

$$
\begin{aligned}
& q_z)/T(1)^{\frac{1}{2}} + (-2e_4R_{A1}(1,2) + 2e_3R_{A1}(2,2) - 4e_2R_{A1}(3,2)) \\
& (-p_y + q_y)/T(1)^{\frac{1}{2}})\mathrm{e}))/(1 + \mathrm{T}(30)^2/\mathrm{T}(28)^2)/\pi - \frac{1}{2}/(\mathrm{T}(22)^2 + \\
& T(21)^2 + T(19)^2)^{\frac{1}{2}}/\lambda_{L1}(2T(22)(-4e_2b_{2x} + 2e_1b_{2y} + 2e_4b_{2z}) + \\
& 2T(21)(2e_1b_{2x} + 2e_3b_{2z}) + 2T(19)(-2e_4b_{2x} + 2e_3b_{2y} - 4e_2b_{2z})) - \\
& \frac{1}{2}((((2e_1R_{A2}(1,1) + 2e_3R_{A2}(3,1))(p_z - q_z)/T(1)^{\frac{1}{2}} + \\
& (-2e_4R_{A2}(1,1) + 2e_3R_{A2}(2,1) - 4e_2R_{A2}(3,1))(-p_y + q_y)/ \\
& T(1)^{\frac{1}{2}})\mathrm{e} + (-4\mathrm{e}_2\mathrm{R}_{\mathrm{A2}}(1,2) + 2\mathrm{e}_1\mathrm{R}_{\mathrm{A2}}(2,2) + 2\mathrm{e}_4\mathrm{R}_{\mathrm{A2}}(3,2)) \\
& T(1)^{\frac{1}{2}}/T(8)^{\frac{1}{2}} + (2e_1R_{A2}(1,2) + 2e_3R_{A2}(3,2))(-p_x + \\
& q_x)(p_y - q_y)/T(8)^{\frac{1}{2}}/T(1)^{\frac{1}{2}} + (-2e_4R_{A2}(1,2) + \\
& 2e_3R_{A2}(2,2) - 4e_2R_{A2}(3,2))(-p_x + q_x)(p_z - q_z)/T(8)^{\frac{1}{2}}/ \\
& T(1)^{\frac{1}{2}})/T(14) - T(16)/T(14)^2((-4e_2R_{A2}(1,1) + 2e_1R_{A2}(2,1) + \\
& 2e_4R_{A2}(3,1))T(1)^{\frac{1}{2}}/T(8)^{\frac{1}{2}} + (2e_1R_{A2}(1,1) + \\
& 2e_3R_{A2}(3,1))(-p_x + q_x)(p_y - q_y)/T(8)^{\frac{1}{2}}/T(1)^{\frac{1}{2}} + \\
& (-2e_4R_{A2}(1,1) + 2e_3R_{A2}(2,1) - 4e_2R_{A2}(3,1))(-p_x + q_x)(p_z - q_z)/ \\
& T(8)^{\frac{1}{2}}/T(1)^{\frac{1}{2}} - ((2e_1R_{A2}(1,2) + 2e_3R_{A2}(3,2))(p_z - q_z)/ \\
& T(1)^{\frac{1}{2}} + (-2e_4R_{A2}(1,2) + 2e_3R_{A2}(2,2) - 4e_2R_{A2}(3,2)) \\
& (-p_y + q_y)/T(1)^{\frac{1}{2}})\mathrm{e}))/(1 + \mathrm{T}(16)^2/\mathrm{T}(14)^2)/\pi \qquad \text{(B.41)}
\end{aligned}
$$

$$
\begin{aligned}
H_{RHCProw}(1,6) \;=\; & \frac{1}{2}/(T(36))^2 + T(35))^2 + T(33))^2)^{\frac{1}{2}}/ \\
& \lambda_{L1}(2T(36))(-4e_3b_{1x} - 2e_4b_{1y} + 2e_1b_{1z}) + 2T(35)) \\
& (2e_4b_{1x} - 4e_3b_{1y} + 2e_2b_{1z}) + 2T(33))(2e_1b_{1x} + 2e_2b_{1y})) + \\
& \frac{1}{2}((((2e_4R_{A1}(1,1) - 4e_3R_{A1}(2,1) + 2e_2R_{A1}(3,1))(p_z - \\
& q_z)/T(1)^{\frac{1}{2}} + (2e_1R_{A1}(1,1) + 2e_2R_{A1}(2,1))(-p_y + q_y)/ \\
& T(1)^{\frac{1}{2}})\mathrm{e} + (-4\mathrm{e}_3\mathrm{R}_{\mathrm{A1}}(1,2) - 2\mathrm{e}_4\mathrm{R}_{\mathrm{A1}}(2,2) + 2\mathrm{e}_1\mathrm{R}_{\mathrm{A1}}(3,2)) \\
& T(1)^{\frac{1}{2}}/T(8)^{\frac{1}{2}} + (2e_4R_{A1}(1,2) - 4e_3R_{A1}(2,2) + 2e_2R_{A1}(3,2)) \\
& (-p_x + q_x)(p_y - q_y)/T(8)^{\frac{1}{2}}/T(1)^{\frac{1}{2}} + (2e_1R_{A1}(1,2) + \\
& 2e_2R_{A1}(2,2))(-p_x + q_x)(p_z - q_z)/T(8)^{\frac{1}{2}}/T(1)^{\frac{1}{2}})/T(28) - \\
& T(30)/T(28)^2((-4e_3R_{A1}(1,1) - 2e_4R_{A1}(2,1) + 2e_1R_{A1}(3,1))T(1)^{\frac{1}{2}}/ \\
& T(8)^{\frac{1}{2}} + (2e_4R_{A1}(1,1) - 4e_3R_{A1}(2,1) + 2e_2R_{A1}(3,1))(-p_x + \\
& q_x)(p_y - q_y)/T(8)^{\frac{1}{2}}/T(1)^{\frac{1}{2}} + (2e_1R_{A1}(1,1) + \\
& 2e_2R_{A1}(2,1))(-p_x + q_x)(p_z - q_z)/T(8)^{\frac{1}{2}}/T(1)^{\frac{1}{2}} -
\end{aligned}
$$

$$
\begin{aligned}
& ((2e_4R_{A1}(1,2) - 4e_3R_{A1}(2,2) + 2e_2R_{A1}(3,2))(p_z - q_z)/T(1)^{\frac{1}{2}} + \\
& (2e_1R_{A1}(1,2) + 2e_2R_{A1}(2,2))(-p_y + q_y)/T(1)^{\frac{1}{2}})\mathrm{e}))/(1 + \\
& T(30)^2/T(28)^2)/\pi - \frac{1}{2}/(T(22)^2 + T(21)^2 + T(19)^2)^{\frac{1}{2}}/ \\
& \lambda_{L1}(2T(22)(-4e_3b_{2x} - 2e_4b_{2y} + 2e_1b_{2z}) + 2T(21)(2e_4b_{2x} - \\
& 4e_3b_{2y} + 2e_2b_{2z}) + 2T(19)(2e_1b_{2x} + 2e_2b_{2y})) - \frac{1}{2}((((2e_4 \\
& R_{A2}(1,1) - 4e_3R_{A2}(2,1) + 2e_2R_{A2}(3,1))(p_z - q_z)/T(1)^{\frac{1}{2}} + \\
& (2e_1R_{A2}(1,1) + 2e_2R_{A2}(2,1))(-p_y + q_y)/T(1)^{\frac{1}{2}})\mathrm{e} + \\
& (-4e_3R_{A2}(1,2) - 2e_4R_{A2}(2,2) + 2e_1R_{A2}(3,2))T(1)^{\frac{1}{2}}/ \\
& T(8)^{\frac{1}{2}} + (2e_4R_{A2}(1,2) - 4e_3R_{A2}(2,2) + 2e_2R_{A2}(3,2))(-p_x + \\
& q_x)(p_y - q_y)/T(8)^{\frac{1}{2}}/T(1)^{\frac{1}{2}} + (2e_1R_{A2}(1,2) + \\
& 2e_2R_{A2}(2,2))(-p_x + q_x)(p_z - q_z)/T(8)^{\frac{1}{2}}/T(1)^{\frac{1}{2}})/ \\
& T(14) - T(16)/T(14)^2((-4e_3R_{A2}(1,1) - 2e_4R_{A2}(2,1) + 2e_1R_{A2}(3,1)) \\
& T(1)^{\frac{1}{2}}/T(8)^{\frac{1}{2}} + (2e_4R_{A2}(1,1) - 4e_3R_{A2}(2,1) + \\
& 2e_2R_{A2}(3,1))(-p_x + q_x)(p_y - q_y)/T(8)^{\frac{1}{2}}/T(1)^{\frac{1}{2}} + \\
& (2e_1R_{A2}(1,1) + 2e_2R_{A2}(2,1))(-p_x + q_x)(p_z - q_z)/T(8)^{\frac{1}{2}}/ \\
& T(1)^{\frac{1}{2}} - ((2e_4R_{A2}(1,2) - 4e_3R_{A2}(2,2) + 2e_2R_{A2}(3,2))(p_z - \\
& q_z)/T(1)^{\frac{1}{2}} + (2e_1R_{A2}(1,2) + 2e_2R_{A2}(2,2))(-p_y + q_y)/ \\
& T(1)^{\frac{1}{2}})\mathrm{e}))/(1 + \mathrm{T}(16)^2/\mathrm{T}(14)^2)/\pi
\end{aligned}
\tag{B.42}
$$

$$
\begin{aligned}
H_{RHCProw}(1,7) \;=\; & \frac{1}{2}/(T(36))^2 + T(35))^2 + T(33))^2)^{\frac{1}{2}}/ \\
& \lambda_{L1}(2T(36))(-2e_3b_{1y} + 2e_2b_{1z}) + 2T(35))(2e_3b_{1x} - 2e_1b_{1z}) + \\
& 2T(33))(-2e_2b_{1x} + 2e_1b_{1y})) + \frac{1}{2}((((2e_3R_{A1}(1,1) - \\
& 2e_1R_{A1}(3,1))(p_z - q_z)/T(1)^{\frac{1}{2}} + (-2e_2R_{A1}(1,1) + 2e_1R_{A1}(2,1)) \\
& (-p_y + q_y)/T(1)^{\frac{1}{2}})\mathrm{e} + (-2\mathrm{e}_3\mathrm{R}_{\mathrm{A1}}(2,2) + 2\mathrm{e}_2\mathrm{R}_{\mathrm{A1}}(3,2)) \\
& T(1)^{\frac{1}{2}}/T(8)^{\frac{1}{2}} + (2e_3R_{A1}(1,2) - 2e_1R_{A1}(3,2))(-p_x + \\
& q_x)(p_y - q_y)/T(8)^{\frac{1}{2}}/T(1)^{\frac{1}{2}} + (-2e_2R_{A1}(1,2) + \\
& 2e_1R_{A1}(2,2))(-p_x + q_x)(p_z - q_z)/T(8)^{\frac{1}{2}}/T(1)^{\frac{1}{2}})/ \\
& T(28) - T(30)/T(28)^2((-2e_3R_{A1}(2,1) + 2e_2R_{A1}(3,1))T(1)^{\frac{1}{2}}/ \\
& T(8)^{\frac{1}{2}} + (2e_3R_{A1}(1,1) - 2e_1R_{A1}(3,1))(-p_x + q_x)(p_y - \\
& q_y)/T(8)^{\frac{1}{2}}/T(1)^{\frac{1}{2}} + (-2e_2R_{A1}(1,1) + 2e_1R_{A1}(2,1)) \\
& (-p_x + q_x)(p_z - q_z)/T(8)^{\frac{1}{2}}/T(1)^{\frac{1}{2}} - ((2e_3R_{A1}(1,2) -
\end{aligned}
$$

$$
\begin{aligned}
&2e_1R_{A1}(3,2))(p_z-q_z)/T(1)^{\frac{1}{2}}+(-2e_2R_{A1}(1,2)+\\
&2e_1R_{A1}(2,2))(-p_y+q_y)/T(1)^{\frac{1}{2}})\mathrm{e}))/(1+\mathrm{T}(30)^2/\mathrm{T}(28)^2)/\pi-\\
&\frac{1}{2}/(T(22)^2+T(21)^2+T(19)^2)^{\frac{1}{2}}/\lambda_{L1}(2T(22)(-2e_3b_{2y}+\\
&2e_2b_{2z})+2T(21)(2e_3b_{2x}-2e_1b_{2z})+2T(19)(-2e_2b_{2x}+2e_1b_{2y}))-\\
&\frac{1}{2}((((2e_3R_{A2}(1,1)-2e_1R_{A2}(3,1))(p_z-q_z)/T(1)^{\frac{1}{2}}+\\
&(-2e_2R_{A2}(1,1)+2e_1R_{A2}(2,1))(-p_y+q_y)/T(1)^{\frac{1}{2}})\mathrm{e}+(-2\mathrm{e}_3\\
&R_{A2}(2,2)+2e_2R_{A2}(3,2))T(1)^{\frac{1}{2}}/T(8)^{\frac{1}{2}}+(2e_3R_{A2}(1,2)-\\
&2e_1R_{A2}(3,2))(-p_x+q_x)(p_y-q_y)/T(8)^{\frac{1}{2}}/T(1)^{\frac{1}{2}}+\\
&(-2e_2R_{A2}(1,2)+2e_1R_{A2}(2,2))(-p_x+q_x)(p_z-q_z)/\\
&T(8)^{\frac{1}{2}}/T(1)^{\frac{1}{2}})/T(14)-T(16)/T(14)^2((-2e_3R_{A2}(2,1)+\\
&2e_2R_{A2}(3,1))T(1)^{\frac{1}{2}}/T(8)^{\frac{1}{2}}+(2e_3R_{A2}(1,1)-2e_1R_{A2}(3,1))\\
&(-p_x+q_x)(p_y-q_y)/T(8)^{\frac{1}{2}}/T(1)^{\frac{1}{2}}+(-2e_2R_{A2}(1,1)+\\
&2e_1R_{A2}(2,1))(-p_x+q_x)(p_z-q_z)/T(8)^{\frac{1}{2}}/T(1)^{\frac{1}{2}}-\\
&((2e_3R_{A2}(1,2)-2e_1R_{A2}(3,2))(p_z-q_z)/T(1)^{\frac{1}{2}}+(-2e_2R_{A2}(1,2)+\\
&2e_1R_{A2}(2,2))(-p_y+q_y)/T(1)^{\frac{1}{2}})\mathrm{e}))/(1+\mathrm{T}(16)^2/\mathrm{T}(14)^2)/\pi \qquad \text{(B.43)}
\end{aligned}
$$

~

Bibliography

[AC95] A. R. Conway, *Autonomous Control of an Unstable Model Helicopter Using Carrier Phase GPS Only,* Ph.D. Dissertation, Stanford University, Dept. of Aeronautics and Astronautics, March 1995

[ADR97] A. Robertson, T. Corazzini, E. LeMaster, J. P. How, "Formation Sensing and Control Technologies for a Separated Spacecraft Interferometer," *Proceedings of the American Control Conference 1997,* San Diego, CA, Jan. 1997

[AG74] A. Gelb, *Applied Optimal Estimation,* MIT Press, Cambridge, MA, 1974

[AH96] A. Hassibi, S. Boyd, "Integer Parameter Estimation in Linear Models with Applications to GPS," *Proceedings of 35th IEEE Conference on Decision and Control,* Kobe, Japan, Dec. 1996

[AJVD96] A. J. Van Dierendonck, "GPS Receivers," *Global Positioning System: Theory and Applications, Volumes 1,* Chapter 8, American Institute of Aeronautics and Astronautics(AIAA), Progress in Astronautics and Aeronautics Series, Volumes 163 and 164, Washington, DC, 1996

[BH75] A. E. Bryson,Jr., Y. C. Ho, *Applied Optimal Control,* Hemisphere Publishing Corp., New York, NY, 1975

[BS91] B. A. Stein, W. L. Tsang, "Stabilization of Low Orbiting Spacecraft Using GPS," *Proceedings of the Institute of Navigation 47th Annual Meeting,* Williamsburg, VA, June 10-12, 1991

[CA96] J. C. Adams, J. P. How, *GPS-on-a-Chip Project Status Report,* Stanford University, Dept. of Aeronautics and Astronautics, Dec. 10, 1996

[CB82] C. A. Balanis, *Antenna Theory: Analysis and Design,* John Wiley and Sons, Inc., New York, NY, 1982

[CB92] C. A. Balanis, "Antenna Theory: A Review," *Proceedings of the Institute of Electrical and Electronics Engineers(IEEE),* volume 80, Jan. 1992

[CC92] C. E. Cohen, *Attitude Determination Using GPS,* Ph.D. Dissertation, Stanford University, Dept. of Aeronautics and Astronautics, Dec. 1992

[CC96] C. Cohen, "Attitude Determination," *Global Positioning System: Theory and Applications, Volumes 2,* Chapter 19, American Institute of Aeronautics and Astronautics(AIAA), Progress in Astronautics and Aeronautics Series, Volumes 163 and 164, Washington, DC, 1996

[CG96] C. Goad, "Surveying with the Global Positioning System," *Global Positioning System: Theory and Applications, Volumes 2,* Chapter 18, American Institute of Aeronautics and Astronautics(AIAA), Progress in Astronautics and Aeronautics Series, Volumes 163 and 164, Washington, DC, 1996

[CL94] C. E. Cohen, E. G. Lightsey, B. W. Parkinson, "Spaceflight Tests of Attitude Determination Using GPS," *International Journal of Satellite Communications,* volume 12, 1994

[DGE98] D. Gebre-Egziabher, R. Hayward, J. D. Powell, "Low-cost GPS/inertial Attitude Heading Reference System (AHRS) for General Aviation Applications," *Proceedings of the 1998 IEEE Position Location and Navigation Symposium,* Palm Springs, CA, 1998

[DK94] D. T. Knight, "A New Method for Instantaneous Ambiguity Resolution," *Proceedings of the Institute of Navigation 7th International Technical Meeting,* Salt Lake City, UT, Sept. 1994

[DL96] D. G. Lawrence, *Aircraft Landing Using GPS,* Ph.D. Dissertation, Stanford University, Dept. of Aeronautics and Astronautics, Sept. 1996

[EGL96] E. G. Lightsey, B. W. Parkinson, "GPS Based Attitude Determination on Nonaligned Antenna Arrays," *Proceedings of the Institute of Navigation ION GPS-96 Conference,* Kansas City, MO, Sept. 1996

[EO98] E. A. Olsen, C.-W. Park, J. P. How, "3-D Formation Flight Using Differential Carrier-phase GPS Sensors," *Proceedings of the Institute of Navigation ION GPS-98 Conference,* Nashville, TN, Sept. 1998

[EO99] E. A. Olsen, *GPS Sensing for Formation Flying Vehicles,* Ph.D. Dissertation, Stanford University, Dept. of Aeronautics and Astronautics, Sept. 1999

[FB96] F. H. Bauer, J. R. O'Donnell, "Space-Based GPS: 1996 Mission Overview," *Proceedings of the Institute of Navigation ION GPS-96 Conference,* Kansas City, MO, Sept. 1996

[FB97] F. Bauer, J. Bristow, D. Folta, K. Hartman, D. Quinn, J. P. How, "Satellite Formation Flying Using an Innovative Autonomous Control System

(AUTOCON) Environment," *Proceedings of the American Institute of Aeronautics and Astronautics (AIAA) Guidance Navigation and Control Conference,* New Orleans, LA, May 1997

[FB98] F. H. Bauer, K. Hartman, E. G. Lightsey, "Spaceborne GPS: Current Status and Future Visions," *1998 IEEE Aerospace Conference Proceedings,*, IEEE, Aspen, CO, March 1998

[FPE86] G. F. Franklin, J. D. Powell, A. Emami-Naeini, *Feedback Control of Dynamic Systems*, Addison-Wesley Publishing Company, New York, NY, 1986

[FPW80] G. F. Franklin, J. D. Powell, M. L. Workman, *Digital Control of Dynamic Systems*, Addison-Wesley Publishing Company, New York, NY, 1980

[FVG91] F. Van Graas, M. Braasch, "GPS Interferometric Attitude and Heading Determination: Initial Flight Test Results," *Navigation,* volume 38, no. 4, Winter 1991-1992, pp. 297-316

[GL97] E. Glenn Lightsey, *Development and Flight Demonstration of a GPS Receiver for Space,* Ph.D. Dissertation, Stanford University, Dept. of Aeronautics and Astronautics, Jan. 1997

[GPS96] B. W. Parkinson, J. J. Spilker,Jr., P. Axelrad, P. Enge, *Global Positioning System: Theory and Applications, Volumes 1 and 2,* American Institute of Aeronautics and Astronautics(AIAA), Progress in Astronautics and Aeronautics Series, Volumes 163 and 164, Washington, DC, 1996

[HH80] P. Horowitz, W. Hill, *The Art of Electronics*, Cambridge University Press, New York, NY, 1980

[HT97] E. Harrison Teague, *Flexible Structure Estimation and Control Using the Global Positioning System,* Ph.D. Dissertation, Stanford University, Dept. of Aeronautics and Astronautics, June 1997

[HU95] H. U. Uematsu, B. W. Parkinson, "GPS Receiver Design and Requirement Analysis for the Stanford Gravity Probe B Relativity Mission," *Proceedings of the Institute of Navigation ION GPS-95 Conference,* Palm Springs, CA, Sept. 1995

[JC97] J. L. Crassidis, F. L. Markley, "New Algorithm for Attitude Determination Using Global Positioning System Signals," *AIAA Journal of Guidance, Control, and Dynamics,* vol. 20, no. 5, Sept.-Oct. 1997

[JCA96] J. C. Adams, A. D. Robertson, K. Zimmerman, J. P. How, "Technologies for Spacecraft Formation Flying," *Proceedings of the Institute of Navigation ION GPS-96 Conference,* Kansas City, MO, Sept. 1996

[JCA98] J. C. Adams, J. P. How, "GPS Attitude Determination for Spinning Spacecraft with Non-aligned Antenna Arrays," *Proceedings of the Institute of Navigation National Technical Meeting ION NTM-98 Conference,* Long Beach, CA, Jan. 1998

[JCA298] J. C. Adams, J. P. How, "Experiments in GPS Attitude Determination for Spinning Spacecraft with Non-aligned Antenna Arrays," *Proceedings of the Institute of Navigation ION GPS-98 Conference,* Nashville, TN, Sept. 1998

[JE79] J. F. Ellis, "Interferometric Attitude Determination with the Global Positioning System," *Journal of Guidance and Control,* volume 2, no. 6, Nov-Dec 1979, pp. 522-527

[JG94] J. I. Galdos, T. N. Upadhyay, T. Doyle, B. Wu, P. Zetocha, "Reconfigurable GPS Receiver for Spacecraft Attitude Determination," *Proceedings of the Institute of Navigation National Technical Meeting ION NTM-94 Conference,* Alexandria, VA, Jan. 1994

[JH99] J. P. How, *ORION Preliminary Design Review Presentation,* Stanford University, Dept. of Aeronautics and Astronautics, April 9. 1999

[JJS91] J. J. Slotine, W. Li, *Applied Nonlinear Control,*"Lyapunov Analysis of Non-Autonomous Systems", Prentice Hall, Englewood Cliffs, NJ, 1991, pp. 105-116

[JS97] J. M. Stone, R. Hayward, *Conversations regarding master-master tracking channel architecture,* Stanford, CA, Jan. 1997, Patent pending, Application No. 09/273235, Filed March 18, 1999.

[JS98] J. M. Stone, J. D. Powell, "Precise Positioning with GPS Near Obstructions by Augmentation with Pseudolites," *Proceedings of the IEEE PLANS 1998,* Palm Springs, CA, 1998

[JS99] J. M. Stone, J. D. Powell, "Precise Positioning Using GPS Satellites and Pseudolites Emphasizing Open Pit Mining Applications," *4th International Space Symposium for Navigation Technology and Applications,* Brisbane, Australia, July 1999

[JSNTM99] J. M. Stone, E. A. LeMaster, J. D. Powell, S. M. Rock, "GPS Pseudolite Transceivers and their Applications," *Proceedings of the Institute of Navigation National Technical Meeting ION NTM-99 Conference,* San Diego, CA, Jan. 1999

[JSGPS99] J. M. Stone, J. D. Powell, "Carrier Phase Model for Satellites and Pseudolites," *Proceedings of the Institute of Navigation ION GPS-99 Conference,* Nashville, TN, Sept. 1999

[JW78] J. R. Wertz, *Spacecraft Attitude Determination and Control,* D. Reidel Publishing Company, Boston, MA, 1978

[JW91] J. T. Wu, S. C. Wu, G. A. Hajj, W. I. Bertiger, S. M. Lichten, "Effects of Antenna Orientation on GPS Carrier Phase," *Advances in the Astronautical Sciences,* 91-537, 1991

[KB94] J. K. Brock, R. Fuller, S. Hur-Diaz, J. Rodden, "GPS Attitude and Orbit Determination for Space," *Proceedings of the Institute of Navigation ION GPS-94 Conference,* Salt Lake City, UT, Sept. 1994

[KB95] J. K. Brock, R. Fuller, B. Kemper, D. Mleczko, A. Tadros, "GPS Attitude Determination and Navigation Flight Experiment," *Proceedings of the Institute of Navigation ION GPS-95 Conference,* Palm Springs, CA, Sept. 1995

[KL97] K. Lau, S. Lichten, L. Young, "An Innovative Deep Space Application of GPS Technology for Formation Flying Spacecraft," *Proceedings of the American Institute of Aeronautics and Astronautics (AIAA) Guidance Navigation and Control Conference,* San Diego, CA, July 1996

[KZ95] K. R. Zimmerman, R. H. Cannon Jr., "Experimental Demonstration of GPS for Rendezvous Between Two Prototype Space Vehicles," *Proceedings of the Institute of Navigation ION GPS-95 Conference,* Palm Springs, CA, Sept. 1995

[KZ96] K. R. Zimmerman, *Experiments in the Use of the Global Positioning System for Space Vehicle Rendezvous,* Ph.D. Dissertation, Stanford University, Dept. of Aeronautics and Astronautics, Dec. 1996

[LK89] L. R. Kruczynski, A. G. Evans, B. R. Hermann, "Using GPS to Determine Vehicle Attitude: USS Yorktown Test Results," *Proceedings of the Institute of Navigation ION GPS-89 Conference,* Colorado Springs, CO, Sept. 1989

[LW95] L. M. Ward, P. Axelrad, "Spacecraft Attitude Determination Using GPS: Methodology and Results for RADCAL," *Proceedings of the Institute of Navigation Annual Meeting,* Alexandria, VA, June 1995

[LW96] L. M. Ward, P. Axelrad, "A Combined Filter for GPS-Based Attitude and Baseline Estimation," *Proceedings of the Institute of Navigation ION GPS-96 Conference,* Kansas City, MO, Sept. 1996

[MC96] M. Colavita, C. Chu, E. Mettler, M. Milman, D. Royer, S. Shakian, J. West, *Multiple Spacecraft Interferometer Constellation (MUSIC),* Jet Propulsion Laboratory - Advanced Concepts Program, Report Number JPL D-13369, Pasadena, CA, Feb. 1996

[MOC97] M. L. O'Connor, *Carrier Phase Differential GPS for Automatic Control of Land Vehicles,* Ph.D. Dissertation, Stanford University, Dept. of Aeronautics and Astronautics, March 1997

[PA91] P. Axelrad, *A Closed Loop GPS Based Orbit Trim System for Gravity Probe-B,* Ph.D. Dissertation, Stanford University, Dept. of Aeronautics and Astronautics, March 1991

[PM93] P. J. Melvin, A. S. Hope, "Satellite Attitude Determination with GPS," *Advances in the Astronautical Sciences*, American Institute of Aeronautics and Astronautics, vol. 85, part 1, pp. 59-78, 1993

[PM96] P. J. Melvin, L. M. Ward, P. Axelrad, "Analysis of GPS Attitude Data from a Slowly Rotating Symmetrical Gravity Gradient Satellite," *Journal of the Astronautical Sciences,* vol. 44, no. 4, Oct-Dec 1996, pp. 515-539

[RB87] R. H. Battin, *An Introduction to the Mathematics and Methods of Astrodynamics*, American Institute of Aeronautics and Astronautics(AIAA), Education Series, New York, NY, 1987

[RB97] R. E. Best, *Phase-Locked Loops: Design, Simulation, and Applications*, McGraw-Hill, Inc., New York, NY, 1997

[RF97] R. Fuller, D. Hong, S. Hur-Diaz, J. Rodden, M. Tse, "GPS Tensor: An Attitude and Orbit Determination System for Space," *Proceedings of the Institute of Navigation ION GPS-97 Conference,* Kansas City, MO, Sept. 1997

[RH97] R. Hayward, D. Gebre-Egziabher, M. Schwall, J. D. Powell, J. Wilson, "Inertially Aided GPS-based Attitude Heading Reference System (AHRS)

for General Aviation Aircraft," *Proceedings of the Institute of Navigation ION GPS-97 Conference*, Kansas City, MO, Sept. 1997

[RH98] R. Hayward, J. D. Powell, "Ultra Short Baseline GPS Attitude," *Proceedings of the Institute of Navigation ION GPS-98 Conference*, Nashville, TN, Sept. 1998

[SAC94] B. R. Schupler, R. L. Allshouse, T. A. Clark, "Signal Characteristics of GPS User Antennas," *Navigation*, volume 41, no. 3, Fall 1994, pp. 227-295

[TC94] T. Clark, D. Varney, F. Bauer, "A Low Cost Spacecraft Receiver for Orbit and Attitude Determination," *Proceedings of the Institute of Navigation ION GPS-94 Conference*, Salt Lake City, UT, Sept. 1994

[TC97] T. Corazzini, A. D. Robertson, J. C. Adams, J. P. How, "Experimental Demonstration of Differential Carrier Phase GPS for Precision Formation Flying Spacecraft,"

[TC98] T. Corazzini, A. Robertson, J. C. Adams, A. Hassibi, J. P. How, "Experimental Demonstration of GPS as a Relative Sensor for Formation Flying Spacecraft," *Navigation*, volume 45, no. 3, Fall 1998, pp. 195-207

[TY96] T. Yunck, "Orbit Determination," *Global Positioning System: Theory and Applications, Volumes 2*, Chapter 21, American Institute of Aeronautics and Astronautics(AIAA), Progress in Astronautics and Aeronautics Series, Volumes 163 and 164, Washington, DC, 1996

[VS76] V. W. Spinney, "Application of the Global Positioning System as an Attitude Reference for Near-Earth Users," *Bicentennial National Aerospace*

Symposium on New Frontiers in Aerospace Navigation,, Institute of Navigation, Warminster, PA, April 1976

[WB83] W. S. Burgett, S. D. Roemerman, P. W. Ward, "Development and Applications of GPS Determined Attitude," *NTC '83 - IEEE 1983 National Telesystems Conference: Space Systems for the National Well-being and Security,*, IEEE, San Francisco, CA, 1983

[WB84] W. H. Beyer, Ed., "Spherical Trigonometry," *CRC Standard Mathematical Tables, 27th Edition*, Chapter V, CRC Press, Boca Raton, FL, 1984